A THEORETICAL AND EXPERIMENTAL ANALYSIS OF THE NO-LOAD AIR GAP MAGNETIC FIELD IN SQUIRREL CAGE INDUCTION MACHINES

BY

Ridha Ahmed Muhammed, M.Sc.

SUBMITTED FOR THE DEGREE OF DOCTOR OF PHILOSOPHY

AT

THE UNIVERSITY OF ASTON IN BIRMINGHAM

DECEMBER, 1976

SUMMARY

In induction machines the tooth frequency losses due to permeance variation constitute a significant portion of the total loss. In order to predict and estimate these losses it is essential to obtain a clear understanding of the no-load distribution of the air gap magnetic field and the magnitude of flux pulsation in both stator and rotor teeth. The existing theories and methods by which the air gap permeance variation in a doubly slotted structure is calculated are either empirical or restricted.

The main objective of this thesis is to obtain a detailed analysis of the no-load air gap magnetic field distribution and the effect of air gap geometry on the magnitude and waveform of the tooth flux pulsation. In this thesis a detailed theoretical and experimental analysis of flux distribution not only leads to a better understanding of the distribution of no-load losses but also provides theoretical analysis for calculating the losses with greater accuracy.

ACKNOWLEDGEMENTS

The author wishes to thank his supervisor Dr.I.Thomas for his advice and valuable assistance throughout the research course. The author is particularly indebted to Mr.B.James for his continuous encouragement and for his careful work in reading and checking the draft thesis and making this work possible.

Profitable discussions were provided by Mr.J.R.Reed (The Department of Mathematics),and Dr.M.Jevons. Experimental help from Mr.A.L.Stevenson and his staff,in particular Mr.J.Lightfoot,in the Electrical Machines Research Centre is gratefully acknowledged.

Special thanks are due to Prof.E.J.Davies for providing University Studentship and his interest in the research work.

CONTENTS

PAGE

LIST OF SYMBOLS

A	vector potential (Wb/m)
A_m	coefficient of the potential function in a stator slot (eqn. 4-1)
A_{sn}	effective amperes per meter of the stator periphery(A/m)
a	width of a rectangular conductor(Ch.3),(m)
$2a$	thickness of a lamination (m)
a_m	amplitude of the potential function along stator slot opening(eqn. 10-29)
B	flux density (T)
B_k	coefficient of the potential function in the air gap (eqn.4-2)
$\hat{B}_m$	amplitude of the radial flux density in the air gap(T)
$\dot{B}_m$	amplitude of the flux density in complex number
b_m	amplitude of the potential function along rotor slot opening (eqn. 10-31a)
C	Carter's coefficient
C_1	Carter's coefficient for the case of smooth rotor and slotted stator
C_2	Carter's coefficient for the case of smooth stator and slotted rotor
C_k	coefficient of the potential function in the air gap (eqn. 4-2)
C_m	Carter's coefficient for the case when the stator's teeth are at opposite potential, coefficient of the field intensity components in rotor laminations(eqns. 10-44,10-45,and 10-46)
D	stator bore (m)

D_m	coefficient of the potential function in rotor slot (eqn. 4-3)
d	depth of penetration $\sqrt{\frac{\rho}{\omega\mu_0\mu}}$ (m), height of a rectangular conductor(ch.3) (m)
dis	displacement of a rotor slot with respect to a stator slot (ch.4 and Fig. 4.1) (mm)
E	electric field strength (V/m)
F	m.m.f. (At)
$\hat{F}$	amplitude of an m.m.f. (At)
F_g	air gap m.m.f. (At)
F_R	stator m.m.f. wave with respect to rotor (At)
F_S	stator m.m.f. (At)
f	fringing cofficient (Appendix 10.3)
g	air gap length (m),(mm in Section 4.3.1. and Ch.6)
H	magnetic field strength (A/m)
$\bar{H}$	conjugate function of the field intensity in rotor iron
H_m	amplitude of the field strength (A/m)
$\dot{H}_m$	amplitude of the field strength in complex number(A/m)
H_{yr}	peripheral component of the field intensity in rotor laminations (A/m)
H_{xr}	axial component of the field intensity in rotor laminations (A/m)
H_{zr}	radial component of the field intensity in rotor laminations (A/m)
h_r	height of rotor slot (mm)(Fig.4.1)
I	current (A)
I_A	r.m.s. phase current (A)
I_S	stator current loading (A/m)
i	integer denoting the order of harmonic(Appendix 10.4)

J	current density (A/m^2)
$\hat{J}$	peak of the current density wave (A/m^2)
J_{yr}	peripheral component the eddy current density in rotor lamination (A/m^2)
J_{xr}	axial component of the eddy current density in rotor lamination (A/m^2)
j	$\sqrt{-1}$
K	current loading (A/m) (Ch.2), complex coefficient (Appendix 10.3)
k	integer indicating the order of the harmonic (Ch.4 and Appendix 10.4)
kd	distribution factor (numeric)
kp	pitch factor (numeric)
k	total winding factor (numeric)
ℓ	length of the J-probes (mm)
$M_{(2m+1)}$	coefficient of the peripheral eddy current density component in rotor lamination (eqn.10-48)
m	number of phases, integer denoting the order of harmonics
$N_{(2m+1)}$	coefficient of the axial eddy current density component in rotor lamination (eqn.10-47)
n	integer indicating the order of harmonics
P	power loss (W), permeance (H)
P_o	average air gap permeance (H)
P_g	air gap permeance wave
Ph_2	fundamental rotor hysteresis loss (W)
P_m	amplitude of the air gap permeance harmonics (H)
P_n	coefficient of the potential function in the air gap (eqn.10-49)

P_r	half of rotor slot width (rad in Ch.4, see also page 243)
P_s	half of stator slot width (rad in Ch.4, see also page 243)
p	number of pole pairs
Q	number of phase-belts per pole
R	winding resistance (Ω)
R_1	resistance of the primary per phase (Ω)
R'_2	resistance of the secondary per phase, referred to the primary (Ω)
S	slot width (m)
S_1	stator slot width (m), (rad in Ch.4, see also page 243)
S_2	rotor slot width (m), (rad in Ch.4, see also page 243)
s	slip (per unit)
T	turns in seies per pole per phase
t	time (S), tooth width (m)
V	line voltage (V)
X	reactance (Ω)
X_1	leakage reactance of the primary per phase (Ω)
X'_2	leakage reactance of the secondary per phase, referred to the primary (Ω)
x,y,z	space co-ordinates
α	$\sqrt{\frac{\omega \mu_0}{2\rho}}$
β	coefficient for permeance loss
θ_1	electrical space angle relative to a fixed point on the stator (deg.)
θ_2	electrical space angle relative to the peak of the fundamental stator m.m.f. (deg.)
μ	relative permeability
$\dot{\mu}$	complex permeability
μ_0	magnetic constant (4×10^{-7} H/m)
μ_2	relative rotor permeability

μ_Δ	incremental relative permeability
ζ	fractional pitch(ratio of coil span to pole pitch)
ρ	resistivity (Ω -m)
σ	permeance loss coefficient, conductivity of conductors
2τ	primary slot pitch (rad) (Fig.4.1, see also page 243)
$2\tau_1$	secondary slot pitch (rad) (Fig.4.1, see also page 243)
Φ	potential function, flux (Wb)
Φ_1	potential function in a stator slot (Ch.4)
Φ_2	potential function in the air gap (Ch.4)
Φ_3	potential function in a rotor slot (Ch.4)
Φ_P	peripheral air gap leakage flux (Wb)
Φ_R	radial air gap flux per pole length (Wb)
ω	angular frequency (rad/S)
ω_1	fundamental angular frequency (rad/S)

1. Introduction

The flux density distribution in the air gap of electrical machines is of fundamental importance in the determination of torque, reactances, losses, and magnetically induced mechanical effects such as noise and vibration. As machine ratings have increased and losses have assumed greater capital importance, the accuracy of predicting various electromagnetic effects associated with the air gap flux density is becoming of increased importance.

It is well known that slot openings cause ripples in the air gap flux density wave and the discontinuities of ampere conductor concentrations and phase grouping cause steps in the m.m.f. wave. Furthermore, saturation of iron imposes an additional distortion on the shape of the flux density wave. Generally, the harmonics due to these irregularities in the resulting air gap flux density wave contribute to dips in the speed-torque curve, additional losses in the iron, copper, and to noise and vibration.

In induction machines the air gap length is small and the effect of slot openings on the harmonic content of flux density wave is substantial. No-load iron losses are defined as the losses associated with the flux required to produce rated terminal voltage on open circuit at rated speed. These losses are normally measured by a no-load test, making appropriate corrections for copper and mechanical losses (i.e. friction and windage losses). Standard elementary theory regards these losses as composed of two components, the one due to the variation of radial flux in the stator teeth and the other one due to the variation of tangential flux in the stator core, and loss calculations are based on these two flux variations and on loss characteristics supplied by the coreplate manufacturers. The air gap flux density wave, in accordance with

this elementary theory, is assumed to be purely sinusoidal. It is, therefore, commonly found that measured losses appreciably exceed the values calculated on this basis. The degree of discrepancy varies widely with the type, size and design of machine. In order to correlate test and calculated losses, it is customary to resort to the use of empirical multiplying factors. This type of empirical factor allows for all the additional components of loss which are not taken into account in the basic analysis and it is, therefore, not surprising that the empirical factors should vary from case to case. The need for resorting to empirical factors arises from the fact that the theoretical analysis of the additional losses is complex and the existing formulae are not reliable. Since the irregularities in the air gap flux density wave are neglected in the elementary theory, it follows that the discrepancy between the measured and calculated losses is due to the flux density harmonics (providing no extra losses are caused by manufacturing imperfections).

The theoretical treatment of flux density harmonics and the losses induced by them is associated with two problems:

(1) Consideration of the non-linear property of the iron and the interaction of field harmonics.

(2) Consideration of the geometry of the machine.

In connection with the first problem a great deal of theoretical and experimental work has been made to investigate the behaviour of the magnetic field inside iron.[1-5] All of these investigations are practically related to a simplified geometry, namely semi-infinite blocks. It is, therefore, a standard practice to reduce the geometry of electrical machines to a simplified form so that the known theories can be applied and a reasonable solution is

obtained. However, most of the confusion and erronous assumptions originate from the process of translating the actual field into that which exists in a simplified geometry.

Although, the technical literature on this subject is abundant and a great deal of work has been done to minimise the empirical factors from loss equations, the basic analysis of the air gap flux density and iron losses suffer from inadequate treatment. This is largely due to the need to make assumption and simplification in order to obtain a relatively simple form of analytical solution. Most of these assumptions and simplifications are either incompatible with the physical phenomena in the actual machine or appreciably over-simplify the geometry of the machine.

This thesis is primarily concerned with the problem of the air gap permeance wave in a doubly slotted induction machine and the resulting tooth pulsation losses in laminated iron.

In Chapter 2 the simplified theory of the air gap field is discussed. This chapter provides a graphical illustration of the total harmonic variation in a smooth air gap and indicates the complex nature of the loss distribution on the rotor surface. The effect of winding factors on the redistribution of flux density harmonics is also illustrated.

In Chapter 3 a detailed discussion of the literature regarding the geometrical factors and the treatment of the basic flux components is given.

Chapter 4 is entirely devoted to the analysis of a doubly slotted air gap (i.e. when both stator and rotor are slotted). In this chapter an analytical solution of the air gap permeance wave is given. It is shown that the air gap geometry is a source of continuous distortion of the air gap flux wave and the losses

are greatly affected by the harmonic contents of the permeance wave. Chapter 5 reviews the linear and non-linear theory of iron losses and a critical appraisal of the literature is given.

Chapters 6, 7 and 8 are concerned with the experimental machine and the measurements of losses and various flux components. Extensive experimental work has been carried out to investigate the waveforms of the flux entering the surface and the tooth body of the rotor. The distribution of current density in the bar of the cage winding is also shown. A detailed discussion on the shape of the waveforms obtained and a comparison between experiment and theory is given.

Chapter 9 concludes the thesis with comments and suggestions for future work.

Chapter 10 is assigned to appendices. In this chapter the mathematical analysis and the derivation of formulae which are given by the author are included. Also, in this chapter, an analytical treatment of eddy current losses in laminated iron (based on linear theory) is given. The proposed analysis may be verified by future experimental work and used for calculating the losses.

The effect of saturation in induction machines may be best treated as a modification of the unsaturated case, therefore no attempt is made in this work to account for saturation, but its effect is illustrated in the experimental part of this thesis.

2.0 The Simplified Theory of the Air Gap Field

2.1 Introduction

The two main sources of high frequency copper and iron losses in the rotors of induction machines are the permeance and winding harmonics. These two types of harmonics always co-exist and the only feasible method of calculating their combined losses is based upon the linear superposition of the induced voltages or currents due to each of them.

Experimental results indicate that the magnitude of losses caused by the winding harmonics varies approximately as the square of the current[6], so that in this respect the effect of winding harmonics is appreciable only when the machine is on load. Although this thesis is mainly concerned with the analysis of the air gap permeance wave, nevertheless it is important to review the nature of the field components due to the winding harmonics, since these components also appear at no load and associated losses can be significant in machines having large magnetizing currents[6].

The winding harmonics are best treated by making use of the simplified assumptions of a smooth air gap and infinitely permeable iron. The latter assumption can be readily dropped and replaced by constant permeability and this is discussed in Chapter 5. The permeance harmonics are a source of h.f. copper and iron losses in both stator and rotor and they are discussed in Chapters 3 and 4.

It is well known that balanced polyphase sinusoidal currents flowing through a polyphase winding produces a travelling m.m.f. wave which is neither, basically, sinusoidal nor of constant shape. This continually changing shape of the travelling wave can be conveniently illustrated by replacing each phase-band of

the stator winding by a current sheet varying sinusoidally in time, but whose instantaneous linear density is constant over the phase-band width. The corresponding m.m.f. wave is then obtained by integrating the resultant current distribution in space at each instant of time. By using this procedure, the diagrams of currents and m.m.fs. space distribution waveforms of a 3-phase, 60° belt, full pitch winding at five consecutive instants of time are shown in Figs. 2.1(a) and 2.1(b). This principle has been used in most text books to give a graphical illustration of the rotating magnetic field.[7,8]

Normally, such travelling waves are analysed into harmonic components using the familiar Fourier method. Such an analysis shows that despite the different shapes of instantaneous m.m.f. distributions, each individual harmonic, including the fundamental, has precisely the same magnitude in all various shapes shown in Fig. 2.1. But, the phase shifts between the harmonics at various instants of time are not the same. In this manner the geometric pattern assumed by the m.m.f. wave is reduced into multitudes of harmonics gliding past each other at different speeds and directions, depending on the order of the harmonic. Generally, the harmonic components of the resultant travelling m.m.f. wave, excluding the fundamental, are divided into two categories:

(i) The phase-band m.m.f. harmonics.

(ii) The slot m.m.f. harmonics.

These two groups produce their own effects, but the loss mechanism is the same for each. Such division is, however, convenient for their analysis (for example, for the calculation

of zig-zag and phase-belt reactances - see Reference 7).

By considering the mathematical expressions of these harmonics, it is difficult to visualise their total effect. A conceptual picture of the effect of all harmonics other than the fundamental may be obtained graphically. If the fundamental m.m.f. harmonic is substracted from the total m.m.f. wave, then the resultant is the total harmonic components. In this way it is possible to obtain the variation of the total harmonic components with respect to stator or rotor by considering the stator m.m.f. wave shapes at various instants of time and by fixing the origin of the co-ordinates relative to a point on stator.

Although, the mathematical and graphical analysis of the harmonic variations given in this chapter are based on the assumption of smooth air gap and absence of saturation, they are important because they provide an indication of the magnitude of losses and their distribution on the rotor surface.

2.2. The m.m.f. Harmonics and the Current Loading Distribution

The resultant expression for the m.m.f. of a balanced 3-phase winding with an integral number of coils per phase group and with the origin of the electrical angle θ_1, measured on the stator, taken to be at the centre line of phase-A, is given by: (See Reference 7 where a routine method for determining the magnitude of the harmonics of the air gap m.m.f. wave produced by a current carrying stator winding, no matter how complicated its arrangements is explained in detail).

$$F_s = \frac{3\sqrt{2}}{\pi p} T \times I_A \left\{ k_{\omega 1} \cos(\theta_1 - \omega_1 t) + \sum_{n=1}^{\infty} \frac{k_{\omega(6n\pm1)}}{(6n\pm1)} \cos\left[(6n+1)\theta_1 \mp \omega_1 t\right] \right\}$$

.....(2-1)

where T – turns in series per pole per phase

n – an integer 1, 2, 3, ... etc.

p – number of pole pairs.

I_A – r.m.s. of the phase-A current.

$\frac{+}{-}, \frac{-}{+}$ – denote pairs of harmonics, the first of which takes the lower sign.

t – time, is taken zero at the instant when the current in phase-A is maximum.

The winding factors $k\omega_1$ and $k\omega_{(6n\pm1)}$ are the product of three factors and these are as follows:

(1) kp_1, and $kp_{(6n\pm1)}$ are the pitch factors and given by

$$\left.\begin{aligned} kp_1 &= \sin\left(\frac{\Psi}{2}\right) \\ kp_{(6n\pm1)} &= \sin\left[\frac{(6n\pm1)\Psi}{2}\right] \end{aligned}\right\} \qquad (2\text{-}2)$$

where Ψ – coil pitch in electrical degrees.

(2) kd_1, and $kd(6n\pm1)$ are the distribution factors and given by

$$\left.\begin{aligned} kd_1 &= \frac{\sin\left(\frac{\pi}{2Q}\right)}{q\sin\left(\frac{\pi}{2qQ}\right)} \\ kd_{(6n\pm1)} &= \frac{\sin\left[\frac{(6n\pm1)\pi}{2Q}\right]}{q\sin\left[\frac{(6n\pm1)\pi}{2qQ}\right]} \end{aligned}\right\} \qquad (2\text{-}3)$$

where Q – number of phase belts per pole.

q – number of slots per phase.

(3) ks_1 and $ks_{(6n\pm1)}$ are the slot width factors and given by

$$\left.\begin{aligned} ks_1 &= \frac{\sin\left(\frac{S}{2}\right)}{\left(\frac{S}{2}\right)} \\ ks_{(6n\pm1)} &= \frac{\sin\left[\frac{(6n\pm1)}{2}S\right]}{\frac{(6n\pm1)}{2}S} \end{aligned}\right\} \qquad (2\text{-}4)$$

where S – slot width in electrical radians.

The slot width factors result from the assumption that each slot

ampere conductor is equivalent to a current, uniformly distributed over a circumferential distance equal to the slot opening. This concept is an improvement on the concentrated slot current used in the usual procedure for determining the air gap m.m.f. The slot width factors are derived from the analogy of distribution factors, by replacing $\frac{\pi}{Q}$ of the equation (2-3) by S, and making q tend to infinity. In Appendix 10.1 it is shown that for a stator winding in which Q = 3, the slot width factors remain positive until the harmonic order becomes greater than $\left[\left(\frac{t}{S} + 1\right) \times (\text{first order of slot harmonic})\right]$, where t is the stator tooth width.

The pitch and distribution factors are comprehensively treated in most text books and particularly useful graphs and tables are given in References 8,9,10

The particular harmonics of the expression (2-1) which merit attention because of their magnitude and the importance of their effect in determining the shape of the total harmonic variation are:

(a) The phase-belt harmonics which are of the order $n=6k\pm1$, where $k \neq q, 2q, 3q \ldots$ and q is the number of slots per pole per phase. These harmonics fit the approximate triangles that form the difference between the stator m.m.f. and the fundamental (see Figure 2.2).

(b) The slot harmonics which are of the order $n=6k\pm1$, where $k=q, 2q, 3q, \ldots\ldots$ These harmonics fit the slot steps in the m.m.f. wave, and they have winding factors equal in magnitude to that of the fundamental (see Fig. 2.6).

The stator current loading can be obtained from the stator m.m.f. wave expressed by equation (2-1). The current loading or the effective amperes per meter of the stator periphery is defined by the following expression:

$$A_{sn}=\frac{2QTI_A k_{\omega n}}{D\pi} \qquad (2\text{-}5)$$

where D – diameter of the stator periphery.

Taking into account the expression (2-5) and differentiating equation (2-1) with respect to θ_1, the corresponding wave of stator current loading is obtained and given by

$$I_S=\frac{\partial F_S}{\partial \theta_1}=-K_1 \sin(\theta_1-\omega t)-\sum_{n=1}^{\infty} K_{(6n\pm1)} \sin\left[(6n\pm1)\theta_1 \mp \omega_1 t\right] \qquad (2\text{-}6)$$

where $K_1=\frac{\sqrt{2}\ D\ A_{sn}}{2p}$

and

$$K_{(6n\pm1)}=\frac{\sqrt{2}\ DA_{s(6n\pm1)}}{2p}$$

for $Q = 3$

for $Q = 3$

As indicated in the introduction of this chapter, it is difficult to form a conceptual picture of the effect of the total harmonics from the mathematical expressions given by equations (2-1) and (2-6). In the following sections, the harmonic analysis of the m.m.f. wave is illustrated graphically by considering the phase-belt and slot harmonics separately.

2.3 The Total Phase-Belt Harmonic Variation Relative to Rotor

2.3.1 Rotor at Synchronous Speed

It was pointed out in section 2.1 that all the different instantaneous shapes of the travelling m.m.f. wave yield corresponding harmonics of exactly the same magnitude. This includes the fundamental m.m.f. harmonic which is therefore of

constant amplitude while travelling synchronously with the rotor. This means that the total (time) variation of the m.m.f. at any point on the rotor surface can be found by subtracting the fundamental from a succession of total m.m.f. waves. The intermediate steps in this procedure are to obtain various instantaneous space distributions of the total stator m.m.f. less the fundamental wave.

When referred to the rotor, the various m.m.f. wave shapes shown in Fig. 2.1(b) do not all have a common zero; but clearly their corresponding fundamentals do, since these represent the fundamental m.m.f. which rotates synchronously with rotor.

In order to illustrate the m.m.f. variation with respect to rotor, consider a point on rotor surface which happened to be in line with the stator electrical angle $\theta_1 = 0^\circ$ at instant $\omega t = 0^\circ$. By assigning the origin of rotor electrical angle θ_2 to this point, the space m.m.f. distribution shown at the top of Fig. 2.2 is the same with respect to both stator and rotor electrical angles (this is obvious, because both co-ordinate systems coincide with each other). At instant $\omega t = 30^\circ$ the rotor together with the fundamental m.m.f. have moved 30 electrical degrees with respect to the origin of stator electrical angle $\theta_1 = 0^\circ$. Thus, by constructing with respect to the stator electrical angle θ_1 the space m.m.f. distributions and their fundamentals at $\omega t = 0^\circ$ and $\omega t = 30^\circ$, the value of total harmonic variation (i.e. the total m.m.f. less the fundamental at $\omega t = 0^\circ$ and $\omega t = 30^\circ$) with respect to the rotor point at which the origin of θ_2 was assigned can be obtained.

This process is illustrated in Fig. 2.2, where two instantaneous shapes of the stator m.m.f. wave differing in time

by 30° and superimposed on the fundamental are shown. Figs. 2.2(c) and 2.2(d) show respectively the difference between two m.m.f. shapes and the fundamental at $\omega t = 0^{\circ}$ and $\omega t = 30^{\circ}$. Fig. 2.2.(b) shows the difference between two m.m.f. shapes. In the same manner the space distributions of the difference between stator m.m.f. and the fundamental at $\omega t = 20^{\circ}$ and $\omega t = 40^{\circ}$ are plotted in Fig. 2.3. The space distribution of the difference between the stator m.m.f. and its fundamental at $\omega t = 60^{\circ}$ repeats that which is shown for $\omega t = 0^{\circ}$ (this is due to the fact that the phase belt is 60°).

As pointed out above, the total harmonic variation (time variation) with respect to any point on rotor can be obtained by considering the four space distributions shown in Figs. 2.2(c), 2.2(d), and 2.3. For example, at instant $\omega t = 0^{\circ}$ the total harmonic m.m.f. at the rotor point corresponding to $\theta_2 = 0^{\circ}$, from Fig. 2.2(c) is 0.09 p.u. At instant $\omega t = 20^{\circ}$ this point has moved 20 electrical degress. Therefore from Fig. 2.3($\omega t = 20^{\circ}$) the total harmonic m.m.f. corresponding to $\theta_1 = -20^{\circ}$ is-0.037 p.u. The same procedure is repeated for other instants of time up to $\omega t = 60^{\circ}$, since the space distribution repeats itself.

In the same manner, the total harmonic variation at other rotor points can be obtained. In Fig. 2.4 the time variation of the total harmonic m.m.f. at rotor points corresponding to $\theta_2 = 0^{\circ}$, $\theta_2 = 45^{\circ}$, and $\theta_2 = 90^{\circ}$ are plotted.

In plotting Figs. 2.2, 2.3, and 2.4 a 3-phase, 60° phase-belt, full pitch, and infinitely distributed stator winding is assumed. It was shown in Section 2.2 that the air gap m.m.f. is affected by the winding factors (see equation 2-1). In order to illustrate these effects graphically, it is convenient to plot the difference between two stator m.m.f. shapes at two intervals of time. The

interval of time must be chosen such that the difference between the two stator m.m.fs. is maximum. It can be seen from Fig. 2.1(b) and 2.2(b) that the maximum difference between two stator m.m.f. shapes occur in the interval $\omega t = 0^{\circ}$ and $\omega t = 30^{\circ}$. In Fig. 2.2(b) the difference is plotted for full pitch winding. In a similar manner this difference can be plotted for other fractional pitches, and this is done in Fig. 2.5. It is seen from Fig. 2.5 that the optimum pitch factor which minimises the total harmonic variation in the travelling m.m.f. wave to be 5/6. The curves of Fig. 2.5 also indicate that the peak phase-band m.m.f. variation is not always at the peak of the fundamental m.m.f. contrary to previous belief.[11,12]

Adderley[13] has shown that the position of the peak phase-band is determined by the sign of the winding factors. If the pitch factors of the pair of m.m.f. harmonics (see equation 2-1) have opposite signs, the maximum variation occurs at the peak of the fundamental ($\theta_2 = 0^{\circ}$). If the pitch factors have the same sign the maximum variation occurs at the zero of the fundamental m.m.f. ($\theta_2 = 90^{\circ}$). In fact these conclusions (which agree with the curves of Fig. 2.5) can be deduced from equations (2-1) and (2-2). The m.m.f. wave of equation (2-1) can be written in terms of an angle θ_2 relative to the peak of the fundamental m.m.f. (which is opposite some point on the rotor) using

$$\theta_2 = \theta_1 - \omega_1 t$$

$$F_R = \hat{F}_1 \cos\theta_2 + \sum_{n=1}^{\infty} \hat{F}_{(6n\pm1)} \times \cos\left[(6n\pm1)\theta_2 + 6n\omega_1 t\right] \qquad (2\text{-}7)$$

where

$$\hat{F}_1 = \frac{3\sqrt{2} \times T \times I_{A.k}\,\omega_1}{p\pi}$$

and

$$\hat{F}_{(6n\pm1)} = \frac{3\sqrt{2} \times T \times I_{A.k}\,\omega_{(6n\pm1)}}{p\pi}$$

The variation of F_R can be now examined by combining the pairs of $(6n \pm 1)$ harmonics which induce the same frequency $6n\omega_1$ in rotor, i.e.

$$F_{6n\omega} = F_{(6n-1)} + F_{(6n+1)} = \hat{F}_{6n\omega} \cos(\eta_n + 6n\theta_2 + 6n\omega_1 t) \qquad (2\text{-}8)$$

where
$$\hat{F}^2_{6n\omega} = \hat{F}^2_{(6n-1)} + \hat{F}^2_{(6n+1)} + 2\hat{F}_{(6n-1)}\hat{F}_{(6n+1)}\cos 2\theta_2 \qquad (2\text{-}9)$$

and
$$\tan\eta_n = \frac{\hat{F}_{(6n+1)} - \hat{F}_{(6n-1)}}{\hat{F}_{(6n+1)} + \hat{F}_{(6n-1)}} \tan\theta_2 \qquad (2\text{-}10)$$

Equation (2-8) shows that the resultant of each pair of $(6n \pm 1)$ space harmonics relative to the rotor is a modulated travelling wave of varying amplitude and wavelength. The amplitude depends on θ_2 and the relative values of the two $(6n \pm 1)$ m.m.fs. At the peak of the fundamental m.m.f. ($\theta_2 = 0^\circ$), equation (2-8) taking into account equation (2-9) gives

$$F_{6n\omega} = (\hat{F}_{(6n+1)} + \hat{F}_{(6n-1)})\cos(6n\omega_1 t) \qquad (2\text{-}11)$$

At the zero of the fundamental equation (2-8) gives

$$F_{6n\omega} = (\hat{F}_{(6n+1)} - \hat{F}_{(6n-1)}) \sin(6n\omega_1 t) \qquad (2\text{-}12)$$

Thus if $\hat{F}_{(6n+1)}$ and $\hat{F}_{(6n-1)}$ have the same sign, the maximum variation occurs at $\theta_2 = 0^\circ$, whilst if the two components have opposite signs the maximum occurs at $\theta_2 = 90^\circ$.

In connection with the sign of other winding factors for a pair of $(6n \pm 1)$ phase-band harmonics with a 60° phase-spread winding, the distribution factors have opposite signs. The slot width factor is positive except for very high order of harmonics as this can be seen from equation (2-4) (see also Appendix 10.1).

2.3.2 Rotor not at Synchronous Speed

The graphical and mathematical analysis given in the previous subsection are related to the synchronous speed. On no-load, however, the rotor slips relative to the travelling fundamental

m.m.f. Therefore, each point on the rotor surface passes gradually through all stages of the time m.m.f. variations shown in Fig. 2.4 but superimposed on the fundamental.

These m.m.f. variations can be presented in a mathematical form by including the rotor slip in equation (2-7). This can be achieved by substituting $\theta_2 = \theta_1 - \omega_2 t$ or $\theta_2 = \theta_1 - (1-s)\omega_1 t$, into equation (2-7), where s is the slip of rotor. Hence the stator m.m.f. wave relative to a rotor moving with slip s is given by

$$F'_R = \hat{F}_1 \cos(\theta_2 - s\omega_1 t) + \sum_{n=1}^{\infty} \hat{F}_{(6n\pm1)} \cos\left[(6n\mp1)\theta_2 + \{6n(1-s)\mp s\}\omega_1 t\right] \quad (2\text{-}13)$$

It can be seen that by making s zero or one, equation (2-13) reduces to equations (2-7) and (2-1) respectively.

2.4 The Total Slot Harmonic Variation Relative to Rotor

The treatment of the travelling stator m.m.f. wave given in the previous section, considered the harmonics of order $n \neq q$. Such an analysis assumes the stator winding to be represented by a uniform current sheet. Since the winding is not infinitely distributed and the conductors are placed in slots, the slot harmonics introduce stepped dis-continuities in the m.m.f. waveform and space pulses in the current loading wave. The effect of this discrete conductor positioning on the m.m.f. waveform can be treated by considering a winding which has as many phases as conductors per pole. Curves, similar to those already given may then be drawn. To illustrate this, corresponding stator m.m.f. and current loading waveforms of Fig. 2.1(a) and 2.1(b) are considered here again. The assumed current sheet is now replaced by slots carrying their corresponding instantaneous current

pulses. In Fig. 2.6(a) and 2.6(b), the space distribution of stator m.m.f. and current loading waveforms relative to a synchronously rotating rotor are shown at instant $\omega t = 0^{o}$. It is clear that the m.m.f. steps and current space-pulses have maximum amplitude where the fundamental m.m.f. is changing most rapidly, corresponding to the maximum of the fundamental of the current loading wave.

Analogous to phase-band harmonics, the effect of winding factors on the total harmonic variation due to slot harmonics may be shown by considering a pair of $(6n \pm 1)$ slot m.m.f. harmonics ($n = q, 2q, \ldots$). The winding factors for a pair of slot harmonics always have opposite signs so that the maximum slot harmonics variation occurs at the zero of the fundamental m.m.f. ($\theta_2 = 90^{o}$). Since, the magnitude of pitch and distribution factors for a pair of slot harmonics are equal to those of the fundamental, and the slot width factors for a pair of harmonics are approximately equal, the total slot harmonic variations at $\theta_2 = 0^{o}$ is therefore small.

2.5 Current Loading Distribution in the Squirrel Cage

In the squirrel cage induction machine the rotor bar resistance is sufficiently small to allow the rotor currents to flow and produce m.m.f. in opposition to that of stator m.m.f. The current in the rotor bar is a composite of a complicated form in which three main components are prominent. In addition to the slip and tooth frequency components, the third main component is caused by the total phase-band harmonic variation. The magnitude and the shape of the latter component can be conveniently plotted by assuming the cage to be infinitely distributed and the

stator m.m.f. harmonics are completely damped out by the circulating rotor currents. With these assumptions the rotor current loading distribution is simply obtained by means of graphical differentiation of the m.m.f. curves shown in Fig. 2.4 and taking the reverse sign of the resultant. In Fig. 2.7 the rotor current loading distribution is shown for three points on a synchronously rotating rotor, for 3-phase, full pitch, and infinitely distributed stator winding. In Fig. 2.7 the rotor electrical angle θ_2 is measured from the zero crossing of the fundamental of the current loading where the fundamental m.m.f. is a maximum. At no-load with a small amount of slip the curves of Fig. 2.7, show some of the phases through which the rotor current loading passes slowly as the bar position changes with reference to the fundamental. For rotor speeds other than the synchronous speed these curves appear superimposed on the fundamental. In the experimental part of this thesis (Chapter 7) it will be shown that the curves obtained graphically on the basis of simplified assumptions give reasonably a satisfactory picture of the total harmonic variation.

The peripheral distribution of the rotor bar current loading has been considered by Gault[14], using the hypothesis given in Bailey's book[15] which states that the resultant current distribution, taking rotor and stator currents together, is sinusoidal. This is because a sinusoidal applied voltage requires the air gap flux density distribution to be sinusoidal, and assuming a uniform air gap, this in turn demands a sinusoidal resultant m.m.f. distribution which must be produced by a sinusoidal current. The procedure by which Gault plotted the bar current loading distribution is the opposite of that used in this section, since

Gault was concerned with the loading current only. On the basis of the obtained curves, Gault derived an analytical formula for the calculation of the current density distribution inside the bar. The given formula , however, is based on one-dimensional analysis of the field inside the slot. The problem of current density distribution and calculation of dynamic impedance of slot embedded conductors is discussed in next chapter, section 3.6.

2.6. Conclusion

It was shown that the total m.m.f. and current loading variations can be conveniently plotted graphically. These curves are useful for predicting the amplitude of the magnetic field variation and they provide a conceptual picture of the loss distribution on the rotor surface. The m.m.f. along the rotor iron surface gives the applied flux density equal to the resultant flux density if the reaction of the induced eddy currents in the iron is weak. The current loading gives the resultant tangential field strength along the rotor bar surface. In practice, the reduction of the applied variation by the air gap must be considered and this is best done by determining the reduction of each harmonic and then recombining to give the total variation.

It was shown that the total phase-band harmonics variation may be a maximum or minimum at the zero of the fundamental m.m.f. depending on the signs of the winding factors. In particular for a 3-phase 60° spread winding with fractional pitch in the range $0.8 \leq \varepsilon \leq 0.85$ gives a minimum variation of the phase-band harmonics. The slot harmonic variation for all windings is a maximum at the zero of the fundamental m.m.f.

It was also shown that the direct method of plotting the total field is in agreement with the harmonic analysis and it is thought that such plottings, besides providing a conceptual picture of the field variation , may be of further use in estimating the total field variation on rotor surface and ultimately the loss.

The graphical plottings carried out in this chapter need to be remembered when the experimental oscillograms of the rotor surface fluxes are discussed in Chapter 7.

3.0 A Review of the Effect of Machine Geometry

3.1 Introduction

The total flux in electrical machines is commonly separated into two components and treated under the following headings:

(1) The working or mutual flux.

(2) The leakage flux.

The working flux is that flux which crosses the air gap and fully links with both stator and rotor windings (this flux is also referred to as the main flux). The term leakage flux is generally attributed to any flux which is diverted from the path of the main flux, thereby linking either the stator or rotor winding (or linking partially with both windings).

These flux components are produced by alternating currents and in accordance with Faraday's law they induce e.m.fs. in the conducting regions. The resultant effect of the induced e.m.fs. is to force the current to concentrate in areas where the variation of the magnitude of the field is maximum. The problems which are encountered in the analysis of the magnetic field in conducting media may be classified into three categories:

(1) The physical parameters of the region (namely the resistivity and permeability) are dependent upon the intensity of the field. This dependence is usually expressed by the non-linear B/H curve and the hysteresis loop for iron.

(2) Consideration of the actual geometry of the region in which the physical parameters are considered to be constant.

(3) Specification of the boundary conditions in a given region.

In connection with the first problem a great deal of theoretical and experimental work has been carried out and they are exclusively related to ferromagnetic media and this subject is discussed in Chapter 5. The second type of problem is related to regions occupied by copper or aluminium (i.e. the slot and end coil regions) and the air gap. The problem of specifying the boundary conditions is common to both types of the above mentioned problems.

In the air gap and other parts of the machine (for example in the top region of the slots) the main exciting and leakage fluxes coexist together in such a manner that their combined treatment by the known methods is either too tedious or yield solutions of little practical significance. For this reason the usual procedure is to investigate the leakage flux components independently and then the total effect is given by superposition. The types of leakage components commonly encountered in electrical machines may be broadly classified as follows:

(1) Air gap leakage.

(2) Slot leakage.

(3) Overhang (or end-coil) leakage.

(4) Skew leakage, if the slots are skewed.

(5) Incremental leakage due to saturation and eddy currents.

The last component is basically introduced as a result of simplifying assumptions made about the boundary conditions. The skew leakage is also introduced because of the assumptions and simplifications made in the calculation of other three components. Obviously all physical fields are three-dimensional, but in cases where the variation of the field in one direction is

negligible (for example in the air gap of an induction machine) the field can be treated as two-dimensional. However, the air gap curvature and other irregularities introduced by the lamination of the iron can be neglected without making a significant loss of accuracy. In machines where the effect of the ventilating ducts is not negligible, an additional component can be added to the total leakage. The most practical three-dimensional problem is the overhang or end-coil leakage. Estimation of this leakage component, mainly due to the geometrical complexity of the windings and the variety of end-coils shape used in different machines, is extremely difficult. The problem of over-hang leakage has been treated in a number of papers [16-19] and the given analysis is either based on the results of limited experimental data or approximated by two-dimensional analysis. At present it is difficult to make a concrete appraisal of this leakage component and for this reason no attempt is made to discuss this problem in this work. The discussion of this chapter is primarily confined to the treatment of the magnetic field in the air gap and slot regions and assessing the methods used in literature with particular reference to the geometrical aspects of the slots and the air gap of induction machines (where the curvature of the air gap can be neglected).

3.2 Peripheral Air Gap Leakage and the Effect of Slot Openings

The magnetic field in the air gap of an induction machine is produced by the combined effect of the m.m.fs. resulting from the flow of currents in the stator and rotor windings. Under linear conditions the resultant air gap field can be expressed

as a linear combination of the magnetic fields produced separately by the stator and rotor currents. Since the analysis of the m.m.fs. of both stator and rotor windings is similar, it is sufficient to consider the filed of stator windings only.

In Chapter 2 the m.m.f. of the stator winding was discussed without reference to the effect of air gap length and slot openings on the resultant magnetic field in the air gap. In order to consider the effect of these factors, it is necessary to examine first how the magnetic field obtained by using the one-dimensional Fourier analysis compares with the exact analysis based on the field theory. By making this comparison it will be shown later (section 3.4) that although the nature of the factors influencing the air gap leakage is well understood, nevertheless they are either misinterpreted or overlooked in order to arrive at relatively simple solutions.

The usual procedure by which the m.m.f. of a winding is determined[7,8] is based on a direct current carried by a full pitch (or fractional pitch) coil to be concentrated at slot openings of negligible width, the iron to be infinitely permeable, and the magnetic flux lines to cross the air gap in the radial direction only. With these assumptions the air gap flux density wave assumes a stepped rectangular form which is then expressed by a Fourier series. This is the basic step of the procedure. The fields of other coils and phases are expressed in a similar manner. From a field theory point of view the above described procedure represents a simplified solution of the magnetic field of line currents disposed on the stator surface. In accordance with field theory[20] a line current (of one ampere) divides the surface of infinitely permeable iron on which it lies into

two halves separated by unit magnetic potential. If a stator conductor carrying a current of 2 amperes is assumed to represent a line separating two adjacent teeth having infinite permeability (this is equivalent to the assumption of negligible slot width), then the magnetic potential of the two teeth can be regarded as +1 and -1 respectively with the smooth rotor surface taken at zero potential. The exact pattern of the magnetic field in the air gap due to this line current can be obtained by the method of conformal transformation and it is shown in Appendix 10.2., Fig 10.2. In Appendix 10.2 it is shown that the amount of the peripheral flux which does not cross the full length of the air gap (see Fig. 10.2) is a function of the air gap length and the pole pitch. It is also shown that the ratio of the fundamental component of the peripheral flux flowing from pole to pole to the fundamental sine wave flux is proportional to

$$\frac{\Phi_p}{\Phi_1} = \frac{2(p.g)^2}{D^2} \qquad (3\text{-}1)$$

where D – the bore diameter

p – the number of pole pairs.

[It should be noted that the same result as equation (3-1) was obtained by Alger (see Reference 7 , Ap B-7) but the method used here is shorter and the mathematics is much simpler.] However, it is not difficult to appreciate that the analysis of the resultant air gap field obtained on the basis of the field theory cannot be expressed in an acceptable analytical form unless the distortions of the field lines bunching around the line currents are neglected and this leads to the same solution as predicted in Chapter 2. In order to compensate for the neglect of these distortions a separate component called the peripheral air gap

leakage is added to the total leakage. As far as the fundamental m.m.f. is concerned, the distortion of the flux density due to the flow of the flux from positive pole to negative pole is negligible in comparison with the overall distortion of the flux wave by several slot openings. On the other hand, considering the flux density harmonics produced by the slot m.m.f. harmonics, the combined distortion of the flux wave due to the peripheral flow and the presence of the slot opening should be taken into account. It is also important to realise that as the flux harmonics rotate in the air gap the degree of flux distortion changes as they move with respect to a fixed point on the stator. To illustrate this, an m.m.f. harmonic and its corresponding flux wave distorted by a slot opening at two instants of time are shown in Fig. 3.1. The distortion of the flux wave at position (a) is predominantly due to the slot opening and the distortion due to the peripheral leakage [not shown in Fig. 3.1(a)] is negligible. At position (b) the distortion of the flux wave is due to the combined effect of the peripheral leakage and the slot opening. In next section it will be shown that the effective air gap for each of these two positions is not the same as commonly expressed in literature.[7,8]

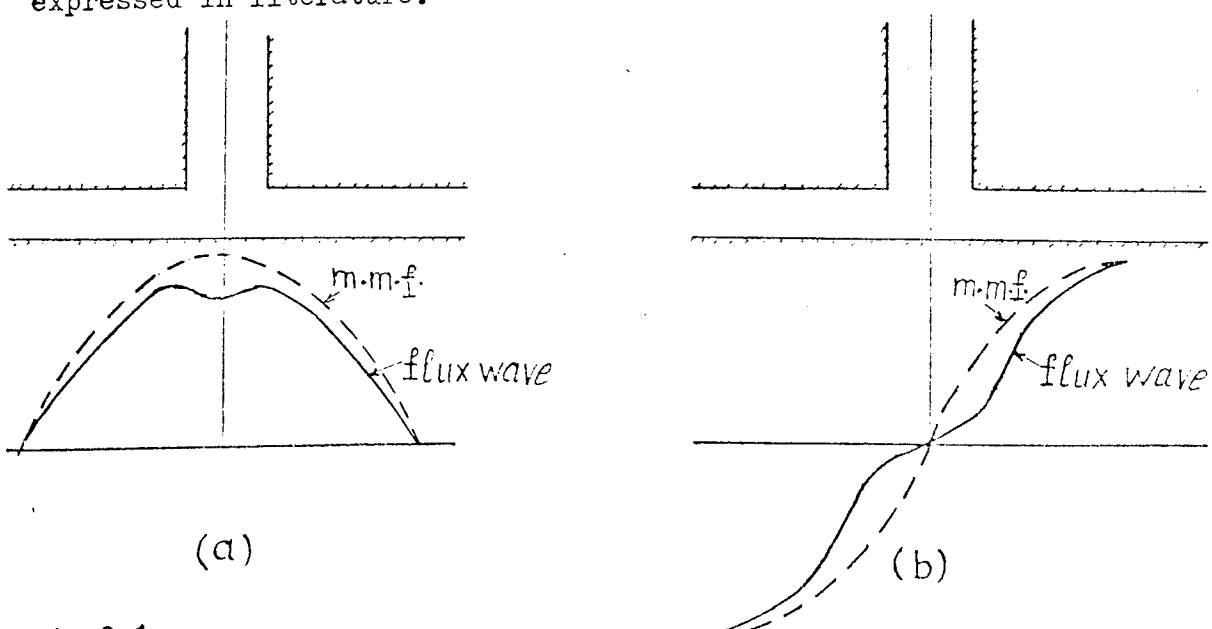

Fig 3.1

The distortion of a rotating flux wave at two instants of time.

3.3 The Distortion of the Flux Wave in an Air Gap With a Succession of Slot Openings

The first detailed contribution to the theoretical solution of the magnetic field in an air gap with slotted stator and smooth rotor (or vice versa) was that of Carter[21] and then extended by Coe and Taylor.[22] Carter assumed that a uniform magnetic potential was applied across the gap and each slot considered to be infinitely deep and infinitely remote from its neighbouring slots. By applying the method of conformal transformation Carter obtained an analytical expression for the flux density distribution along the smooth surface. An example of such air gap flux density distribution is shown in Fig. 3.2.

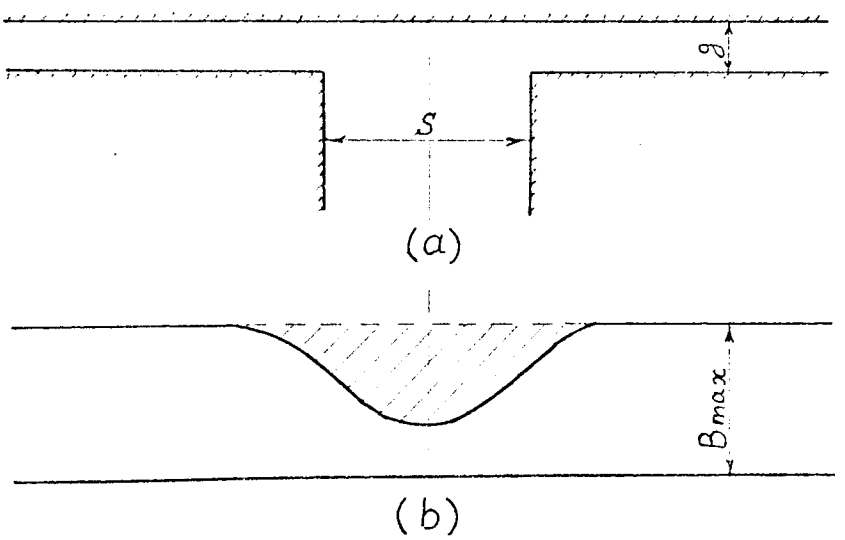

Fig 3.2
The shape of air gap flux density distribution

An important quantity emerging from Carter's analysis is the area between the flux density curve caused by the slot opening and the line representing the constant flux density which exists in the absence of the slot (see Fig. 3.2). This area represents the magnitude of a lost flux caused by the slot, when compared

with a smooth air gap. Taking the smooth air gap flux density to be unity, the lost flux is given by

$$\Phi_\ell = S\delta \tag{3-2}$$

where the well known coefficient δ is expressed by

$$\delta = \frac{2}{\pi}\left\{\tan^{-1}\frac{S}{2g} - \frac{g}{S}\ln\left[1+\left(\frac{S}{2g}\right)^2\right]\right\} \tag{3-3}$$

where S and g are the width of the slot opening and the air gap width respectively.

Carter's coefficient which is widely used by engineers is the ratio of the flux which crosses a smooth air gap over one slot pitch to the actual flux that crosses the same slot pitch in the presence of the slot opening and it is given by

$$C = \frac{t+S}{t+S-S\delta} \tag{3-4}$$

where t is the tooth width and δ given by equation (3-3).

It will be shown later (section 3.4) that in induction machines, Carter's coefficient can only be interpreted as per unit ratio of the amplitude of the fundamental flux density which exists in a smooth air gap to the amplitude of the fundamental of the distorted flux density in the presence of stator slot openings only (or rotor slot openings only).

As the derivation of the coefficient δ is based on the assumption of infinitely wide teeth, this has caused uncertainty about the application of Carter's coefficient as given by equation (3-4), to practical cases where the slot openings are separated by teeth of comparable or smaller width. This doubt arises from the fact that the reduction in the magnitude of flux density on the smooth surface opposite the slot extends considerably

beyond the width of the slot itself. Gibbs[23] in his book gives a detailed analytical treatment of the air gap in which the slotted member is represented by a succession of slots and allows the tooth widths to be smaller than the slot openings. The application of conformal transformation to such an air gap geometry yields a solution containing elliptic functions. Gibbs shows that the shape of the dip and the magnitude of the harmonics considerably differ from those obtained by Carter's analysis. On the other hand Carter's coefficient given by equation (3-4) is remarkably accurate when compared with that calculated using elliptic functions. This precise agreement is intriguing when it is realised that the two expressions respectively contain trigonometric and elliptic functions. Commenting on this situation, Neville[24] stated that "the use of δ assumes that the flux distribution over a succession of slots is that which is obtained by superimposing the distribution curves for all the slots that are near enough to have any appreciable effect". On this basis Neville used a synthetic graphical method and obtained various flux density waves for different ratios of S/t and has shown that they are in close agreement with those determined from elliptic functions. The usefulness of Neville's method lies in that the flux density waveforms can be determined without having to evaluate laborious elliptic functions. Since Neville's method is essentially graphical and requires high precision, Freeman[25] devised a routine computer programme for numerical manipulation of the equations obtained from the analysis of conformal transformation. For a practical range of S/t and S/g, Freeman represents in graphical form the harmonic contents of the flux density waveforms.

In connection with average flux in the air gap and calculating Carter's coefficient two well known formulae are commonly used by engineers. These two formulae which are known by the names of their authors, namely Pohl[26] and Baillie[27], are essentially based on the graphical method of flux plotting[28]. By replacing the curved elemental flux tubes which cross the air gap by an equivalent uniform flux tube both Pohl and Baillie expressed Carter's coefficient by simple formula. Carter's δ (see equation 3-3) was expressed by Pohl as

$$\delta_{Pohl} = 1 - \frac{4.6 \log(1+\beta\frac{S}{2g})}{S/g}$$

where $\beta = 1$ for $S/g \leqslant 10$

and $\beta = 1.4$ for $S/g > 10$

and Baillie expressed Carter's coefficient by a much simpler expression

$$C_{Baillie} = \frac{t + S}{t + 5S/(5+S/g)} \qquad (3\text{-}4a)$$

Both expressions given above, in particular Baillie's formula, are convenient for slide rule calculation of Carter's coefficient. The accuracy of these formulae is claimed to be better than 1%.

Although the analysis and the methods outlined above are strictly speaking applicable to machines in which the stator only (or rotor only) is slotted and the m.m.f. across the air gap is constant, their application is extended to induction machines where both stator and rotor are slotted and the m.m.f. across the gap is non-uniform (see section 3.4).

It is important to bear in mind that the treatment of the magnetic field given in this section is based on parallel sided infinitely deep slots. In practice the slot depth is finite and

various semi-enclosed slots are used. The effect of the slot shape is discussed in next section.

3.3.1 The Effect of Slot Configuration on Carter's Coefficient

In induction machines and other electrical machines a variety of semi-enclosed slots are used. Typical examples of semi-enclosed slots used in induction machines are shown in Fig.3.3. Any variation in the slot shape not only affects the magnitude of the slot leakage but also to a certain degree the air gap flux which fringes into the sides of the slot. As far as the working flux is concerned, a slot of any shape can be replaced by an equivalent infinitely deep open slot. The problem is, however, what equivalent slot width should be chosen and at the same time taking into account the effect of slot leakage.

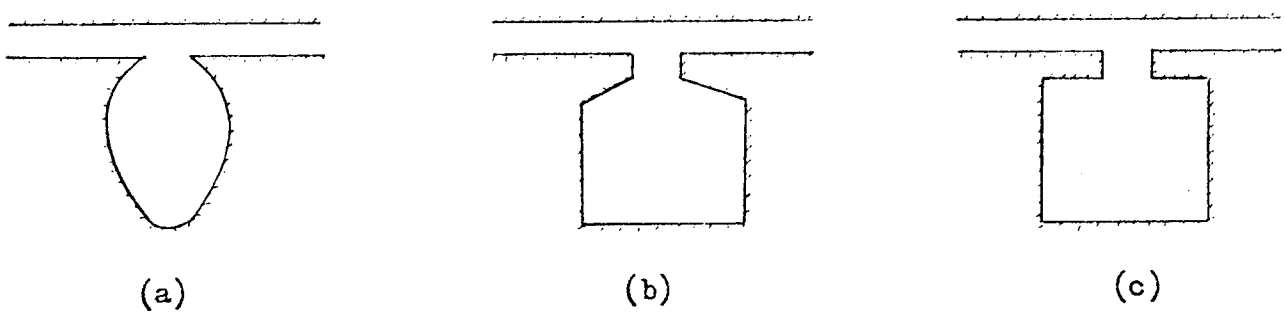

Fig 3.3

Typical slot shapes used in electrical machines

For a semi-enclosed slot, it is clear that less flux enters the slot sides than would be the case with a parallel sided slot of width equal to the slot opening. To account for the effect of tooth lips Wieseman[29] used the technique of flux plotting, and claimed to have calculated the air gap permeance with satisfactory

accuracy. As a rule the technique of flux plotting by hand gives only a rough result and this technique is usually used for calculating leakage fluxes such as end-coil leakage where high accuracy is not essential. In connection with the problem of semi-enclosed slots, Alger[7] suggests that Carter's (1-6) should be reduced by 10%. Due to the fact that nearly all of the working flux enters the top of the teeth and fringes into the first few millimeters of their sides a 10% reduction is most likely to be excessive. However, the problem of overhang tooth has been treated in a paper by Morath[30] who investigated three slot shapes as shown in Fig. 3.4, all with the same slot opening width. One of these slots (Fig. 3.4 c) is hypothetical with its infinitely thin tooth lips, but its analysis reasonably represents a slot opening having the shape of that shown in Fig. 3.3(a).

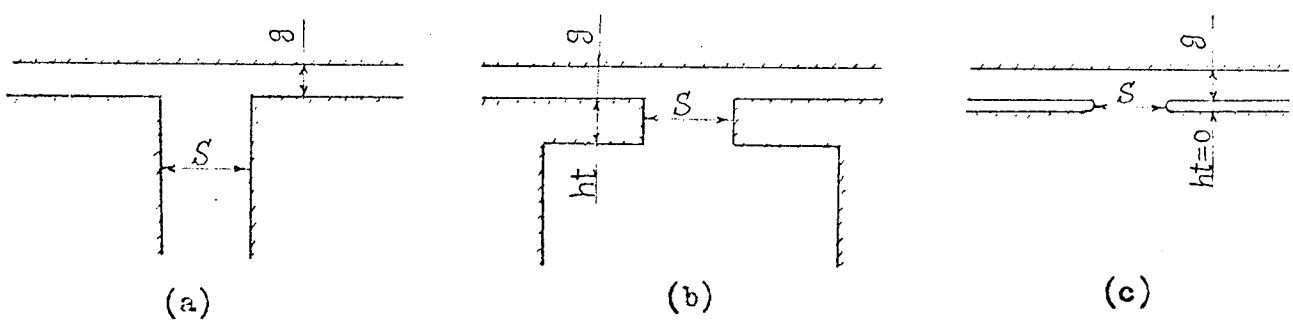

Fig 3.4

Three slot openings with different tooth overhang

Using the method of conformal transformation, Morath calculated the loss of permeance due to three types of slot opening (i.e. the coefficient $\acute{o}$) and compares the result for Figs. 3.4(a) and 3.4(c) by means of curves reproduced in Fig. 3.5 (a). The result of analysing the slot shape of Fig. 3.4 (b) is reproduced in Fig. 3.5 (b) where ht/g is plotted against S/g for constant

values of the lost permeance factor . This factor may be compared with Carter's [which is for the slot shape of Fig. 3.4(a)]. Fig. 3.5 (b) shows that the effect of tooth overhang becomes appreciable only when the height of the tooth lip (ht) is of the same order as the air gap length and relatively large values of S/g. On the basis of the obtained results it can be said that in case of semi-enclosed slots (where the ratio of S/g is usually not high) Carter's analysis remains unaltered if the width of the tooth lips is sufficiently greater than the air gap length. These conditions commonly prevail in induction machines with semi-enclosed slots. However, the important factor that should be borne in mind is that under load conditions or with high slot leakage flux density, the tooth lips become saturated and this means that an effectively wider slot opening must be taken to estimate the lost permeance factor. On the other hand when the tooth lips become saturated the reluctance path of the slot leakage increases and this leads to decreased effective slot conductor impedance (see section 3.6) and hence decreased I^2R losses. Therefore, the decreased losses in part compensate for the increased permeance losses when the tooth lips become saturated. On this subject no reliable method or data are available to predict the combined effect of the slot leakage and the leakage of the main flux. Due to the reasons stated above, it is suggested that at present, estimation of the air gap permeance on the basis of unsaturated tooth lips yields more accurate results than using dubious factors to account for saturation.

3.4 The principle of Analogy and its Application to Induction Machines

In induction machines the applied m.m.f. across the air gap is neither constant nor sinusoidal. Also both members of the machine (stator and rotor) are slotted. The analysis of the air gap field and the distortion of the flux wave discussed in section 3.3 were based on the assumptions that a constant m.m.f. is acting across the air gap and either side of the gap is slotted. With these assumptions it was possible to use the method of conformal transformation and obtain an analytical solution. It is well known that treatment of Laplacian fields confined within multiple boundaries along which the magnetic potential distribution is non-constant cannot be dealt with by the method of conformal transformation or method of images.[31] Application of other conventional methods (such as the method of separation of variables or Fourier transform method[32]) to the actual geometry of the air gap yields either no practical solution or involve unmanagable mathematics (see Chapter 4).

One possible way of tackling the problem of the air gap field in induction machines is to make use of the analogy that exists between the electric and magnetic circuit theory. In accordance with this analogy it is possible to regard the m.m.f. as equivalent to the voltage, the flux to the current, and the permeability to the conductivity, i.e.

$$F_g \equiv V$$

$$\phi_g \equiv I$$

$$P_g \equiv \frac{1}{R}$$

The magnetic quantity P_g which is usually referred to as the air gap permeance can be directly obtained using the conformal

transformation providing the peripheral leakage from pole to pole is neglected. This is due to the fact that the component of peripheral leakage does not appear in the analysis of conformal transformation, because the meeting point of the two surfaces separated by the air gap, one with unit positive potential and the other one with zero potential is always considered to be at infinity.[20,23]

Thus, if the applied fundamental m.m.f. acting across an air gap in which the rotor is assumed to be smooth and the stator to be slotted is expressed with respect to a fixed point on the stator by

$$F_1 = k_1 \cos(px - \omega t) \tag{3-5}$$

where k_1 - is a constant

p - pairs of poles

ω - angular velocity

and the air gap permeance wave obtained from the analysis of conformal transformation is resolved into Fourier series with respect to the same point on stator surface by

$$P = P_o + \sum_{m=1}^{\infty} P_m \cos\left(\frac{\pi m}{\tau} x\right) \tag{3-6}$$

where P_o - is the average permeance

P_m - is the amplitude of the harmonic

2τ - is the slot pitch

the resultant air gap flux wave is then the product of equations (3-5) and (3-6).

By using this method of analogy, Alger[7] suggested that it can be used for all m.m.f. harmonics. However, as indicated in section 3.2 the flux waves produced by the fundamental and the principal phase-belt m.m.f. harmonics span over several slot openings and the distortion of the flux waves due to the flux

which flows from positive to negative poles in comparison with overall distortion due to the slot openings may be neglected. Therefore application of the method of analogy to these harmonics is justifiable. On the other hand in the case of slot m.m.f. harmonics it is necessary to consider the combined distortion of the flux wave due to the peripheral leakage and the effect of slot opening as this was schematically shown in Fig. 3.1(b). In order to account for the combined effect it is necessary to modify the potential values used in the method of conformal transformation. This can be done by assuming the magnetic potential of the adjacent teeth are at +1 and -1, with rotor surface taken at zero magnetic potential. In Appendix 10.3 it is shown that the magnitude of the lost flux caused by the slot opening is not the same as predicted by Carter's coefficient. The implication of this is that as the slot m.m.f. harmonic rotates with respect to a slot opening the magnitude of the lost flux changes with m.m.f. position and the average value of the lost flux is somewhere inbetween that obtained by Carter's analysis and that given in Appendix 10.3. In calculating the differential air gap reactance (see next section) this point is either neglected in literature[8] or referred to as a modifying factor for the main m.m.f. only.[7]

It was indicated earlier that in induction machines besides the non-uniform m.m.f. distribution across the air gap the rotor is also slotted. In order to include the effect of rotor slottings, the common approach used in literature is to superimpose the effects produced by stator and rotor slot openings each obtained separately. The premise of such superposition is based on the hypothesis that the combined Carter's coefficient given as a sum of two Carter's coefficients (one for

stator and one for rotor) gives the resultant air gap permeance. In early 1920 Lehmann[33] used the technique of flux plotting and showed that a straightforward summation of Carter's coefficients (i.e. $C_1 + C_2$) gives erroneous result and he concluded that $(C_1 + C_2 - 1)$ gives a reasonably accurate combined Carter's coefficient if each of C_1 and C_2 were less than 1.4. The combined Carter's coefficient is commonly expressed by the product C_1C_2 instead of $(C_1 + C_2 - 1)$ on the basis that it gives a better representation of the permeance wave. However, whether the summation or product rule is used the resultant air gap permeance wave is expressed by an average permeance and two series of permeance harmonics one due to the stator slot openings and one due to rotor slot openings. Usually, the higher harmonics of these two series are ignored (see References 7 and 34). Despite the fact that this method of superposition is not based on any theoretical analysis, no attempt has been made by the authors who used this method[7,34] to justify its application by any published experimental evidence (although Alger[7] used this method in his book, but actually he did not include the effect of rotor slot openings in his analysis).

On the subject of the combined effect of stator and rotor slot openings several papers have been published in which various analytical and semi-analytical methods are used to predict the total average air gap permeance. For example Domboor[35] used Pohl's method to a doubly slotted air gap for two combinations of stator and rotor parameters only. Higginson[36] also attempted to use Baillie's method to such an air gap geometry but he found the discrepancy between the experimental results obtained from Teledeltos plot and Baillie's method is substantial.

In literature the overlap method (this is briefly discussed in next section) is also widely used to predict the air gap permeance. However, all these methods in general give an approximate picture of the air gap permeance wave and none of them is adequate to represent the shape of the permeance wave since they are based on doubtful assumptions made about the path of air gap flux tubes.

One of the analytical methods that has been used by Binns[37] for calculating the total permeance variation in an air gap containing two slots (one stator slot and one rotor slot) is the conformal transformation method incorporated with numerical integration. By assuming the tooth widths of both stator and rotor to be infinitely wide, Binns obtained the solution of the Laplacian field in the air gap for various positions of the single rotor slot relative to the single stator slot. The result of his analysis shows that the average air gap permeance calculated by either rule C_1C_2 or $(C_1 + C_2 - 1)$ under-estimates (or over-estimates) the actual average value. However, Binns' analysis is not suitable for calculating the magnitude of permeance harmonics and hence its application is limited. The harmonic analysis of the air gap permeance wave is discussed in Chapter 4.

3.5 The Differential Reactance

Calculation of losses, torques and performance of electrical machines is commonly performed by using the equivalent circuit. The equivalent circuit of induction machines, which consists of pure resistances and reactances, is extensively treated in most textbooks. One of the principal elements of the equivalent circuit is the differential reactance. The chief requirement for

calculating the reactance of a winding is obviously the task of determining the flux linkage with the winding that produces it. This means that a sound knowledge of the path of the flux linking the winding is essential for accurate calculation of the reactance.

As shown in Chapter 2, the air gap field produced by stator windings includes, besides the fundamental sinewave, a series of harmonic waves with multiples of the fundamental number of poles, revolving at sub-multiples of the synchrous speed. All these induce fundamental frequency voltages in the winding that produces them and, therefore, add to the winding reactance. The voltages they generate in the opposing rotor winding when the motor is at speed are not at a slip frequency and consequently they produce no useful result. The total reactance due to all these harmonic fields of both stator and rotor is known as the differential reactance and the corresponding flux as the air gap leakage flux. The differential reactance is commonly considered as the sum of two arbitrary elements, the zig-zag and the belt leakage.

It is sometimes asserted that the zig-zag reactance cannot be separated into two parts one for the stator and one for the rotor. This point of view was rejected by Binns[37] on the basis that the reactances are in reality separate, and the resulting self induced e.m.fs. are in different windings of the machine. Although Binns' point of view is acceptable, it will be seen below that this controversy arises because when the differential reactance of each member of the machine is calculated separately the mutual effect of stator and rotor slot openings on the path of the leakage is not taken into consideration. Therefore, in

order to include this combined effect it is sometimes convenient to link the rotor reactance with the stator reactance as if they were one quantity.

The commonest method used in textbooks for calculating the stator or rotor differential reactance consists of obtaining the reactance due to each e.m.f. induced by the field harmonic (taking into account the winding factors, the order of the harmonic and the effective air gap) and then add all the reactances obtained in this way.

Another well known method which was first developed by Chapman[38] and is extensively treated in Alger's book[7] is the difference method. The essence of this method consists of obtaining the total linkage of the resultant air gap field due to the stator and rotor currents assumed to be concentrated in slot openings of negligible width, and then subtracting the linkage due to the fundamental flux. In both above mentioned methods the effect of the slot openings is included by introducing the effective air gap factor. This factor is based on the magnitude of the lost flux obtained from Carter's conformal transformation analysis and it is assumed to be the same for all field harmonics including the fundamental.

The air gap leakage reactance due to the slot m.m.f. harmonics is often calculated by an approximate method known as the overlap method. This method which is developed by various authors[39-42] is based on an entirely different principle than those mentioned above. By using overlap method, the leakage is calculated by applying the combined m.m.f. of rotor and stator winding to a path which zig-zags along the air gap crossing it at overlapping stator and rotor teeth. Having evaluated the

m.m.f. difference between two opposing teeth, the magnetic flux is then calculated on the assumption that it crosses the air gap in straight lines over a peripheral distance confined to the geometric overlapping of the relevant pair of teeth (i.e. at both stator and rotor slot openings the flux is assumed to abruptly fall to zero. Since the basic assumptions (namely the abrupt fall of the flux) used in overlap method is dubious, a better result is obtained by making some allowances for flux fringing into tooth sides. However, as shown in previous section the effective air gap length (or the magnitude of lost flux) for various field harmonics is not the same and also the principle of combining Carter's coefficients linearly (which is used in all these methods) is inaccurate.

It can be, therefore, concluded that the methods available in literature for calculating the differential leakage are approximate and their accuracy depends upon the air gap geometry and the degree of the combined effect of rotor and stator slot openings on the resultant air gap field.

3.6 Dynamic Resistance and Inductance of Slot-Embedded Conductors

The flow of a.c. currents along the stator and rotor slots gives rise to leakage fluxes across the slots, which alternate in the stator slots at the fundamental frequency and in the rotor slots at various frequencies depending on the rotor speed. The effect of these leakage fluxes is to force the current to flow at the top of the conductor where the linkage of the flux is the smallest. Due to this effect which is known as the "skin effect" the values of a.c. resistances and inductance are different from their corresponding d.c. values calculated on the basis of uniform current density distribution.

Generally, the stator windings are stranded to minimise the skin effect. The type of windings which are employed for this purpose, for instance Roebel and Inverted turn transposition, are widely known and treated in most textbooks (see, for example, Reference 8, vol I).

In squirrel cage induction machines, the rotor conductors are made of solid deep bars in which the skin effect is used to increase the starting torque. When the rotor is at speed the skin effect causes higher I^2R losses. The magnitude of these losses depends upon the distribution of current density in the rotor bars. It was shown in Chapter 2 that the rotor current loading distribution is highly complex and it includes besides the slip frequency harmonic, higher harmonics. The theoretical analysis of the magnetic field in the rotor bars can only be usefully expressed if the principle of superposing the effects of the harmonics is employed.

The equations which govern the magnetic field in slots occupied by conductors can be written in terms of instantaneous quantities as follows:[28]

$$\nabla^2 A = -\mu_o \mu J \qquad (3\text{-}7)$$

$$J = \delta E \qquad (3\text{-}8)$$

$$E + \frac{\partial A}{\partial t} = \nabla V \qquad (3\text{-}9)$$

$$B = \text{curl } A \qquad (3\text{-}10)$$

(the notations of equations (3-7) - (3-10) are described in the list of symbols).

Equation (3-9) is given on the basis that the potential V is constant over the cross-section of the conductor. Also all vectors are assumed to be in the axial direction of the slot.

As indicated in the introduction of this chapter, the magnetic field in the slots can be treated as two dimensional. The assumption of two-dimensional field is justifiable, since the end effects are usually taken into consideration separately.

The simplest method which is widely used in literature for the solution of the magnetic field in a slot embedded conductor is based upon the assumption that all flux lines cross the slot width in straight lines. With this assumption the problem is reduced to one-dimensional and the differential equation (3-7) can be written in terms of the current density and flux density as follows:

$$\frac{d^2J}{d^2y} = 2\,j\alpha^2 J \tag{3-11}$$

and

$$\frac{d^2B}{d^2y} = 2\,j\alpha^2 B \tag{3-12}$$

where $\alpha = \sqrt{\frac{\omega\mu_o}{2\rho}}$

and, the positive direction of the co-ordinates variable y is taken along the height of the conductor.

The general solution of equations (3-11) and (3-12) is treated in all textbooks on mathematics. In particular, the solution of equations (3-11) and (3-12) for the case of a rectangular slot of width W, embedded symmetrically with a rectangular conductor of width (a) and height (d) and carrying an r.m.s. current I are given by

$$J = \frac{(1+j)\alpha\, I}{r.W}\left[\frac{\cosh(1+j)\alpha\, y}{\sinh(1+j)\alpha\, d}\right] \tag{3-13}$$

and

$$B = \frac{\mu_0 I}{W}\left[\frac{\sinh(1+j)\alpha\, y}{\sinh(1+j)\alpha\, d}\right] \qquad (3\text{-}14)$$

where $r = \frac{a}{W}$

The a.c. resistance and reactance can be obtained from equations (3-13) and (3-14) and making use of the relation

$P = I^2(R + jX)$

The mathematical analysis given above is the essence of all one-dimensional treatments given in literature. On this subject, the earliest practically useful calculations of dynamic resistance of the bars are given by Field[43] using the assumption that the current density distribution is uniform in the peripheral direction of the conductor but radially non-uniform. The same assumption of one-dimensional non-uniformity of current density was employed by Putman[44] for the problem of T-shaped bar conductor. In squirrel cage induction machines a variety of deep bar rotors are used to obtain a desirable ratio of starting to running resistance. The analysis of all these deep bar rotors is also given on the basis of one-dimensional treatment of the magnetic field. The detailed treatment of various deep bar rotors is extensively discussed in the classical papers of Liwschitz-Garik[45,46] as well as in Alger's book[7], Chapter 8.

However, the magnetic field in the slot-embedded conductor is actually two-dimensional, particularly at the top of the slot-opening. For two-dimensional problems, the differential equation (3-7) contains the x-dependence and this makes the solution more difficult. In order to solve the differential equation (3-7) with two (x and y) variables, the following assumptions are

commonly made:

1. that the shape of the slot and the conductor is either rectangular or circular. The trapezoidal shape can also be treated by using the cylindrical co-ordinate system (application of cylindrical co-ordinate systems usually involves tedious mathematics). In the case of rectangular slots the Cartesian co-ordinate system is used and in the case of circular slots the polar system is used.
2. that the embedded conductors are considered to fill the slot completely.
3. that the flux line bounding the conductors at the top of the slot is straight in the case of rectangular slots, and semi-circular in the case of circular slots.
4. that the iron is infinitely permeable and is laminated so that eddy currents in the iron can be neglected.

and 5. that the electric and magnetic fields are time harmonics. With this assumption the time dependence can be eliminated by expressing the partial differential $\frac{\partial A}{\partial t}$ in a complex form $j\omega A$.

With these assumptions, the solution of equation (3-7) can be obtained either by the method of separation of variables or by Fourier transform method.[32,47] The methods of images and conformal transformation are not suitable for this type of problem because the current density distribution in the conductor is non-uniform and its shape is unknown.[31] If the conductor is surrounded by thick insulation, in this case the slot area must be divided into five regions. Four of these regions are occupied by the insulation and the fifth by the conductor. These five regions must be

interconnected by the four boundary conditions on the surfaces of the conductor which are unknown. It is not difficult to appreciate that the mathematics involved in the analysis of these five regions is not only cumbersome, but the required computation is unmanageable. For this reason, the thickness of the insulation is assumed to be infinitely thin.

The most well known two-dimensional analysis of semi-closed slots is that given by Swann and Salmon.[48,49] By making use of the assumptions outlined above, Swann and Salmon obtained the solution of equation (3-7) for semi-circular and rectangular slots. By repeating the analysis of Swann and Salmon in a cylindrical co-ordinate system, Buchholz[50] obtained an analytical solution for a trapezoidal shape. In connection with Swann and Salmon analysis, Jones,et al[47] published a paper in which they re-examined the assumption of straight flux line bounding the conductor surface. By extending the neck of a T-shaped slot and making this distance as a variable, Jones,et al were able to assess the distribution of the magnetic field intensity along the top surface of the rectangular conductor embedded in the T-shaped slot. The result of their analysis showed that the dynamic impedance calculated on the basis of one-dimensional field distribution is accurate within 5% in the case of semi-enclosed slots. For open slots they have shown that the error can be of the order of 15%.

The dynamic resistance and reactance of slot embedded conductors has been also treated by using the numerical methods. Silvester[51] has formulated a method of solution for a conductor of arbitrary shape in any shape of slot. By using this method,

Silvester analysed the problem of semi-enclosed embedded conductors, taking into account the air gap length and the thickness of the insulation. Considering the analysis of all papers mentioned above the following points can be summarised:

1. The assumption of a straight flux line at the top of a semi-enclosed slot does not affect significantly the value of the a.c. resistance. Also, the error involved in one-dimensional analysis is not substantial for semi-enclosed slots.
2. The width of the slot opening in the semi-enclosed slots has a substantial effect on the resistance characteristic. Swann and Salmon concluded from aqualitive argument that little alteration of the resistance characteristic is likely to occur for different widths of slot openings. It should be noted that in induction machines, when the rotor is at standstill the value of the starting current is high and the tooth lips become saturated. From this point of view, therefore, Swann and Salmon's argument is valid. On the other hand when the motor is at speed and if the induction in the tooth lips is moderate the effect of the slot opening width cannot be ignored. The effect of the ratio of the top slot opening to the width of the slot was investigated by Silvester and the result of his analysis is reproduced in Fig. 3.6. It can be seen from Fig. 3.6 that the effect of the slot opening on the resistance frequency characteristic is substantial. The implication of wider slot opening due to the saturation of tooth lips was mentioned in section 3.3.1 in connection with the permeance effect on the main flux.

It can be seen from Fig. 3.6 that as the permeance losses increase due to the saturation of tooth lips the I^2R losses due slot leakage decreases and this in part compensates for the increased permeance losses.

3. Silvester has shown that the effect of insulation thickness on the resistance frequency characteristic is considerable. This conclusion was based on the analysis of a rectangular conductor surrounded by an insulation layer equal to 1/12 of the conductor's width. However, in squirrel cage induction machines, the thickness of insulation layers in practice is too small in comparison with the bar's width. Besides this, Silvester did not produce any conclusive result on the effect of varying the insulation thickness. On this basis it is believed that the effect of the insulation on the resistance frequency characteristic is negligible.

3.7 Conclusion

The total field in induction machines can be divided into several components, provided the treatment of each individual component is not affected by the others. This condition can only happen if the magnetic circuit of the machine is not saturated.

The treatment of three-dimensional fields such as that in end-coil windings is too difficult mainly due to the geometrical complexity and no exact solution is available in literature. The field in the air gap and slot regions can be conveniently treated as two-dimensional if the air gap curviture, ventilating ducts, and other irregularities are neglected. In induction machines the effect of these factors (other than the effect of ventilating ducts which can be significant) may be ignored.

The main flux is primarily affected by the slot openings and its magnitude is independent of the slot shape if the ratio of the width of tooth lips to the air gap length is greater than 5 and the ratio of the slot opening to the air gap length is less than 10. For combination other than these it is necessary to use the curves of Fig. 3.5. The combined effect of the stator and rotor slot openings on the main field and other field harmonics may be considered approximately by using the linear combination of Carter's coefficients obtained separately for stator and rotor. The accuracy of such superposition is doubtful since it is based on hypothetical considerations and not upon any rigorous analytical method.

The dynamic impedance of the slot embedded conductors is extensively treated in literature by using both one-dimensional and two-dimensional analysis. The result of computations shows that one-dimensional analysis gives a satisfactory accuracy for semi-enclosed slots. The error in open slots can be of the order of 15%

4.0 Harmonic Analysis of the Permeance Wave in a Doubly Slotted Air Gap

4.1 Introduction

Owing to the relative movement between the stator and rotor teeth the air gap permeance wave fluctuates from maximum to minimum. This variation of air gap permeance causes periodic change in the magnitude of the main flux entering each tooth and slot as well as a continuous change in the flux distribution.

From air gap permeance point of view, the main factors which contribute to the pulsation of the main flux inside a tooth are firstly the rapid change of the permeance averaged over a tooth pitch and secondly the penetration of tooth ripple flux harmonics into the sides of the slot. If the stator and rotor teeth combination is such that the average permeance over a tooth pitch remains unchanged with rotor movement and also the slot leakage would be small, then no flux pulsation would occur inside the teeth. However, this does not necessarily mean that under such conditions no iron losses occur. The fact that the shape of the air gap permeance wave continuously changes with rotor movement, the field of permeance harmonics penetrate the surface of the tooth and induces losses which are known as surface losses. In general cases, the variation of the air gap permeance wave causes both surface and tooth pulsation losses. It is common practice to treat these two components separately. One reason for this is that for tooth pulsation it is necessary to know the maximum and minimum of the total permeance variation whereas in case of surface losses the knowledge of the shape of permeance wave is essential. This arbitrary division of losses, however, results from the lack of sound theoretical methods by which the

complicated geometry stator/air gap/rotor can be adequately treated.

It was shown in Chapter 3 that the methods used in literature to express the combined effect of the stator and rotor slotting are either empirical or inadequate to represent the permeance wave.

In this chapter, the problem of doubly slotted air gap is investigated and an analytical method is described by which the flux entering the tooth surface as well as its sides can be determined. The only simplification made about the geometry of the slots is that they are assumed to be rectangular. This assumption is not only practicable but also justifiable since it was shown in Chapter 3 that the effect of the actual shape of the slot on the main flux, in practice, is negligible.

4.2 The Scope of the Analytical and Experimental Methods for the Solution of Air Gap Permeance Wave

It is well known that the method of superposition cannot be applied to geometrical boundaries. In other words it is not permissible to split a given set of boundaries into two component sets treating each set separately and then adding the two results. It should be noted that although, the superposition of the two permeance waves discussed in section 3.4 is based on different principles, nevertheless the actual air gap geometry as a whole must be considered. A typical air gap geometry of induction machines consists of a succession of stator slots and a succession of rotor slots separated by a small air gap. Generally the slot pitch of both stator and rotor is not the same. An example of such an air gap geometry is shown in Fig. 4.1. In order to obtain the field distribution in the air gap and the

slot regions it is necessary to obtain the solution of the Laplacian field produced by a constant m.m.f. applied across the boundaries. The analytical methods which are available for the treatment of such problems are:

a) The method of separation of variables or Fourier transform.

b) The method of conformal transformation.

Both methods, the separation of variables and Fourier transform, are applicable to rectangular regions in which the four boundary conditions must be known. It will be shown in next section that application of these methods in a straightforward manner leads to no practical solution.

Application of Schwartz-Christoffel transformation to the geometry of Fig.4.1 must be, obviously, ruled out because the closed polygon involves an infinite number of right angles. It was mentioned in Section 3.4 that Binns[30] used this method by assuming the width of both stator and rotor teeth to be infinite and both stator and rotor slots to be infinitely deep. With these assumptions the air gap geometry of Fig.4.1 was reduced into two single slots displaced with respect to each other. Despite this simplification the analysis of Schwartz-Christoffel transformation leads to insoluble integral and to more unknown coefficients than can be accounted for by the known relationships. To overcome this problem Binns used the numerical technique of integration[52] in conjunction with an iterative method of solving a set of equations. However, the solution obtained in this manner was suitable for calculating the pulsation of the flux entering the slots only. As far as tooth pulsation is concerned Binns' method remains impractical mainly due to the fact that the tooth

widths are assumed to be infinitely wide. Also any method similar to that used by Freeman[25] (see Section 3.3) cannot be employed because of the difficulties involved in determining the wavelength of the air gap flux density, and also the amount of computation required for calculating any assumed flux wave would be laborious and excessive.

Often the finite difference and analogue methods (these include Teledeltos and electrolytic tanks) are used to plot the equipotential and flow lines of the Laplacian fields. All these methods are essentially based on the same principle, namely a model is constructed for each set of parameters and the field is mapped. Besides the laborious experimental precision which is required to ensure high accuracy (in case of Teledeltos plotting an error of the order of 10-15% may be expected) it is difficult to locate with certainty the boundary conditions in the air gap. In case of geometrical symmetry, i.e. tooth-opposite-tooth the straight flux lines at the centre of the teeth can be accurately used as boundary conditions. For non-symmetrical positions, there are no simple natural boundary conditions. In such cases it is common to place the electrodes sufficiently remote from the pair of stator and rotor teeth regardless of the flux lines at the positions of the electrodes. Although, this procedure entails negligible error (see next section), the area which must be mapped is enlarged and this in turn consumes time and also results in less accuracy. Another disadvantage of these methods is that no general solution can be derived unless a large set of parameters is mapped and then an empirical equation is obtained. However, non-analytical methods are usually used whenever an analytical method is either not available or the solution involves excessive computations.

In the past two decades the advent of digital computers has greatly stimulated the analytical methods involving evaluation of convergent series. In view of this, the disadvantage of the analytical methods in many problems is removed. In the next section it will be shown that the solution of the Laplacian field can be obtained by evaluating rapidly convergent series and by making use of orthogonal functions, the amount of computation is substantially reduced.

4.3 Fourier Analysis of the Laplacian Field in a Doubly Slotted Air Gap

The necessary and sufficient requirement for obtaining the solution of the Laplacian field in Fig.4.1 is to obtain a potential function which satisfies Laplace's differential equation and the imposed boundary conditions. It is clear from Fig.4.1 that the potential function along the broken lines bounding the slot openings and the air gap are unknown. Also in the air gap the potential distribution is unknown except where the flux lines are straight. Therefore, in order to solve the Laplacian field by the conventional methods it is necessary to divide the region between the two surfaces into multiple rectangles. Such an approach is obviously impractical because by interconnecting the multiple rectangles no solution of practical significance will emerge.

The alternative feasible approach is to consider the variation of the air gap potential distribution with respect to a stator slot pitch or rotor slot pitch. The pulsation of the flux which enters the tooth surface and its sides is solely dependent upon this variation.

Consider a stator slot pitch indicated by 2τ in Fig. 4.1 The magnitude of the flux which crosses this slot pitch is a function of the potential distribution in the stator slot and in those rotor slots which are immediately opposite the stator slot pitch.

The potential distributions in the adjacent stator slots as well as in the rotor slots which are remote from the stator slot pitch have no effect on the magnitude of the flux under consideration. The only way that the potential distribution in the adjacent stator slots can affect the flux density distribution along the stator slot pitch is when the stator tooth is too thin and the air gap is sufficiently wide so that the permeance reduction extends beyond the centre of the stator tooth. It should be noted that this permeance reduction is not the same as that discussed in connection with Carter's coefficient (see section 3.3). In the case of Carter's analysis the flux density at the centre of the stator tooth is assumed to be the same as if the teeth widths were infinitely wide. In the present case the reduction of flux density at the tooth centre due to finite widths of the teeth is being already taken into account. However, for practical gap dimensions used in induction machines such condition cannot happen. Binns[37] and Higginson[36] have carried out experimental plots and they showed that the effect of adjacent stator slots is negligible. Although Binns did not specify the gap dimensions, Higginson's plots were made on an air gap geometry in which the widths of the slots were wider than the widths of the teeth.

On the basis of the above considerations, it is therefore possible to consider the potential function on the broken line

bounding the stator slot and the air gap to be periodic (despite the fact that potential function along the adjacent broken lines are not so). Since the potential functions along the stator slot openings are not, actually, periodic, the harmonic analysis is therefore restricted within the slot pitch interval.

As far as the rotor slots are concerned, the same argument is not applicable, unless further considerations are taken into account. This is due to the fact that when the rotor slots are displaced with respect to the stator slot, a situation can arise where two adjacent rotor slots are positioned against the stator slot pitch and each of them is affected by the stator slot differently (for instance, see the combination shown in Fig.4.1). In order to assume the potential function along the broken line bordering the rotor slot and the air gap to be periodic it is necessary to formulate the air gap potential function in such a way that the mutual effect of both stator and rotor slot openings is taken into account. This can be achieved by relating the flux components which cross the stator and rotor surfaces. On this account the air gap potential function is expressed by two waves superimposed on each other (see equation 4-2 below). The first component of this potential function is expressed by a function which gives straight flux lines at the centre of stator teeth in the absence of the effect of the potential function along the rotor slot opening. Similarly, the second component is given by a function which gives straight flux lines at the centre of rotor teeth. (It should be noted that by superimposing these two potential components it does not mean that the slotted boundaries are treated separately.) Thus, the air gap flux due to each of the potential components is confined

between two straight flux lines and this enables to relate the corresponding fluxes which cross the stator and rotor surfaces.

In Fig.4.1 , the potential function in the stator slot (rectangle I) is denoted by Φ_1 , the potential function in the rotor slot (rectangle II) is denoted by Φ_3 , and the air gap potential function is denoted by Φ_2 . The origin of the co-ordinate system and other dimensions are also indicated in Fig. 4.1 . For convenience the dimension τ is taken as reference and made equal to π . The value of all other dimensions are given as per unit of π . This procedure simplifies the form of the potential functions and it only affects the scale of the field. The solution of the potential functions given below are based upon the method of inspection. This method selects a likely solution and is a not unfamiliar approach to many problems.

The solution of the potential function Φ_1 is given by:

$$\Phi_1 = 1 + \sum_{m=1}^{\infty} A_m \frac{\sinh\frac{m\pi}{2P_s}(h_s+g-y)}{\sinh(\frac{m\pi}{2P_s}h_s)} \sin\frac{m\pi}{2P_s}(x-\tau+P_s) \qquad (4-1)$$

The functions forming equation (4-1) satisfy Laplace's differential equation ($\nabla^2\Phi = 0$) and also the three boundary conditions of the sides having unity potential. The unknown coefficient A_m is determined from the fourth boundary condition along the broken line (which is unknown).

The solution of the potential function Φ_2 in the air gap is given by:

$$\Phi_2 = \sum_{k=0}^{\infty} B_k \frac{\sinh(ky)}{\sinh(kg)} \cos kx + \sum_{k=0}^{\infty} C_k \frac{\sinh\frac{k\pi}{\tau_1}(g-y)}{\sinh\frac{k\pi}{\tau_1}g} \cos\frac{k\pi}{\tau_1}(x-\tau+\tau_1-dis) \qquad (4-2)$$

Again the form of equation (4-2) is chosen to satisfy Laplace's differential equation. The unknown coefficients B_K and C_K are determined from the boundary conditions along the stator slot pitch and rotor slot pitch (both potential functions are unknown). The solution of the potential function Φ_3 is expressed by:

$$\Phi_3 = \sum_{m=1}^{\infty} D_m \frac{\sinh\frac{m\pi}{2P_r}(h_r + y)}{\sinh\frac{m\pi}{2P_r}h_r} \sin\frac{m\pi}{2P_r}(x + P_r - \tau - dis) \qquad (4\text{-}3)$$

The potential function given by equation (4-3) satisfies Laplace's equation and the three boundary conditions of zero potential. The unknown coefficient D_m is determined from the fourth boundary condition along the broken line (which is unknown).

The determination of the four unknowns A_m, B_k, C_K, and D_m cannot be conveniently handled by conventional methods, because the resulting equations lead to multiple Fourier series. This problem has been tackled by making use of Fredholm Integral[53] equations in conjunction with Galerkin[54] method of approximation. The essence of the technique and the details of the mathematics are given in Appendix 10.4.

Having obtained the solution of the potential functions Φ_1, Φ_2 and Φ_3, it is now possible to determine the flux density distributions along the stator slot pitch (or rotor slot pitch) as well as inside the stator and rotor slots. In order to obtain the flux variation from maximum to minimum, it is sufficient to displace the rotor slot (rectangle II, Fig. 4.1) from the symmetrical position (stator slot - opposite - rotor slot) by half rotor slot pitch to the position (stator slot - opposite - rotor tooth).

The flux entering the surface of the stator tooth can be calculated by integrating the normal derivative of the potential

function Φ_2 at $y = g$ in the range ($0 \leqslant x \leqslant \pi - \beta_s$) and ($\pi + \beta_s \leqslant x \leqslant 2\pi$). The amount of the flux entering the sides of the stator tooth is obtained by integrating the tangential derivative of the potential function Φ_1 at $x = \pi - \beta_s$ and $x = \pi + \beta_s$ in the range ($g \leqslant y \leqslant h_s + g$). In the same manner the flux entering the surface of rotor tooth and its side is determined. The computer programme which is written for estimating the rotor and stator tooth flux variation and also the print out of the computed results are attached at the end of the thesis. (see pages 243-272)

4.3.1 The Result of Some Computed Tooth Flux Waveforms

Owing to the fact that there are no reliable analytical or empirical formulae by which the shape of the tooth flux waveforms can be calculated, no attempt is made to correlate the computed results with the formulae which are either used or proposed in literature. The latest formula which is based upon a limited experimental test was given by Binns[37]. Besides the fact that the proposed experimental formula leads to an error of the order of 75% (this was noted by Binns), the given formula is based upon the maximum and minimum tooth flux and it excludes the slot pitch parameter.

The experimental flux waveforms which are used for the purpose of correlation are obtained from search coils, sepcifically constructed for investigating the various flux components entering the rotor tooth surface as well as the tooth body. Since the details of these search coils and their positions and also the flux waveforms of the taken oscillograms are discussed in the experimental part of this thesis (chapters 6 and 7),

the result of correlation is illustrated later. However, it will be seen in Section 7.6 that the correlation between theory and experiment is very good for all flux waveforms obtained from various search coils.

In order to establish the accuracy of the analysis it is possible to make use of symmetrical positions of rotor tooth against stator tooth (with equal slot widths) for which the average flux density in the air gap can be calculated by the method of conformal transformation. In Table 4-1 the magnitude of the average air gap flux density obtained by Baillie's formula given by equation(3-4a), (see chapter 3, section 3.3) and by author's analysis is compared for a selected ratio of the slot opening width to the air gap length. (see page 249)

Table 4-1

Per unit average air gap flux density for various S/g

S/g	2	4	6	8
Baillie's formula (*) $\frac{t+\frac{5g'S}{5g'+S}}{t+S}$	0.9714	0.9111	0.8363	0.7538
Author's analysis	0.9571	0.8906	0.8269	0.7698
Discrepancy %	1.47	2.25	1.12	2.11

The reason for considering only one symmetrical position of rotor tooth against stator tooth is that the average air gap flux density at this position is maximum and the effect of truncating the series representing the air gap potential function is more prominent than at other positions of the rotor tooth.

The slight inaccuracy shown in Table 4-1 is due to the fact that the series is truncated up to 10 terms. If an inaccuracy less

(*) g' is half of the air gap length g

than 1% is desired, the number of terms should be increased. However, it is believed that an accuracy of 1% - 3% for the d.c. component of the air gap flux density waveform is quite satisfactory for all practical purposes. The accuracy of the magnitude of other harmonics is much better than the d.c. component, because the series for the harmonics converge much faster (see Appendix 10.4).

In order to illustrate the total variation of the rotor tooth flux for various combinations of slot widths and tooth pitches, a few computed waveforms are shown in Figs. 4.2-4.6 . The rotor tooth flux waveforms are computed for a fixed air gap length and a fixed stator slot width. The rotor slot width and rotor slot pitch are varied to show their effect on the shape of the flux waveform. The result of computation shows that the shapes of the tooth flux waves are, generally, non sinusoidal. By increasing the rotor slot pitch, the flux waveform approaches a sinusoidal variation, if the ratio of the rotor slot width to the stator slot width is not too high (compare Figs. 4.5 and 4.6). When the ratio of the rotor slot width to the stator slot width increases the shape of the flux waveform tends to a rectangular variation (see Figs. 4.4 and 4.6).

In connection with the magnitude of the tooth flux pulsation Binns commented that for ratios

$$\frac{\text{stator tooth width}}{\text{rotor tooth width}} = 0.5$$

the magnitude of tooth pulsation becomes small. It can, however, be seen from Figs. 4.5 and 4.6 that by increasing the rotor tooth width with respect to the stator tooth width the magnitude of the tooth pulsation slightly increases. Despite this, the losses in the case of wider rotor tooth (see Fig. 4.5) are clearly less than in the case of narrower rotor tooth (see Fig. 4.6),

because the harmonic content in the latter flux waveform is higher than in the former flux waveform. Generally speaking, it is unwise to make broad conclusions on the basis of limited parameters.

The analytical method described in this chapter is particularly appropriate for predicting the magnitude and the shape of the tooth flux pulsation.

4.4 Squirrel Cage Pulsation Losses due to Permeance Variation

Generally, with relative movement of rotor and stator teeth the reluctance path of the total flux produced by the stator winding, changes everywhere in the machine. Considering the constituents of the total flux to be the working (or main) flux, the air gap leakage flux due to the m.m.f. harmonics, and the slot leakage fluxes; then in the presence of the slot openings all these flux components pulsate with rotor movement. The pulsation of the leakage fluxes in the slots (particularly at the top of the slots) results from the pulsations of both the main and air gap leakage fluxes.

On no-load the pulsation of the air gap leakage flux is usually neglected on the basis that the magnitude of the magnetising currents corresponding to the m.m.f. harmonics is too small in comparison with the fundamental m.m.f.

The problem of a sinusoidal applied m.m.f. across the air gap was discussed in detail in Section 3.4, and it was shown that by using the principle of analogy the air gap flux density can be expressed by multiplying the sinusoidal m.m.f. and the air gap permeance wave obtained on the basis of constant applied m.m.f. (providing the peripheral air gap flow from positive pole

to the negative pole is neglected).

Often the treatment of the air gap flux density obtained on the basis of constant applied m.m.f. is directly employed to represent the distortion of the fundamental flux density. For instance Walker[34] in his paper stated that "no appreciable error is involved if the sinusoidal half waves of the m.m.f. are replaced by rectangular half waves whose amplitudes are equal to the mean value of the half sine waves". On the basis of this substitution Walker applied the rule $C_1 + C_2 - 1$ (see Section 3.4) and obtained the resultant flux density wave. Such substitution could be acceptable if the object is to investigate the effects of rectangular m.m.f. waves. But, if the object is to determine the distortion of the fundamental flux density wave then such substitution is questionable (because the harmonic content of the distorted flux density wave, particularly the magnitude of the harmonics, in the case of the rectangular m.m.f. wave can be substantially different than in the case of sinusoidal applied m.m.f.). Another opinion which is widely expressed by the engineers is that the wavelength of the fundamental m.m.f. is sufficiently long to make the assumption of constant m.m.f. justifiable. This opinion, essentially, assumes the shapes of the distortions along the fundamental flux density to be the same. This assumption is credible if the slope of the fundamental m.m.f. with respect to a stator (or rotor) slot pitch is sufficiently small and this may happen if the number of the slots per pole is too large. However, both the above propositions are put forward, because the principle of analogy discussed in Section 3.4 cannot be stricty speaking applied to a doubly slotted air gap. This is due to the fact

that the permeance analysis obtained on the basis of constant applied m.m.f. is restricted to a limited region of the air gap. It should be noted that this restriction is not only related to the analytical method given in the previous section, but to all practical methods by which the tooth pulsation is being investigated. Generally, the total air gap permeance wave, besides the harmonics of the order of stator and rotor slots, contains permeance harmonics of long wavelength (the order of these harmonics is equal to the product of the stator and rotor slots). It was noted in Section 4.3 that in induction machines as well as in most practical air gap geometry the magnitude of these harmonics is not important. Therefore it is justifiable to express the flux density wave by the product of the fundamental m.m.f. and the permeance variation resulting from one cycle displacement of the rotor slot with respect to a stator slot pitch.

In squirrel cage induction machines the flux pulsations in rotor teeth, to a large extent, are damped out by the high frequency currents circulating in the short-circuited bars. Hence, this suggests that tooth pulsation losses appear as I^2R losses. Since copper losses are much smaller than their corresponding iron losses, it follows that the magnitude of tooth pulsation losses in open-circuited cage should be significantly greater than in short-circuited cage.

On the subject of high frequency losses due to permeance variation a series of well co-ordinated papers by Spooner and his associates[55-58] were published in early 1920's. In connection with tooth pulsation Spooner[56] carried out an extensive experimental work whereby he measured these losses in both short-circuited and open-circuited cage. Although, the result of

these experimental works has been published as early as 1920's, it appears that the significance of the published results is either glossed over or forgotten in later publications. Spooner has shown that within a wide range of air gap flux densities the measured tooth pulsation losses remain the same in both cases of short-circuited and open-circuited cage. By using Field's methods of calculating the a.c. resistance of the bars (see Chapter 3, Section 3.6) Spooner calculated the pulsation I^2R losses. It was found that the calculated losses are a comparatively small percentage of the observed losses. Spooner could not find an adequate explanation for this large discrepancy and he, therefore, concluded that the extra losses are due to the increased tangential slot leakage fluxes (due to the increased magnetomotive force between the adjacent bars). In the discussion on Spooner's paper, Alger commented that the observed discrepancy is due to the m.m.f. of the circul ting currents in the bars which set up in the stator teeth flux pulsation which lead to iron losses approximately equal to those losses due to undamped rotor flux pulsations. In Alger's words the induced circulating currents 'shove' the pulsating flux from rotor teeth back into the stator teeth. In support of Alger's stipulation, Weighsel (see the discussion on Spooner's paper[56]) produced some experimental evidence. In this experiment a search coil was placed over a stator tooth and the voltage induced in the search coil was measured (under the same conditions) in both short-circuited and open-circuited cage. The oscillograms obtained showed that the induced voltage in the cage short-circuited case is much greater than in the cage open-circuited case. On the basis of these experimental and qualitative

explanations it was concluded that tooth pulsation losses should be calculated as rotor iron losses (assuming the cage to be disconnected).

25 years later Walker[34] reviewed the analysis of Spooner's paper (apparently unaware of the discussion given on the paper) he confused the high frequency stator iron losses due to the permeance effect of rotor slot openings (i.e. the losses which occur due to the passage of rotor slots over the stator surface) and the high frequency stator iron losses due to the rotor slot m.m.f's. Later, Alger, et al[59] published a paper in which, contrary to the previous belief, they concluded that the high frequency stator losses produced by rotor slot m.m.f. harmonics are too small. Although, Alger et al implicitly assumed that the width of the rotor slot openings is negligible and despite the fact that they included the rotor slot m.m.f. harmonics in the equivalent circuit, the loss equations were given on the basis of a sinusoidal air gap variation due to the stator slot openings. It is clear that, besides neglecting the effect of rotor slot openings, the assumption of a sinusoidal permeance variation is a gross simplification of the actual permeance wave. In calculating the circulating high frequency I^2R losses, it is a common practice to introduce into the loss equations a factor called the 'damping factor'. This factor was given by Christofides[60] as the ratio of the secondary differential reactance to the secondary slot reactance. These reactances are, of course, calculated in accordance with the approximate rules discussed in Chapter 3. Also in order to include the effect of rotor slot openings in the calculation of surface losses, Christofides has arbitrarily increased the losses by 50%.

This brief survey of literature is given to illustrate that the squirrel cage losses obtained on the basis of the equivalent circuit are approximate and the given loss equations involve empirical factors in addition to the inaccurate analysis of the reactances.

With reference to the experimental results obtained by Spooner and others, and also on the basis of the experimental work carried out by the author (see Chapters 7 and 8) it is concluded that the appropriate approach for estimating the pulsation losses in rotor is to assume the cage to be disconnected and calculate the losses as iron losses.

4.5 Conclusion

The magnetic potential distribution in a doubly slotted air gap is given by using an analytical method and including the effect of rotor slots on the flux density distribution along the stator slot pitch. From the analysis of the Laplacian fields, the flux pulsation entering a stator tooth and its sides (or a rotor tooth and its sides) is determined by displacing the rotor from maximum permeance position to minimum position. The flux waveforms computed for various parameters indicate that the tooth flux pulsation, generally, contains higher harmonics of significant magnitude and the losses induced by these harmonics cannot be ignored.

It was shown that the methods used in literature for calculating the tooth pulsation (as well as the surface losses) due to the permeance variation are based upon dubious factors and inaccurate analysis of the air gap leakage reactances. It was shown that the experimental results indicate that the pulsation losses in both short-circuited and open-circuited

squirrel cage are effectively the same. It is, therefore, argued that the appropriate approach for estimating permeance losses in the squirrel cage is to assume the cage to be disconnected and the rotor losses to be iron losses.

5.0 General Discussion of Iron Losses in Induction Motors

5.1 Introduction

The study of physical phenomena occurring in ferromagnetic material subjected to an applied field is closely related to the possibility of determining the analytical relationship between the parameters of the region and the applied field. It has been mentioned in the introduction of Chapter 3 that in regions occupied by air and conductors, the resistivity and permeability can be assumed to be constant (although, the resistivity varies with temperature). In these regions the linear theory can be applied for each applied field harmonic and superimpose the effects produced by each individual harmonic to obtain the resultant field. As far as the total field (or the resultant induced currents) is concerned, the application of linear theory is valid providing the incurred losses and forces are estimated on the basis of the total field and not on the basis of individual harmonics.

In ferromagnetic materials the relationship between the flux density and the intensity of the field is non-linear and its function is highly complex. The difficulties which are encountered in the analysis of the magnetic field in ferromagnetic materials may be summarised in the following:

1. The alternating magnetic field is described by the diffusion equation

$$\text{curl}_s H = -\mu \frac{\partial H}{\partial t} \qquad (5\text{-}1)$$

where

$$\mu = f\left(\frac{B}{H}\right)$$

2. The amplitude of both flux density B and the field intensity H are a function of space and time, and each of these functions behaves differently. The relationship between the space functions of B and H describes the normal magnetising curve and the relationship between the time functions of B and H describes the hysterisis loop.
3. Since the parameter μ is a highly complex function of space and time, it is not difficult to appreciate that the solution of the diffusion equation (5-1) cannot be derived if both non-linear functions of μ and $\frac{\partial H}{\partial t}$ are taken into account.

It was shown in Chapter 2 that the travelling air gap field in induction machines is neither sinusoidal nor of constant shape. Furthermore, it was shown in Chapter 3 that the effect of slot opening impose additional distortions. Besides these complications the non-linear theory has not been included in the travelling wave theory. Also no law has been discovered for calculating the hysteresis loss as a function of a travelling flux density wave of an arbitrary shape.

In view of the above considerations, it is clear that application of non-linear theory to the magnetic field of induction machines (without making further simplified assumptions) no practical solution can be predicted. At present, the only practical approach by which this problem can be tackled is to make use of the principles of the linear theory. In practice the application of linear theory can only provide an approximate indication of losses and thus the introduction of empirical factors becomes unavoidable. In view of this situation, a common view is expressed by engineers that any modification of the

existing inexact but simple loss formula is unjustifiable. The author does not accept this point of view for two reasons:

a) Introduction of empirical factors into loss equations can only serve a useful purpose if the loss equations derived on the basis of linear theory are accurate. It is unwise to add an arbitrary amount into an inaccurate formula.

b) Generally, the empirical factors are introduced on the basis of experimental data obtained from a limited test and limited range of parameters. Therefore, without a sound theoretical analysis, though based on simplified assumptions, it is not possible to make a satisfactory appraisal of new or unconventional designs.

With these points in mind, the primary object of this chapter is to make a critical assessment of the present linear and non linear theories and give a rational treatment of iron losses based on constant permeability.

5.2 The Scope of Non-Linear Theory

The applied field intensity is commonly assumed to vary sinusoidally with time everywhere in the iron. With this assumption the time dependence $\frac{\partial H}{\partial t}$ can be replaced by a complex notation and thus simplify the diffusion equation (5-1). On the other hand such an assumption would contradict the non-linear property of the iron because, by assuming the field intensity to vary sinusoidally with time everywhere, this in turn implies that the current densities induced by the e.m.fs. must also vary sinusoidally with time everywhere. Since the e.m.fs. vary sinusoidally with time everywhere, this means that

the flux density, also, varies sinusoidally with time everywhere which is not admissible. Therefore, it is not possible to assume the field intensity to vary with time sinusoidally everywhere in the iron, unless prior conditions are imposed. In theory both B and H may vary sinusoidally with time everywhere in the iron if the hysteresis loop is expressed by an ellipsoid. In such a case the flux density lags the field intensity by an angle θ . In order to replace the actual hysteresis loop with an equivalent ellipsoid it is necessary to determine the angle θ such that both areas of the actual loop and the ellipsoid become equal. By using this principle, the flux density and the field intensity can be written in complex form and hence introduce the concept of complex permeability, namely,

$$\dot{B} = \dot{B}_m e^{j\omega t}$$

$$\dot{H} = \dot{H}_m e^{j\omega t}$$

and

$$\dot{\mu} = \frac{\dot{B}_m}{\dot{H}_m} = \mu e^{-j\theta}$$

By making use of the concept of complex permeability, the differential equation (5-1) can be written in complex form with $\dot{\mu}$ replacing μ . The solution of the differential equation (5-1) in a complex form is commonly applied to cylindrical bodies or semi-infinite blocks. In both cases the resulting equations involve laborious complicated functions. In the case of cylindrical bodies the solution involves Bessel functions in which the evaluation of the moduli and phase angle θ is too difficult,[61] because they are not tabulated for complex arguments. In order to make an analytical solution tractable, the differential

equation (5-1) is solved on the basis of an effective permeability obtained experimentally.[1-4] This approach involves laborious experimental as well as mathematical analysis (see Reference 1 and 62). However, although these methods are, to a large extent, dependent upon the experimental results their applicability is confined to smooth solid blocks subjected to sinusoidally varying applied fields. Also the principle of superposition for two or more applied fields cannot be used.

For the reasons indicated in the introduction of this chapter and also due to the complicated nature of the non-linear analysis described above, no justification can be found for applying the loss formulae obtained by these methods to the field of induction machines.

A practical approach for tackling the problem of iron losses in induction machines, would be more appropriate to consider the hysteresis and eddy current losses as two separate components. Usually, the hysteresis loss in solid rotors is considered to be small in comparison with the eddy current losses. In induction machines, however, the rotor is laminated and the hysteresis loss is likely to form an appreciable fraction of the whole loss. The first theoretical approach for calculating the hysteresis loss as a separate component is that of Carter.[63] Carter suggested that if the law of loss discovered by Ball's[64] investigations be assumed an appropriate for an applied travelling field along a smooth rotor surface, then the hysteresis loss can be determined by integrating the flux density which penetrates the laminations (taking into account the skin effect but neglecting the eddy current reaction on the applied field). The same approach was adopted later by Gibbs,[65] by modifying Carter's formula. It is

clear that both Carter's and Gibbs' formulas (which are given for tooth frequency losses) are based upon two hypothetical considerations, namely:

a) That Ball's formula which is derived for biased asymmetrical loops is valid. In reality the unsymmetrical loops due to tooth frequency fluxes are minor loops superimposed on the main loop due to the fundamental flux. Both Spooner[66] and Ramsden[62] have shown that the hysteresis loss calculated on the basis of Ball's formula is valid only for a limited range of field variation.

b) The depth of flux density penetration in laminated iron is assumed to be the classical one, although it is well known that the depth of penetration in laminated iron is far more complex than in solid iron.

Besides Carter's and Gibbs' formulas there are a number of empirical formulas which are discussed in details by Spooner.[55] However, the experimental results carried out by Spooner showed that none of the formulae derived on theoretical basis (although some of the formulas were modified by empirical factors) give an adequate approximation to the actual hysteresis losses. Generally, the hysteresis losses are calculated by formulas which are derived purely on the basis of experimental results. Strictly speaking these experimental formulas are also inadequate because as mentioned earlier they are based on a limited tests and parameters. For instance, Spooner's experimental formula[55] is based upon the tests carried on one type of material, and in this connection Spooner stated that for other kind of materials the loss should be either increased or decreased according to the known difference in the hysteresis characteristic of the material. However, Spooner's proposition appears to be the only

satisfactory way for calculating the hysteresis loss.

In literature the non-linear analysis of eddy currents is, usually, given on the basis of idealised magnetising curves such as the rectangular curve. This approach has been used by Agarwal whereby he obtained a relatively simple formulae for calculating eddy current losses in both solid and laminated iron subjected to a sinusoidally time varying applied field. The non-linear analysis given by Agarwal[5] is not applicable to induction machines, because the applied field along the rotor laminations is not constant (as assumed by Agarwal) but attenuate hyperbolically with depth. Besides this, the accuracy of Agarwal's formulae entirely depends upon the choice of suitable value of permeability. However, the problem of eddy current losses can be treated with satisfactory accuracy by using the linear theory. This problem is discussed in the following sections.

5.3 The Linear Theory for Eddy Current Losses

The basic principles for analytical calculation of eddy current losses on the basis of linear theory were published as early as 1906 by Rüdenberg[67]. On the same line of thought, Adams, et al[68] published a classical work in which they investigated the distribution of the induced currents in a semi-infinite solid block subjected to sinusoidal travelling wave at the surface. The result of these analyses were applied to the rotor of synchronous and induction machines on the basis that the applied air gap field remains the same irrespective of the air gap length or the effect of stator permeability (i.e. on the basis of undamped flux density). In order to include the effect of the air gap and proximity of the stator several papers[69-75] were

published. The common feature of all the published works is to make the following assumptions:

1. that the air gap length is too small in comparison with the stator and rotor diameters so that the air gap curvature can be neglected.
2. that both the stator and rotor are solid semi-infinite blocks.
3. that the machine is infinitely long so that the end effects can be neglected.
4. that the effects of eddy currents in the stator iron and copper are small.

and 5. that the resistivity and permeability of both rotor and stator are constant.

The above assumptions and simplifications enable a relatively simple linear theory to be developed in terms of rectangular co-ordinates in two dimensions. Since the problem of solid iron is extensively treated in literature (see References 69-75 and also 62), the details of the solution of the field in solid iron are not included in this chapter.

Often the results of field analysis obtained on the basis of solid iron are used for laminated iron. Although, the analysis of solid iron provides a conceptual picture of the eddy current phenomenon and gives an indication of the field behaviour in the iron, it would be inappropriate to represent the analysis of the laminated iron as a modified version of the solid iron.

In laminated iron the axial flow of eddy currents is prevented by the interlamina insulations and the currents are forced to flow in the peripheral direction. As an illustration, the path of eddy currents, induced by an applied wave, on the face of a solid and laminated iron is schematically shown in

Fig. 5.1.

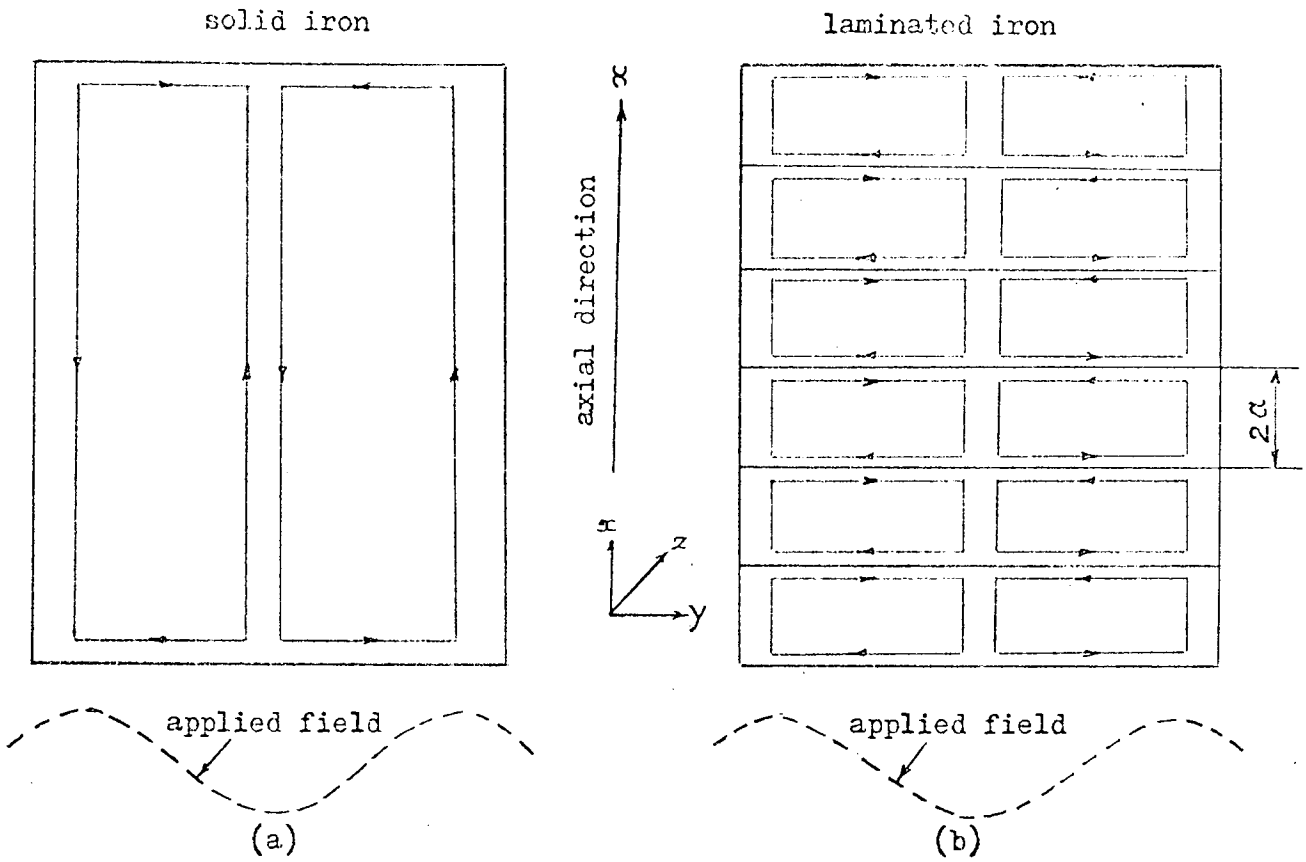

Fig 5.1

The paths of eddy currents on the face of solid and laminated iron

The currents which flow in the axial direction are called "damping currents", because these currents damp the flux which penetrates the iron surface radially. The currents which flow in the peripheral direction are called "screening currents", because the effect of these currents is to crowd the flux towards the surface of the individual lamination. Further from the surface of the iron, the induced eddy currents attenuate with depth. However, due to the lamination the applied field penetrates the iron along the interlaminal surfaces and hence the induced eddy currents sustain their magnitude within a significant depth from the surface of the iron. By virtue of this deep flux

penetration, the distribution of eddy currents in laminated iron is more complex than in solid iron.

Considering a single lamination, it is possible to distinguish two types of induced eddy currents. The first type of eddy currents which are induced due to the radial penetration of the flux may be illustrated by horizontal planes (an example of such horizontal plane is shown in Fig. 5.1a). Within the classical depth, the function of the induced eddy currents in such horizontal planes is to expel the inducing flux from the inside of the lamination. Above the classical depth the induced eddy currents crowd at the surfaces of the lamination in order to keep the expelled flux out of the iron. These eddy currents contribute significantly to the total eddy current losses. The second type of eddy currents which are induced due to the angular variation of the applied field may be illustrated by vertical cross-sectional planes perpendicular to the peripheral direction as shown in Fig. 5.2.

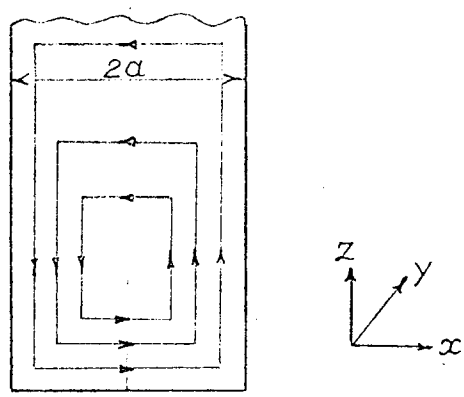

Fig 5.2

Eddy current distribution in a vertical plane of a single lamination

From loss point of view, these induced eddy currents are not important, because the field intensity which produces them is weak.

The first purely analytical analysis of eddy current losses in laminated iron was given by Carter.[63] Assuming the current flow in the lamination to be purely peripheral, Carter derived an analytical formula in which the losses appeared to be proportional to the square of the lamination thickness. The derivation of Carter's formulae was based upon two principal assumptions, a) the induced eddy currents are confined within the classical depth and b) the current flow in a single lamination is purely peripheral. The implication of assuming the current flow to be purely peripheral effectively amounts to neglecting the effect of lamination thickness on the distribution of eddy currents. In connection with this assumption, C.W. Carter[76] noted in his paper that Carter's formulae is applicable not to the thinest laminations but to laminations which are thick enough to ensure that the transverse component of current density is negligible in comparison with the longitudinal component. Although these remarks are correct; the inadequacy of Carter's formulae to a large extent lies in the second assumption that the induced eddy currents are confined within the classical depth.

As a matter of fact most of early theoretical works[68,77,78] on laminated iron were based on the analysis of solid iron. For instance, Adams, et al[68] introduced into the loss formulae for solid iron an empirical factor which accounts for the change of the path of eddy currents in the lamination (i.e. the resistivity of the iron is modified by an additional multiplying factor). This approach has been used by several authors,[34,65,72] and the loss formulae obtained in this way appears as a first power of the lamination thickness (in contrast with Carter's formulae which is proportional to the square of lamination thickness). As indicated by G.W. Carter[76] all these formulas are inadequate to give an

acceptable approximated value of the losses when they are applied to a particular design of induction machine.

The complexity of eddy current distribution in laminated iron has been known for a long time, and for this reason attempts were made to investigate the losses experimentally.[55,79,80] The work of Spooner and Kinnard[55] is possibly the earliest comprehensive investigation in this field. Spooner and Kinnard found that the magnitude of the total losses (hysteresis and eddy currents) is proportional to the square of lamination thickness when the iron is finely laminated. In the case of thick laminations the losses appeared to be proportional to the first power of the lamination thickness.

The first detailed analysis of the deep penetration phenomena was published by Bondi and Mukherji.[81] On the basis of this paper several authors[82-85] investigated the eddy current losses in a laminated pole shoe. The experimental results obtained by these authors revealed that the measured components of the field inside a lamination substantially deviates from the values predicted by theory (see in particular Reference 85 and their Fig. 6). On this account, the author revised the analysis of Bondi and Mukherji and it was found that their analysis is mathematically over-defined. In the analysis of Bondi and Mukherji the solution of the total field (i.e. the applied field and the field of the induced eddy currents) involves five unknowns. In order to determine these five unknowns, Bondi and Mukherji have, twice, made use of the boundary condition at the surface of the iron. This boundary condition which dictates that the radial component of current density at the iron surface to be zero, is once implicitly used in connection with the undamped applied flux density (which exists in the absence of eddy currents, see

their equation 16). The same boundary condition is again used for the total field (i.e. the undamped flux density in conjunction with flux density created by the induced eddy currents, see their equation 12). The implication of using the same boundary condition twice is tantamount to introducing an unknown exciting field which could lead to erroneous results.

The same problem investigated by Bondi and Mukherji is treated in Appendix 10.5 on the basis of two separate field components namely, the applied field and the field of the induced currents. Owing to the limited time it was not possible to verify the given theoretical analysis experimentally. For this reason it was decided not to include in this work the results of theoretical eddy current loss calculation. However, the field analysis given in Appendix 10.5 not only provides an alternative approach for treating electromagnetic problems of complicated nature, but it can be tested in the future work for estimating eddy current losses in laminated iron.

5.4 The Scope and Application of the Linear Theory

The methods in common use for the calculation of losses due to the winding and slot-permeance harmonics are based upon the linear theory which does not allow for superposition in detail. According to the linear theory, the permeability of iron is taken to be constant for all field harmonics irrespective of the shape of the total field waveform and the change in the magnitude of the field strength inside the iron. Apart from the superposition of the total harmonic variation on the fundamental, there is also the superposition of the harmonic fields themselves to be considered.

The diagrams illustrated in Chapter 2 indicate possible features about the resultant fields. For example Figs. 2.3 and 2.4 show that the resultant m.m.f. variation for a full pitched, infinitely distributed winding is likely to be un-symmetrical, having larger positive peaks, than negative peaks where the fundamental is positive and vice-versa where the fundamental is negative. Besides the non-symmetrical shape of the waveforms, the field variations are superimposed on the fundamental and hence a continuous change in the magnitude of the bias field. In addition to the phase band and slot m.m.f. harmonics, there are slot-permeance harmonics which are also superimposed on the fundamental. All these harmonic variations form incremental loops on the fundamental with various bias. In the case of incremental loops with a small bias, the incremental permeability is of the same order as the normal (unbiased) permeability, but the loss is affected by the asymmetry of the loop. In the case of incremental loops with large bias the incremental permeability is considerably less than the normal permeability. Apart from this there is the question of the appropriate permeability for the varying bias. On this subject an extensive discussion is given in literature[62,66,86,87], and the points made above are given only to illustrate the nature of the problems associated with the analysis of superposition and hence the use of linear theory. However, the common view expressed in literature is to use one value of incremental permeability for all the harmonics. The representative value of the incremental permeability depends upon the material and the magnitude of eddy current reaction, and its value, generally, lies within a fairly wide range, namely $100 < \mu_\Delta < 1000$. The accurate knowledge of the permeability

is of importance, only, if an accurate loss formula is available (as in the case of solid iron). In the case of laminated iron it was shown in the previous section that no accurate analysis of the losses is available in literature and the effect of permeability on the loss remains to be investigated.

With regard to the superposition of the slot m.m.f. and slot-permeance harmonics, it is common practice to ignore the interaction of the harmonics and calculate the losses due to each of them separately and add the calculated losses. This procedure is not acceptable for the following reasons. In Chapter 2 it was shown that on no-load the slot m.m.f. harmonics are concentrated about the zero position of the fundamental and the shape of the total harmonic variation at rotor surface is of triangular form. Away from the zero position of the fundamental, the shape of the variation gradually changes (see Fig. 2.6) and the magnitude of the variation at the peak position of the fundamental reduces to a small amount. On the other hand, the magnitude of the slot-permeance harmonics is maximum at the peak position of the fundament and it reduces as it approaches the zero position of the fundamental. In between these two positions (i.e. between zero and peak) the slot m.m.f. and slot-permeance harmonics combine together and the shape of their resultant variation is neither triangular nor a ripple (see Figure 7.12 where a detailed oscillogram of the variation of the flux waveforms at the secondary surface is shown). Therefore, along rotor surface there are two distinct waveforms of the total harmonic variations, one due to the slot m.m.f. harmonics (which is of triangular form) and the other one due to the slot permeance harmonics (which is a wave of ripples).

By considering one rotor tooth, it can be seen that when this tooth is at the zero position of the fundamental the tooth losses are primarily determined by the harmonic contents of the triangular waveform of the field variation. When the tooth is at the peak position of the fundamental, the losses are determined by the harmonic contents of the permeance ripple. If the magnitude of the field variation inbetween the zero and peak positions of the fundamental is not higher than either of the field variations at the zero or peak position, then the average rotor loss is somewhere between the losses calculated on the basis of the slot m.m.f. harmonics and that calculated on the basis of the slot permeance harmonics (i.e. assuming the shape of the waveform of the total harmonic variation in each case to be the same in all rotor teeth). As far as the variation of the field inbetween the zero and peak positions of the fundamental is concerned, the result of experimental work discussed in Chapter 7 shows that the magnitude of the variation is not higher than the magnitude of the field variation at the peak position of the fundamental. However, the shape of the total harmonic variations at these intermediate positions (as explained earlier) are not the same. This means that the average loss is not necessarily the same as the mean value of the two loss components referred to earlier. Despite this, the average value of the combined losses is unlikely to be considerably different from the mean value. Therefore it is suggested to calculate rotor losses on the basis of the mean value of the two loss components calculated separately.

Although the theoretical analysis of the problems outlined above is too difficult, the linear theory remains to be the

most convenient method for estimating the losses in induction machines. By making an appropriate analysis of the field variation in the air gap, the losses can be calculated with greater accuracy. However, the accuracy of the calculated losses depends to a large extent upon the validity of the loss formula used and the method by which appropriate allowances are made for the detailed field distribution in the air gap, (in connection with the latter point further suggestions are proposed in Chapter 9, to be considered in the future work).

6.0 The Experimental Machine

6.1 Introduction

In normal induction machines, the secondary flux components and induced currents are usually measured by search coils and J-probes whose leads are connected to a separate slip-ring on the rotor shaft. Owing to low level of the signals, the susceptibility to noise pick up, and the complexity of the equipment required to transmit a large number of signals, the flux and current density measurements are either inaccurate or too costly. In order to avoid these difficulties, a special inverted induction motor was designed in which the rotor (secondary member) is stationary and the stator (primary member) is rotating.

Owing to the special feature of the inverted induction motor, it is possible to make a detailed study of the secondary flux and current density components with maximum accuracy.

In this chapter, the technical details of the experimental machine, the search coils, J-probes, and the instrumentations used for conducting the tests are described.

6.2 The Design of the Inverted Induction Machine

The experimental machine is nominally rated at 35 h.p., 415 V, 50 Hz, and 1500 rev/min. In order to drive the motor externally, the shaft of the primary is coupled to a precision dynamometer which is also used to measure the losses of the secondary. The three-phase power supply to the primary windings is connected via slip-rings. Two photographs each illustrating the primary and secondary separately are shown in Figs.6.1 and 6.2. The surface search coils and the terminal boards to which

the leads are connected can be also seen in Fig. 62 .

The general details of the primary member (stator) are listed in Table 6-1.

Table 6-1

General details of the primary member (stator)

Number of slots	36
Number of poles	4
Type of winding	double two layer lap
Material of the laminations	Transil 107, $\rho = 48 \times 10^{-6}$ Ω/cm
Thickness of the laminations	0.35 mm
Axial length of the machine	260 mm
Outside diameter	287.72 mm
Inside diameter	88.9 mm
Width of the slot opening	4 mm
Slot pitch	25.1 mm

The slot and tooth configuration of the stator is illustrated in Fig. 6.3

The general details of the secondary member are given in Table 6-2

Table 6-2.

General details of the secondary member (rotor)

Number of slots(parallel sided slots)	32
Conductors per slot(insulated conductors)	1
Material of the laminations	Transil 107, $\rho = 48 \times 10^{-6}$ Ω/cm
Thickness of the laminations	0.35 mm
Outside diameter	444.5 mm
Inside diameter	288.92 mm
Width of the slot opening	3 mm
Slot pitch	28.36 mm

The details of the slot and tooth configuration of the secondary are shown in Fig.6.4 . The bars of the cage are made of solid rectangular copper to fit the shape of the slots. At each end of the bar a hole is drilled and through flexible leads each bar is connected to the end-rings. This arrangement is especially designed to enable the bars to be connected or disconnected from the rings (i.e. to facilitate disconnected cage test).

The details of the network of search coils and J-probes constructed on the secondary are described in next section.

6.3 The Construction of Search Coils and J-probes

6.3.1 The Search Coils

The secondary member is provided with a large number of search coils for measuring the components of the flux entering various parts of the tooth body and the surface of the tooth.

Generally, application of search coils is unsuitable for the purpose of investigating the flux density distribution, because the e.m.f. induced in a search coil is generated by the total flux enclosed by the area of the search coil. However, if a large number of search coils of sufficiently small width is employed, it is possible to obtain an approximate picture of the flux density distribution. On the other hand, construction of a large number of search coils in induction machines is not practical due to, firstly a small air gap length and secondly, the signals obtained from narrow search coils are too low. Therefore, in the present experiment a compromise is made by choosing the search coil width to be sufficiently small with respect to the tooth width, and sufficiently wide to obtain an adequate signal.

In previous experimental works, the technique of printed circuit search coils was developed for the purpose of surface flux measurement. However, it was found that the method of printed search coils requires a special technique and it is a costly method. Instead a simple and economical technique is developed, which consists of sandwiching the pattern of the search coil between two very thin sheets of melinex using a fine layer of araldite.

The pattern and widths of the surface search coils used in the experiment are shown in Fig.6.5 . The leads of the search coils are twisted and brought out through the slot opening to a terminal board and then connected to multiple rotating selector switch. The connections of the rotating switch are arranged in such a manner that thirteen combinations of search coils of different widths can be selected. The widths of these search coils and also the numbers assigned to each of them are indicated in Fig. 6.5 .

The search coils constructed for the measurement of the flux components entering various parts of the tooth body are shown in Fig.6.6 . As shown in Fig.6.6 , the width of each tooth lip is divided into three equal parts. Search coil 42 is located at the edge of the tooth lip, search coil 41 at the middle, and search coil 40 at the corner of the tooth. Similarly, three search coils are symmetrically wound on the other tooth lip. In order to investigate the flux in the tooth body, three search coils (one at the top, one at the middle, and one at the bottom of the tooth) are constructed (see Fig.6.6).

6.3.2 J-probes

The theory and construction of J-probes (i.e. a filament type current density probe) have been treated in detail by Burke and Alden[89]. These probes consist of an open circuited filament of wires which are placed on the surface of a solid conductor. The entire length of the filament with the exception of the two extreme ends is insulated electrically from the conductor. The two extreme ends are electrically connected to the conductor by making two negligibly small holes on the surface of the conductor. Two leads are then twisted together and connected to a high impedance voltmeter.

If the filament is aligned with the current direction and is of suitable length, such that the current density and conductor resistivity do not change significantly over the length, then the terminal voltage is proportional to current density, namely

$$V = \rho \ell J \qquad (6\text{-}1)$$

where ρ is the resistivity of the conductor, and

ℓ is the length between the two end points.

It is clear from equation (6-1) that in order to obtain an accurate measurement of current density, the filament length must be sufficiently short such that the current density and resistivity can be considered to be constant. On the other hand if the length of the filament is too short, the signal would be also too low which leads to the susceptibility of noise pick up and difficulties in amplification. However, the lengths of the J-probes which were constructed along the surface of the bar are chosen such that the induced signal is sufficiently large and at the same time making the effect of the ventilating ducts as small as possible. The details of the

locations and lengths of the J-probes are shown in Figs.6.7-6.8

Also along the surface of the lamination of the inverted rotor four J-probes are located and these are shown in Fig.6.9

6.4 The Circuit Diagram and the Instrumentation

6.4.1 Measurement of the Input Power

The general lay out of the circuit diagram used in the experimental work is shown in Fig.6.10

For the purpose of gradual and smooth regulation of the excitation, the supply voltage is connected to a manual auto-transformer. By means of the step-up transformer (see Fig.6.10) it was possible to increase the input voltage above the nominal 415 volts to a maximum 600 volts (on no-load, at 600 volts excitation the magnetising current is approximately equal to the full load rated current). The input line voltages are measured by three identical Solatron digital voltmeters.

Input current measurements are made via three identical current transformers. The primary winding of each transformer had three terminal connections which gave three selections of the ratio of the primary current to the secondary current, namely: 1, 5, 10.

All of the ammeters connected in the secondary windings of the current transformers are also identical (see Fig. 6.10). Due to the low power factor of the experimental induction machine, the measurement of the input power is made on a special polyphase wattmeter capable of reading power at 0.1 power factor with accuracy better than 1%.

In order to ensure maximum accuracy, all of the apparatus were recalibrated and the maximum possible error of each instrument is less than 0.5%.

6.4.2 Instrumentation of Current Density and Flux Measurements (Fig. 6.11)

The leads of search coils and J-probes shown in Figs. 6.6-6.9 are brought out to a terminal board located on the secondary. By means of multicore-screened cables, the terminal board is connected to two 50-way selector switches. For each position of the two selector switches a number is assigned, and the incircled figures denoted in Figs.6.6-6.9 correspond to these positions.

The amplification and integration of the signals obtained from search coils and J-probes are performed on 'O' type Tektronix unit. This unit contained two identical operational amplifiers of very low drift. The accuracy of the amplification is less than 1.0 %.

The amplified and integrated signals are connected to two identical Solatron digital voltmeters. These signals are also fed to the inputs of a Solatron Oscilloscope for photographic recording.

6.4.3 Measurement of the Slip

Due to the small difference between the speeds of the rotating magnetic field and rotor, the accuracy of the slip measurement is important. The method used in the present experimental work is based upon the direct measurement of the input and output frequencies. For this purpose two digital frequency meters (with accuracy not more than 0.1%) are employed to read the period of the input voltage to the induction machine and the period of the rotation, simultaneously. The period of the rotation is counted by pulses generated from a sensitive photo-element positioned against the primary shaft

at a small distance. A narrow white strip of paper which was fixed on the dark shaft triggered the photo element on and off by the movement of the primary. By using the readings of the frequency meter connected to the photo-element, a digital voltmeter was calibrated to give direct reading of the rotor speed.

In connection with the slip measurement it is necessary to point out that after each reading of the frequency meters, it was necessary to re-record the measurements. Since the slip could change while making the initial measurements, the readings of the frequency meters were noted again after each set of recordings. However, the greatest accuracy in such experiments can be achieved only by means of an electronic logging device which records all of the data instantaneously. Usually, construction and application of such instrumentation is limited to the investigation of transient behaviour in which the visual recordings cannot be performed. For the present experimental work, however, the maximum accuracy can be achieved by making the adequate precautionary steps noted above.

6.4.4 Temperature Measurement

The temperature rise of the windings due to the flow of the current is measured by means of a thermistor (type TH - B11) embedded in the winding.

The calibration of the thermistor (i.e. the variation of the internal resistance of the thermistor versus temperature) is obtained by using a standard thermometer and a Universal Cambridge Bridge, both of which had 0.1% accuracy.

As the primary member of the machine is rotating, the leads of the thermistor are brought out to a separate slip-ring and the resistance of the thermistor is read by a Solatron digital

meter (0.1% accuracy). The additional resistances in the circuit of the temperature measurement namely, the contact resistance of the slip ring and the resistance of the extra leads were sufficiently negligible to cause any error in the accuracy of the calibration curve.

The temperature measurement obtained in this experiment is based upon the assumption of uniform heat dissipation and that the same temperature prevails everywhere in the winding.

6.4.5 The Precision Dynamometer

The primary shaft of the inverted induction machine is coupled to a precision dynamometer (of cradle-type). This dynamometer is an ordinary d.c. machine except that its stator is hung on bearings co-axial with the rotor shaft and is equipped with radius arms which hold the stator in a fixed position while in operation.

The details of the design and operation of this dynamometer is given in Reference 90

The net torque of the shaft of the induction machine is measured by placing weights on the scales of the measuring arms which bring the stator into a balancing position. The length of the measuring arm is 30.218 cm.

The precision dynamometer is rated at 50 h.p., 3000 rev/min., and its accuracy is specified by the manufacturer to be within 0.1%.

7.0 An Experimental Analysis of Secondary Flux and Current Density Waveforms

7.1 Introduction

The total harmonic variation with respect to rotor, and the graphical methods for determining the shape of these variations in a smooth air gap, were discussed in Chapter 2. Also, in Chapters 3 and 4 a detailed discussion on the effect of slot openings on the shape of air gap flux density was given. In order to make an experimental appraisal of the given theoretical analysis a large number of oscillograms showing the details of the secondary flux and current density waveforms are taken at various applied voltages.

The positions and other details of the search coils and J-probes constructed for this purpose were described in Chapter 6. The oscillograms of the flux and current density waveforms are taken at synchronous speed, thus eliminating the slip frequency induced by the main flux. The relative position of the main flux is determined as follows.

The induction motor was driven slightly below the synchronous speed and the flux and current density waves were observed on the screen of the oscilloscope. The input to the driving dynamometer was then adjusted such that the motor pulled into synchronism at the desired position of the main field. Only two relative positions of the main flux with respect to the search coils are investigated. These two relative positions correspond to the peak and zero positions of the fundamental flux. All the oscillograms taken at the zero position of the fundamental are shown at the top of the figures [these oscillograms are indicated by Fig(a)] , and all the oscillograms taken at the peak of

the fundamental are shown at the bottom of the figures [these oscillograms are indicated by Fig. (b)] .

In order to illustrate the flux waveforms at various relative positions of the fundamental flux only one oscilligram is shown (Fig. 7.12). The oscillograms taken at high applied voltage (550 volts) are presented to illustrate the effect of saturation on the shape of flux waveforms.

It is important to note that, since one amplifier was used, the oscillograms were not taken simultaneously. In the following sections the details of the waveforms obtained and their analysis with reference to theory are discussed.

7.2 The Oscillograms of Surface Flux Waves

It was noted in Chapter 2, Section 2.3, that for 60°-spread, full pitch, infinitely distributed winding the time variation due to phase-band harmonics is maximum at the peak of the fundamental m.m.f., and this variation is minimum at the zero of the fundamental. Conversely, the time variation due to slot m.m.f. harmonics is maximum at the zero of the fundamental m.m.f., and minimum at the peak of the fundamental. These two types of the total harmonic variations were graphically illustrated in Figs. 2.4 and 2.6 . Fig. 2.6 shows the space distribution at one instant of time, but as explained in Section 2.3 the time variation at any point on the secondary may be obtained by constructing intermediate space distributions at various instants of time. Since, Figs. 2.4 and 2.6 represent m.m.f. waves at points (or flux density in the absence of saturation) and the oscillograms taken represent flux waves, any comparison between them should be interpreted in terms of an average flux density across the width of the search coil.

The components of the surface flux are investigated for two cases. In the first case the squirrel cage is disconnected and in the second case the cage is short-circuited. Due to the fact, that the number of search coils are too large, only a selected number of oscillograms are shown and discussed in this section. The search coils which are chosen for this purpose are 25, 26, 28, 31 and 34 (see Fig. 6.5). It should be noted that the sweeping of the flux waves on the screen of the oscilloscope is magnified ten times (in some cases less, however, the scales of the waveforms are indicated in the shown figures). The primary purpose of such magnification is to illustrate the minute detail of the waveforms of slot frequency. Owing to the large sweeping magnification and also due to relatively large magnitude of the slot harmonics, the effect of phase-band harmonics is hidden in the oscillograms (particularly in the case of relatively small width search coils). However, the effect of phase-band harmonics is clearly illustrated in the oscillogram of search coil 31 which covers the full width of the secondary tooth (see Fig. 7.9).

7.2.1 The Case of Disconnected Cage

a) The Oscillograms of Search Coil 25.

The oscillograms of search coil 25 are shown in Figs. 7.1 - 7.3*. These oscillograms are taken at synchronous speed, and at three different applied voltages, namely 300, 415, 550 volts. The lower and upper waves on each oscillogram represent the induced e.m.f. and the flux respectively. The flux waves at zero position of the main flux are saw-toothed shaped, but at peak position the shape of the flux wave changes into a dip.

* The flux wave in Fig. 7.2 (b) is reversed.

This situation is in accordance with the theoretical and graphical analysis given in Chapter 2. As expected, the total harmonic variation due to slot m.m.fs. is maximum at the zero position of the main m.m.f. The saw-toothed shape of the flux waves also confirm the validity of the graphical procedure adopted in Fig. 2.6 (in Fig. 2.6 the m.m.f. due to each super-conductor is being represented by a linear step along the width of the primary slot-embedded conductor, making the shape of the total m.m.f. a semi-stepped rectangular). The lines of the saw-toothed flux waves taken at low applied voltage (300 volts) are straight. At higher excitation (550 volts) these lines become curved mainly due to the saturation of the iron. These curved lines, also, indicate that the shape of the main flux is flat-topped. Further distortion which can be noticed at both ends of each curved line (see Fig. 7.3) is due to the saturation of the tooth lips.

The shapes of the flux waves taken at the peak of the main flux indicate that the dip of the flux wave is primarily caused by the permeance effect of the stator slot openings (oscillogram (b) in Figs.7.1,7.2 and 7.3). At this position of the main flux, the harmonic variation due to slot m.m.fs. is practically absent (this is also in accordance with the analysis of Chapter 2). The additional distortions of the flux waves taken at higher excitations (oscillogram (b) in Figs. 7.2-7.3) indicate the effect of tooth and tooth lips saturation.

It is important to point out that as search coil 25 is in close proximity with the slot opening of the secondary member, the permeance effect of the doubly slotted air gap should be noticed (i.e. the mutual effect of the primary and secondary

slot openings). This effect can be seen in the asymmetrical shape of the dips in the flux waves. It is not difficult to notice that the slope of the flux wave on the left hand side of each dip is steeper than that on the right hand side (see oscillogram (b) in Fig.7.1). This asymmetrical shape is less noticeable in the oscillograms taken at higher excitations mainly due to the saturation. The effect of saturation is such that the leakage fluxes into the sides of the slot openings tend to increase and thus offsetting to a certain degree the dissemmetry of the dips. The asymmetry of the dips, due to doubly slotted air gap, is prominent in the oscillograms of search coil 42, since this search coil embraces the leakage flux entering the side of the slot opening.

The oscillograms which are presented in Figs. 7.1,7.2 and 7.3 do not illustrate the variations of the total phase-band harmonic. As mentioned earlier, the reason for this is due to the fact that the magnitude of the permeance harmonics linking this search coil is much greater than the magritude of the phase-band harmonics. Also, the sweeping of the flux waves is magnified ten times, therefore the oscillograms do not show the full wavelength of the phase band frequency.

b) The Oscillograms of Search Coil 28.

The width of this search coil is roughly half of the primary slot pitch and it is about four times greater than the width of search coil 25. Since the width of the search coil is approximately half of the primary slot pitch, the slot m.m.f. and permeance harmonics fully link the width of search coil 28. Also due to this factor, the linkage of the harmonics of even order is not appreciable.

The oscillograms taken for the search coil 28 are shown in Figs.7.4,7.5, and 7.6.* In a similar manner as in the case of search coil 25, these oscillograms are taken at 300, 415, 550 volts excitation and at two relative positions of the main flux.

In order to illustrate how the linkage of various harmonic orders affect the shape of the flux wave, two oscillograms of search coil 26 is shown in Fig.7.7 . The width of search coil 26 is roughly half the width of search coil 28. Therefore, the harmonics of even orders fully link the width of search coil 26 (the shapes of the flux waves induced in search coils 26 and 28 clearly illustrate the magnitude of the harmonic orders linking with each of the search coils).

The shape of the flux wave at the zero position of the main flux is triangular because the net effect of the even harmonics is small.

The shape of the flux wave at the peak position of the main flux is of rectangular form. The flux wave at this position of the main flux illustrates how the phase shift between the harmonics of the stationary permeance wave (caused by the secondary slot openings) and the harmonics of the rotating permeance wave (caused by the primary slot openings) changes as a result of rotation. It can be seen from the oscillograms that when a primary slot opening is in the region around the middle of the search coil, the phase shift between the harmonics (of the two primary and secondary permeance waves) is such that the net reduction in the flux remains relatively unchanged. The asymmetrical shape of the troughs in the flux wave also indicates the effect of the stationary permeance wave which has a wavelength greater than the primary slot pitch.

---

* The flux waves in Figs. 7.5(b) and 7.6(b) are reversed.

At low excitation (300 volts) the lines of the triangular and semi-rectangular waves are straight. At higher excitations these lines become curved mainly due to the saturation. The curved flux waves indicate that in the case of saturation the magnitude of low order harmonics substantially increases and the effect of high order harmonic is less than in the case of unsaturated iron.

c) The Oscillograms of Search Coil 31.

The width of this search coil is slightly greater than the slot pitch of the primary, and it covers nearly the whole width of the secondary tooth surface. Therefore, the flux linking with this search coil corresponds to the net flux entering radially the surface of the tooth and tooth lips of the secondary. Because of the width of the search coil the magnitude of the flux density induced by the slot m.m.f. and permeance harmonics is small.

For this search coil 3 oscillograms are shown in Figs.7.8 and7.9*. The two oscillograms shown in Fig.7.8 are taken at 300 volts excitation and at two positions of the main flux. Since the width of the search coil is slightly greater than the primary slot pitch, only part of the slot m.m.f. and permeance harmonics links with search coil 31. For this reason, the shape of the flux waves due to the total slot harmonic variation is similar to those induced in a small width search coil such as search coil 25. However, at the peak position of the main flux the magnitude of the flux density due to the total phase band harmonics is of the same order as that due to the permeance harmonics. In Fig.7.9 , the sweeping of the flux wave which corresponds to the peak position of the main flux is not magnified. The oscillogram shown in Fig.7.9 clearly illustrates

* The flux waves in Figs. 7.8(b) and 7.9 are reversed.

the effect of the total phase band harmonics.

d) The Oscillograms of the Search Coil 34.

The width of this search coil is relatively small in comparison with the primary slot pitch and is slightly wider than the width of search coil 25 (only 1 mm. wider), but from position point of view it differs from search coil 25 in that it occupies the middle of the tooth surface (search coil 25 situated at far end of the tooth surface, see Fig.6.5). The oscillograms taken for this search coil are shown in Figs.7.10* 7.11, and 7.12.

The oscillogram shown in Fig.7.12 is taken at 300 volts excitation and 0.25 slip. At this slip, as the main flux changes its position with respect to the search coil from maximum to zero, the shape of the total harmonic variation also changes correspondingly. Thus, the shape of the flux wave, illustrated in this oscillogram, gradually changes from the saw-toothed shape at the zero position of the main flux into the shape of a dip at the peak position of the main flux.

As mentioned above, one of the particulars of search coil 34 is that it is situated at the middle of the tooth surface and sufficiently away from the adjacent slot openings. Therefore, fromatheoretical point of view the permeance wave can be treated as though the secondary surface is smooth. The relevant analytical treatments in connection with such air-gap boundary configuration under linear conditions were discussed in Chapter 3. In connection with the effect of iron saturation on the shape of the permeance wave little information can be found in literature. On this topic, however, a paper has been

---

* The flux wave in Fig. 7.10(b) is reversed.

published by Smolensky[91], et al in which the effect of the tooth permeability on the air gap flux density distribution is dealt with analytically. In this paper the air gap configuration is being represented by a succession of slots opposite a smooth surface as shown in Fig7.13 . By assuming the smooth surface to be infinitely permeable, Smolensky et al calculated the normal flux density distribution along the smooth surface for various constant permeabilities of the slotted member. The result of their calculations is being reproduced here in Fig.7.14

By comparing the shapes of the flux density distributions shown in Fig.7.14 and the flux waves shown in Figs.7.10(b) and7.11(b) , it can be seen that the qualitive correlation between them is agreeable (Smolensky, et al did not supplement their analytical results with experimental data). However, although the analytical method adopted by Smolensky, et al involved extremely laborious and excessive computations, their findings clearly indicate that the magnitudes of the permeance harmonics are considerably affected by saturation.

7.2.2 The Case of Short-Circuited Cage

In the case of short-circuited cage, the flux components which link with the bars induce circulating currents in the conductors. These induced currents set up opposing fluxes and hence damp out the variation of the inducing fluxes. The flux components which induce currents in the bars of the cage are:

a) the flux components which penetrate the tooth body,

b) the flux components which leak into the secondary slot openings.

The waveforms of above flux components are discussed in the next section. At the tooth surface, the flux components due to the total m.m.f. and permeance harmonics do not change substantially since they close on the top of the tooth surface. On the other hand, the magnitude of the flux component due to the total phase band harmonics would be reduced at the tooth surface because they link with the secondary conductors.

As the difference between the surface flux waves in both short-circuited and open-circuited cage is not too significant therefore the oscillograms are not discussed in detail. Also, for this reason, the oscillograms of only three search coils are shown for illustration. These search coils are 25, 28, 34 and their oscillograms are shown respectively in Figs. 7.15, 7.16 and 7.17. These oscillograms are taken at 415 volts excitation and at two positions (zero and peak) of the main flux. In the case of small search coils 25 and 34, it is seen that the shapes of the flux waves are practically the same as in the case of open-circuited cage (compare Figs. 7.2, 7.15 and Figs. 7.10, 7.17). It should be noted that the difference which can be observed between the flux waves which are taken at the zero position of the main flux is due to the fact that these oscillograms are not taken exactly at the zero position of the main flux. In the case of wide search coil 28, it can be seen that the magnitude of the phase band harmonics is less than in the case of open-circuited cage. The reduction of the phase band harmonics is particularly visible in the oscillogram taken at the peak position of the main flux, where the total variation of the phase band harmonics is maximum [compare Figs. 7.5(b) and 7.16 (b)].

7.3 The Oscillograms of Tooth-Lip Flux Waves

The secondary tooth lip flux components are investigated by a number of search coils positioned at the top, middle, and far end of the tooth lips. The details of these search coils are shown in Fig.6.6 . It should be noted that the length of tooth lips search coils extends over the entire axial length of the secondary member.

In this section the tooth lip flux waves are illustrated by the oscillograms of search coils 40, 41, 42. In a similar manner, as in the case of surface search coils, the oscillograms are taken at synchronous speed, two positions of the main flux (i.e. the zero and peak positions), for two cases of open-circuited and short-circuited cage, and at various applied voltages.

7.3.1 Tooth Lip Flux Waves in Open-Circuited Cage

a) The Oscillograms of Search Coil 42.

Search coil 42 is situated at the edge of the slot opening and, therefore, it measures only the peripheral leakage flux entering the side of the tooth lip.

The oscillograms of this search coil which are taken at 415 volts excitation and at two positions of the main flux are shown in Fig. 7.18*

The shapes of the flux waves shown in Fig.7.18 are (in general) similar to the flux waves of the surface search coil 25 shown in Fig.7.2 . The most prominent features which distinguish the oscillograms of these two search coils from others are the mutual permeance effect of the primary and secondary slot openings on the flux waves. The oscillograms

---

* The flux wave in Fig. 7.18(b) is reversed.

of Fig.7.18 clearly illustrate that the distortions of the flux curves with respect to the movement of a primary slot opening is not only dsymmetrical at the peak positions of the main flux but also at the zero position of the main flux. This indicates that flux waves due to slot m.m.f. harmonics are significantly distorted by the presence of the primary and secondary slot openings (as mentioned earlier in the discussion of the oscillograms of search coil 25, the effect of doubly slotted air gap is particularly strong on the leakage flux). In order to illustrate the effect of saturation on the shape of the flux wave, only one oscillogram taken at 550 volts excitation and at the peak position of the main flux is shown in Fig. 7.19 . This oscillogram illustrates that at higher saturation the shape of the dips in the flux wave becomes more symmetrical [compare the shapes of the e.m.f. signals in Figs.7.18(b) and 7.19(b)]. However, with higher saturation, further distortion arises due to the saturation of the tooth lips which in turn leads to higher harmonic content.

b) The Oscillograms of Search Coil 41.

This search coil is situated at the middle of the tooth lip, therefore it measures not only the flux which leaks into the side of the tooth lip but also part of the flux which enters the surface of the tooth lip. The oscillograms of this search coil are shown in Fig.7.20 *. The shapes of the flux waves obtained from this search coil differ from the previous one (search coil 42) in that the variation of the flux with respect to the centre of a primary slot opening is more symmetrical. The reason for this is due to the fact that search coil 41 is further away from the secondary slot opening. In case of oscillogram (b) in Fig. 7.20 , besides the distance mentioned above, the magnitude of the

---

* The flux wave in Fig. 7.20(b) is reversed.

flux which enters the portion of the tooth lip surface is greater than the leakage flux entering the side of the tooth lip.

c) The Oscillograms of Search Coil 40.

This search coil is situated at the corner between the tooth and the tooth lip. This search coil links with the entire flux entering the tooth lip surface as well as with the flux leaking into the side of the tooth lip.

The oscillograms of this search coil are shown in Fig. 7.21 Since search coil 40 is sufficiently far away from the secondary slot opening, the shapes of the flux waves are practically symmetrical.

7.3.2 Tooth-Lip Flux Waves in Short-Circuited Cage

The oscillograms of the same tooth-lip search coils, namely search coils 40, 41, 42, taken under the short-circuited cage condition are shown in Figs. 7.22-7.24

Similar to the case of open-circuited cage, these oscillograms are taken at 415 volts excitation and at two positions (peak and zero) of the main flux.

The oscillograms shown in Figs.7.22-7.24 , indicate that in comparison with the disconnected cage no significant change can be observed (in both the magnitude and shape of the flux waves). The same situation was observed in connection with the surface search coils. These findings suggest that the effect of the circulating bar currents is to damp only those flux components which penetrate the iron sufficiently deep from the surface of the tooth. It was mentioned in Chapter 4 (section 4.5) that due

to this damping action of the bar currents, the rotor tooth pulsation is reflected back into the stator and hence the losses result in short-circuited cage are of the same order as in disconnected cage (see the result of loss measurements given in Chapter 8).

7.4 The Oscillogram of Tooth Flux Waves

The components of tooth flux waves are investigated by three search coils wound around a tooth at different levels of the tooth height. As shown in Fig.6.6 , search coil 45 is positioned at the top of the tooth just beneath the tooth lips, search coil 44 is positioned at the middle of the tooth, and search coil 43 is situated at the bottom of the tooth.

The phenomena of flux penetration into thin laminations of iron was discussed in Chapter 5 and it was shown that the depth of penetration in case of thin lamination is substantially greater than the classical depth of penetration (based on the analysis of solid iron).

The oscillograms which are discussed in this section not only confirm the theoretical considerations of Chapter 4 and 5 (as well as the experimental works carried out by other authors)[82,83], but also they illustrate the detailed shapes of the waveforms of the total harmonic variations along the length of the tooth for various applied voltages.

Due to the fact that the search coils embracing the tooth link with both flux components which enter the tooth surface radially and the flux entering the sides of the tooth, the shapes of the flux waveforms are more complex than those shown in previous sections.

The oscillograms which are discussed in this section are also taken for both open and short-circuited cage. The details of the flux waves are given in the following sections.

7.4.1 Tooth Flux Waves in Disconnected Cage

The oscillograms which are taken for this condition are shown in Figs.7.25-7.28 These oscillograms are taken at synchronous speed, and at two positions (peak and zero) of the main flux. The sweeping of the flux waves is magnified only two times so that the effect of phase band harmonics be noticed (it should be remembered that the oscillograms were not taken simultaneously). For search coil 44 (which is situated at the middle of the tooth) the oscillograms are taken at two values of applied voltage 300 and 415 volts (see Figs.7.26 and 7.27). At 300 volts excitation, the air gap induction is low and, therefore, a direct comparison between the experimental and the computed tooth flux waves (due to permeance effects) can be made (see Section 7.6)

The oscillograms of other search coils are taken at 415 volts excitation only. In these oscillograms (see Figs.7.25,7.27,7.28) the effect of phase band harmonics and also the saturation of the tooth tips (in particular the stator tooth tips which are relatively thin) imposes further distortion on the shape of the flux waves. If the effect of phase band harmonics is excluded, it can be seen that the effect of wider slot opening is to make the shape of the flux wave (at the peak position of the main flux) more rectangular. This effect is also in agreement with the analysis of Chapter 4.

As far as the penetration of the flux harmonics is concerned, the oscillograms clearly illustrate that both permeance and slot

m.m.f. harmonics penetrate the tooth body right down to the bottom of the tooth. Also, the magnitude of the flux pulsation remains practically unchanged along the whole tooth length. This constancy of the flux penetration has been also observed by other authors and this in turn signifies the phenomena of deep penetration of the flux in laminated iron.

7.4.2 Tooth Flux Waves in Short-Circuited Cage

In short circuited cage the tooth flux pulsation are damped by the induced bar conductors. The degree of the damping for a particular flux harmonic inside the tooth body depends upon the degree of the linkage of that harmonic with the bar conductor. The linkage of phase-band harmonics with the bar conductors is so effective that the induced bar currents practically damp out these harmonics.

Although, the flux components due to slot m.m.f. and permeance harmonics (as shown in previous section) penetrate deep into the tooth body, the damping effect for these harmonics at different levels of the tooth is not the same. It will be seen below, the flux pulsation at lower parts of the tooth is less than at its top. This situation indicates that the induced bar currents are confined within a relatively small depth from the surface of the bar conductor.

The search coils which are used in short-circuited cage are the same as those used in open-circuited cage (i.e. search coils 43, 44, 45). Due to the fact that the total phase band harmonic variation in the tooth is small, the sweeping of the flux waves is magnified ten times so that the details of the total slot m.m.f. and permeance harmonics can be clearly illustrated.

The oscillograms of the tooth flux waves at the top, middle, and bottom of the tooth are respectively shown in Figs.7.29-7.31

In Fig.7.29(b) only one oscillogram of search coil 45, taken at 415 volts and corresponding to the peak of the fundamental flux wave is shown. In order to illustrate the effect of saturation, two oscillograms showing the flux wave at the peak and zero positions of the main flux are shown in Fig. 7.29(a)*

Since search coil 45 is situated at the top of the tooth, it can be seen from Fig.7.29(a) that, despite the damping effect of the induced bar currents the magnitude of flux pulsation is still appreciable. By comparing the oscillograms taken in short-circuited and disconnected cage it can be seen that the shape of the flux wave in the case of short-circuited cage is considerably improved. This improvement is due to the concentration of the bar currents at the surface of the conductor which prevent the flux component entering the sides of the tooth from penetrating further into rotor tooth (see the bar current density distribution discussed in the next section).

The flux waves at the middle of the tooth are shown in Fig.7.30 . In contrast with the oscillograms of search coil 45, the flux pulsation is considerably reduced (the flux pulsation due to phase-band harmonics is virtually absent in this search coil).

The flux waves at the bottom of the tooth is shown in Fig.7.31 . At this position of the tooth the flux pulsation is virtually damped out.

The analysis of the oscillograms shown in Figs.7.29-7.31 indicate that the induced bar currents damp out efficiently, only, those flux components which penetrate the iron sufficiently beyond the level which is parallel to the bar surface. The flux component which enter the sides of the slot opening and penetrate into the tooth body are, in particular, effectively

---

* The flux wave at the bottom of Fig. 7.29(a) is reversed.

damped out and this leads to an improved shape of flux waveform at the top of the tooth. Thus, in short circuited cage the flux pulsations due to slot m.m.f. and permeance harmonics are confined within a comparatively small distance from the tooth surface. It is essential to bear in mind that this distance is not the classical depth which is used in connection with surface iron losses.

7.5 The Oscillograms of Surface Bar Current Density

The principles and operation of J-probes (or current density probes) were briefly discussed in Chapter 6. Also, the positions and other details concerning the J-probes which are constructed for investigating the surface current density waveform were shown in Figs. 6.7 and 6.8.

In the present experimental measurement, the variation of the magnetic field along the axial direction due to the ventilating ducts are neglected. In order to minimise the involved error, the axial length of all J-probes are made equal and sufficiently long in comparison with the length of the duct. Also the positions of the J-probes are chosen such that no more than one ventilating duct is situated over the filament length of the J-probes. The copper resistivity used in calculation is $1.72 \times 10^{-8}\ \Omega.m$

As shown in Figs. 6.7 and 6.8 five J-probes at different positions are constructed on the top surface of the bars and four J-probes at various depths along the side of the bar conductor are constructed.

The oscillograms of current density waveforms are taken at 415 volts excitation only. These oscillograms are discussed below.

a) The Oscillograms of J-probe 6.

The filament of J-probe 6 is positioned along the bar surface exactly at the middle of the slot opening. The axial

length of the filament is 86 mm and part of this length (namely 16 mm) is situated under the ventilating duct. The effect of the ventilating duct for the reasons stated above, is not taken into consideration.

The oscillograms taken for J-probe 6 are shown in Fig. 7.32 . Both current density waveforms shown in Fig. 7.32 have symmetrical shapes. This symmetry is expected, because the filament of J-probe 6 has a geometrical symmetry with respect to the two adjacent teeth. In connection with this symmetry a comparison may be drawn between the waveforms shown in Fig. 7.32 and the flux waveforms of search coil 34 shown in Fig. 7.17 (since search coil 34 is also symmetrically positioned with respect to a secondary tooth).

b) The Oscillograms of J-probe 5.

The filament position of J-probe 5 is halfway between the middle and the end corner of the bar conductor. The axial length of J-probe 5 is equal and parallel to J-probe 6 (see Fig. 6.7). Since the filament of J-probe 5 is 3 mm away from J-probe 6, its position is under the tooth lip.

The oscillograms of J-probe 5 are shown in Fig. 7.33 . The general character of the current density waveforms is the same as those obtained from J-probe 6, except that the shape of each cycle is less symmetrical. This asymmetry is due to the non symmetrical position of the filament with respect to the slot width. It should be noted that the marked asymmetry in the oscillogram (b) of Fig.7.33 is due to the fact that this oscillogram happened to be taken not exactly at the peak of the fundamental.

c) The Oscillograms of J-probe 4.

The filament of this J-probe is positioned at the corner of

the bar conductor. The oscillograms of J-probe 4 are shown in Fig7.34 . It is of interest to note that the magnitude of current density variation at the peak of the fundament is of the same order as in the corresponding case of J-probe 6. On the other hand, the magnitude of current density variation at the zero position of the fundamental is less than in the corresponding oscillogram of J-probe 6. The reason for this is that the radial field strength at the corner of the slot is greater than the tangential field strength. In other words the concentration of the radial flux density due to permeance variation at the corner of slot is much more than the corresponding tangential flux density due to slot m.m.f. variation.

d) The Oscillograms of J-probes 1, 2, and 3.

These J-probes are equally spaced along the depth of the bar and all are of the same axial length (see Fig.6.8). The position of J-probe 1 is halfway down the conductor's side, J-probe 2 is 4 m.m. above J-probe 1 and 8 m.m. away from the surface of the bar. J-probe 3 is only 4 m.m. away from the surface of the bar.

The oscillograms of J-probes 1, 2, 3 are respectively shown in Figs. 7.35, 7.36, and 7.37 . The general character of the current density waveforms of all J-probes 1, 2, and 3 are identical with the waveforms of J-probe 4 shown in Fig. 7.34 . However, the magnitude of the current density variation attenuates with depth along the side of the bar. The oscillograms shown in Figs. 7.35-7.37 also indicate that the attenuation of slot frequency harmonics is faster than the phase-band frequency harmonics.

7.5.1 The Oscillograms of Laminations Surface Current Density

The waveforms of the induced current density on the surface of iron laminations were investigated by four J-probes. The location and length of these J-probes were shown in Fig. 6.9 . The taken oscillograms showed that the current density waveforms obtained from all these J-probes are identical. Therefore, two oscillograms of one J-probe is shown in Fig. 7.38.

In Fig. 7.38, the oscillogram (a) shows the current density waveform induced by the total slot m.m.f. harmonic variation. The oscillogram (b) shows the current density waveform due to the total permeance harmonics variation. The shapes of the waveforms are analogous to the shapes of the surface flux waves which induce these currents.

It should be noted that the current density waveforms shown in Fig. 7.38 represent the peripheral component of the induced current density. The oscillograms of Fig. 7.38 also show that the magnitude of the induced current density on the surface of the lamination is much lower than the induced current density on the surface of the bar's conductor.

7.6 Correlation between the Computed and Experimental Flux Waveforms

In Chapter 4, section 4.3.1, the accuracy of the analytical method developed for calculating the flux distribution in the air gap and also the result of some computed tooth flux waveforms were discussed. In order to establish the validity of the given analysis, the flux waveforms obtained from four search coils of different widths and at various positions are selected for comparison with the computed flux waveforms. These search

coils are 25, 26, 42 and 44 (see section 6.3 and Figs. 6.5 and 6.6). The oscillograms of search coils 25 and 26 which represent the surface flux waves are, chosen particularly for comparison; because in the case of search coil 25 the shape of the flux waveform is prominently affected by the combined effects of the stator and rotor slot openings. The oscillogram of search coil 26 is selected because the effect of all permeance harmonics is present in this oscillogram.

Search coil 42 measures the flux entering the side of the secondary tooth lip. This search coil is, also, important because it is situated along the side of the rotor slot and measures the flux which fringes into the side of the tooth.

Search coil 44 measures the total rotor tooth flux. It was shown in section 7.4 that the magnitude of the tooth flux remains practically unchanged along the tooth height. The implication of this is that besides the fact that the flux harmonics penetrate deep inside the tooth, the magnitude of the flux which fringes into the sides of the tooth beyond the tooth lips is negligible.

The computed flux waveforms corresponding to the positions of search coils 25, 26, 42 and 44 are shown in Figs. 7.39-7.42.* The oscillograms of the corresponding flux waveforms [which were illustrated in Figs. 7.1 (b), 7.7(b), 7.18(b) and 7.26(b)] are also shown on the same diagrams for comparison. It should be noted that the computed flux waveforms are based on per unit air gap flux density and per π unit lengths.** This only effects the scale factor, but as far as the shapes of the flux waveforms are concerned it can be seen that the correlation is very good

---

* The flux wave in Fig. 7.41(b) is reversed.

** See page 243 for further detail.

for all the search coils. It is obvious that two identical waveforms yield the same harmonic content. With regard to the accuracy of the magnitude of the harmonics, it was shown in section 4.3.1 that for the d.c. component of the flux density wave an error of the order of 1% - 3% is expected because the series representing the air gap potential function is truncated at N = 10. Such an accuracy for the d.c. component of the flux density wave is believed to be very satisfactory and the analytical method given in Chapter 4 can be used with confidence.

In order to make a comparison between the magnitudes of the flux pulsations in both primary and secondary teeth, the waveform of the primary tooth flux is computed for one cycle of secondary displacement. The primary tooth flux waveform is shown in Fig. 7.43 (the results of all computed flux waveforms are given at the end of the thesis, see pages 260-272)

8.0 No-Load Tests

8.1 Introduction

The components of no-load losses can be divided into two categories:

1. Fundamental frequency losses. These losses consist of
   a - stator core losses due to tangential and radial flux,
   b - stator tooth losses due to radial flux.
2. High frequency losses. These losses may be divided into the following components
   a - stator and rotor tooth pulsation losses due to the reluctance changes in the air gap,
   b - stator and rotor surface losses due to the air gap permeance harmonics,
   c - stator and rotor copper eddy currents due to high frequency slot leakage fluxes.

The above division of no-load losses is based upon the theoretical consideration for calculating each of the loss components. On no-load, however, there are other losses such as end-coil and manufacturing imperfection losses. Estimation of these losses, in particular those due to manufacturing imperfections is either not possible or extremely difficult. These losses are, usually, labelled as additional losses. It should be noted that on no-load test, an appropriate correction for I^2R and mechanical losses (i.e. friction and windage) is always made.

The main object of no-load test is to separate the component losses so that each of them could be compared with the calculated values. As mentioned in Chapter 4 some of high frequency losses (for example tooth pulsation and surface losses) are arbitrarily

divided into separate components. Although an ideal no-load test by which all the loss component can be separated is not always possible, there are few simple no-load tests whereby the separation of losses on the basis of harmonic frequencies that cause them can be made, such as the Rawcliffe-Menon and driven rotor tests. These two methods are dealt with in this chapter and the measured loss components are discussed.

8.2 Rawcliffe-Menon Test[92]

In induction machines the tooth pulsation losses due to permeance variation act as retarding torques. In order to balance these torques the input power is converted into mechanical power. In the same manner the friction and windage losses are supplied by the mechanical power.

The losses due to the fundamental component such as stator copper and iron losses are supplied directly by the stator electrical input power. These deductions originate from the statement that only power losses at fundamental frequency can be supplied from an a.c. supply of a sine-waveform. In accordance with this hypothesis Rawcliffe-Menon described a simple no-load test by which the high frequency losses are separated from the fundamental frequency losses. Since the detail of Rawcliffe-Menon test is treated in literature[10], a very brief discussion of this test is given below.

The classical theory of induction machines shows that the mechanical output power of an m-phase induction motor operating at slip s is

$$P_{mech} = \frac{m \cdot V^2 \frac{R_2'}{s}(1-s)}{\left(R_1 + \frac{R_2'}{s}\right)^2 + \left(X_1 + X_2'\right)^2} \qquad (8\text{-}1)$$

with the usual notation (see the list of symbols).

For small values of s, as measured in running light test, equation (8-1) reduces to $\frac{msV^2}{R_2'}$, to a high degree of accuracy. The mechanical output power, which is equal to the sum of friction and windage losses plus the high frequency losses is proportional to sV^2. Thus, by measuring the slip over a range of voltages and then extrapolating the sV^2 curve to zero voltage, it is possible to separate the high frequency and fundamental loss components.

Since the extrapolated value of sV^2 at zero voltage is proportional to the friction and windage losses the value of sVo^2 can be used for calibrating the sV^2 scale, i.e.

$$\frac{s\,V^2 - s\,V_o^2}{sV_o^2} = \frac{\text{high frequency losses}}{\text{friction and windage losses}} \qquad (8\text{-}2)$$

The values of high frequency losses determined in this manner do not allow for the hysteresis torque of the main flux on the rotor iron. The mechanical power due to hysteretic action at rotor speed just below the synchronism is equal to the hysteresis loss which would occur in the rotor at full frequency. If Ph_2 is the rotor hysteresis loss at standstill, the mechanical power developed by the hysteretic action is equal to $(1-s)Ph_2$ and at small values of slip this mechanical power is equal to Ph_2.

The test procedure adopted was to note a series of stator currents, input powers, and slips at various applied voltages down to 12% of the rated voltage, with the motor running light. Each test condition is maintained until steady temperatures are established before readings are taken. Accurate slip measurements are essential for such test. The details of the instrumentation used for slip measurement were described in Chapter 6, section 6.4. Since, the primary member of the special experimental machine is

fed through slip-rings, the brush losses are determined on a separate test and the results are plotted in Fig.8.1 against the line current. The resistance of the primary winding was measured on Cambridge Bridge with accuracy no less than 0.02 (the measured resistance across the terminal was 0.0722 ohms). The temperature rise of the windings was measured by a thermistor embodied in the primary winding.

For each applied voltage, sV^2 and stator input less stator I^2R and brush losses are plotted against V^2 and then the curves are linearly extrapolated to zero voltage as shown in Fig.8.2 By using the curves of Fig.8.2 and expression (8-2) the fundamental and high frequency losses are separated. As indicated earlier, the plotted curves in Fig.8.2 should be corrected for hysteresis Ph_2 and also for the voltage drop in the primary winding. The friction and windage losses obtained by extrapolating the curves to zero voltage also involves a small error. In calculating the high frequency losses, the corrected values of sV^2 (the hysteresis loss Ph_2 was obtained from driven rotor test described in next section) and friction and windage losses (also obtained from driven rotor test) were used in the expression (8-2). The details of the measured and calculated values are given in Table 8-1.

In order to illustrate the variation of iron losses as a function of the exponent of the applied voltage, the fundamental and high frequency iron losses are plotted against the voltage on a log-log graph (see Fig.8.3).

The results of the experiments are discussed in section 8.4 where both Rawcliffe-Menon and driven rotor tests are compared.

Table 8-1

The result of Rawcliffe-Menon test

Line voltage (V)	50	100	150	200	250	300	350	400	450	500
Line current (A)	3.98	3.66	5.0	6.56	8.37	10.35	12.71	15.93	20.55	27.9
Input power (W)	310	335	395	445	525	610	730	900	1160	1600
Slip$\times 10^{-3}$ (p.u.)	40.3	9.8	4.413	2.57	1.75	1.347	1.083	0.946	0.901	0.867
sV^2	100.75	98	99.3	102.8	109.37	121.23	132.37	151.36	182.57	216.72
Stator I R losses (W)	8.52	8.0	12.0	18.0	26.38	37.8	53.12	80.4	124.4	222.6
Fund. iron losses (W)		28.5		88.2		144.8		258.4		547
High freq. losses (W)		48.5		88.8		177.3		311.2		580

8.3 The Driven Rotor Test

It was noted in the previous section that for accurate separation of loss components by Rawcliffe-Menon test, it is necessary to know the accurate values of hysteresis loss Ph_2 as well as the friction and windage losses. The driven rotor

test is the appropriate experimental method for determining these loss components and also for separating the components of the fundamental frequency losses. The procedure by which the loss components are separated is well known and treated comprehensively in literature (see References 55 and 93). Since the aim of present experimental test is to obtain the high frequency loss component on no-load (for both cases of short-circuited and open-circuited cage) both loss components the fundamental and high frequency are given as the sum of hysteresis and eddy current losses.

In driven rotor test the cage is open circuited and the rotor is driven by a precision dynamometer (it should be noted that the experimental machine is inverted so that the stator is driven by the dynamometer. However, in order to avoid confusion the normal term used for rotor is used). The operation of the dynamometer was briefly discussed in Chapter 6, section 6.5. The test procedure adopted is to drive the rotor of the induction machine below and above the synchronous speed with the excitation being switched on and off.

When the excited motor is driven at speed corresponding to the light running, the input power to the stator supplies the following losses.

1. Stator fundamental frequency losses which consist of a) I^2R, b) brush losses and c) hysteresis and eddy current stator iron losses.

   At small slip the rotor slip frequency losses are small and may be neglected.

2. Rotor mechanical power due to the fundamental rotor hysteresis torque. This hysteresis torque is constant

(with a given air gap flux) at all speeds below synchronism, but reverses as the motor passes through zero slip. Therefore, as the rotor speed passes through synchronism the stator input is abruptly reduced by twice the hysteresis torque.

The dynamometer supplies the friction and windage losses as well as the retarding torque due to high frequency losses. At synchronous speed the shaft input power increases by twice the hysteresis torque. Since the accuracy of the measured torques by the dynamometer is high, the hysteresis loss Ih_2 is measured by the dynamometer and checked with the wattmeter readings. It was found both readings were practically the same. The fundamental stator iron losses are obtained from the stator input less stator I^2R loss at synchronism, minus hysteresis torque. The high frequency losses are obtained from the increase of mechanical losses, plus the hysteresis torque. Since the variation of the power readings near the synchronous speed were important, very closely spaced readings were taken near the synchronous speed. The summary of the test results obtained from driven rotor tests are given in Tables 8.2 - 8.4. In Fig.8.4 the friction and windage losses measured by the dynamometer are plotted against rotor speeds.

Table 8-2

Friction and windage losses versus rotor speed

Rotor Speed (rev/min)	500	700	900	1100	1200	1300	1400	150
Friction and Windage Losses (W)	61.7	89.5	123	153	177	198	228	250

Table 8.3 Rotor Hysteresis Loss Versus Excitation

Excitation (V)	100	200	300	400	500
P_{h_2} (W)	10.3	36.5	70.8	116.5	193

Table 8.4 The Summary of Driven Rotor Test

Line Voltage (V)	100	200	300	400	500
Line Current (A)	3.1	6.26	10.2	16.2	30
Input Power (W)	41.7	141.5	248.2	480.5	1137
Friction and Windage Losses (W)	250	250	250	250	250
Stator Fundamental Iron Losses (W)	25.3	89.5	142	281	444
High Frequency Iron Losses (W)	30	65	162	334	674

8.4 Discussion of the Experimental Results

In order to make a comparison between the no-load short-circuited and open-circuited cage losses, the fundamental and high frequency iron losses determined from Rawcliffe-Lenon and driven rotor tests (see Tables 8.1 and 8.4) are plotted in Figs. 8.5 and 8.6

The curves of Fig. 8.5 indicate that the fundamental losses in short-circuited cage at higher excitations are more than the corresponding losses in disconnected cage. The reason for this is that in short-circuited cage the fundamental air gap flux

wave is more sinusoidal (due to the bar currents) than in open-circuited cage. Hence the induction in stator teeth and losses are higher in short-circuited cage. At lower voltages, despite the small discrepancy in the magnitude of losses, the situation is reversed. This is due to the effect of phase band harmonics which is more in the case of disconnected cage than in short-circuited cage.

The curves of Fig.8.6 indicate that the magnitude of high frequency losses in both connected and disconnected cage is of the same order. As mentioned in Chapter 4, section 4.4 the damping effect of rotor bar currents does not significantly alter the magnitude of high frequency losses. This observation which is illustrated in Fig. 8.6 is not related to the present experimental machine only. Spooner[56] has carried out the same experimental test on a squirrel cage induction motor which is essentially very different than the present one. For illustration, the result of Spooner's experiment is reproduced here in Fig.8.7 where it can be seen the discrepancy between losses is not too significant. These experimental evidences support the proposition of estimating tooth pulsation losses assuming the cage to be disconnected.

The relationship between the iron losses and the exponent of the applied voltage was shown in Fig.8.3 . The slope of the line representing the fundamental frequency losses is about 1.5 in the range of 25% - 85% of the rated voltage. This slope increases to 2.3 in the range of 85% - 120% of the rated voltage. On the other hand the slope of high frequency losses at lower excitations is slightly less (i.e. 1.3) than that of the fundamental frequency losses. At higher excitations the slope

of high frequency losses is the same as for the fundamental losses. However, the exponent 2.3 in the range of 80% - 120% of the rated voltage is in agreement with the previous experimental tests carried out by Spooner and his associates.[55,57]

9.0 General Conclusions and Future Work

The main problems encountered in the analysis of the air gap magnetic field and loss calculations are summarised as follows.

(a) to obtain an understanding of the flux distribution in the air gap and in both stator and rotor teeth.

(b) to produce a sound theoretical analysis for the combined effect of the stator and rotor slot openings on the main field.

(c) to include the damping effect of the circulating secondary bar currents.

(d) to investigate eddy current distribution inside laminated iron.

and (e) to account for the effect of the superposed fields and the distribution of the flux components in the iron.

The aspects (a) - (c) were considered in detail in Chapters 2 - 4, the aspects (e) - (d) were discussed in Chapter 5. The experimental analysis given in Chapters 7 and 8 provided not only a clear picture of the detailed flux distribution but also verified the validity of the theoretical considerations made in this thesis.

The existing theories for the calculation of high frequency losses are somewhat empirical and inadequate because they are expressed in overall terms and do not allow for the detailed flux distribution in the machine. It is not difficult to appreciate that each of the problems mentioned above involves a considerable theoretical and experimental analysis which cannot be all covered in a limited work. Owing to this factor the work of this thesis has been primarily focused on the problem of

permeance effect on the main flux. All other problems were discussed in this work in order to give an appropriate account of the factors influencing the magnitude of the losses and their calculation. The theoretical analysis developed in Chapter 4 removes the main obstacle in predicting the flux distribution along the tooth surface as well as the total flux pulsation inside the rotor and stator tooth owing to the relative movement of the rotor teeth with respect to the stator teeth. An accurate knowledge of these flux components leads not only to a better understanding of the behaviour of the machine on no-load, but also enables the losses to be calculated with a greater accuracy.

It has been shown that an accurate estimation of losses can only be achieved if a) an accurate loss formula is used, and b) an appropriate allowance for the effect of superposed fields and the flux distribution in the iron are made.

The problem of eddy current distribution in laminated iron was discussed in Chapter 5, and an alternative theoretical treatment of the eddy current losses (based on linear theory) is proposed in Appendix 10.5. The results of these analyses can be verified in future experimental work and used for calculating eddy current losses in laminated iron. In connection with the problem of superposition, it is necessary to make a study of the eddy current losses induced in a simple sample of laminated iron by various non-sinusoidal fields representing the waveforms appearing in the machine. The results of such experiments can be used as a first step towards solving the travelling wave problem.

It was shown in Chapter 7 that along the secondary surface the flux waveforms due to the total slot m.m.f. and slot-permeance harmonics are distributed between the zero and peak positions of the fundamental. The manner of this distribution is such that at the zero position of the fundamental the losses are predominantly induced by the slot m.m.f. harmonics: and at the peak position of the fundamental the losses are predominantly induced by the slot permeance harmonics. It is, therefore, incorrect to add the losses calculated for each of them independently.

Tooth pulsation losses are usually calculated on the basis of the harmonic contents of the total tooth flux variation. The losses determined in this way can under-estimate the actual losses, because the harmonic fluxes which appear in each section of the tooth may combine in such a manner that the harmonic contents over the total tooth surface become small. This problem was recognised by Higginson[36] and in order to overcome this he introduced a loss factor for each harmonic of the total tooth flux wave. This loss factor was derived on the basis of flux measurement across small sections along the tooth surface and then comparing their resultant vectorial summation with the total tooth flux. Despite the fact that the procedure adopted by Higginson is to a large extent empirical, the given loss factors were applicable only to a specific air gap geometry. In addition to these loss factors an extra loss factor of the order (1.2 - 1.4) was included in the loss calculation in order to obtain a satisfactory answer. However, the problem of accounting for the flux distribution in the tooth can be readily treated by

using the analysis of Chapter 4. It can be seen from equation (4-2) that the magnitude of the flux density harmonics at rotor surface (or stator surface) vary with rotor position. The implication of this continuous variation of the amplitudes of the flux density harmonics is that tooth losses should be calculated for each relative rotor position on the basis of the resulting flux density wave. The actual tooth losses then represent the mean value of the losses determined at various rotor displacements. To obtain the mean value of the tooth losses it is not necessary to consider all rotor positions describing one cycle of rotor displacement. For this purpose it is sufficient to consider only two rotor positions each representing the maximum and minimum conditions of the air gap permeance. The mean value of the losses between these two extreme positions can be then compared with the losses of a third rotor position representing the condition of the mean air gap permeance.

The problem of damping effect of the circulating bar currents was eliminated by considering the total pulsation losses to be purely iron losses, as in the case of the disconnected cage. Such a consideration was verified by the experimental results obtained in Chapter 8. In support of this proposition the experimental results obtained by other authors were quoted in section 4.5 and reproduced in Fig. 8.7.

10.1 Appendix 1

The Slot Width Factors

The slot-opening factors result from assuming each slot ampere conductors to be equivalent to a current uniformly distributed over a circumferential distance equal to the slot opening. This concept is an improvement on the concentrated slot currents referred to in Section 2.2.

The slot opening factors may be derived from the distribution factors given by equations (2-3) and (2-4) (see Section 2.2) by replacing $\frac{\pi}{Q}$ by S, and making q tend to infinity.

From equation (2-~~5~~4) it can be seen that $k_{s(6n+1)}$ becomes negative when

$$(6n+1)S > 2\pi$$

or

$$n > \frac{\pi}{3S} - \frac{1}{6}$$

By making use of the equality

$$S = \frac{\pi S}{Q q \tau}$$

it can be seen that when Q = 3, the slot width factor becomes negative when

$$n > \frac{q\tau}{S} - \frac{1}{6} > q\left(\frac{t}{S}+1\right) - \frac{1}{6} \qquad (10\text{-}1)$$

Therefore, when the slot is too wide (i.e. $S \longrightarrow t$), the sign of k_s also must be included.

For harmonic order

$$m > 6q\left(\frac{t}{S}+1\right)$$

the followings can be written

$$m > (6q-1)\left(\frac{t}{S}+1\right) + \left(\frac{t}{S}+1\right)$$

or

$$m > \left(\frac{t}{s} + 1\right) \frac{6q}{6q-1} \qquad (10\text{-}2)$$

Hence, the slot width factors remain positive until the harmonic order becomes greater than $\left[\left(\frac{t}{s} + 1\right) \times \text{first order slot harmonic}\right]$. The sign of k_s cannot be neglected if it is necessary to consider the net effect of an infinite series of harmonics.

10.2 Appendix 2

Equipotential and Stream Lines of a Source in a Smooth Air Gap

Consider a semi-infinite strip of very thin conducting material in which a source line is placed at the origin '0' as shown in Fig. 10.1.

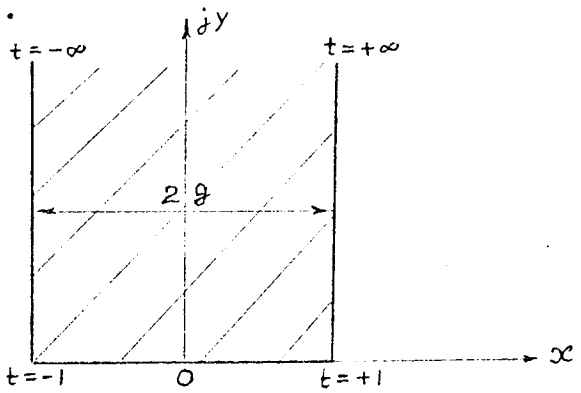

Fig 10.1

A semi-infinite strip in complex Z- plane

The whole area inside the strip can be transformed into the upper half of a complex t-plane by using Schwartz-Christofel transformation, namely

$$\frac{dz}{dt} = K(t^2 - 1) \qquad (10\text{-}3)$$

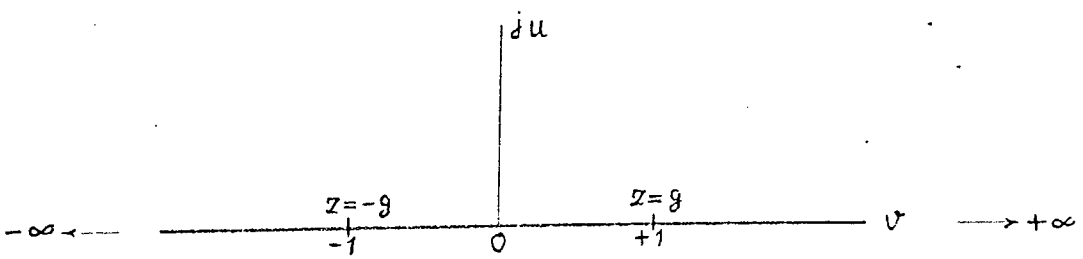

complex t- plane

The solution of equation (10-3) is given by

$$Z = K \cosh^{-1} t + k$$

$$t = \cos\left(-\frac{\pi Z}{2g}\right)$$

where K and k are constants.

The transformation of the regular field between two infinitely parallel plates apart by a distance π , is given by

$$w = \log t$$

or

$$w = \log \left(\cos \frac{\pi z}{2g} \right) \qquad (10\text{-}4)$$

Taking into account the properties of conjugate functions, the equipotential and stream lines can be determined by substituting the real and imaginary parts for Z and W in equation (10-4). Thus

$$\varphi + j\psi = \log \left[\cos(x + jy) \right] \qquad (10\text{-}5)$$

where

φ = constant, gives the equipotential lines.

ψ = constant, gives the stream lines.

The whole family of equipotential and stream lines for the problem of Fig. 10.1 has been treated in Gibbs' book[23] and they are reproduced in Fig. 10.2.

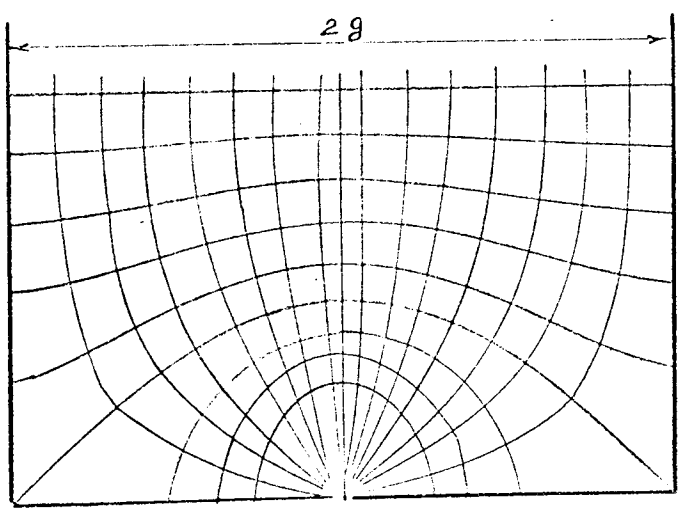

Fig 10.2

Equipotential and stream lines in a semi-infinite conducting strip

By interchanging the equipotential and stream lines in Fig. 10.2, the magnetic field of a line current positioned midway in the air gap between two infinitely permeable iron

blocks can be represented. Since, the equipotential line along the y-axis is constant, and also along the lines $0, g$ and $g, +\infty$ the picture of the magnetic field on the right half side of Fig. 10.2 represent the exact pattern of the air gap field due to a line current.

10.2.1 The Peripheral Air Gap Leakage Flux

Consider a smooth air gap and a full pitch winding represented by current lines as shown in Fig. 10.3.

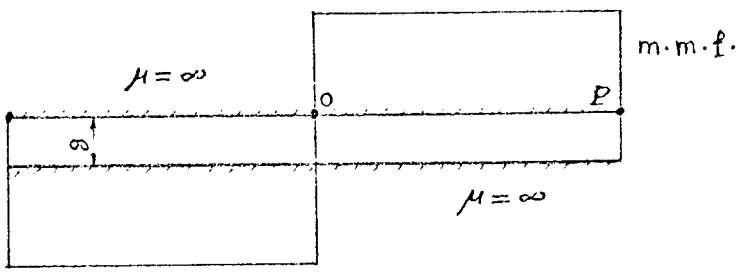

Fig 10.3

A smooth air gap and the m.m.f. of full pitch winding.

The peripheral air gap flux flowing from pole to pole can be determined by considering the boundary conditions shown in Fig. 10.4.

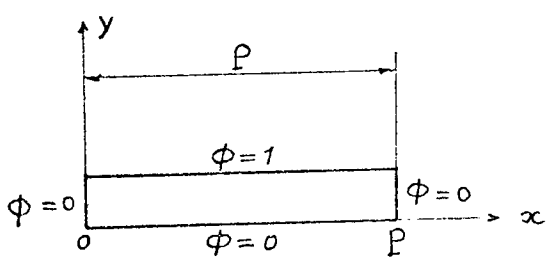

Fig 10.4

The potential boundary conditions corresponding to Fig. 10.4

The function describing the potential distribution inside the rectangle of Fig. 10.4 can be conveniently obtained by using the harmonic functions which satisfy both Laplaces

differential equation and the given boundary conditions.

The solution of the potential function for the problem shown in Fig. 10.4 is given by

$$\phi = \sum_{K=1}^{\infty} A_K \sinh \frac{K\pi}{P} y \cdot \sin \frac{K\pi}{P} x$$

where

$$A_K = \frac{1}{P} \int_0^P \frac{\sin \frac{K\pi}{P} x}{\sinh \frac{K\pi}{P} g} dx = \begin{cases} \dfrac{2}{K\pi \sinh \frac{K\pi}{P} g} & (\text{for } K = 1, 3, 5, \ldots) \\ 0 & (\text{for } K = 2, 4, 6, \ldots) \end{cases}$$

Therefore, the potential function becomes

$$\phi = \sum_{K=1,3}^{odd} \frac{2 \sinh \frac{K\pi}{P} y}{K\pi \sinh \frac{K\pi}{P} g} \cos \frac{K\pi}{P} x \qquad (10\text{-}6)$$

Differentiating equation (10-6) with respect to x, gives the peripheral component of the flux density at any point.

$$B_x = \sum_{K=1,3}^{odd} \frac{2 \sinh \frac{K\pi}{P} y}{P \sinh \frac{K\pi}{P} g} \cos \frac{K\pi}{P} x$$

The peripheral fluxes which cross the surfaces at $x = 0$ and $x = p$ are obtained by

$$\phi_P = \int_0^g B_x \, dy = \sum_{K=1,3}^{odd} \frac{4}{K\pi \sinh \frac{K\pi}{P} g} \left(\cosh \frac{K\pi}{P} g - 1 \right) \qquad (10\text{-}7)$$

The radial flux which cross the surface at $y = g$ is obtained by

$$\phi_R = \int_0^P B_y \, dx = - \sum_{K=1,3}^{odd} \frac{2 \coth \frac{K\pi}{P} g}{K\pi} (\cos K\pi - 1) \qquad (10\text{-}8)$$

The ratio of the fundamental peripheral air gap flux to the fundamental of the radial flux, from equations (10-7) and (10-8) is

$$\frac{\phi_{P1}}{\phi_{R1}} = \left(1 - \frac{1}{\cosh \frac{\pi}{P} g} \right) \qquad (10\text{-}9)$$

By expanding the term $\cosh \frac{\pi}{P} g$ into polynomial series

$$\cosh \frac{\pi}{P} g = 1 + \frac{\left(\frac{\pi}{P} g\right)^2}{2!} + \frac{\left(\frac{\pi}{P} g\right)^4}{4!} + \cdots$$

and neglecting the higher powers other than $\left(\frac{\pi}{P} g\right)^2$, the ratio given in equation (10-9) becomes

$$\frac{\Phi_{P1}}{\Phi_{R1}} = \frac{\left(\frac{\pi}{P} g\right)^2}{2!} \qquad (10\text{-}10)$$

Equation (10-10) can be also written in terms of the stator diameter D and pairs of poles p, by using

$$P = \frac{\pi D}{2P}$$

Thus equation (10-10) becomes

$$\frac{\Phi_{P1}}{\Phi_{R1}} = 2\left(\frac{P}{D} g\right)^2$$

Knowing the fundamental air gap flux, the peripheral air gap leakage (the fundamental component) can be determined from the above expression.

10.3 Appendix 3

The Effective Air Gap Length for Slot m.m.f. Harmonics

The effect of a slot opening on the shape of flux harmonics corresponding to slot m.m.f. harmonics varies as these harmonics revolve with respect to a slot opening. In Fig. 3.1 two examples of this variation was shown. In Section 3.2 it was noted that the reduction in the average air gap flux corresponding to Fig. 3.1(a) can be estimated by using Carter's analysis, because the effect of peripheral air gap leakage (in comparison with the overall distortion of the air gap flux) is negligible.

This appendix investigates an equivalent analysis for the case of Fig. 3.1(b)

The magnetic field in the air gap of Fig. 3.1(b) can be synthesised from a line current assumed to be situated deep inside the slot [see Fig. 10.5 (a)].

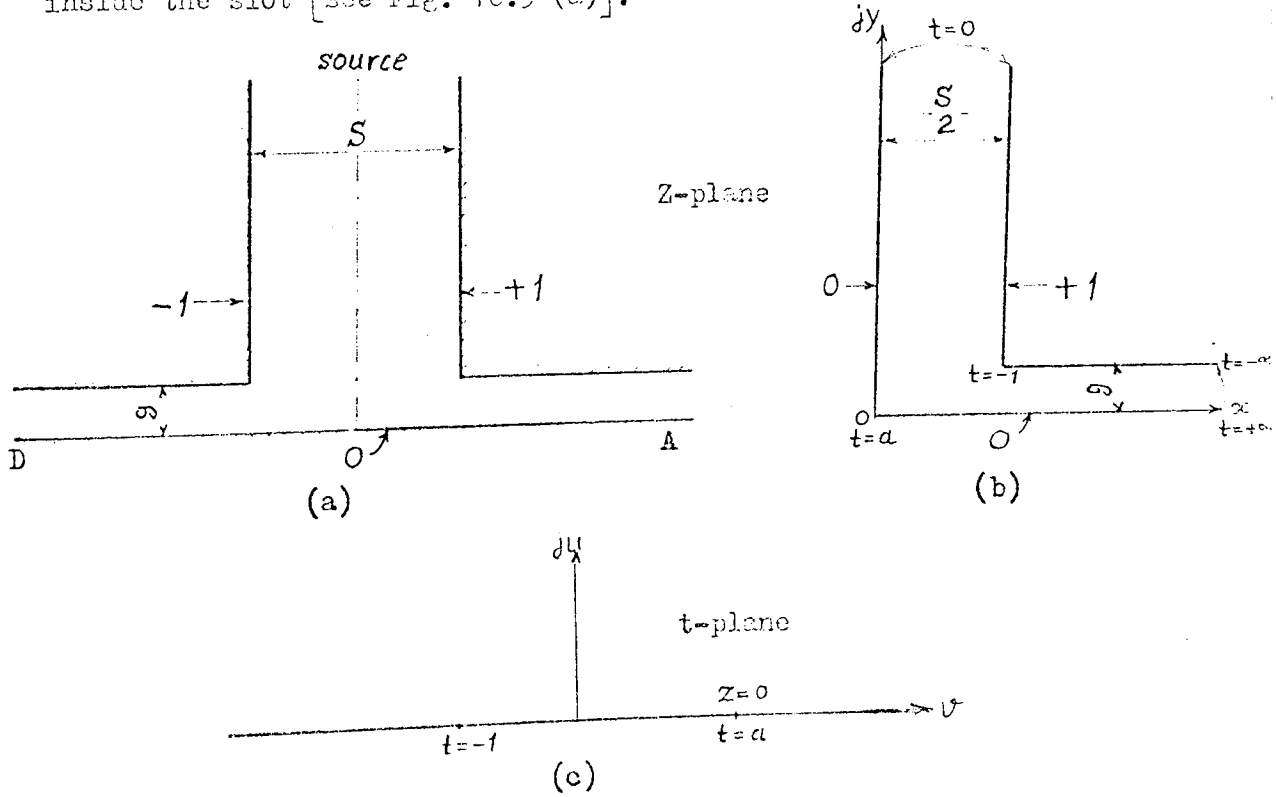

Fig. 10.5

The complex Z-plane and t-plane

For a current of 2 ampere the potentials of the adjacent teeth [as shown in Fig. 10.5(a)] are +1 and -1 with respect to the plane surface at zero potential. The potential on the line of symmetry down the slot centre is also zero.

Because of the symmetry, only one half of the air gap geometry [as shown in Fig. 10.5 (b)] is considered. The conformal transformation of Fig. 10.5 (b) into the upper half of t-plane is indicated in Fig. 10.5 (c).

The transformation equation which connects the two complex Z and t-planes is

$$\frac{dZ}{dt} = K \frac{\sqrt{(t+1)}}{t\sqrt{(t-a)}} \qquad (10\text{-}11)$$

By using the method of residues, the constants K and a can be obtained and they are given by

$$K = \frac{g}{\pi}$$

and

$$a = \left(\frac{2g}{s}\right)^2$$

The transformation of a uniform field (in a complex w-plane) between two parallel plates separated by the distance g into the upper half of the t-plate is given by

$$\frac{dw}{dt} = \frac{C}{t} \qquad (10\text{-}12)$$

The flux density at any point in the Z-plane is expressed by

$$\left|\frac{dw}{dZ}\right|$$

Hence, the expression for flux density is given by

$$B = \left|\frac{dw}{dt} \times \frac{dt}{dZ}\right| = \frac{\sqrt{(t-a)}}{g\sqrt{(t+1)}} \qquad (10\text{-}13)$$

It is clear from equation (10-13) that when t tends to infinity, the flux density in the air gap becomes uniform and equal to $\frac{1}{g}$ (this is the maximum flux density in the air gap). At the origin of Z-plane which corresponds to t = a the flux density is zero. Thus the flux density along the smooth surface DA rises from zero to its maximum value $(\frac{1}{g})$. The area between the straight line representing the maximum flux density in the air gap and the curve of the flux density distribution along the smooth surface DA gives the magnitude of the lost flux due to the slot opening.

Thus, the lost flux is expressed by

$$\Phi_\ell = \int_0^\infty (B_{max} - B)\, dZ \qquad (10\text{-}14)$$

Taking into account the expressions (10-11) and (10-13) and also noting that the point Z = 0 corresponds to t = a, the integral of equation (10-14) becomes

$$\Phi_\ell = \int_a^\infty \left[\frac{1}{g} - \frac{\sqrt{(t-a)}}{g\sqrt{(t+1)}} \right] \frac{g\sqrt{(t+1)}}{\pi t \sqrt{(t-a)}}\, dt$$

or

$$\Phi_\ell = \frac{1}{\pi} \int_a^\infty \left[\frac{\sqrt{(t+1)} - \sqrt{(t-a)}}{t\sqrt{(t-a)}} \right] dt \qquad (10\text{-}15)$$

The integration of each term in equation (10-15) leads to infinity, but their difference is finite. However, a finite solution of the integral of equation (10-15) is not possible in its present form. For this reason, the integral of equation (10-15) is represented in terms of a new variable (u).

Let

$$u = \sqrt{\frac{(t-a)}{(t+1)}}$$

Hence

$$t = -\frac{(u^2+a)}{(u^2-1)} \tag{10-16}$$

and

$$dt = \frac{2(1+a)u}{(u^2-1)^2}$$

The limits of integration for the new variable (u), from equation (10-16) are:

when $t \longrightarrow a$, $u = 0$

and

when $t \longrightarrow \infty$, $u = 1$

Substitution of t and dt into equation (10-15) gives

$$\Phi_\ell = \frac{2(1+a)}{\pi} \int_0^1 \frac{du}{(u+1)(u^2+a)} \tag{10-17}$$

By solving the integral and substituting the limits, the solution for the lost flux is

$$\Phi_\ell = \frac{2}{\pi}\left(\ln\left\{\frac{\frac{4g}{S}}{\left[1+\left(\frac{2g}{S}\right)^2\right]^{1/2}}\right\} + \frac{S}{2g}\tan^{-1}\frac{S}{2g}\right) \tag{10-18}$$

In a similar manner as Carter's coefficient, the ratio of the flux crossing a slot pitch in a smooth air gap to that actual flux in the presence of the slot opening is

$$C_m = \frac{t+S}{t+S-2\Phi_\ell} \tag{10-19}$$

where Φ_ℓ is given by equation (10-18).

The coefficient C_m also represents the ratio of the total to the effective air gap area. Alger expresses this ratio by

$$C_m = \frac{t+S}{t+fg} \tag{10-20}$$

where f is the fringing coefficient.

From equations (10-19) and (10-20) the fringing coefficient f is given by the following expression

$$f = \frac{S}{g} - \frac{4}{\pi g}\left[\ln\left\{\frac{\frac{4g}{S}}{\sqrt{1+\left(\frac{2g}{S}\right)^2}}\right\} + \frac{S}{2g}\tan^{-1}\frac{S}{2g}\right] \qquad (10\text{-}21)$$

The table shown below gives the value of the fringing coefficient f, calculated by using equation (10-21) and also the corresponding values calculated from Carter's analysis for a few selected ratios of s/g.

Table 10-1

The fringing coefficients calculated by eqn.(10-21),and by Carter's C

s/g	4	6	8	10
The fringing coefficient (f),from eqn.(10-21)	1.32	1.84	2.18	2.48
The fringing coefficient (f),from Carter's C	2.205	2.695	3.051	3.330

10.4 Appendix 4

Determination of the Unknown Coefficients of the Potential Functions Φ_1, Φ_2 and Φ_3 (section 4.3)

The unknown coefficients A_m, B_K, C_K and D_m of the potential functions Φ_1, Φ_2 and Φ_3 [see equations (4-1)-(4-3), section 4.3] can be determined from the continuity of the potential function and its normal derivatives along the boundary lines bordering the air gap region and the rectangles I and II (see Fig. 4.1).

At the surface $y = g$, both potential functions Φ_1 and Φ_2 in the interval $\tau - P_s \leqslant x \leqslant \tau + P_s$ are unknown. (Note, at $x = \tau - P_s$ and $x = \tau + P_s$ the potential is unity). Let the unknown potential function in the interval $\tau - P_s \leqslant x \leqslant \tau + P_s$ which is common to both potential functions Φ_1 and Φ_2 be denoted by $1 + \Psi_1(x)$. The value of the unknown potential function $\Psi_1(x)$ at the points $x = \tau - P_s$ and $x = \tau + P_s$ must be zero, since unity is introduced in the expression of the unknown potential function.

From the boundary condition at $y = g$ and in the interval $\tau - P_s \leqslant x \leqslant \tau + P_s$ the unknown coefficient A_m of the potential function Φ_1 can be expressed by

$$A_m = \frac{1}{P_s} \int_{\tau - P_s}^{\tau + P_s} \Psi_1(x) \cdot \sin \frac{m\pi}{2P_s}(x - \tau + P_s)\, dx \qquad (10\text{-}22)$$

Similarly, from the same boundary condition, the unknown coefficient B_K of the potential function Φ_2 is given by

$$B_K = \frac{1}{\tau} \int_0^{2\tau} \cos Kx \cdot dx + \frac{1}{\tau} \int_{\tau - P_s}^{\tau + P_s} \Psi_1(x) \cdot \cos Kx \cdot dx \qquad (10\text{-}23)$$

In the same manner, at $y = 0$ and in the interval $\tau + dis - P_r \leqslant x \leqslant \tau + dis + P_r$ the unknown potential function which is common to both potential functions Φ_2 and Φ_3 is denoted by $\Psi_2(x)$. Hence, the unknown coefficients C_K and D_m of the potential functions Φ_2 and Φ_3 are expressed by

$$C_K = \frac{1}{\tau_1} \int_{\tau+dis-P_r}^{\tau+dis+P_r} \Psi_2(x) \cdot \cos \frac{K\pi}{\tau_1}(x - \tau + \tau_1 - dis) \cdot dx \qquad (10\text{-}24)$$

and

$$D_m = \frac{1}{P_r} \int_{\tau+dis-P_r}^{\tau+dis+P_r} \Psi_2(x) \cdot \sin \frac{m\pi}{2P_r}(x - \tau - dis + P_r) \cdot dx \qquad (10\text{-}25)$$

It will be seen below that by choosing the appropriate form of the unknown potential functions along the boundary lines, the number of the unknowns is effectively reduced into two (namely $\Psi_1(x)$ and $\Psi_2(x)$). In integral form, however, the number of the unknowns is four. Moreover, the Fourier series representing the potential function Φ_2 (see equation 4-2) consists of two terms and each of them involves functions of different wavelengths. In order to relate the potential function $\Psi_1(x)$ to the potential function $\Psi_2(x)$, it is necessary to make use of the equality of the flux components which cross the air gap. It can be shown that by considering the flux components which cross the air gap by one stator slot pitch and one rotor slot pitch (these flux components arise from each term of the potential function Φ_2) the following relationship can be obtained.

$$\sum_{K=0}^{\infty} \frac{K}{\tau} \coth K g \left[\int_{\tau-p_3}^{\tau+p_3} \psi_1(x) \cdot \cos Kx \cdot dx \right] \times \int_0^{2\tau} \cos^2 Kx \cdot dx -$$

$$- \sum_{K=0}^{\infty} \frac{K\pi}{\tau_1^2 \cdot \sinh \frac{K\pi}{\tau_1} g} \left[\int_{\tau+dis-p_r}^{\tau+dis+p_r} \psi_2(x) \cdot \cos \frac{K\pi}{\tau_1} (x - \tau + \tau_1 - dis) \cdot dx \right] \times$$

$$\times \int_{\tau-\tau_1+dis}^{\tau+\tau_1+dis} \cos^2 \frac{K\pi}{\tau_1} (x - \tau + \tau_1 - dis) \cdot dx =$$

$$\sum_{K=0}^{\infty} \frac{K}{\tau \cdot \sinh Kg} \left[\int_{\tau-p_3}^{\tau+p_3} \psi_1(x) \cdot \cos Kx \cdot dx \right] \times \int_0^{2\tau} \cos^2 Kx \cdot dx -$$

$$- \sum_{K=0}^{\infty} \frac{K\pi}{\tau_1^2} \coth \frac{K\pi}{\tau_1} g \left[\int_{\tau+dis-p_r}^{\tau+dis+p_r} \psi_2(x) \cdot \cos \frac{K\pi}{\tau_1} (x - \tau + \tau_1 - dis) \cdot dx \right] \times$$

$$\times \int_{\tau-\tau_1+dis}^{\tau+\tau_1+dis} \cos^2 \frac{K\pi}{\tau_1} (x - \tau + \tau_1 - dis) \cdot dx \qquad (10-26)$$

or (remembering that $\tau = \pi$)

$$\int_{\tau-p_3}^{\tau+p_3} \psi_1(x) \cdot \cos Kx \cdot dx = \frac{\pi^2 \left(\frac{1}{\sinh \frac{K\pi}{\tau_1} g} - \coth \frac{K\pi}{\tau_1} g \right)}{\tau_1^2 \left(\coth Kg - \frac{1}{\sinh Kg} \right)} \times$$

$$\times \int_{\tau+dis-p_r}^{\tau+dis+p_r} \psi_2(x) \cdot \cos \frac{K\pi}{\tau_1} (x - \tau + \tau_1 - dis) \cdot dx \qquad (10-27)$$

The next condition which must be satisfied is the continuity of the normal derivatives of the potential functions along the boundary lines between the air gap region and the rectangles I and II. Taking into account equation (10-27), the continuity of the normal derivative of the potential functions ψ_1 and ψ_2

at $y = g$ and in the interval $\tau - P_s \leqslant x \leqslant \tau + P_s$ gives the following relationship.

$$\sum_{K=0}^{\infty} -\frac{K}{\pi}\cdot\coth K\cdot g\left[\int_{\tau-P_s}^{\tau+P_s}\psi_1(x)\cdot\cos K\cdot x\cdot dx\right]\cdot\cos K\cdot x +$$

$$+\sum_{K=0}^{\infty}\frac{K\cdot\left(\frac{1}{\sinh K\cdot g}-\coth K\cdot g\right)}{\pi\cdot\sinh\frac{K\pi}{\tau_1}g\left(\frac{1}{\sinh\frac{K\pi}{\tau_1}g}-\coth\frac{K\pi}{\tau_1}g\right)}\times\left[\int_{\tau-P_s}^{\tau+P_s}\psi_1(x)\cdot\cos K\cdot x\cdot dx\right]\times$$

$$\times\cos\frac{K\pi}{\tau_1}(x-\tau+\tau_1-dis)+$$

$$+\sum_{m=1}^{\infty}\frac{m\pi}{2P_s}\left[\int_{\tau-P_s}^{\tau+P_s}\psi_1(x)\cdot\sin\frac{m\pi}{2P_s}(x-\tau+P_s)\cdot dx\right]\cdot\sin\frac{m\pi}{2P_s}(x-\tau+P_s)=-\frac{1}{g} \qquad (10\text{-}28)$$

(It should be noted in the above equation the value of $\coth\frac{m\pi}{2P_s}h_s$ does not appear, because for most practical dimensions this value is unity)

Equation (10-28) represents a non-homogeneous integral equation of Fredholm type which can be solved by using the method of Galerkin approximation. The essence of Galerkin method consists of the following.

In order to solve equation (10-28) the unknown function $\psi_1(x)$ is chosen as a sum of n terms of functions $U_1(x)$, $U_2(x), \ldots U_n(x)$ such that each of these functions satisfies the boundary conditions at $x = \tau - P_s$ and $x = \tau + P_s$, i.e.

$$\psi_{1n}(x) = \sum_{m=1}^{n} a_m U_m(x)$$

where $\psi_{1n}(x)$ is an approximation of the actual function $\psi_1(x)$. The form of the function $\psi_{1n}(x)$ which satisfies the potential values at $x = \tau - P_s$ and $x = \tau + P_s$ can be expressed by the harmonic functions

$$\psi_{1n}(x) = \sum_{m=1}^{n} a_m \sin\frac{m\pi}{2P_s}(x-\tau+P_s) \qquad (10\text{-}29)$$

By substituting the approximate function $\Psi_{1n}(x)$ into equation (10-28) some error would result. The magnitude of the error involved, diminishes as the number of the terms in the series (10-29) increases. Theoretically, the approximate function $\Psi_{1n}(x)$ approaches the actual potential function $\Psi_1(x)$ as $m \longrightarrow \infty$.

By Galerkin method, the coefficients of the finite series (10-29) can be determined such that the truncated series gives the best approximation.

Suppose the error which would result by substituting the approximated function $\Psi_{1n}(x)$ with n terms into equation (10-28) is $R(x)$. In accordance with Galerkin method the truncated series of $\Psi_{1n}(x)$ is the best approximation if the coefficients a_m are determined from the condition

$$\int_{\tau-P_s}^{\tau+P_s} R(x)\cdot \sin\frac{i\pi}{2P_s}(x-\tau+P_s)\cdot dx = 0 \qquad (10\text{-}30)$$

where $i = 1, 2, \ldots\ldots, n.$

In the present analysis, the series of the function $\Psi_{1n}(x)$ is truncated up to ten terms.

Exactly in the same manner the unknown potential function $\Psi_2(x)$ is approximated by the series

$$\Psi_{2n}(x) = \sum_{m=1}^{n} b_m \sin\frac{m\pi}{2P_r}(x-\tau-dis+P_r) \qquad (10\text{-}31a)$$

and the series is truncated up to 10 terms.

Also the coefficient b_m is determined from the condition

$$\int_{\tau+dis-P_r}^{\tau+dis+P_r} R(x)\sin\frac{i\pi}{2P_r}(x-\tau-dis+P_r)\cdot dx \qquad (10\text{-}31b)$$

By solving the linear systems of the simultaneous equations represented by (10-30) and (10-31b) the complete solution of the potential functions Φ_1, Φ_2 and Φ_3 is obtained.

From equation (4-2) the d.c. component of the normal derivative of the potential function Φ_2 (in terms of a_m and b_m) is given by

$$B_0 = \frac{1}{g} + \frac{4 \cdot P_s}{\pi^2 \cdot g} \times \sum_{m=1,3}^{odd} \frac{a_m}{m} - \frac{4 \cdot P_r}{\pi^2 \tau_1 \cdot g} \times \sum_{m=1,3}^{odd} \frac{b_m}{m} \qquad (10\text{-}32)$$

The amplitude of the k harmonic of the normal derivative of the potential function Φ_2 (in terms of a_m and b_m) is given by

$$B_K = \frac{2 \cdot P_s \cdot K \cdot \cosh K y}{\pi^2 \cdot \sinh K g} \times \sum_{m=1}^{n} m \cdot a_m \cdot \left[\frac{\cos K\pi(\tau - P_s) - \cos m\pi \cdot \cos K\pi(\tau + P_s)}{m^2 - 4\left(\frac{K P_s}{\pi}\right)^2} \right] -$$

$$- \frac{2 \cdot P_r \cdot K \cdot \cosh \frac{K\pi}{\tau_1}(g - y)}{\tau_1^2 \cdot \tanh \frac{K\pi}{\tau_1} g} \times \sum_{m=1}^{n} m \cdot b_m \left[\frac{\cos \frac{K\pi}{\tau_1}(\tau_1 - P_r) - \cos m\pi \cdot \cos \frac{K\pi}{\tau_1}(\tau_1 + P_r)}{m^2 - 4\left(\frac{K P_r}{\tau_1}\right)^2} \right]$$

(10-33)

It can be seen from equations (10-32) and (10-33), the series representing the harmonics attenuates much faster than the d.c. component. The result of computation shows that for slot openings smaller than the tooth width (which is commonly used in induction machines with semi-enclosed slots), the truncation of the series up to 10 terms leads to a maximum error of the order 1 - 3% for the d.c. component (see section 4.4.1 and table 4.1). In the case of harmonics, the magnitude of the error

is much smaller because the attenuation of the series is faster.

The details of the computer programme written for the calculation of the coefficients a_m and b_m, and also the results of the computations are attached at the end of the thesis.

10.5 Appendix 5

The Analysis of Eddy Current Distribution in Laminated Rotors

In induction machines the rotor is laminated in axial direction (x-axis). At any point inside the laminations the current density has three component Jx, Jy, Jz. Owing to the insulation, the axial component Jx at the surfaces of the laminations vanishes. The radial component Jz at the rotor surface is also zero. As laminations repeat with thickness (2a), it follows that all the field variables are periodic functions of x. Moreover, the field variables have certain symmetry in their dependence on x (see Figs.5.1(a) and 5.2). Taking the origin of the co-ordinate system at the centre of a lamination, the component Jx is an even function and it is zero at $x = \pm a$. The component Jy and Jz are odd functions of x (Jz is zero at the rotor surface). Similarly it can be seen from the field relationship (curl H = J) that the components Hy and Hz are even functions of x, whereas Hx is an odd function of x. If the interlamina insulation is assumed to be infinitely thin, then the component Hx must vanish at the surface of the lamination because, Hx is an odd function and

$$\left[H_x\right]_{x=a} = -\left[H_x\right]_{x=-a}$$

All the field components Hx, Hy, Hz and eddy current density components Jx, Jy, Jz approach zero as $z \longrightarrow \infty$.

In order to determine the field and current density components, the following assumptions and simplications (which are commonly applied to linear problems) are made.

1. The air gap curvature is neglected.
2. The rotor is assumed to be made up of an infinite number of semi-infinite laminations of finite thicknesses.
3. The laminations are assumed to be perfectly insulated and the thickness of insulation is negligible.
4. The source of the inducing field is assumed to be a current sheet travelling on a smooth stator surface.
5. The problem is assumed to be linear, i.e. the resistivity and permeability of the rotor iron are constant. The stator resistivity and permeability are assumed to be infinite.
6. The current density component Jz is neglected. This current density component, as indicated in Section 5.3, is induced in vertical cross-sectional planes due to the angular variation of the applied field (see Fig. 5.2). Since the intensity of the field producing this component is weak no significant error would result by neglecting Jz.

10.5.1 The Field Equations

The rectangular Cartesian system is used and the direction of the axis are defined as follows.

x is parallel to the axial direction, y to the peripheral and z to the radial direction. The plane of stator surface is taken at $z = 0$, the rotor is positioned along the positive direction of z and its surface is at $z = g$. The plane $x = 0$ is taken to coincide with the central plane of one of the laminations. The positive direction of y is taken along the direction of the motion of the current sheet.

The field equations for the rotor region are as follows

$$\text{div } H = 0 \tag{10-34}$$

$$\text{curl } H = J \tag{10-35}$$

$$\text{curl } \rho J = -\mu \frac{\partial H}{\partial t} \tag{10-36}$$

and from the above relationships it can be shown that

$$\nabla^2 H = \frac{\dot{}}{d^2} H \tag{10-37}$$

$$\nabla^2 J = \frac{\dot{}}{d^2} J \tag{10-38}$$

where $d = \sqrt{\frac{\rho}{\mu\omega}}$

ρ and μ are the resistivity and permeability of the rotor lamination respectively.

ω - is the angular velocity of the travelling wave.

The field equation for the stator and air gap regions, excluding the position of the current sheet are as follows

$$\text{div } H = 0$$

$$\text{curl } H = 0 \tag{10-39}$$

$$H = \text{grad } \Phi \tag{10-40}$$

$$\nabla^2 \Phi = 0 \tag{10-41}$$

where Φ is a scalar potential function.

The reason for excluding the current sheet is explained in the following section.

10.5.2 The Inducing and Induced Fields

If the resistivity of the rotor laminations were infinite, no eddy currents would have been induced. Since the stator permeability is assumed to be infinite, it is possible to synthesise the applied field from a scalar potential distribution on the stator surface. The potential distribution can be given in terms of a current sheet which produces the same undamped applied flux density at the rotor surface.

From the analysis of the magnetic field in solid iron it can be shown that the amplitude of the radial undamped flux density at the rotor surface produced by a current sheet of amplitude $\hat{J}$ lying on the stator surface is expressed by

$$\hat{B}_m = j\mu_0 \frac{\hat{J}}{\sinh \kappa g} \qquad (10\text{-}42)$$

where $\kappa = \frac{2\pi}{\tau}$

and τ is the pole pitch of the harmonic,

and g is the air gap length.

(The derivation of equation (10-42) and the detail of the field analysis in solid rotors are given in Reference 62 , Chapter 6).

However, since the resistivity of the rotor laminations is finite, eddy currents flow in the laminations and produce their own fields. The field in the air gap due to the induced eddy currents alone, is primarily determined by the magnitude of the eddy currents induced on the surface of rotor laminations. Also, since the stator permeability is assumed to be infinite and the air gap field is dependent only upon the surface eddy currents, it is permissible to assume the m.m.f. of the surface eddy currents is entirely consumed in the air gap. The air gap field due to the rotor surface eddy currents can be similarly synthesised from a scalar potential distribution along the rotor surface. In this case the scalar potential distribution must be such that it gives the same flux density components as produced by the rotor surface current density components.

10.5.3 The Solution of the Inducing Field in the Air Gap

In the absence of rotor induced eddy currents, the solution of the inducing field in the air gap can be given in terms of

a potential function which gives the same undamped flux density at rotor surface as obtained from a travelling current sheet lying on the stator surface.

The potential function which satisfies this condition is expressed by

$$\phi_1' = \frac{\hat{J}}{\kappa \sinh \kappa g} e^{j(\omega t - \kappa y)} \times \cosh \kappa z \qquad (10\text{-}43)$$

where J is given by equation (10-42), namely

$$\hat{J} = \frac{\hat{B}}{j\mu_0} \sinh \kappa g$$

and $\hat{B}$ is the amplitude of the undamped flux density in terms of which all the resulting unknowns must be determined.

$\kappa = \frac{2\pi}{\tau}$, where τ is the pole pitch of the harmonic.

Although the undamped flux density at the surface of laminated iron is also a function of the variable **x**, nevertheless owing to the assumption of infinitely thin insulation and also due to the proximity effect of the laminations; this dependence cannot be expressed by a continuous function. G.W. Carter[76] erroneously expressed this dependence in terms of Fourier series which led to non-zero axial flux density component (B_x) at the surfaces of the laminations.

10.5.4 The Solution of the Current Density and Field Components in a Rotor Lamination

The solution of the current density and field components inside the laminations must satisfy the field equations (10-34) - (10-38) and the boundary conditions specified in Section 10.5

The field components in one lamination in the range $-a \leqslant x \leqslant +a$ are given by

$$H_{x_r} = \sum_{m=1}^{\infty} \left\{ C_m \, e^{-z\left[\left(\frac{m\pi}{a}\right)^2 + \kappa^2 + \frac{j}{d^2}\right]^{\frac{1}{2}} + j(\omega t - \kappa y)} \right\} \sin \frac{m\pi}{a} x \qquad (10\text{-}44)$$

$$H_{y_r} = \frac{j\pi\kappa}{a} \sum_{m=1}^{\infty} \left\{ \frac{m C_m}{\left(\frac{m\pi}{a}\right)^2 + \left(\frac{j}{d^2}\right)} e^{-z\left[\left(\frac{m\pi}{a}\right)^2 + \kappa^2 + \frac{j}{d^2}\right]^{\frac{1}{2}} + j(\omega t - \kappa y)} \right\} \cos \frac{m\pi}{a} x \qquad (10\text{-}45)$$

$$-H_{z_r} = -\frac{\pi}{a} \sum_{m=1}^{\infty} \left\{ \frac{m C_m}{\left(\frac{m\pi}{a}\right)^2 + \left(\frac{j}{d^2}\right)} e^{-z\left[\left(\frac{m\pi}{a}\right)^2 + \kappa^2 + \frac{j}{d^2}\right]^{\frac{1}{2}} + j(\omega t - \kappa y)} \right\} \cos \frac{m\pi}{a} x \qquad (10\text{-}46)$$

Similarly the current density components in one lamination in the range $-a \leqslant x \leqslant +a$ are given by

$$J_{x_r} = \sum_{m=0}^{\infty} \left\{ N_{(2m+1)} \, e^{-z\left\{\left[\frac{(2m+1)\pi}{2a}\right]^2 + \kappa^2 + \frac{j}{d^2}\right\}^{\frac{1}{2}} + j(\omega t - \kappa y)} \right\} \cos \frac{(2m+1)\pi}{2a} x \qquad (10\text{-}47)$$

$$J_{y_r} = \sum_{m=0}^{\infty} \left\{ M_{(2m+1)} \, e^{-z\left\{\left[\frac{(2m+1)\pi}{2a}\right]^2 + \kappa^2 + \frac{j}{d^2}\right\}^{\frac{1}{2}} + j(\omega t - \kappa y)} \right\} \sin \frac{(2m+1)\pi}{2a} x \qquad (10\text{-}48)$$

The unknown coefficients C_m, $N_{(2m+1)}$, $M_{(2m+1)}$ will be determined from the continuity of the field along the lamination surface.

It should be noted that although the current density and field components are related with each other by the field equation curl H = J, their dependence with respect to the variable x is expressed by functions of different form. This has been compulsorily preimposed in order to satisfy the boundary conditions.

However, any continuous function in a limited interval can be expanded into Fourier series, and hence the relationship between J and H involves double Fourier series.

10.5.5 The Solution of the Air Gap Field due to the Induced Eddy Currents

The solution of the air gap field due to the induced eddy currents can be specified by a potential function. This potential function must satisfy the relationship between the current density and field components at the surface of the lamination and also the zero potential distribution on the stator surface (since the stator permeability is assumed to be infinite).

The functions which express the x-dependence of the current density and field components, in this case, are chosen to be of the same form. In doing so, the boundary condition which dictates that the axial flux density component at the surface of the lamination to be zero would be violated. Therefore, an additional term (see below) is introduced in the potential function in order to satisfy this boundary condition.

Thus, the potential function which satisfies the above conditions is expressed in terms of the surface current density components by

$$\Phi_1'' = \sum_{m=0}^{\infty} \left\{ \left[\frac{j}{\kappa} N(2m+1) - \frac{M(2m+1)}{\left[\frac{(2m+1)\pi}{2a}\right]} \right] \frac{e^{-g\left\{\left[\frac{(2m+1)\pi}{2a}\right]^2 + \kappa^2 + \frac{j}{d^2}\right\}^{\frac{1}{2}}}}{\sinh(g)\left\{\left[\frac{(2m+1)\pi}{2a}\right]^2 + \kappa^2\right\}^{\frac{1}{2}}} \times e^{j(\omega t - \kappa y)} \times \right.$$

$$\left. \times \sinh(z)\left\{\left[\frac{(2m+1)\pi}{2a}\right]^2 + \kappa^2\right\}^{\frac{1}{2}} \right\} \cos\frac{(2m+1)\pi}{2a} x \quad +$$

$$+ \sum_{n=1}^{\infty} P_n \cosh\left[\left(\frac{n\pi}{g}\right)^2 + \kappa^2\right]^{\frac{1}{2}}(x) \times e^{j(\omega t - \kappa y)} \times \sin\frac{n\pi}{g} z \qquad (10\text{-}49)$$

The coefficients $N_{(2m+1)}$, $M_{(2m+1)}$, and In are unknowns.

10.5.6 The Eddy Current Loss

In order to obtain the eddy current loss it is necessary to determine the four unknown coefficients C_m, $N_{(2m+1)}$, $M_{(2m+1)}$ and P_n. The four unknowns are determined from the continuity of the total field components along the surface of the lamination, namely

$$\left[\frac{\partial \Phi'}{\partial x} + \frac{\partial \Phi''}{\partial x}\right]_{Z=g} = \left[Hx_r\right]_{Z=g} \qquad (10\text{-}50)$$

$$\left[\frac{\partial \Phi'}{\partial y} + \frac{\partial \Phi''}{\partial y}\right]_{Z=g} = \left[Hy_r\right]_{Z=g} \qquad (10\text{-}51)$$

$$\left[\frac{\partial \Phi'}{\partial z} + \frac{\partial \Phi''}{\partial z}\right]_{Z=g} = \left[\mu_2 Hz_r\right]_{Z=g} \qquad (10\text{-}52)$$

and the fourth equation is obtained from the boundary condition that the axial flux density component B_x in the air gap due to the induced eddy currents (see equation 10-49) is zero, i.e.

$$\left[\frac{\partial \Phi''}{\partial x}\right]_{x=\pm a} = 0 \qquad (10\text{-}53)$$

The eddy current loss per unit area in accordance with Poynting vector is given by

$$P_e = \frac{\mathcal{P}}{2}\left[\text{real}\int_S (\bar{H} \times J)\, dS\right]$$

where $\bar{H}$ is the complex conjugate function of H.

REFERENCES

1. NEJMAN, L. R. : 'Skin effect in ferromagnetic bodies', Gosenergoizdat,Leningrad,1949(In - Russian)

2. POHL, R. : 'Electromagnetic and mechanical effect in solid iron due to an alternating or rotating magnetic field',J.IEE,1944, 91-II,pp 239-248

3. MacLEAN, W. : 'Theory of strong electromagnetic waves in massive iron',J.Appl.Phys., 1954,25,pp 1267-1270

4. ASPDEN, H. : 'Eddy currents in solid cylindrical cores having non-uniform permeability', J.Appl.Phys.,1952,23,pp 523-528

5. AGARWAL, P. D. : 'Eddy current losses in solid and laminated iron',Trans.AIEE.,1959, 78-I,pp 169-181

6. SCHWARZ, K. K. :'Survey of basic stray losses in squirrel cage induction motors',Proc. IEE,1964,111,pp 1565-1573

7. ALGER, P. L. : 'Induction machines',(Gordon and Brech,1970)

8. LIWSCHITZ-GARIK, M. : 'Electric machinery'(D.Van Nostrand,1946,vols.I and II)

9. SAY, M. G. : 'Performance and design of alternating current machines',(Pitman,1936)

10. CHALMERS, B. J. : 'Electromagnetic problems of A.C. machines',(Chapman and Hall,1965)

11. POLLARD, E. I. : 'Load losses in salient pole synchronous machines',Trans.AIEE,1935,54, pp 1332-1340

12. RICHARDSON, P. : 'Stray losses in synchronous electrical machinery',Proc.IEE,1945,92-II, p 291

13. ADDERLEY,K. J. : 'A study of the pole face loss caused by armature reaction m.m.f. harmonics', (M.Sc. Thesis,The University of Aston in Birmingham,1968)

14. GAULT, J. S. : 'Rotor-bar currents in squirrel cage induction motors',Trans.AIEE,1941,60, p 784

15. BAILEY, B. F. : 'The induction motor',(McGraw Hill)

16. BARNES, E. C. : 'An experimental study of induction motor end turn reactance',Trans.AIEE, 1951,70.Prt.III, p 671

17. HANSINGER, V. N. : 'Theory of end winding leakage reactance',Trans.AIEE,1959,78,Part. III, p 426

18. ROSA, E. B. AND GROVER, F. W. : 'Formulae and tables for the calculation of mutual and self-inductance',Bull. of the U.S. Bureau of Standards,1912,8,pp 1-237

19. SMITH, R. T. : 'End component of armature leakage reactance of round rotor geometry', Trans.AIEE,1958,77,Part III, p 636

20. BINNS, K. J. and LAWRENSON, P. J. : 'Analysis and computation of electric and magnetic field problems',(Pergamon Press,1963)

21. CARTER, F. W. : 'Air gap induction',Elect. World,N.Y. 1901,38,p 884

22. COE, R. T.,and TAYLOR, H. W. : 'Some problems in electrical machine design involving elliptic functions',Phil.Mag.,1928, 6,p 100

23. GIBBS, W. J. : 'Conformal transformation in electrical engineering',(Chapman and Hall,1958)

24. NEVILLE, S. : 'Use of Carter's cofficient with narrow teeth',Proc.IEE,1967,114,p 1245

25. FREEMAN, E. M. : 'The calculation of harmonics,due to slotting,in the flux density waveform of dynamo-electric machines',Proc. IEE,1962,109 C,p 581

26. POHL, R. : 'Theory of pulsating field machines', J.IEE,1946,93,p 67

27. BAILLIE, T. C. : 'A diagram of correction coefficient for air gap reluctance',The Electrician, 1908-1909,62,p 494

28. VITKOVITCH, D. : 'Field analysis :experimental and computational methods',(Van Nostrand, 1966)

29. WIESEMAN, R. W. : 'Graphical determination of magnetic fields',Trans.AIEE,1927,46,p 141

30. MORATH, E. : 'Nutkontraktionsfaktoren für holbgeschlossene Nuten',Archiv für Electrotechnik,1971,54,p 164(Springer-Verlag)

31. WEBER, E. : 'Electromagnetic theory-Static fields and their mapping',(Dover Publications, 1965)

32. MULLINEUX, N., REED, J. R., and SYLVIA A. S. : 'Present mathematics syllabuses and the analytical solution of field problems',Int.J.elect.Engng Educ.,1970, 8, p 289

33. LEHMANN, T. : 'Sur la reluctance de l'entrefer des machines a encoches ouvertes dans le stator et dans le rotor',Revue Generale de l'Electricite,1923,13,p 165

34. WALKER, J. H. : 'A theory of induction motor surface losses',J.IEE,1948,95,Part II,p 597

35. DOMBOOR, L. E. : 'The magnetic field in the air gap of inductor machines on no-load,with slotted stator',Contactless Electrical Machines,Riga,1965,4(In Russian)

36. HIGGINSON, A. M. : 'A theoretical and experimental study of the Guy-type inductor alternator',(Ph.D. Thesis,The University of Aston in Birmingham,1971)

37. BINNS, K. J. : 'Calculation of some basic flux quantities in induction and other doubly-slotted electrical machines', Proc.IEE,1964,3,pp 1847-1858

38. CHAPMAN, F. T. : 'A study of induction motor',(John Wiley,1930)

39. ADAMS, C. A. : 'Design of induction motors',Trans. AIEE,1905,24,p 649

40. ARNOLD, E. : 'Wechselstromtecknik',Vol. 5-'Die asynchronen Wechselstrommachinen' (Springer,Berlin,1907)

41. CARR, L. H. A. : 'Zig-zag leakage',The Electrician, 1921,87,p 76

42. ALGER, P. L.,and WEST, H. R. : 'The air gap reactance of polyphase machines',Trans.AIEE, 1947,66,p 1331

43. FIELD, A. B. : 'Eddy currents in large slot-wound conductors',Trans.AIEE,1905,24,p761

44. PUTMAN, H. V. : 'Starting performance of synchronous motors',Trans.AIEE,1927,46,p 794

45. LIWSCHITZ-GARIK, M. : 'Skin effect bars of squirrel cage rotors',Trans.AIEE,1954,73,p 255

46. LIWSCHITZ-GARIK, M. : 'Computation of skin effect in bars of squirrel cage rotors',Trans. AIEE,1955,74,p 768

47. JONES, D. E. ,MULLINEUX, N.,REED, J. R. and STOLL, R.L.: 'Solid rectangular and T-shaped conductors in semi-closed slots', J. of Engng. Mathics.,1969,3,p 123

48. SWANN, S. A. and SALMON, J. W. : 'Effective resistance and reactance of a rectangular conductor placed in a semi-closed slot',Proc.IEE,1963,110.p 1656

49. SWANN,S. A.,and SALMON, J. W. : 'Effective resistance and reactance of a cylindrical conductor placed in a semi-closed slot',Proc.IEE,1962,109 C,p 611

50. BUCHHOLZ, H.: 'Die zweidimensionale stromverdrangung in ciner wechselstromdurachflossenen trapezfomigen nut',Archiv fur Electrotechnik,1965,49,p 291

51. SILVESTER, P. : 'Dynamic resistance and inductance of slot embedded conductors',Trans.IEEE, 1968,PAS-87,p250

52. BINNS, K. J. : 'The magnetic field and centring force of displaced ventilating ducts in machine cores',Proc.IEE,1960,108 C, p 64

53. SCHECHTER, M. : 'Principles of functional analysis', (Academic Press,1971)

54. SMIRNOV, V. I. : 'A course of higher mathematics', (Pergamon Press,1971)

55. SPOONER, T.,and KINNARD, I. F. : 'Surface iron losses with reference to laminated materials', Trans.AIEE,1924,43,p 262

56. SPOONER, T. : 'Squirrel cage induction motor core losses',Trans.AIEE,1924,44,p 155

57. SPOONER, T.,and KINCAID, C. W. : 'No-load induction motor core losses',Trans.AIEE,1929, 48,p 645

58. SPOONER, T. : 'Tooth pulsation in rotating machines', Trans.AIEE,1924,43,p 252

59. ALGER, P. L.,ANGST , G.,and DAVIES, E. J. : 'Stray load losses in polyphase induction machines',Trans.AIEE,1959,p 349

60. CHRISTOFIDES, N. : 'Origins of stray load losses in induction motors with cast aluminium rotors',(Ph.D. Thesis, Imperial College, London,1966)

61. McLACHLAN, N. W. : 'Bessel functions for engineers', (Oxford,1934)

62. RAMSDEN, V. S. : 'The loss in solid poles of synchronous machines on load',(Ph.D. Thesis, The University of Aston in Bimingham, 1972)

63. CARTER, F. W. : 'Pole face losses',J.IEE,1916,54,p 168

64. BALL, J. D. : 'The unsymmetrical hysteresis loop', Trans.AIEE,1915,34,p 2693

65. GIBBS, W. J. : 'Tooth ripple losses in unwound pole-shoes',J.IEE,1947,94,Part II,p 2

66. SPOONER, T. : 'Permeability',J.AIEE,1923,42,p 42

67. RUDENBERG, R. : 'Energi der wirbelstrome in elektrischen Bremen und Dynamomaschinen',(Enke, stuttgart,1906)

68. ADAMS, C. A., LANIER,A. C., and SCHOOLEY, C. O. : 'Pole face losses',Trans.AIEE,1909, p 1133

69. CONCORDIA, L.,and PORITSKY, H. : 'Synchronous machines with cylindrical rotor',Trans.AIEE, 1937,56,p 49

70. KUYPER, W. W. : 'Pole face losses in solid rotor turbine generators',Trans.AIEE,1943, 62,p 827

71. BARELLO, G. : 'Courants de Foucault engendres dans les pieces polaires massives des alternateurs par les champs tournants parasites de la reaction d'induit', Revue Generale de l'Electricite,1955, 64,p 557

72. POSTNIKOV, I.M. : 'Eddy currents in synchronous and asynchronous machines with solid rotors',Elektrichestvo,1958,10,p 7

73. BRATOLJIC, T. : 'Recent studies of stray losses in solid pole pieces of synchronous machines',The Brown Boveri Review, 1966,53,p 521

74. RICHTER, R. : 'Electische maschinen',(Birkhauser, Basl/Stuttgart,1963,Vol II)

75. LAWRENSON, P. J., REECE, P.,and RALPH, M. C. : 'Tooth ripple losses in solid poles', Proc.IEE,1966,113,p 567

76. CARTER, G. W. : 'A note on the surface loss in a laminated pole-face',Proc.IEE,1955, 102 C,p 217

77. RUDENBERG, R. : 'Electrotechnische Zeitschrift',1905, 26,p 181

78. POTIER, A. : 'L'Industrie Electrque',1905,p 35

79. WALL, T. F.,and SMITH, C.F. : 'Losses in pole shoes', Proc.IEE,1907,40,p 577

80. HANSSEN, I. E. : 'Calculation of iron loss in dynamo electric machinery',Trans.AIEE,1909

81. BONDI, H.,and MUKHERJI, K.C. : 'An analysis of tooth ripple phenomena in smooth laminated pole-shoes',Proc.IEE,1957,104 C,p 349

82. GREIG, J.,and MUKHERJI, K.C. : 'An experimental investigation of tooth ripple flux pulsation in smooth laminated pole-shoes',Proc.IEE,1957,104 C,p 332

83. GREIG, J.,and SATHIRAKUL, K. : 'Pole face losses in alternators',Proc.IEE,1961,108 C,p 130

84. GREIG, J.,and FREEMAN, E. M. : 'Simplified presentation of the eddy current loss equation for laminated pole shoes',Proc.IEE,1963, 110,p 1255

85. GREIG, J., BEEVERS, C. L.,and FFOULKES, T. H. O. : 'Tooth ripple losses in electrical machines',Proc.IEE,1971,118,p 1269

86. SPOONER, T. : 'Effect of a superposed alternating field on apparent magnetic permeability and hysteresis loss',J.IEE,1923,42,p527

87. CHARLTON, O. E.,and JACKSON, J. E. : 'Losses in iron under the action of superposed alternating and direct current excitations', Trans.AIEE,1925,44,p 824

88. CHALMERS, B. J.,and SARKAR, B. R. : 'An inverted induction motor set for fundamental studies',The Engineer,1968

89. BURKE, P.E.,and ALDEN, R. T. H. : 'Current density probes',Trans.IEEE,1969,PAS-88,p 181

90. THOMPSON, W. G.,and LEDBETTER, J. : 'Precision dynamometry in testing electrical machines',G.E.C. Journal,1965,32,p 38

91. IVANOV-SMOLENSKY, A. V., and MNATSAKANIAN, M. C. : 'An analytical method of calculating the air gap magnetic field of electrical machines with slotted stator', Elektrichestvo,1972,3,p 57(In - Russian)

92. RAWCLIFFE, G. H.,and MENON, A. M. : 'A simple new test for harmonic frequency losses in a.c. machines',Proc.IEE,1952,98,Part II, p 145

93. ALGER, P. L.,and EKSERGIAN, R. : 'Induction motor core losses',J.AIEE,1920,39,p 906

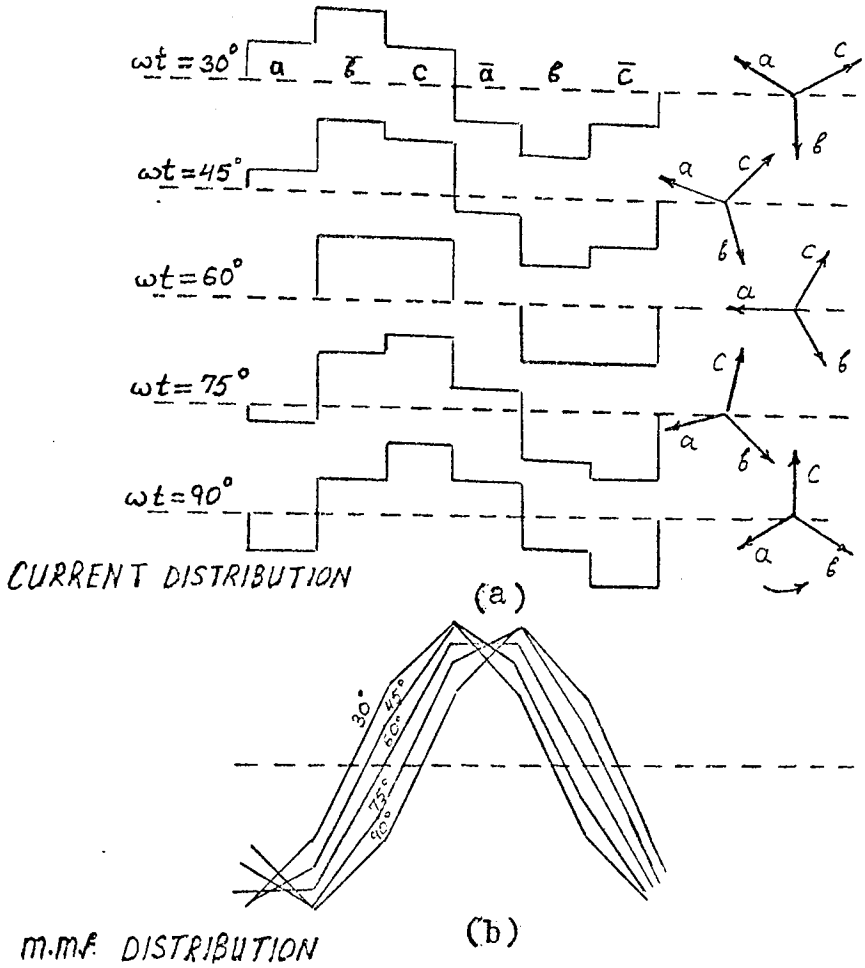

Fig 2.1

Diagrams of stator space current and m.m.f.distributions at five instants of time, for 3-phase, 60° belt, full pitch, infinitely distributed windings

(Reproduced from Alger's book [7])

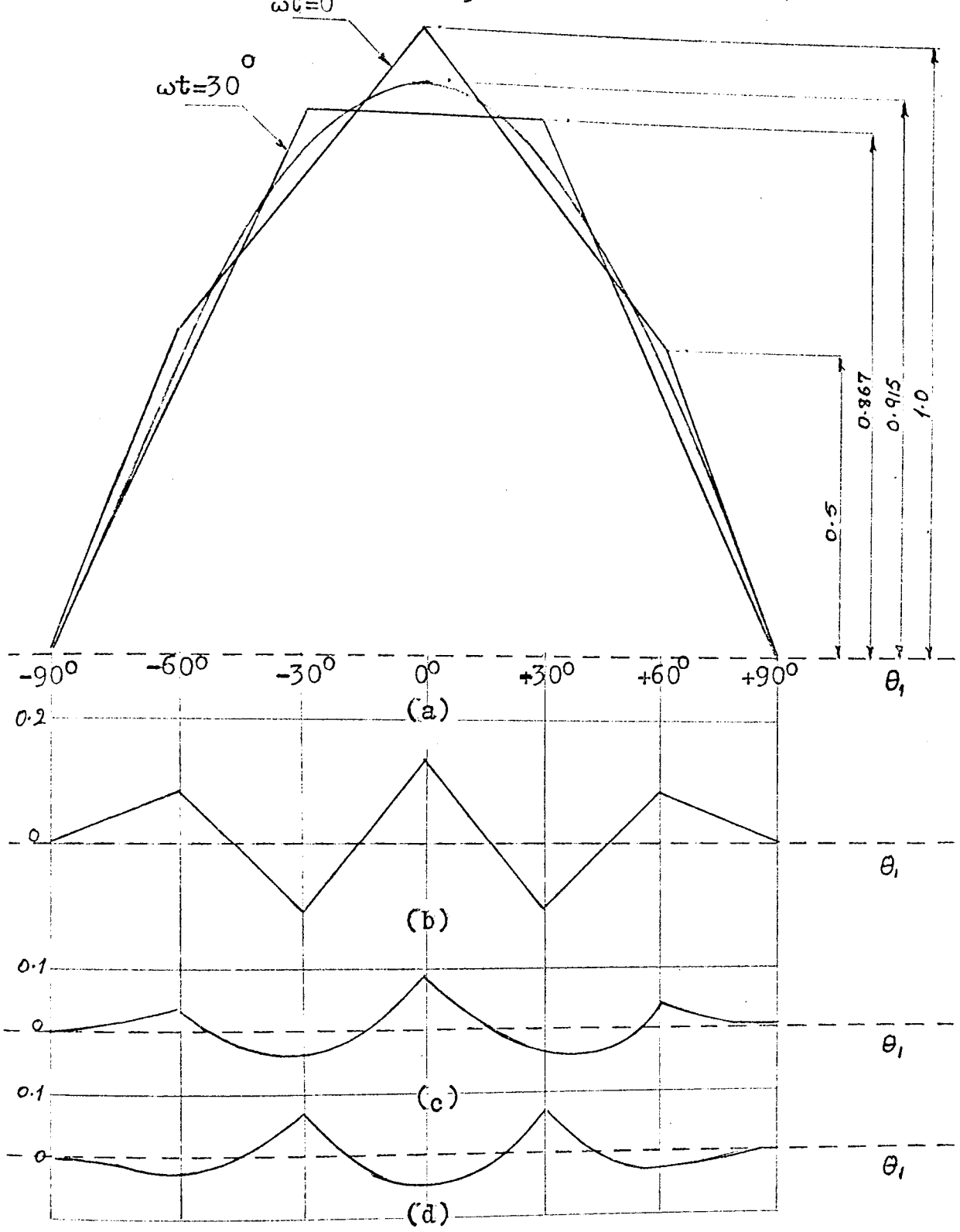

Fig 2.2

(a)-Two m.m.f. waves at $\omega t=0^\circ$ and $\omega t=30^\circ$ with the fundamental superimposed.
(b)-The difference between stator m.m.fs. at $\omega t=0^\circ$ and $\omega t=30^\circ$.
(c)-The difference between stator m.m.fs. at $\omega t=0^\circ$ and the fundamental.
(d)-The difference between stator m.m.fs. at $\omega t=30^\circ$ and the fundamental.

(For 3-phase, 60° belt, full pitch, and infinitely distributed windings and zero slip)

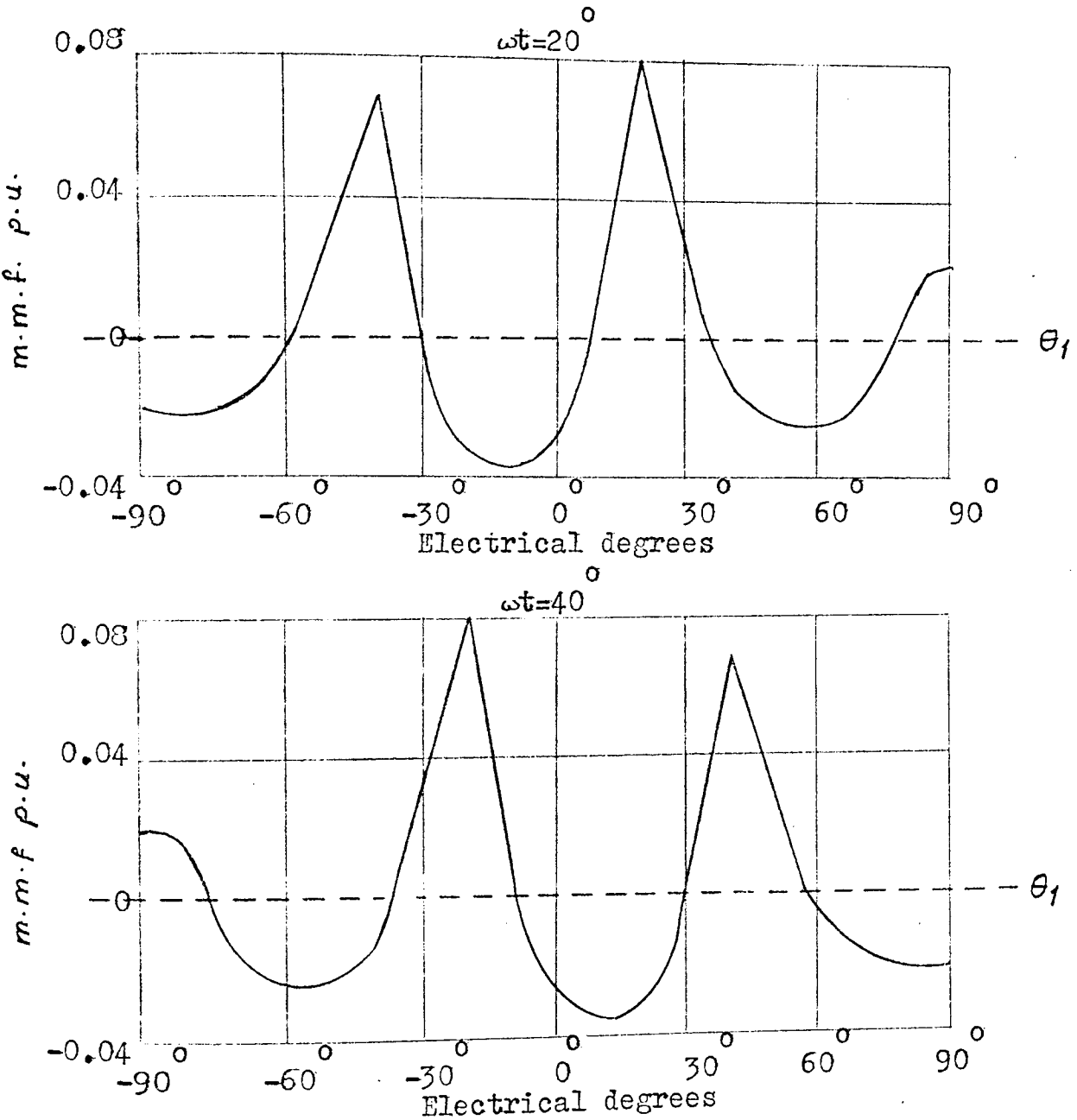

Fig 2.3

The difference between stator m.m.fs. and the fundamental at $\omega t=20^{\circ}$ and $\omega t=40^{\circ}$
(For 3-phase, 60° belt, full pitch, and infinitely distributed windings and zero slip)

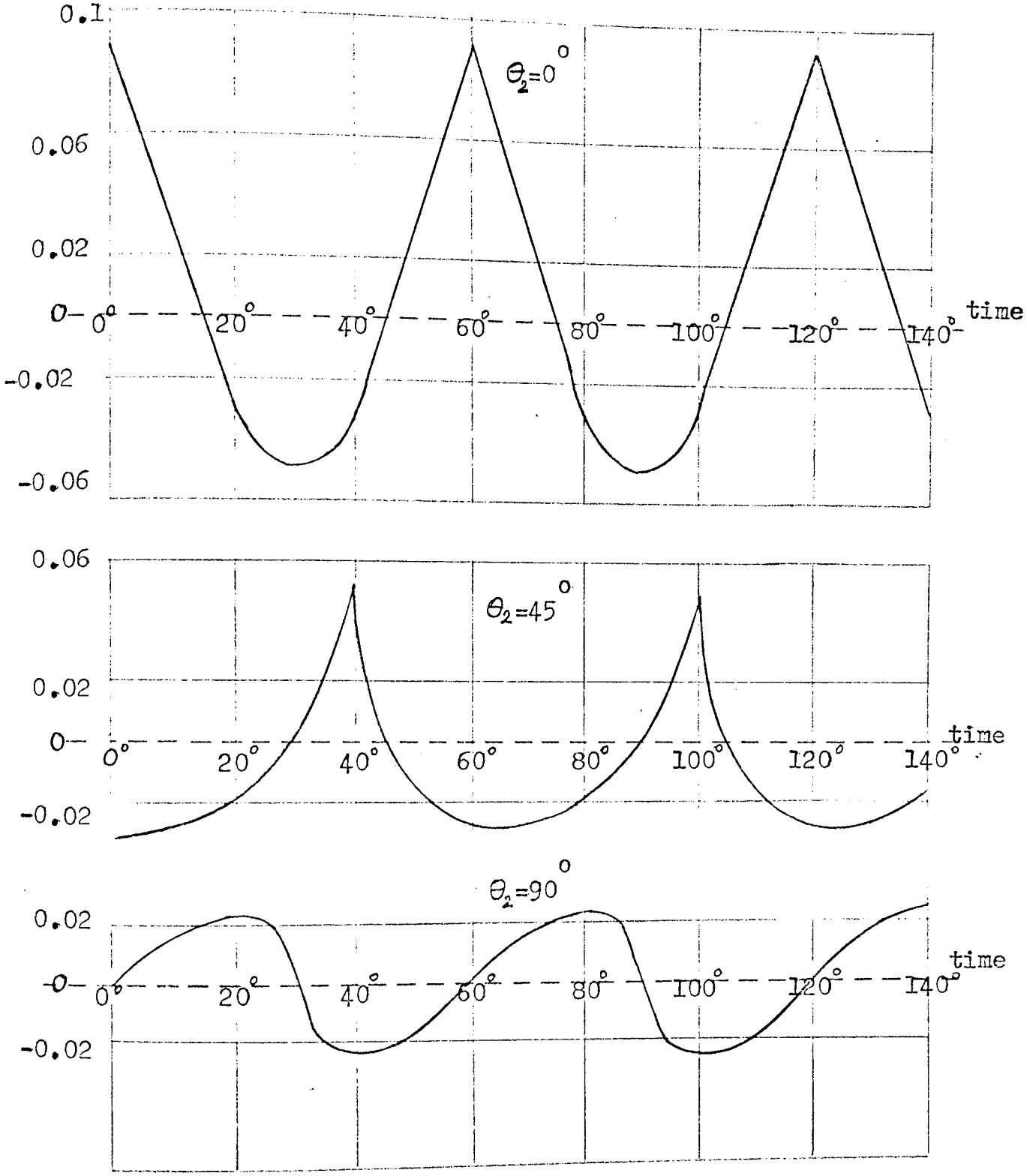

Fig 2.4

m.m.f. distributions at 3 points on rotor surface, $\theta_2=0^o$, $\theta_2=45^o$, and $\theta_2=90^o$, for 3-phase, 60^o belt, full pitch infinitely distributed windings and zero slip

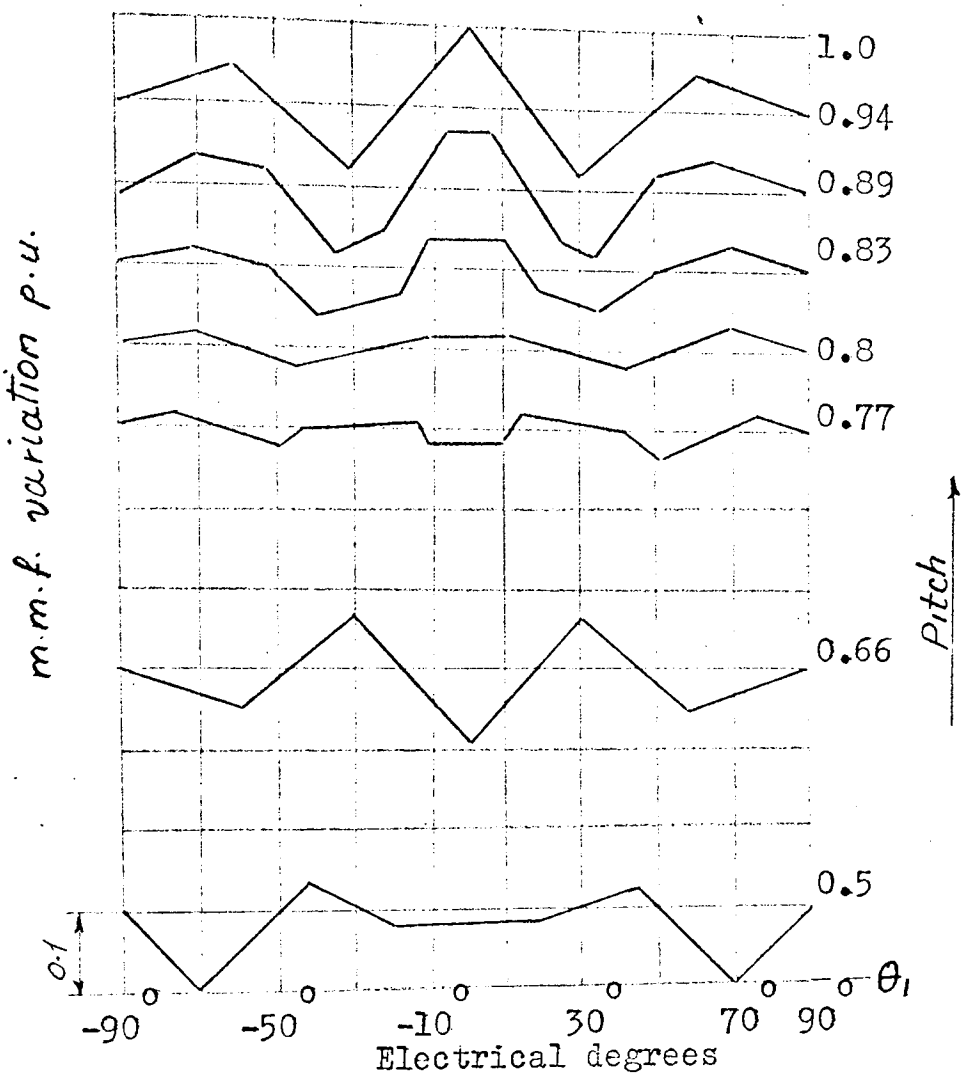

Fig 2.5

The difference between two stator m.m.fs. at $\omega t=0^{o}$ and $\omega t=30^{o}$, for 3-phase, 60^{o} belt, infinitely distributed windings with various pitches

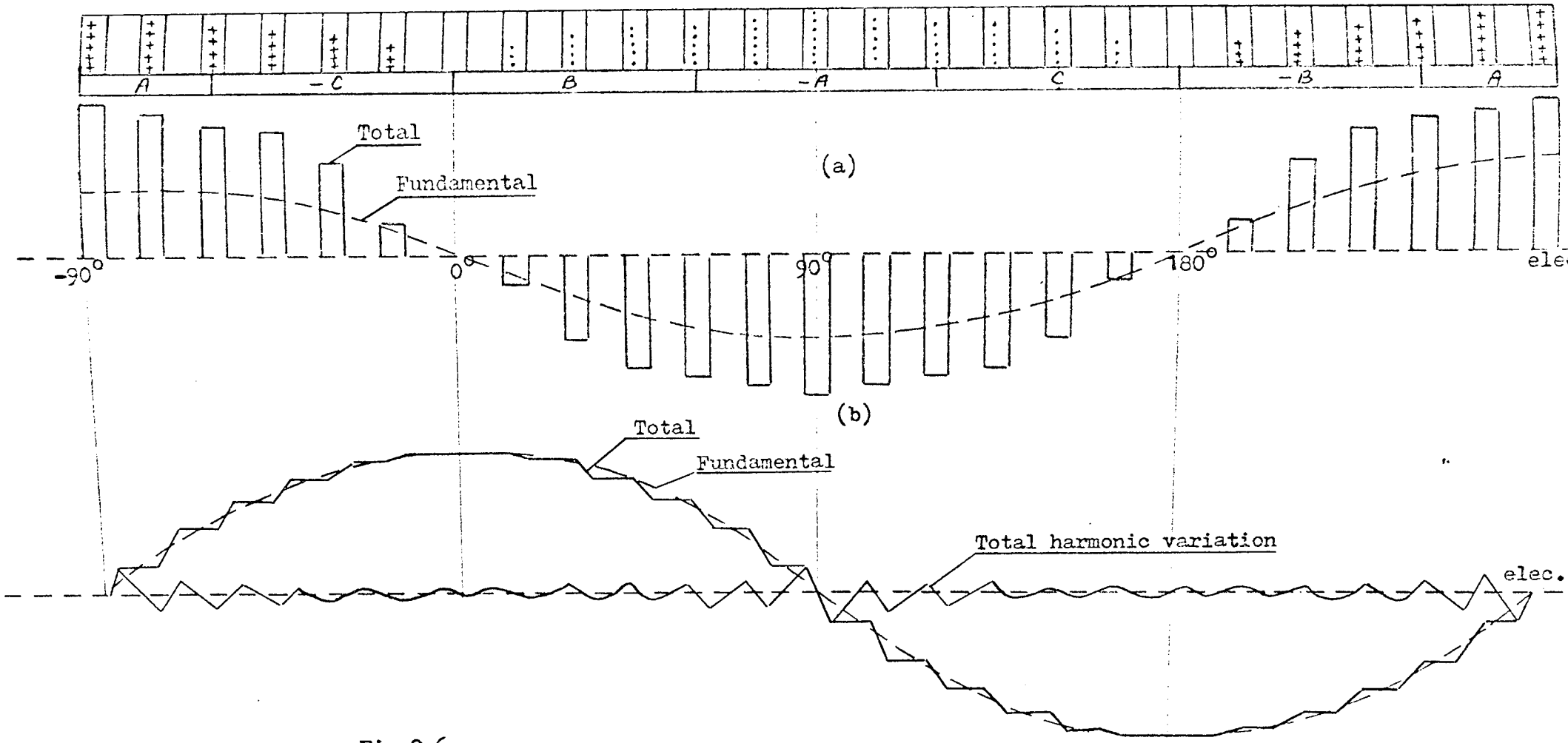

Fig 2.6

A diagram of pulses and steps in stator current loading and m.m.f. waves

(a)current loading

(b)m.m.f.

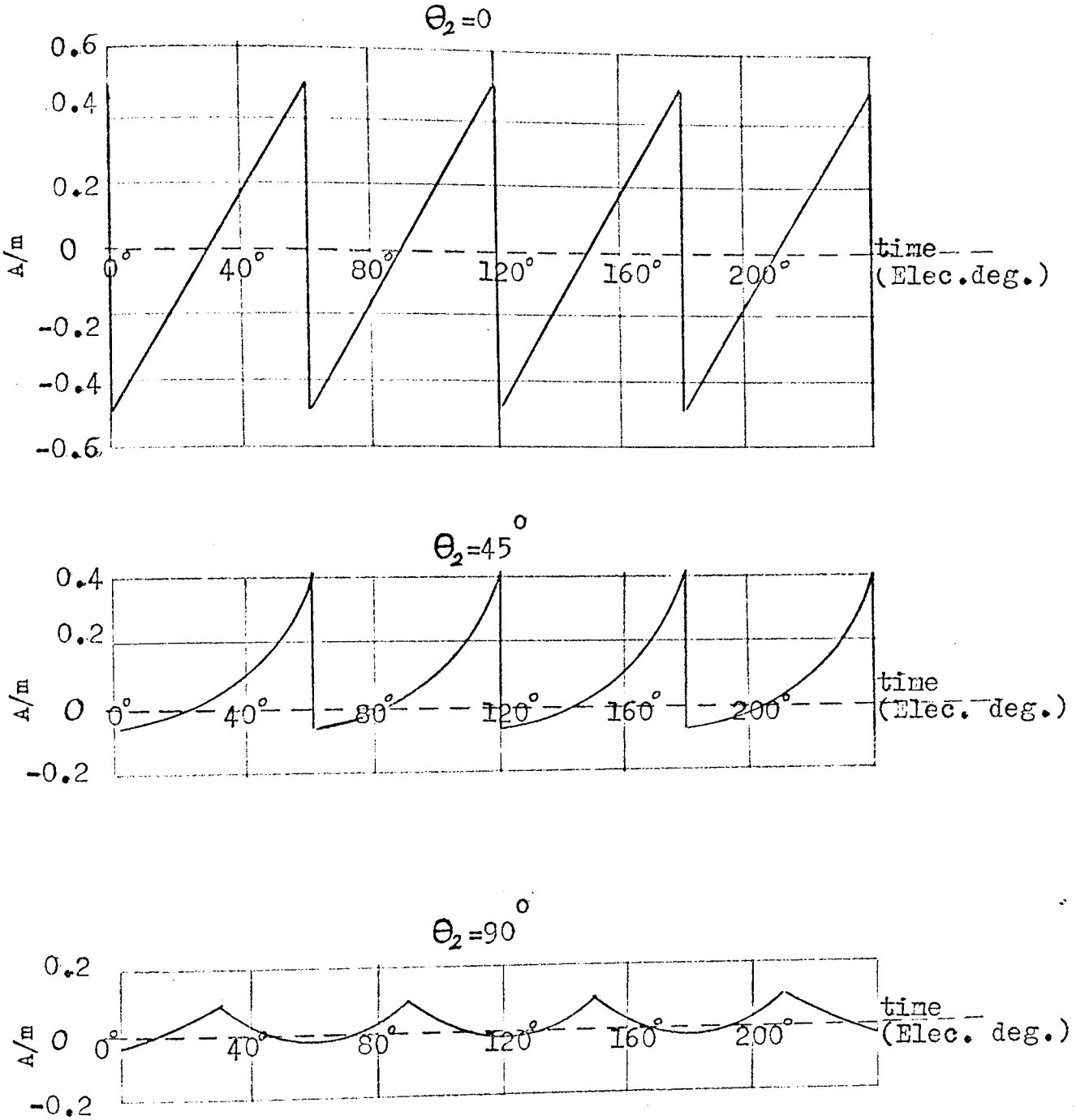

Fig 2.7

Variation of rotor current loading with time at three points $\theta_2 = 0°$, $\theta_2 = 45°$, and $\theta_2 = 90°$, for 3-phase, 60° belt and infinitely distributed stator winding and zero slip

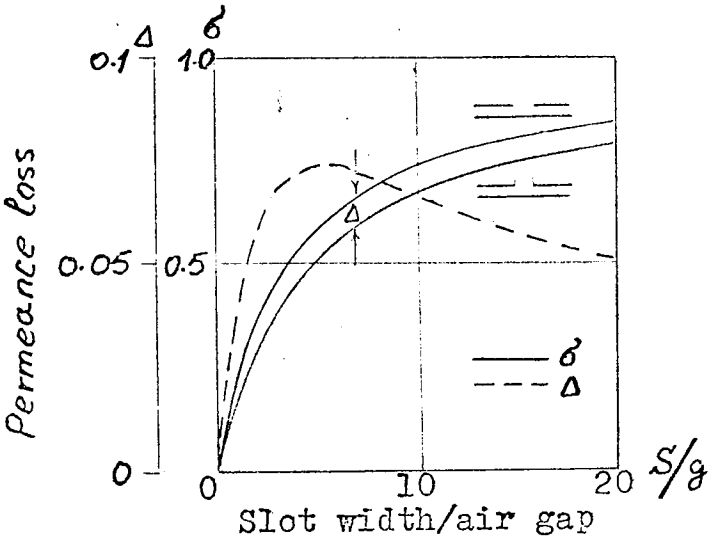

(a)

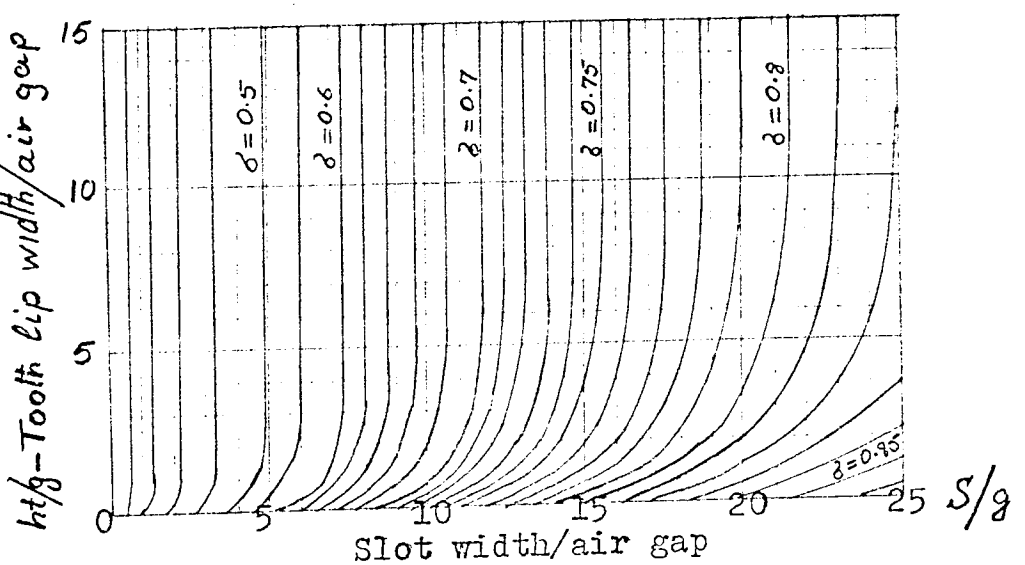

(b)

Fig 3.5

(a)-Permeance loss corresponding to Fig 3.4(a) and Fig 3.4(c)

(b)-Permeance loss corresponding to Fig 3.4(b)

(Reproduced from Morath's paper[30])

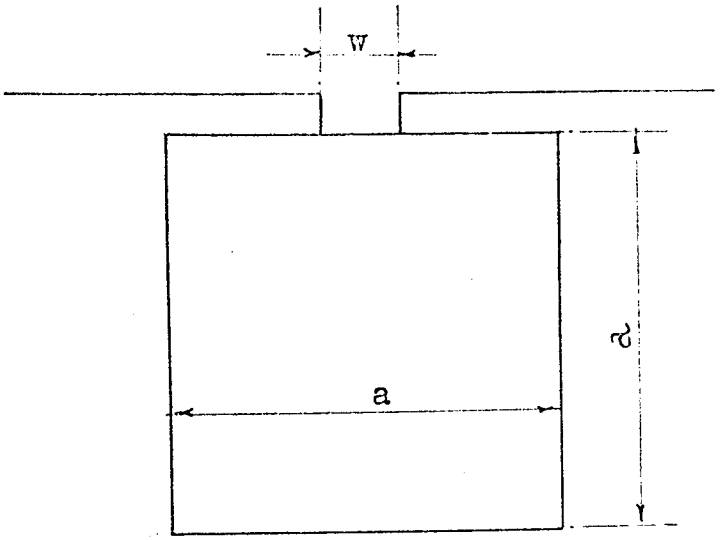

Slot-embedded conductor

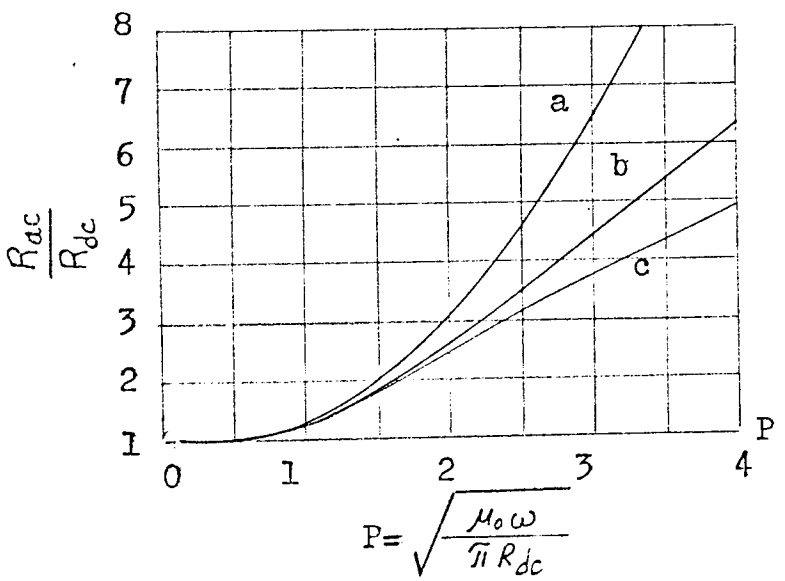

Fig 3.6

Calculated resistance ratios for slot opening ratios w/a of:curve a,one-seventh :curve b,four-sevenths;curve c,fully open slot.

(Reproduced from Silvester's paper[51])

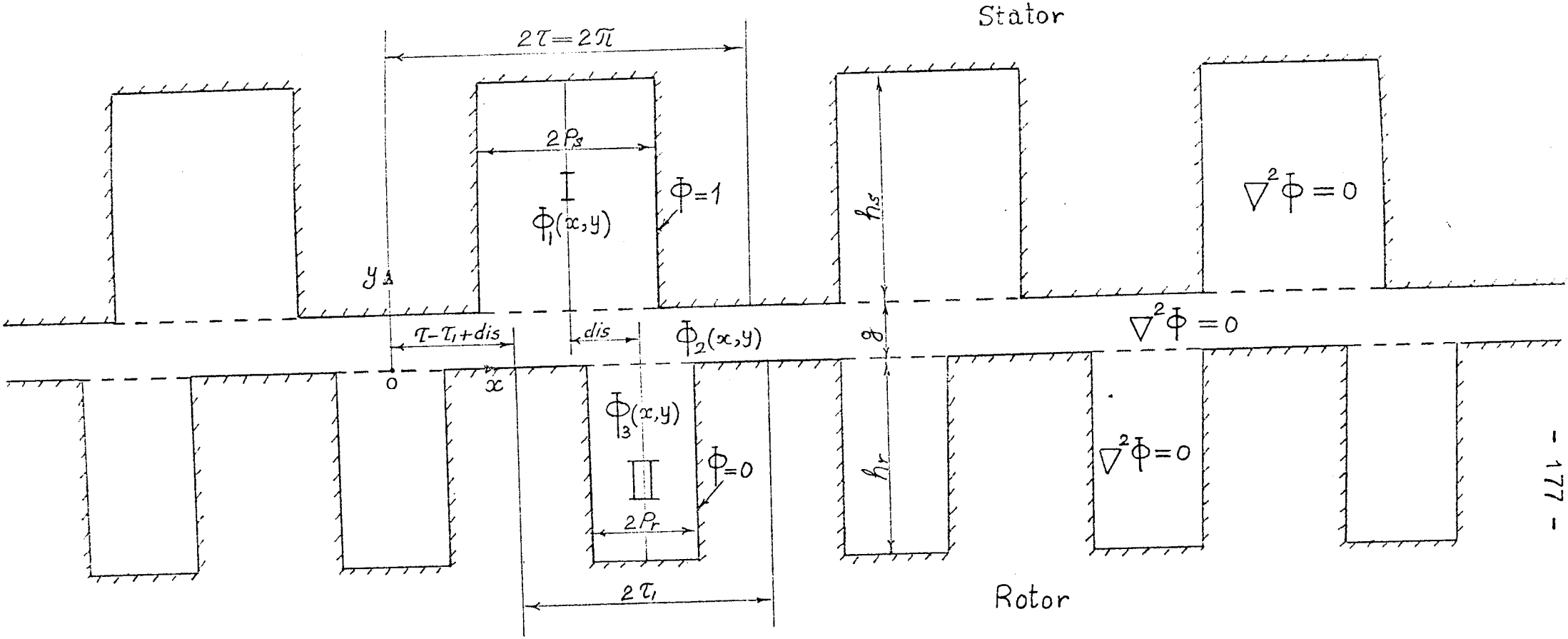

Fig 4.1

A typical simplified geometry of a doubly slotted air gap

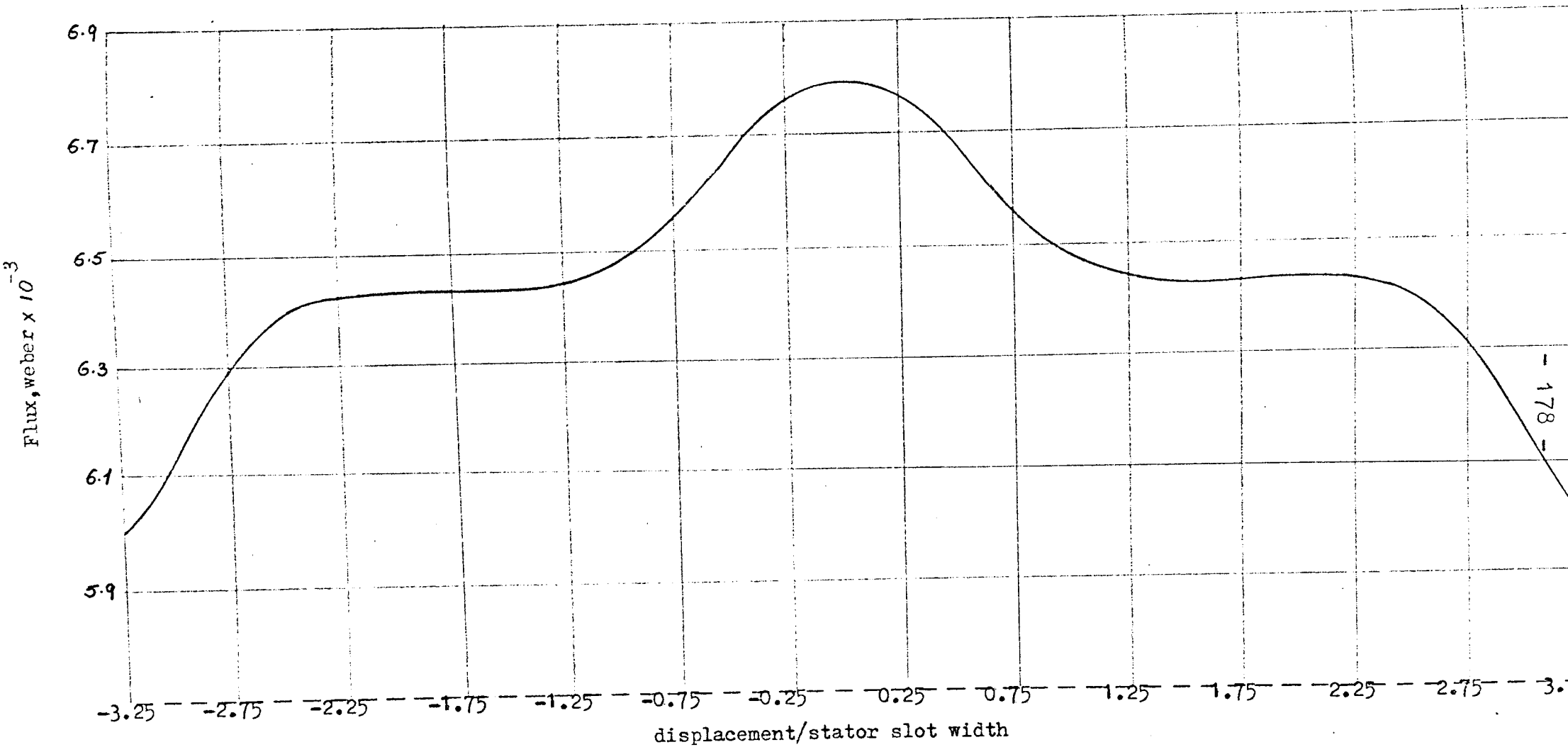

Fig 4.2 Computed variation of the total rotor tooth flux, for $S_2/S_1 = 1$, and $\tau_1/\tau = 1.1$

S_1 -stator slot width
S_2 -rotor slot width
τ -stator slot pitch
τ_1 -rotor slot pith

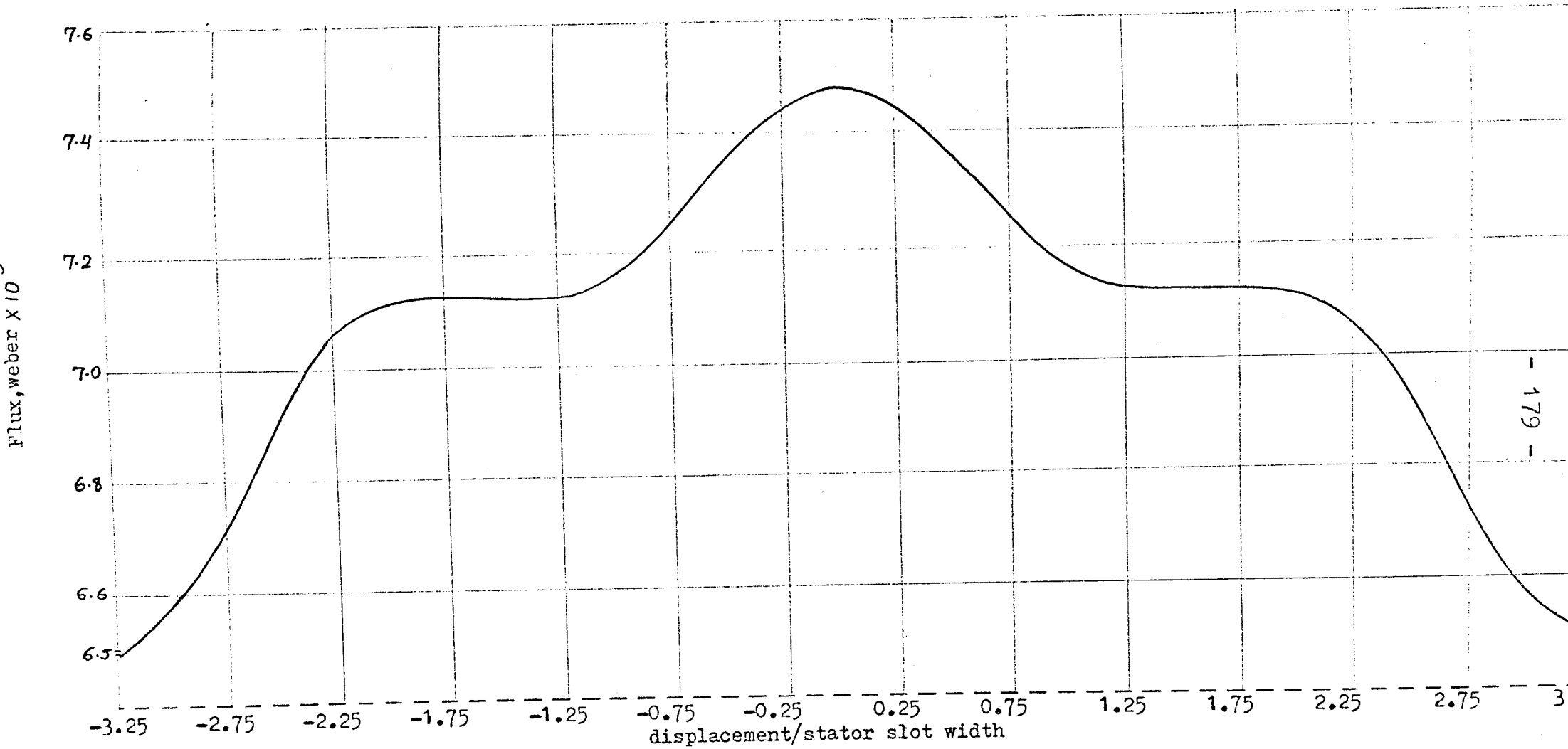

Fig 4.3 Computed variation of the total rotor tooth flux, for $S_2/S_1 = 1$, and $\tau_1/\tau = 1.2$

S_1 - stator slot width

S_2 - rotor slot width

τ - stator slot pitch

τ_1 - rotor slot pitch

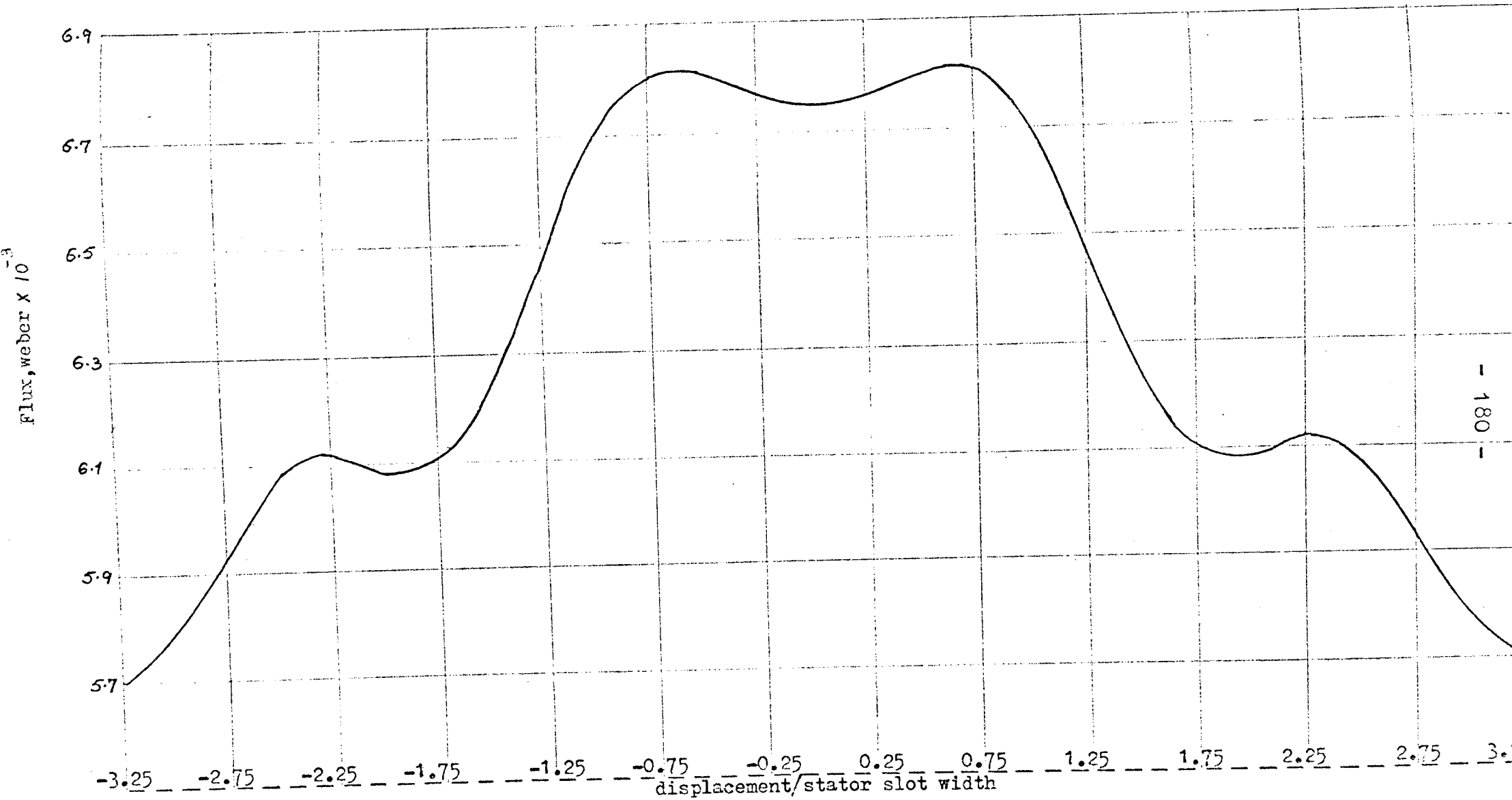

Fig 4.4 Computed variation of the total rotor tooth flux, for $S_2/S_1 = 3$, and $\tau_1/\tau = 1.2$

S_1 - stator slot width

S_2 - rotor slot width

τ - stator slot pitch

τ_1 - rotor slot pitch

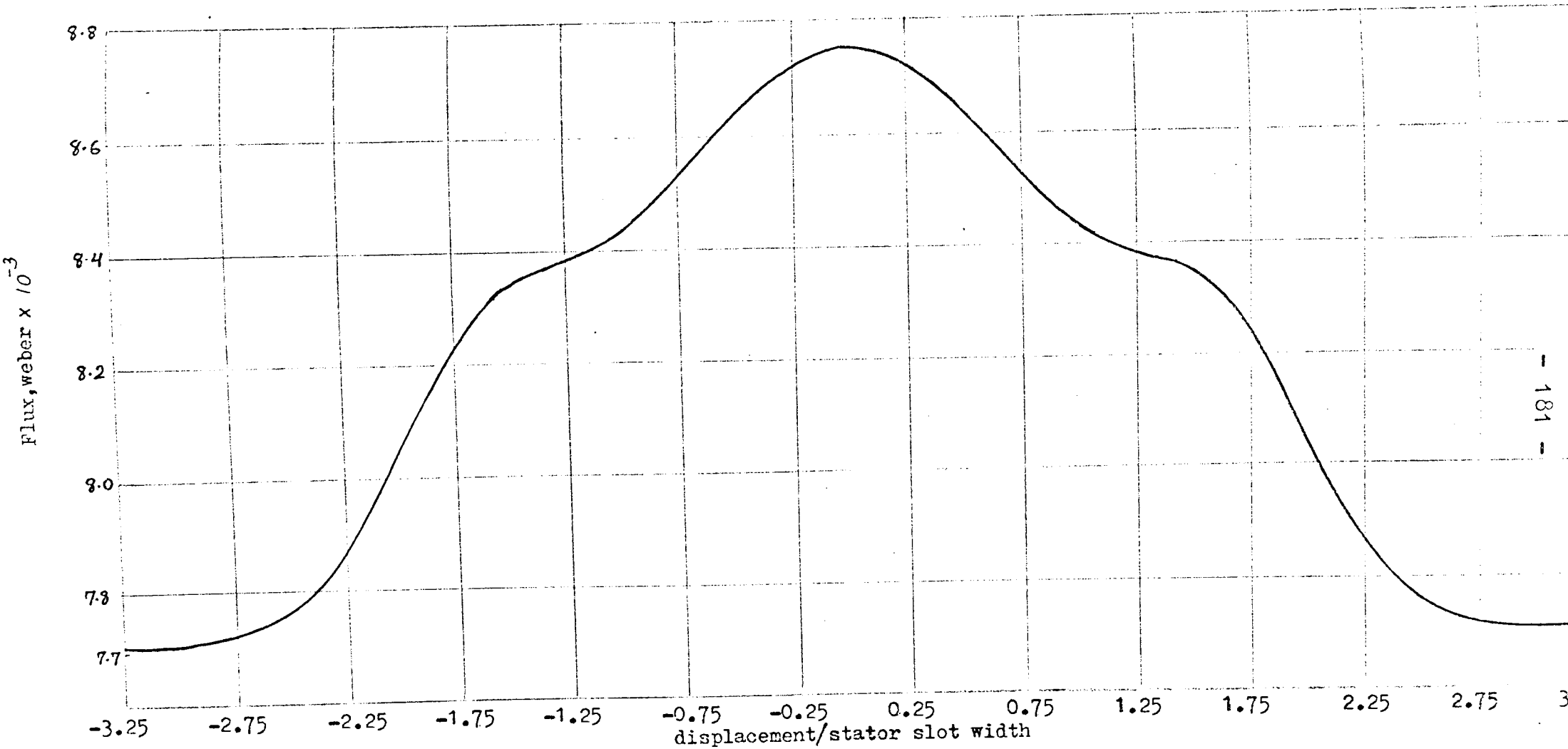

Fig 4.5 Computed variation of the total rotor tooth flux, for $S_2/S_1 = 1$, and $\tau_1/\tau = 1.4$

S_1-stator slot width
S_2-rotor slot width
τ-stator slot pitch
τ_1-rotor slot pitch

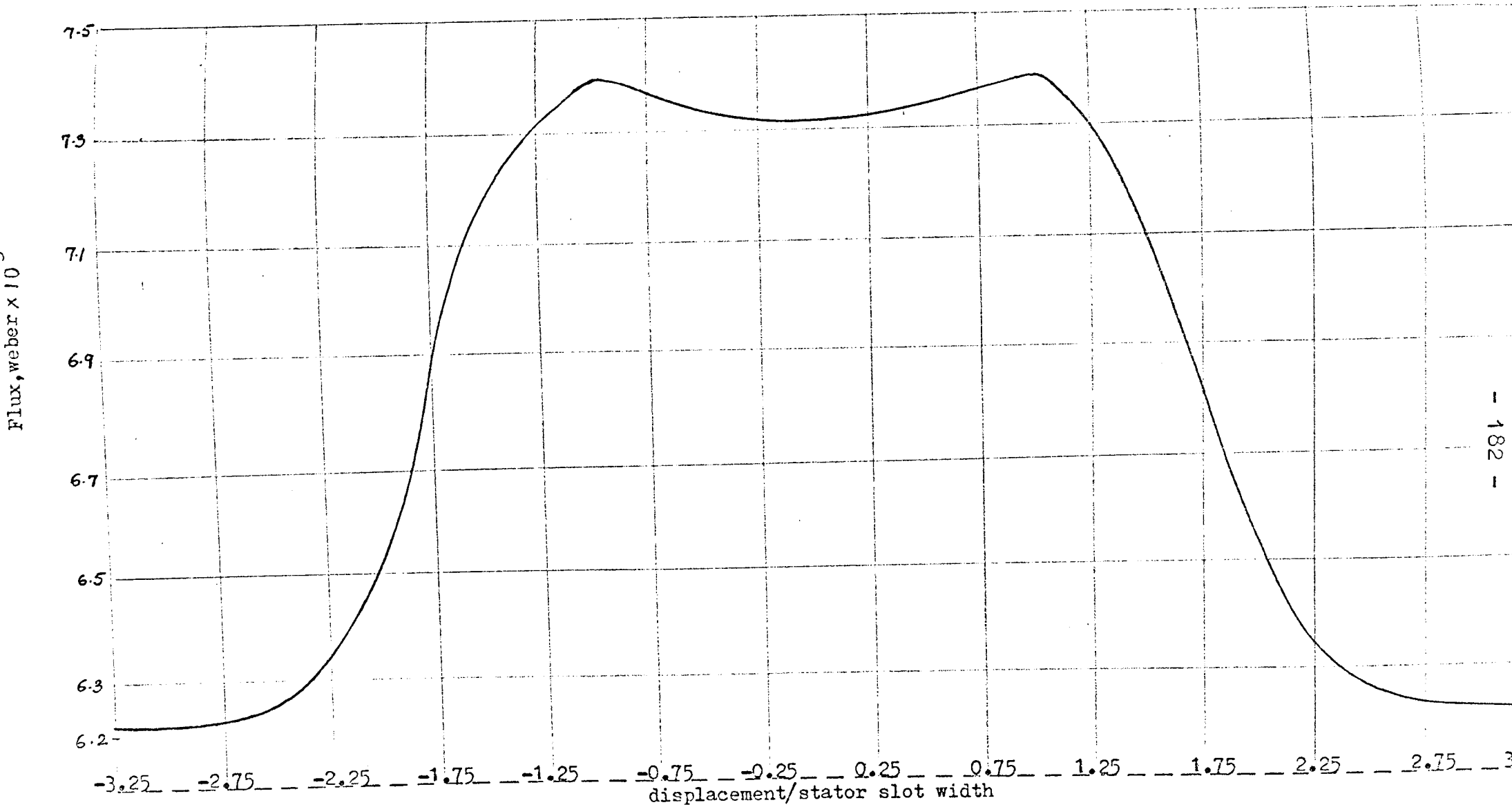

Fig 4.6 Computed variation of the total rotor tooth flux, for $S_2/S_1 = 3$, and $\tau_1/\tau = 1.4$

S_1 - stator slot width

S_2 - rotor slot width

τ - stator slot pitch

τ_1 - rotor slot pitch

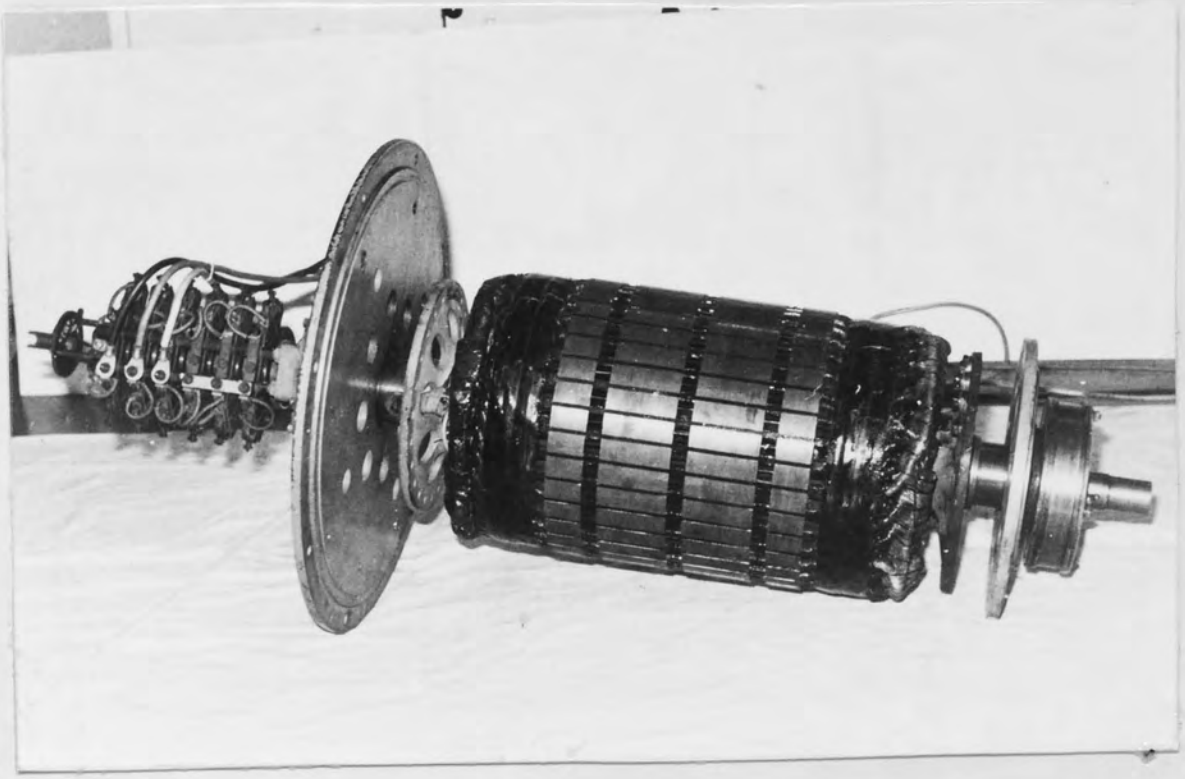

Fig 6.1

A photograph of the primary member
of the experimental machine

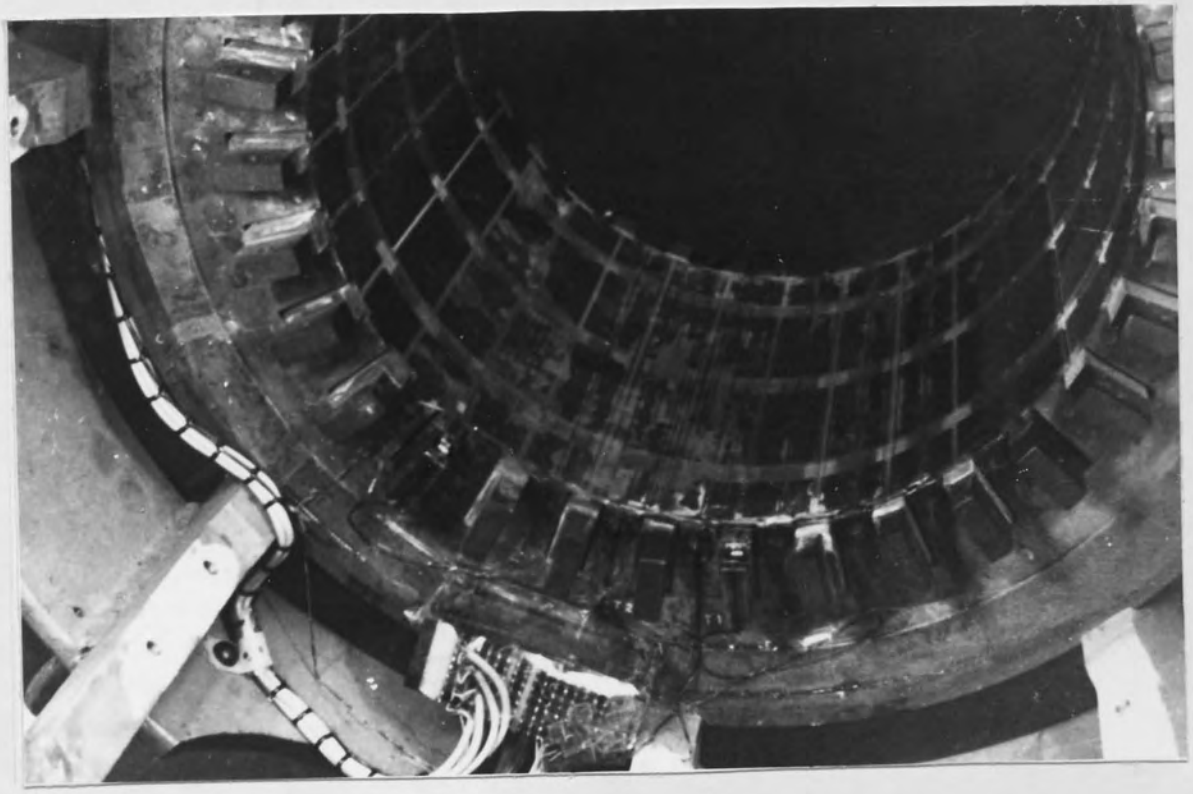

Fig 6.2

A photograph of the secondary member
of the experimental machine

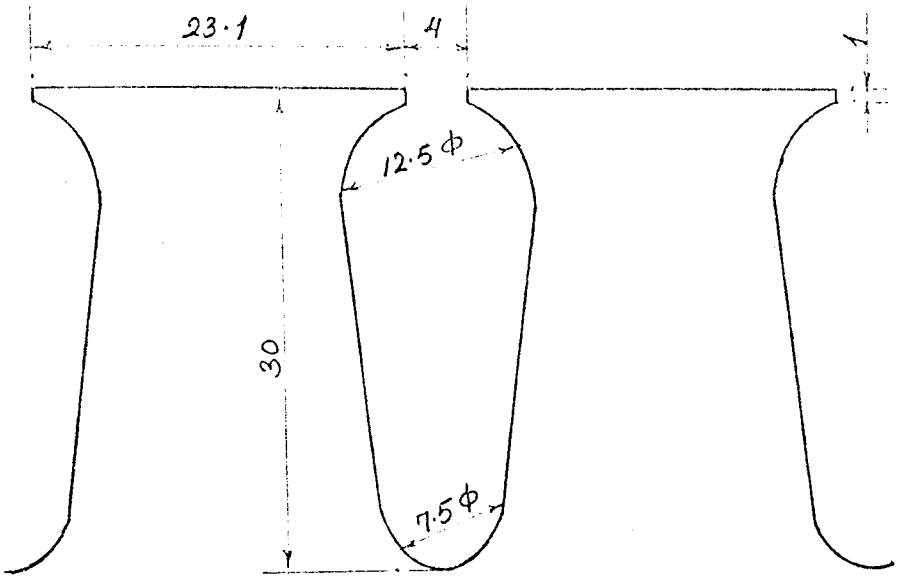

Dimensions in mm

Fig 6.3

Tooth and slot configuration of the primary member

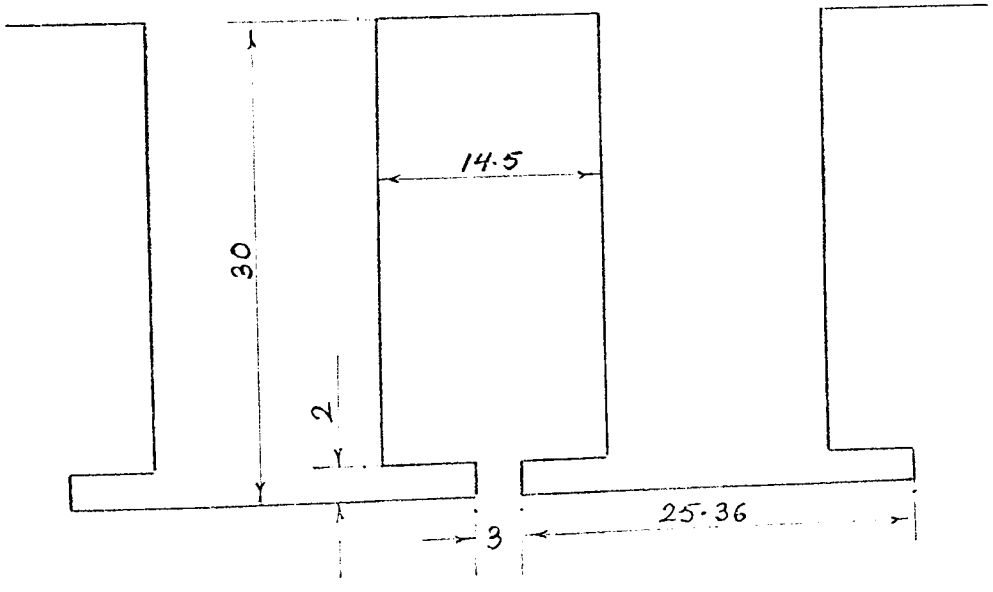

Dimensions in mm

Fig 6.4

Tooth and slot configuration of the secondary member

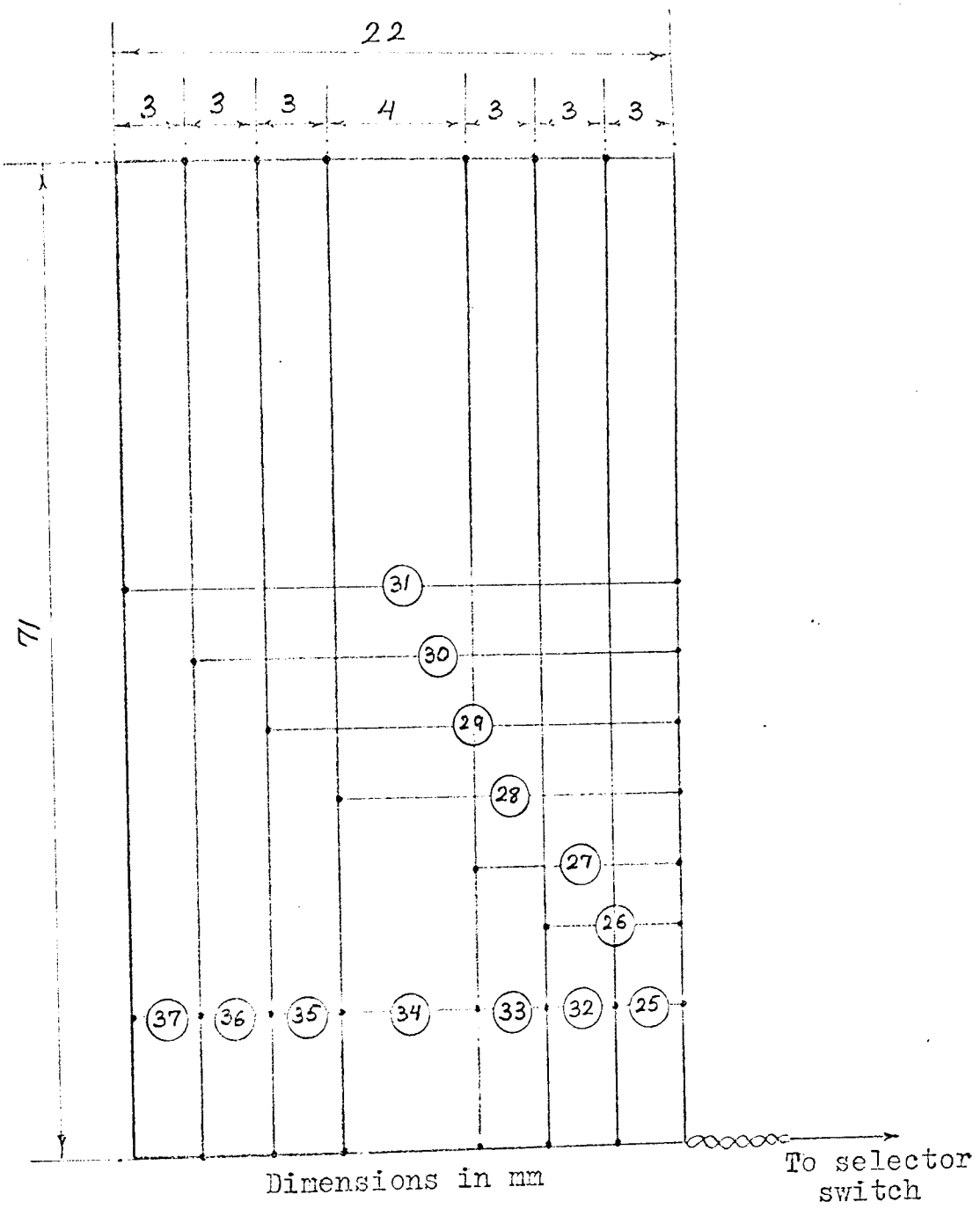

Fig 6.5

Secondary tooth surface search coils
(Encircled figures correspond to the number of search coils)

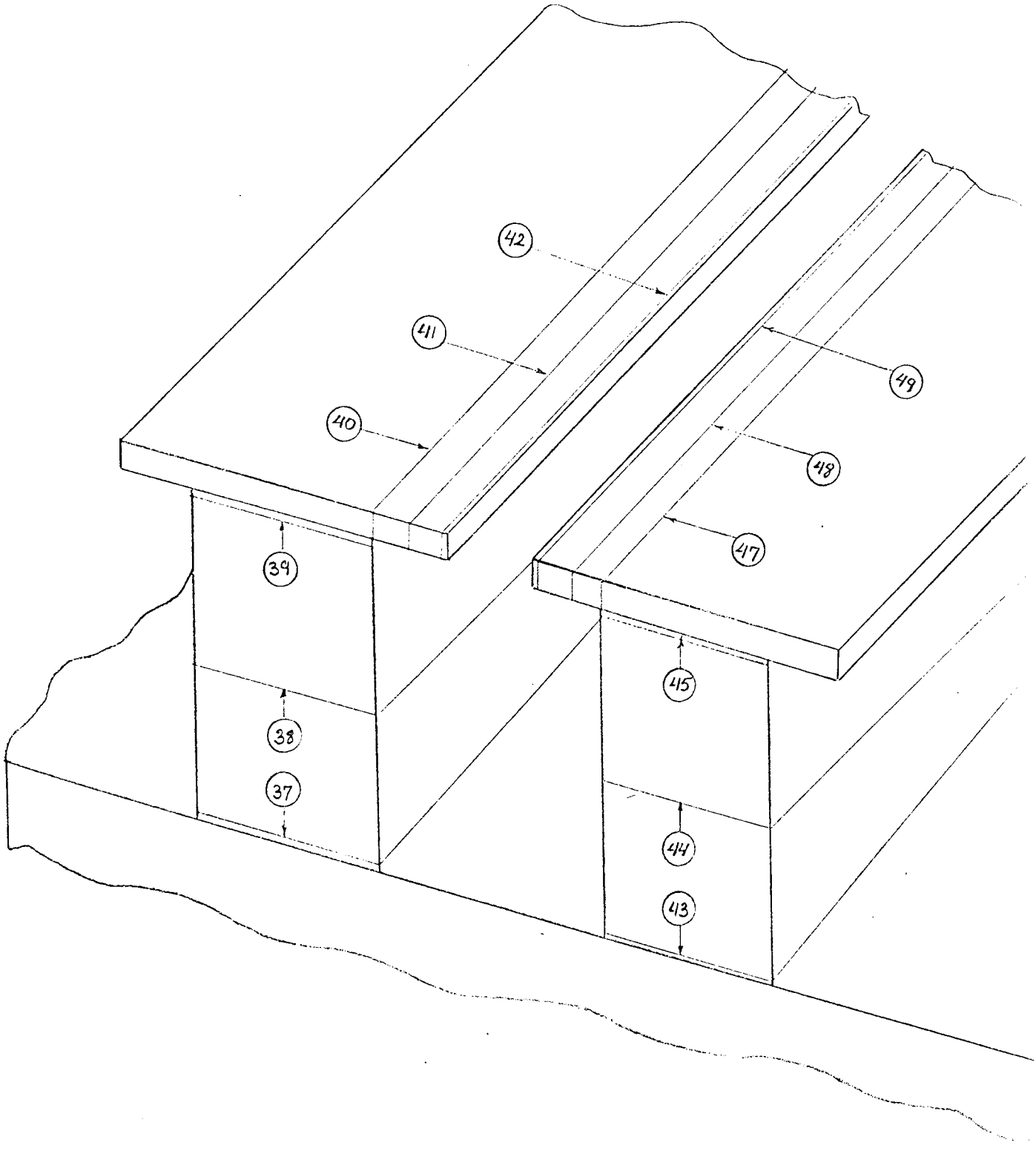

Fig 6.6

Secondary tooth and tooth lip search coils

(Encircled figures correspond to the number of search coils)

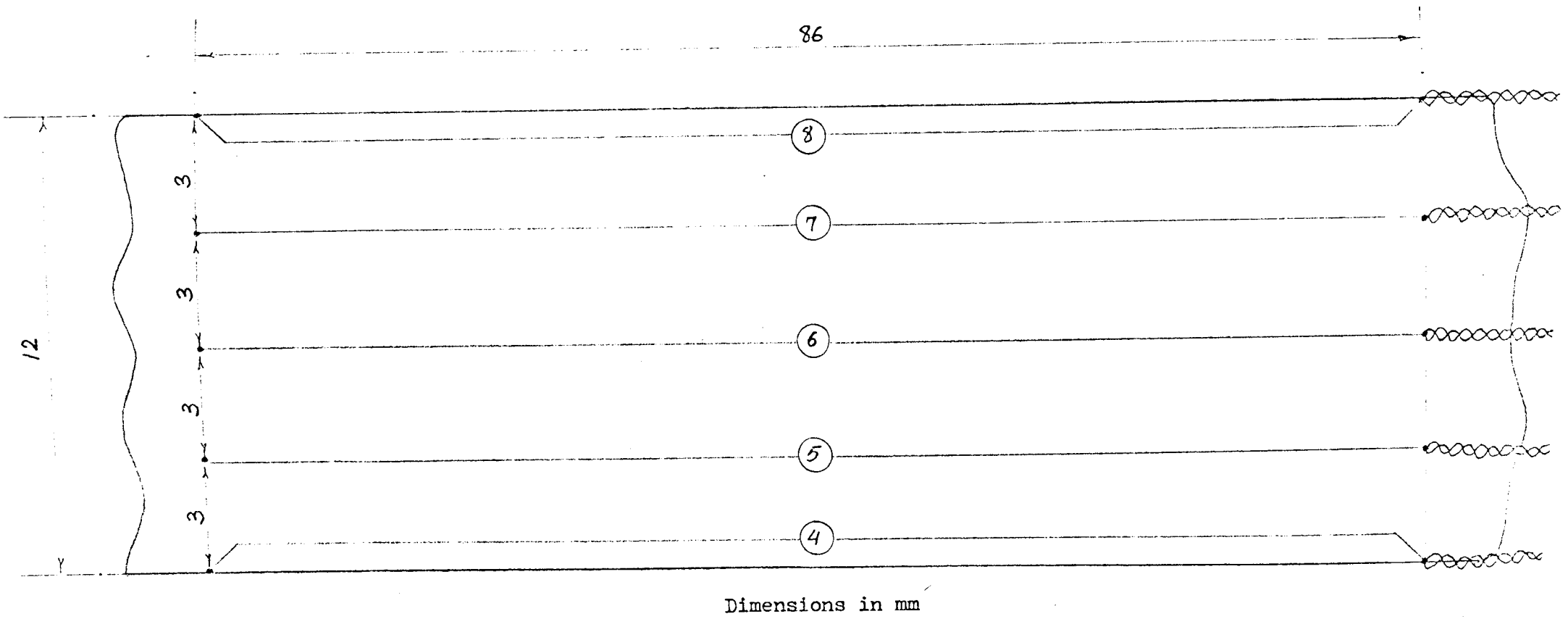

Dimensions in mm

Fif 6.7 Locations of the J-probes on the top surface of the secondary bar

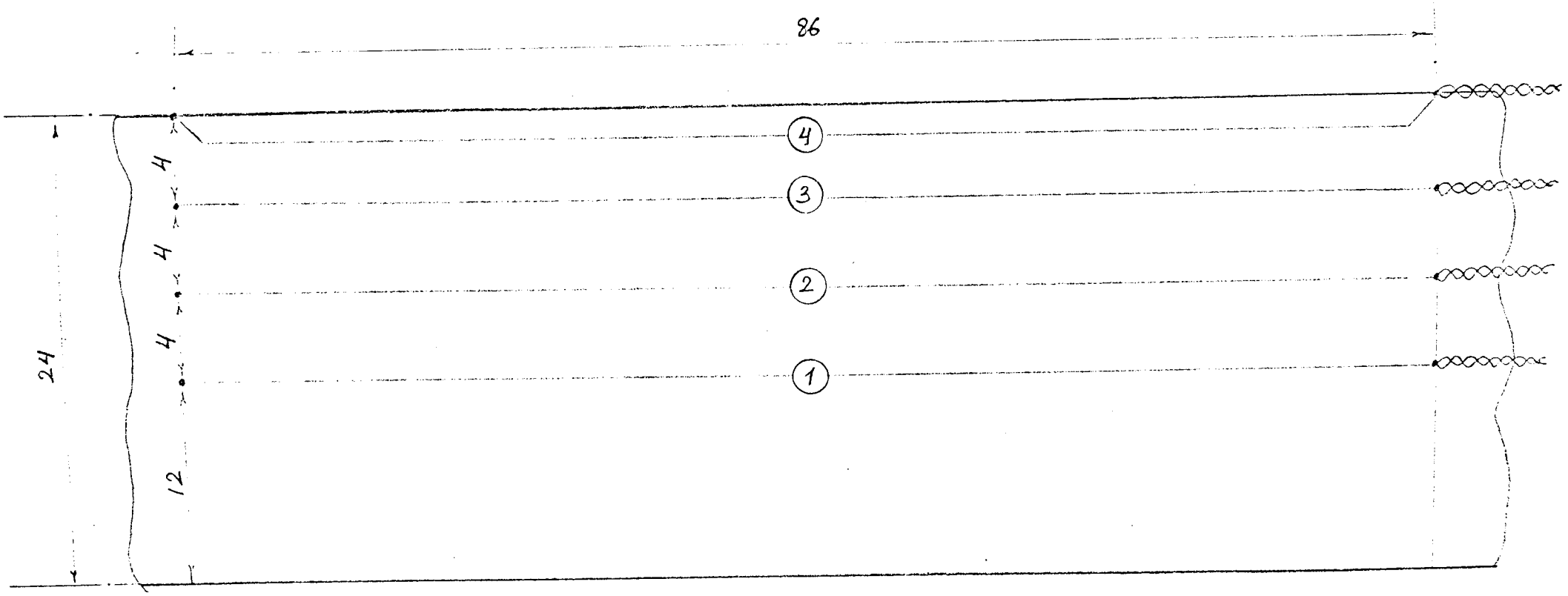

Dimensions in mm

Fig 6.8 Locations of the J-probes on the side surface of the secondary bar

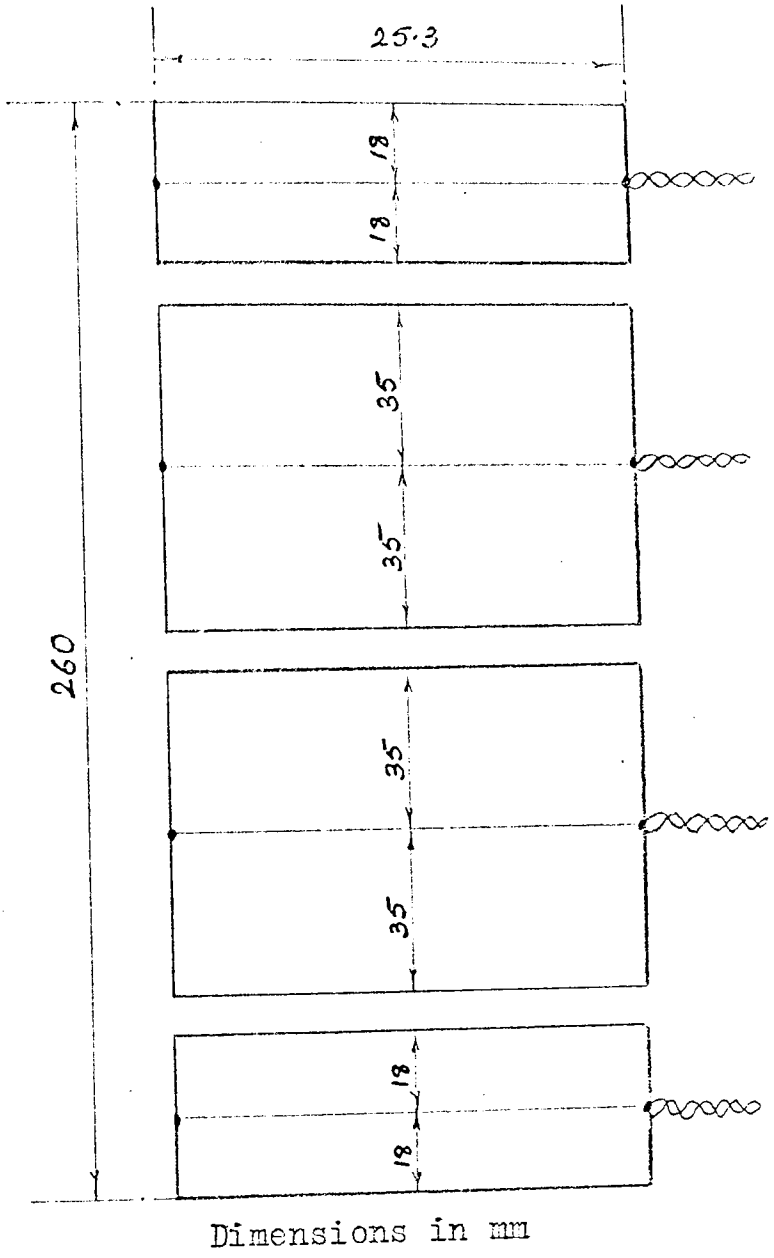

Fig 6.9

Locations of the four J-probes on the surface of the secondary core stack

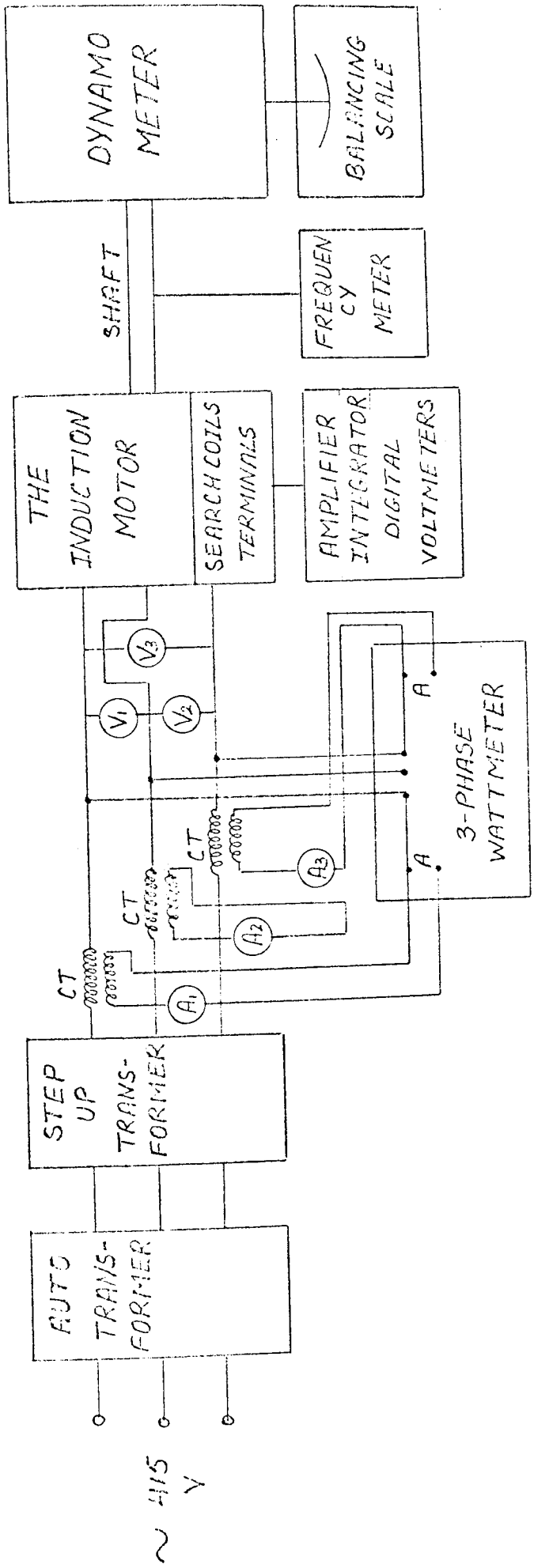

Fig 6.10 General diagram of the instrumentation circuit

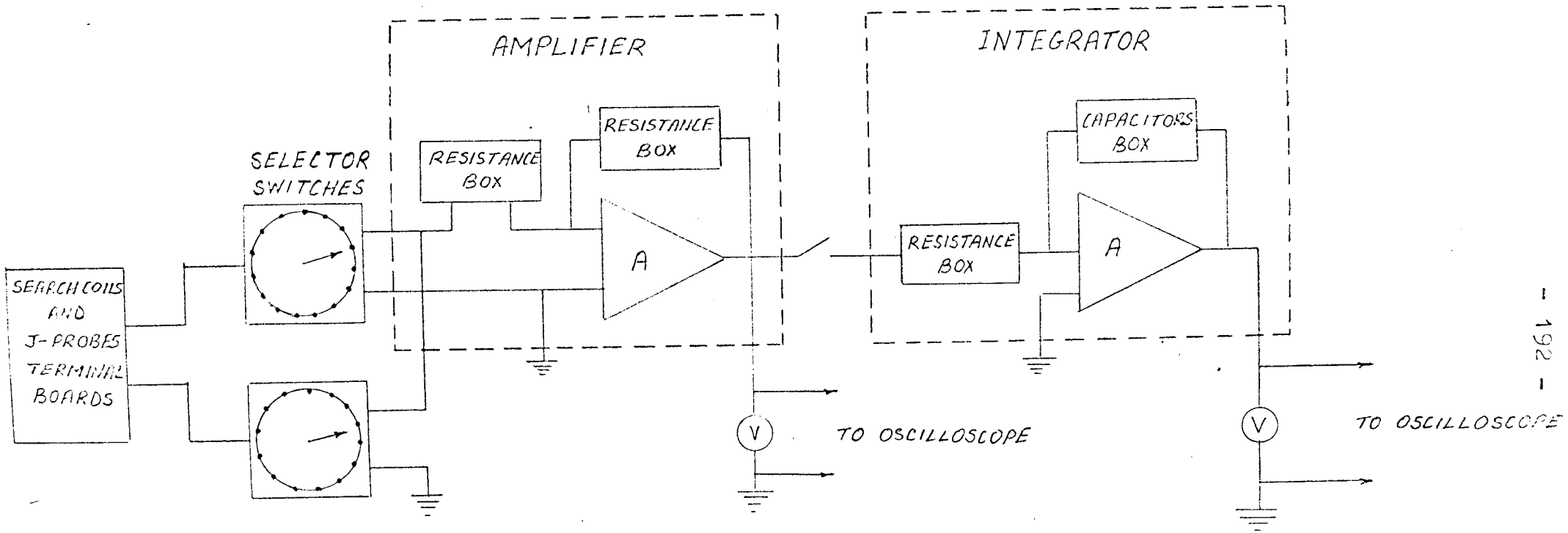

Fig 6.11

Circuit diagram for the measurement of secondary flux and bar current density components

(a)

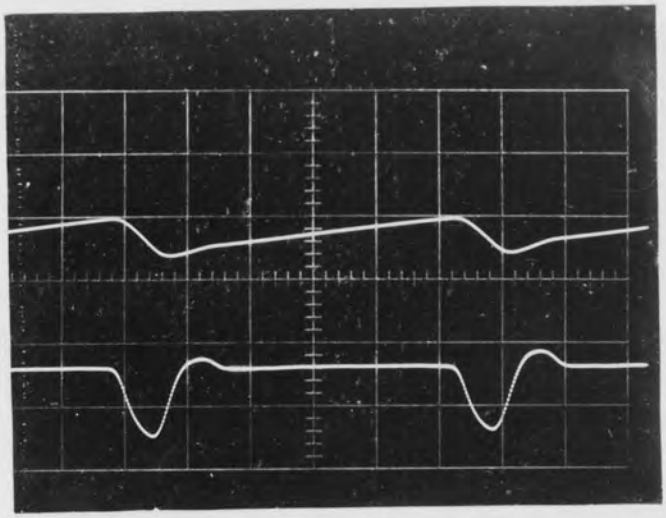

Total harmonic variation at the zero position of the fundamental

Scales:

Top curve(flux wave)	0.05 mWb/cm
Bottom curve(e.m.f.)	1.0 V/cm
Time base	2 ms/cm
Sweeping magnification	10
e.m.f. amplification	100

(b)

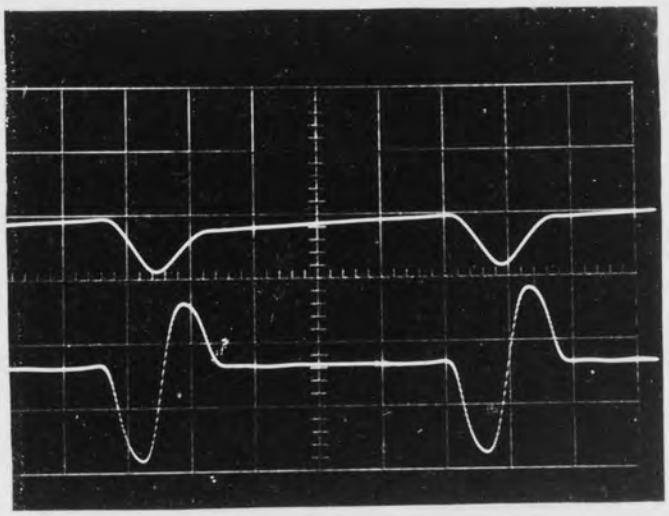

Total harmonic variation at the peak position of the fundamental

Scales:

Top curve(flux wave)	0 05 mWb/cm
Bottom curve(e.m.f.)	1.0 V/cm
Time base	2 ms/cm
Sweeping magnification	10
e.m.f. amplification	100

Fig 7.1 Oscillograms of search coil 25 taken at synchronous speed, 300 V applied line voltage and disconnected cage

(SECONDARY SURFACE SEARCH COIL)

(a)

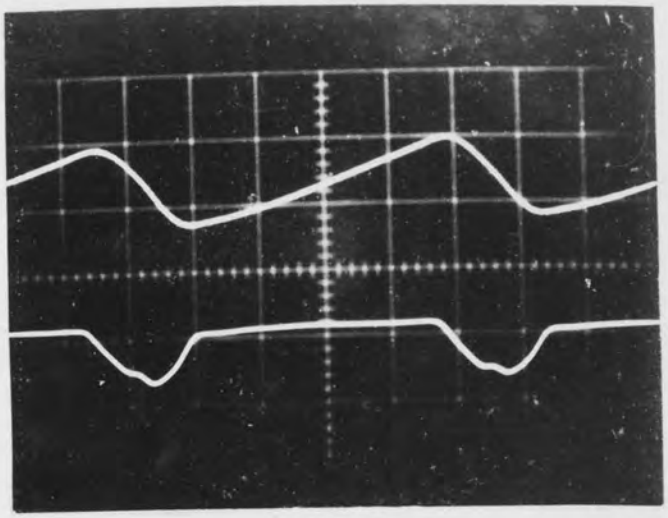

Total harmonic variation at the zero position of the fundamental

Scales:

Top curve(flux wave)	0.05	mWb/cm
Bottom curve(e.m.f.)	0.5	V/cm
Time base	2	ms/cm
Sweeping magnification	10	
e.m.f. amplification	50	

(b)

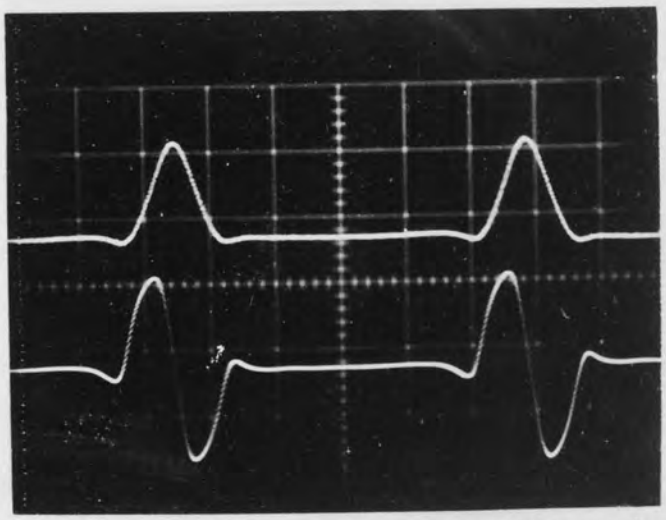

Total harmonic variation at the peak position of the fundamental

Scales:

Top curve(flux wave)	0.05	mWb/cm
Bottom curve(e.m.f.)	0.5	V/cm
Time base	2	ms/cm
Sweeping magnification	10	
e.m.f. amplification	50	

Fig 7.2 Oscillograms of search coil 25 taken at synchronous speed, 415 V applied line voltage and disconnected cage (SECONDARY SURFACE SEARCH COIL)

(a)

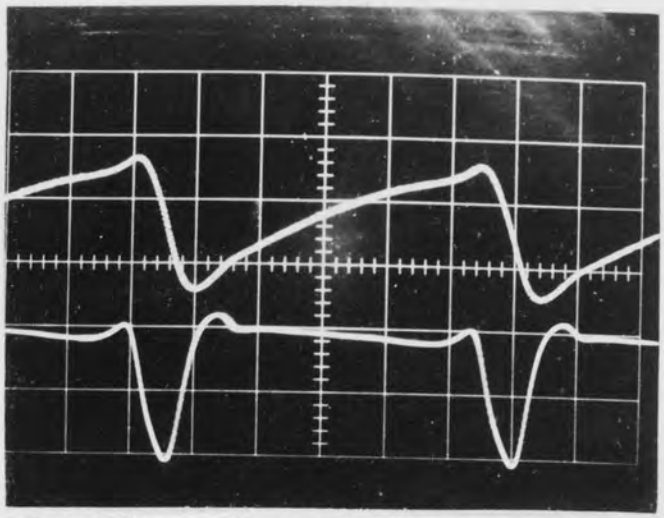

Total harmonic variation at the zero position of the fundamental

Scales:

Top curve(flux wave)	0.05 mWb/cm
Bottom curve(e.m.f.)	0.5 V/cm
Time base	2 ms/cm
Sweeping magnification	10
e.m.f. amplification	50

(b)

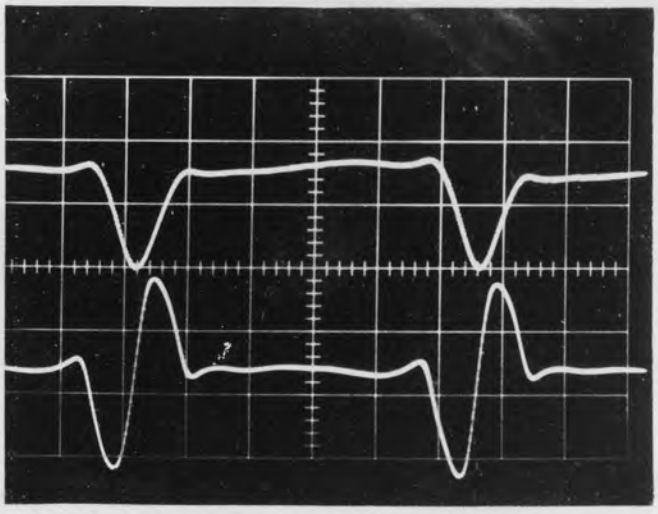

Total harmonic variation at the peak position of the fundamental

Scales:

Top curve(flux wave)	0.05 mWb/cm
Bottom curve(e.m.f.)	0.5 V/cm
Time base	2 ms/cm
Sweeping magnification	10
e.m.f. amplification	50

Fig 7.3 Oscillograms of search coil 25 taken at synchronous speed, 550 V applied line voltage and disconnected cage

(SECONDARY SURFACE SEARCH COIL)

(a)

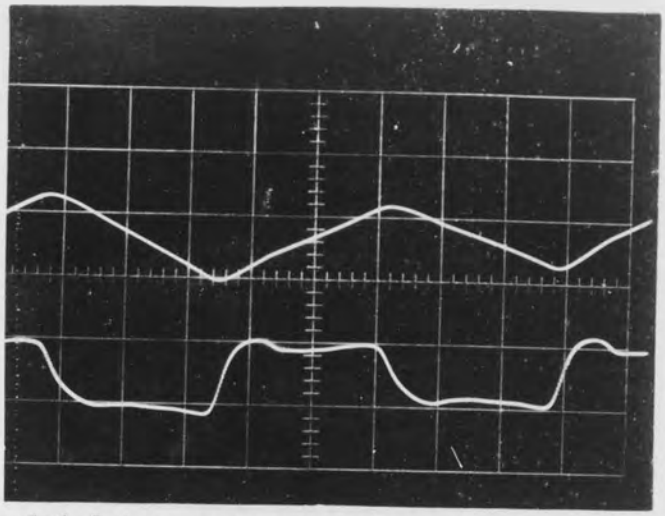

Total harmonic variation at the zero position of the fundamental

Scales:

Top curve(flux wave)	0.05 mWb/cm
Bottom curve(e.m.f.)	1.0 V/cm
Time base	2 ms/cm
Sweeping magnification	10
e.m.f. amplification	100

(b)

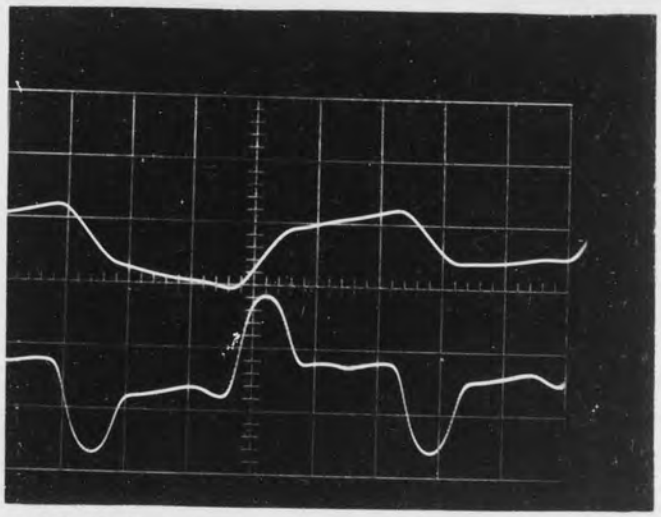

Total harmonic variation at the peak position of the fundamental

Scales:

Top curve(flux wave)	0.05 mWb/cm
Bottom curve(e.m.f.)	1.0 V/cm
Time base	2 ms/cm
Sweeping magnification	10
e.m.f. amplification	100

Fig 7.4 Oscillograms of search coil 28 taken at synchronous speed, 300 V applied line voltage and disconnected cage

(SECONDARY SURFACE SEARCH COIL)

(a)

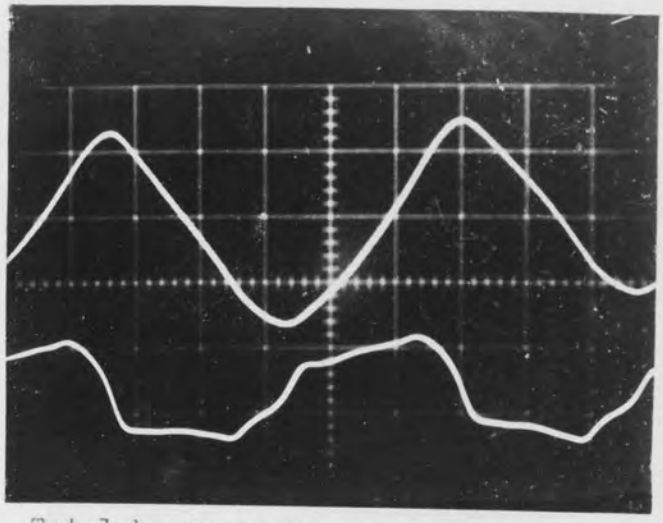

Total harmonic variation at the zero position of the fundamental

Scales:

Top curve(flux wave)	0.05	mWb/cm
Bottom curve(e.m.f)	0.5	V/cm
Time base	2	ms/cm
Sweeping magnification	10	
e.m.f. amplification	50	

(b)

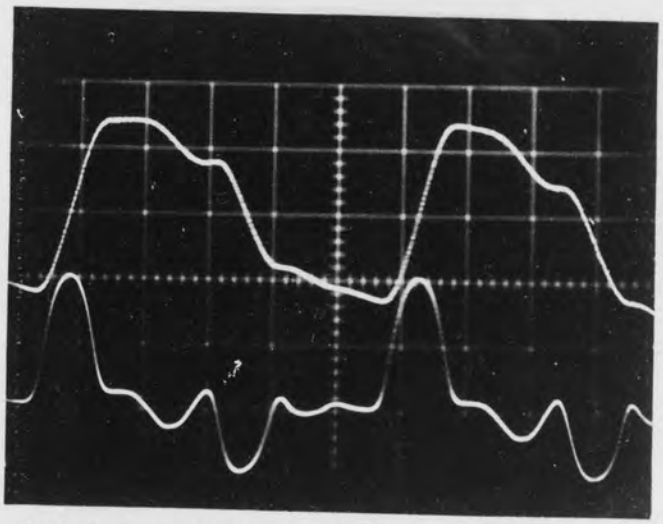

Total harmonic variation at the peak position of the fundamental

Scales:

Top curve(flux wave)	0.05	mWb/cm
Bottom curve(e.m.f.)	0.5	V/cm
Time base	2	ms/cm
Sweeping magnification	10	
e.m.f. amplification	50	

Fig 7.5 Oscillograms of search coil 28 taken at synchronous speed, 415 V applied line voltage and disconnected cage (SECONDARY SURFACE SEARCH COIL)

(a)

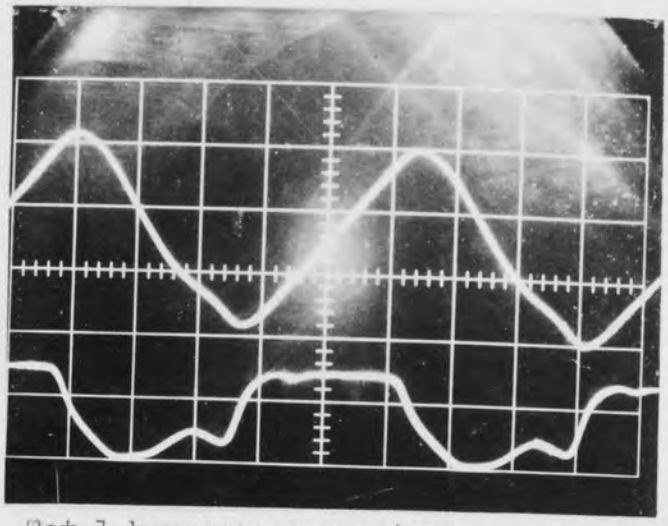

Total harmonic variation at the zero position of the fundamental

Scales:

Top curve(flux wave)	0.1 mWb/cm
Bottom curve(e.m.f.)	1 V/cm
Time base	2 ms/cm
Sweepingmagnification	10
e.m.f. amplification	50

(b)

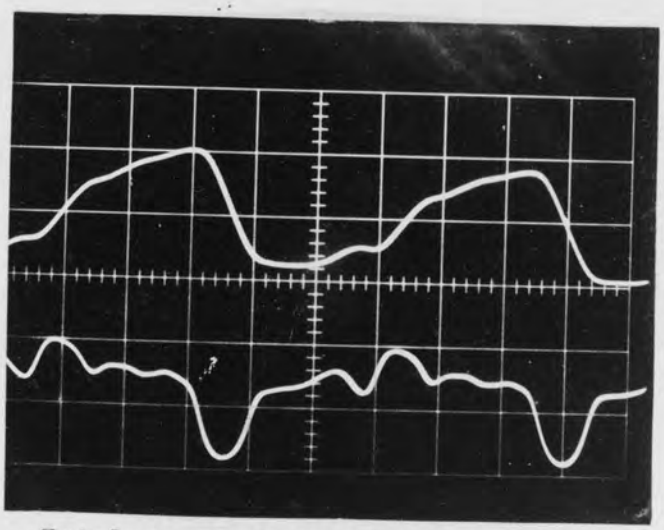

Total harmonic variation at the peak position of the fundamental

Scales:

Top curve(flux wave)	0.1 mWb/cm
Bottom curve(e.m.f.)	1 V/cm
Time base	2 ms/cm
Sweeping magnification	10
e.m.f. amplification	50

Fig 7.6

Oscillograms of search coil 28 taken at synchronous speed, 550 V applied line voltage and disconnected cage
(SECONDARY SURFACE SEARCH COIL)

(a)

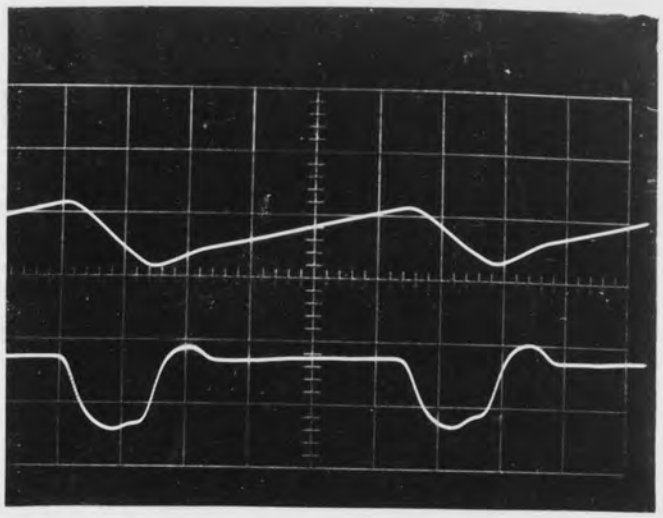

Total harmonic variation at the zero position of the fundamental

Scales:

Top curve(flux wave)	0.05 mWb/cm
Bottom curve(e.m.f.)	1.0 V/cm
Time base	2 ms/cm
Sweeping magnification	10
e.m.f. amplification	100

(b)

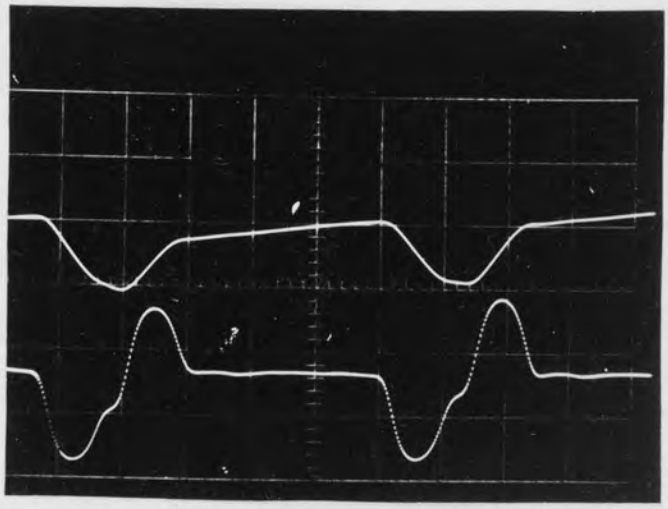

Total harmonic variation at the peak position of the fundamental

Scales:

Top curve(flux wave)	0.05 mWb/cm
Bottom curve(e.m.f.)	1.0 V/cm
Time base	2 ms/cm
Sweeping magnification	10
e.m.f. amplification	100

Fig 7.7 Oscillograms of search coil 26 taken at synchronous speed, 300V applied line voltage and disconnected cage

(SECONDARY SURFACE SEARCH COIL)

(a)

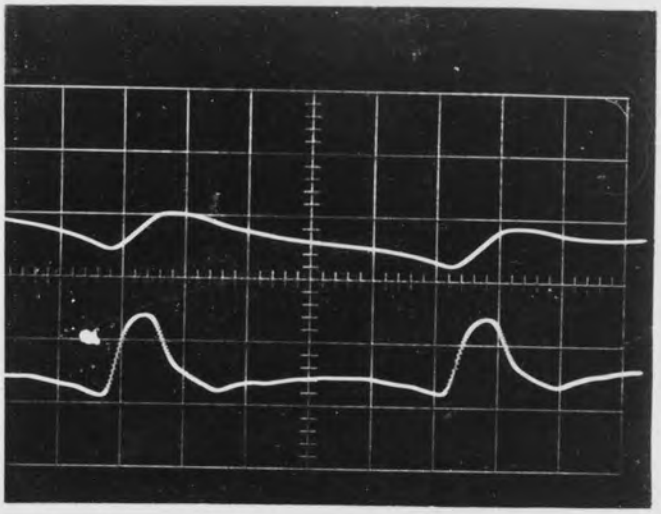

Total harmonic variation at the zero position of the fundamental

Scales:

Top curve(flux wave)	0.05 mWb/cm
Bottom curve(e.m.f.)	1.0 V/cm
Time base	2 ms/cm
Sweeping magnification	10
e.m.f. amplification	100

(b)

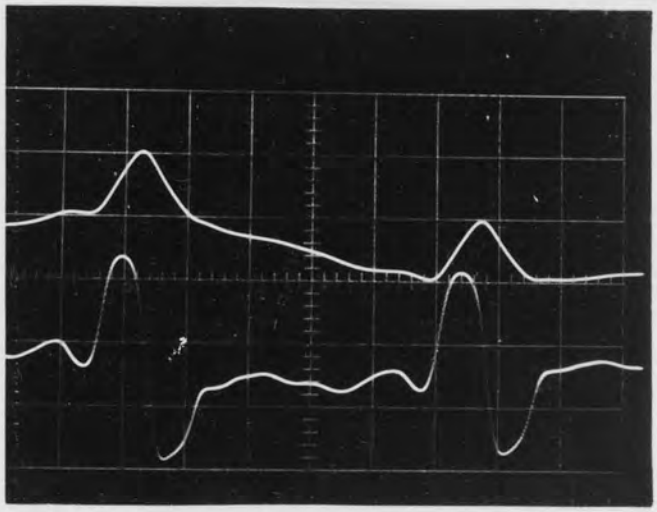

Total harmonic variation at the peak position of the fundamental

Scales:

Top curve(flux wave)	0.05 mWb/cm
Bottom curve(e.m.f.)	1.0 V/cm
Time base	2 ms/cm
Sweeping magnification	10
e.m.f. amplification	100

Fig 7.8 Oscillograms of search coil 31 taken at synchronous speed, 300 V applied line voltage and disconnected cage (SECONDARY SURFACE SEARCH COIL)

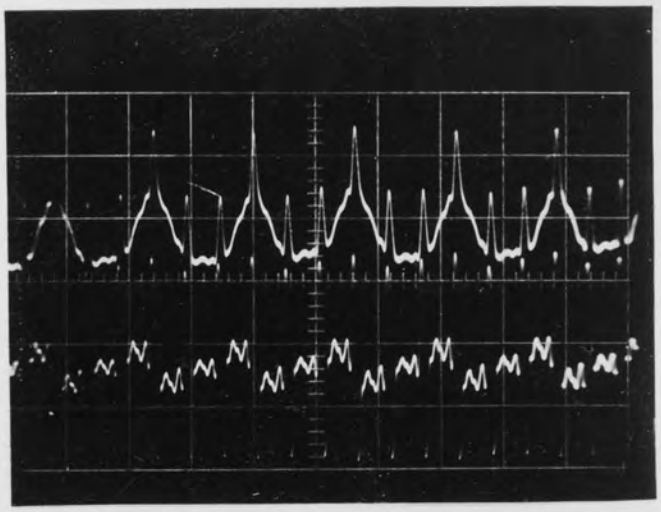

Total harmonic variation at the peak position of the fundamental

Scales:

Top curve(flux wave)	0.05 mWb/cm
Bottom curve(e.m.f.)	1.0 V/cm
Time base	2 ms/cm
Sweeping magnification	normal
e.m.f. amplification	100

Fig 7.9

Oscillogram of search coil 31 taken at synchronous speed, 300 V applied line voltage and disconnected cage

(SECONDARY SURFACE SEARCH COIL)

(a)

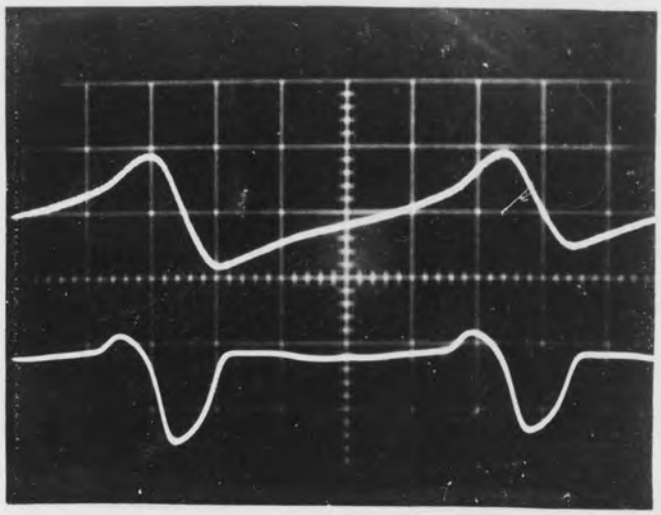

Total harmonic variation at the zero position of the fundamental

Scales:

Top curve(flux wave)	0.05	mWb/cm
Bottom curve(e.m.f.)	0.5	V/cm
Time base	2	ms/cm
Sweeping magnification	10	
e.m.f. amplification	50	

(b)

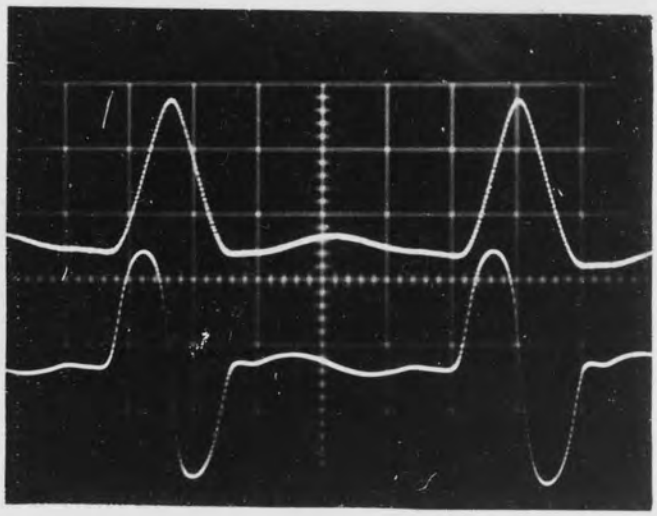

Total harmonic variation at the peak position of the fundamental

Scales:

Top curve(flux wave)	0 05	mWb/cm
Bottom curve(e.m.f.)	0.5	V/cm
Time base	2	ms/cm
Sweeping magnification	10	
e.m.f. amplification	50	

Fig 7.10 Oscillograms of search coil 34 taken at synchronous speed, 415 V applied line voltage and disconnected cage
(SECONDARY SURFACE SEARCH COIL)

(a)

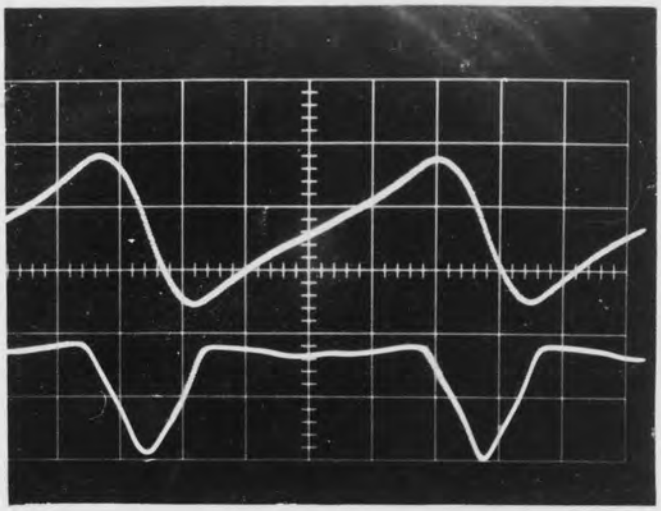

Total harmonic variation at the zero position of the fundamental

Scales:

Top curve(flux wave)	0.05	mWb/cm
Bottom curve(e.m.f.)	0.5	V/cm
Time base	2	ms/cm
Sweeping magnification	10	
e.m.f. amplification	50	

(b)

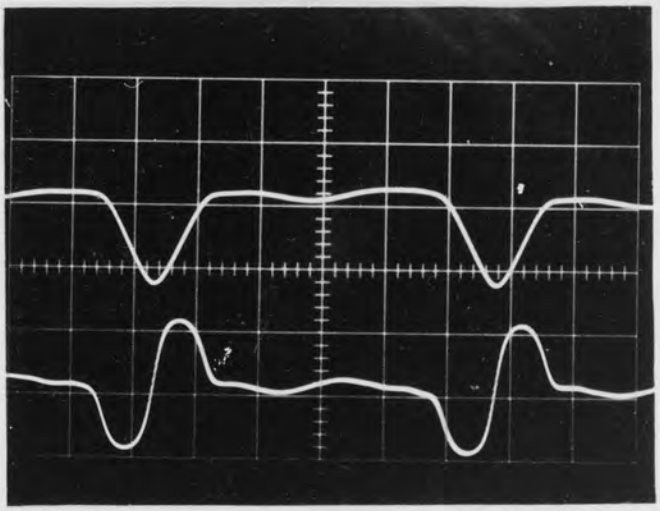

Total harmonic variation at the peak position of the fundamental

Scales:

Top curve(flux wave)	0.1	mWb/cm
Bottom curve(e.m.f.)	1	V/cm
Time base	2	ms/cm
Sweeping magnification	10	
e.m.f. amplification	50	

Fig 7.11 Oscillograms of search coil 34 taken at synchronous speed, 550 V applied line voltage and disconnected cage (SECONDARY SURFACE SEARCH COIL)

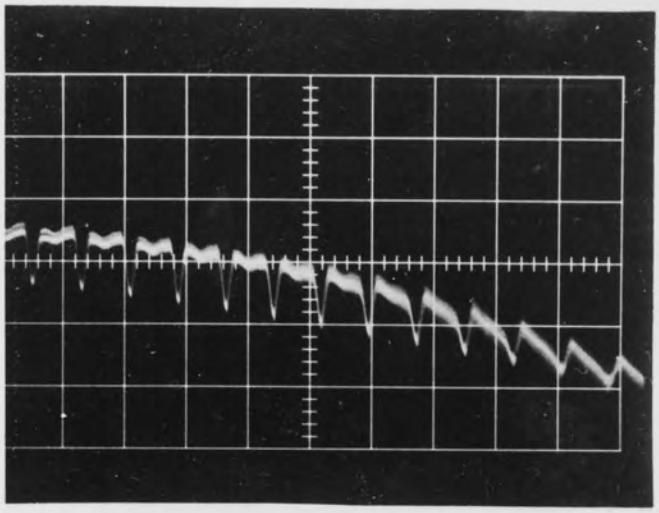

Total harmonic variation at various positions of the fundamental
Scales:
Time base 2 ms/cm
Sweeping magnification 5

Fig 7.12

Oscillogram of search coil 34 taken at 300V applied line voltage and disconnected cage

(SECONDARY SURFACE SEARCH COIL)

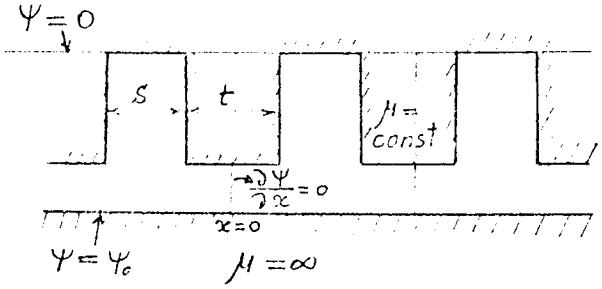

Fig 7.13 An air gap geometry and the assumed potential boundary conditions

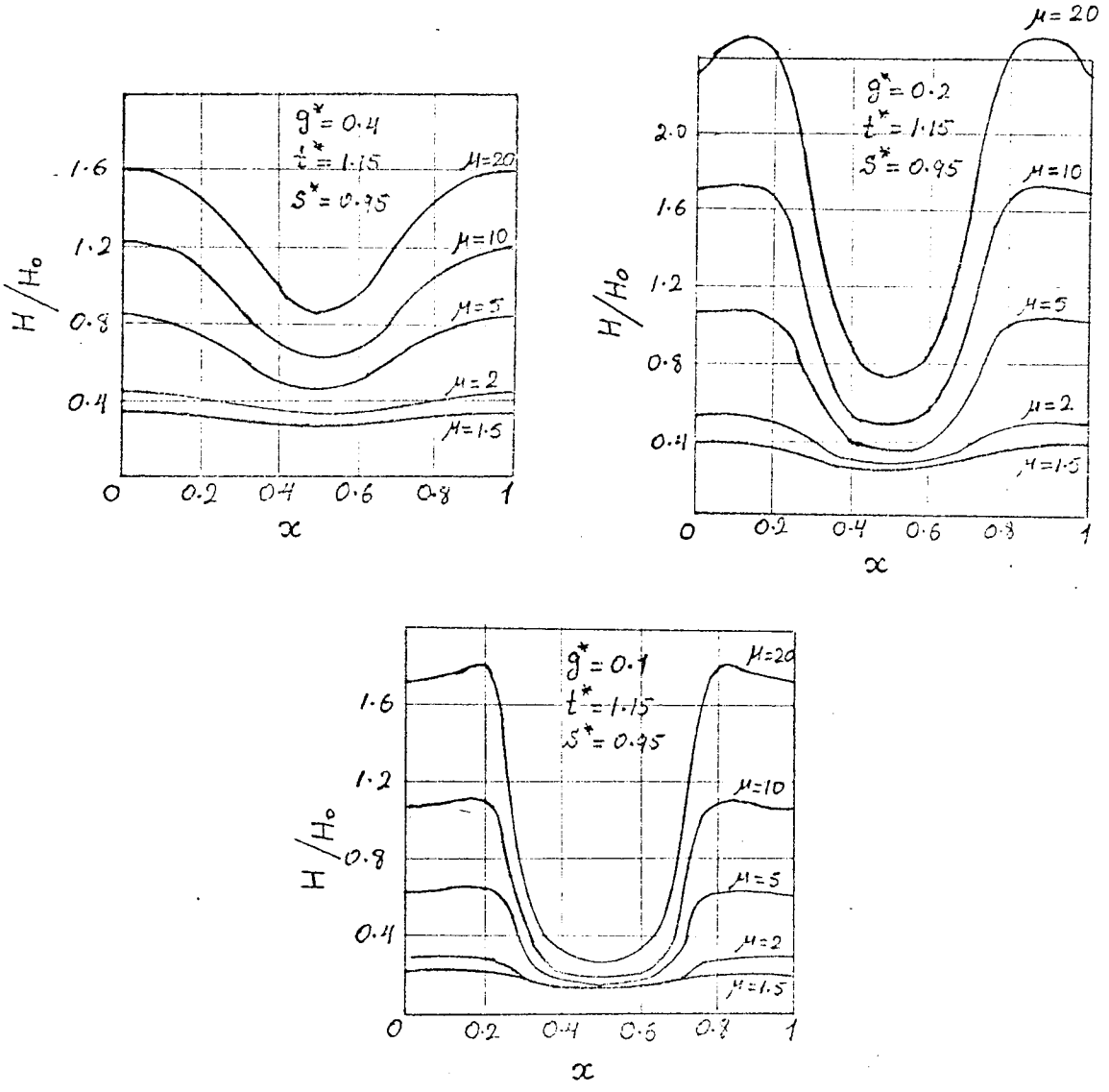

Fig 7.14 Magnetic field intensity distribution along the smooth surface of Fig 7.13 [8]
(Reproduced from Smolensky's paper)
Dimensions g^*, t^*, s^*, are given per half slot pitch

$$H_0 = \Psi_0 \times \frac{t+s}{2}$$

(a)

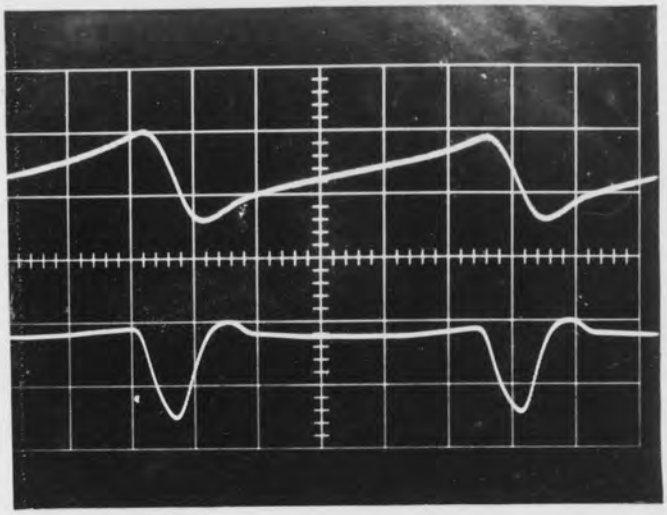

Total harmonic variation at the zero position of the fundamental

Scales:		
Top curve(flux wave)	0.05	mWb/cm
Bottom curve(e.m.f.)	0.5	V/cm
Time base	2	ms/cm
Sweeping magnification	10	
e.m.f. amplification	50	

(b)

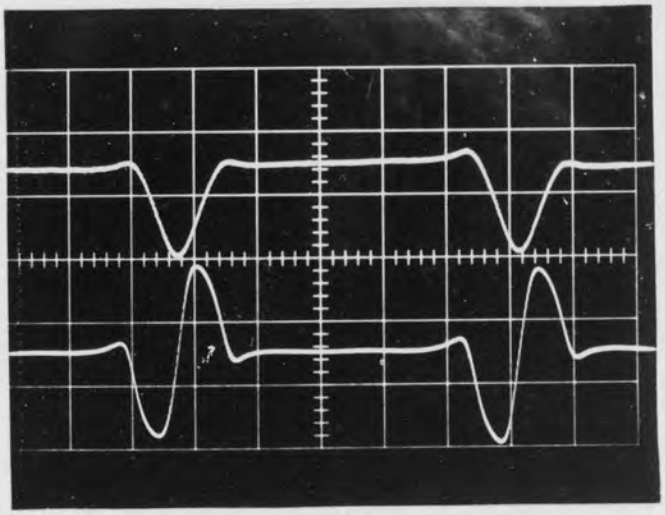

Total harmonic variation at the peak position of the fundamental

Scales:		
Top curve(flux wave)	0.05	mWb/cm
Bottom curve(e.m.f.)	0.5	V/cm
Time base	2	ms/cm
Sweeping magnification	10	
e.m.f. amplification	50	

Fig 7.15 Oscillograms of search coil 25 taken at synchronous speed, 415 V applied line voltage and short-circuited cage (SECONDARY SURFACE SEARCH COIL)

(a)

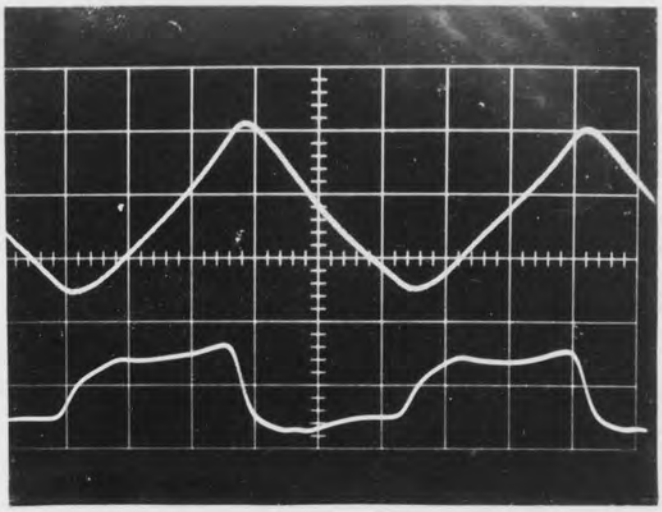

Total harmonic variation at the zero position of the fundamental

Scales:

Top curve(flux wave)	0.05	mWb/cm
Bottom curve(e.m.f.)	0.5	V/cm
Time base	2	ms/cm
Sweeping magnification	10	
e.m.f. amplification	50	

(b)

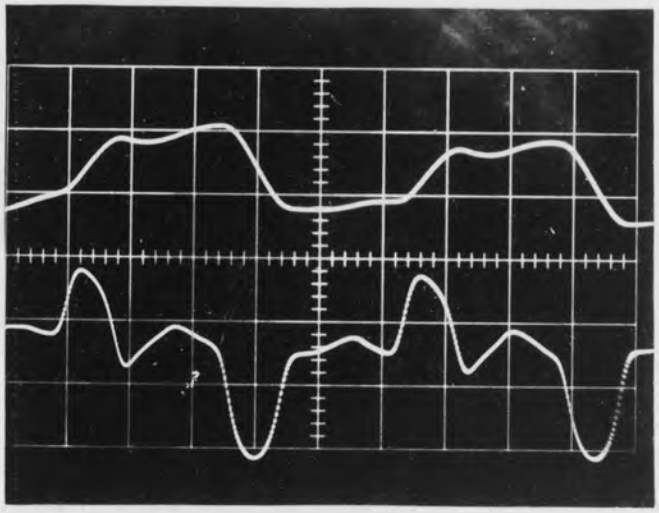

Total harmonic variation at the peak position of the fundamental

Scales:

Top curve(flux wave)	0.1	mWb/cm
Bottom curve(e.m.f.)	0.5	V/cm
Time base	2	ms/cm
Sweeping magnification	10	
e.m.f. amplification	50	

Fig 7.16 Oscillograms of search coil 28 taken at synchronous speed, 415 V applied line voltage and short- circuited cage

(SECONDARY SURFACE SEARC COIL)

(a)

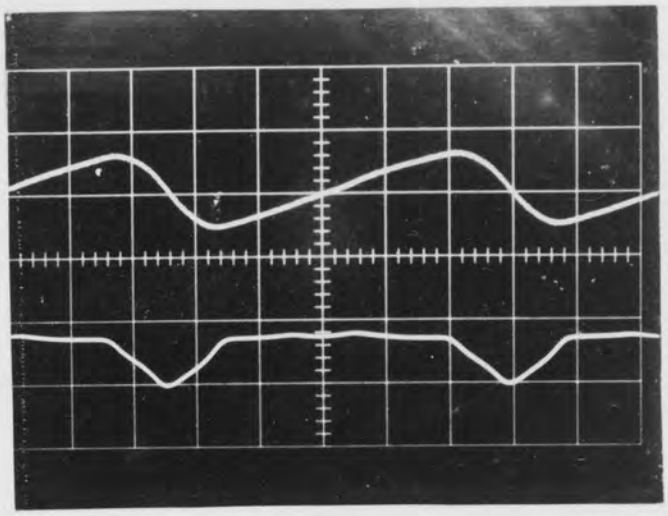

Total harmonic variation at the zero position of the fundamental

Scales:		
Top curve(flux wave)	0.05	mWb/cm
Bottom curve(e.m.f.)	0.5	V/cm
Time base	2	ms/cm
Sweeping magnification	10	
e.m.f. amplification	50	

(b)

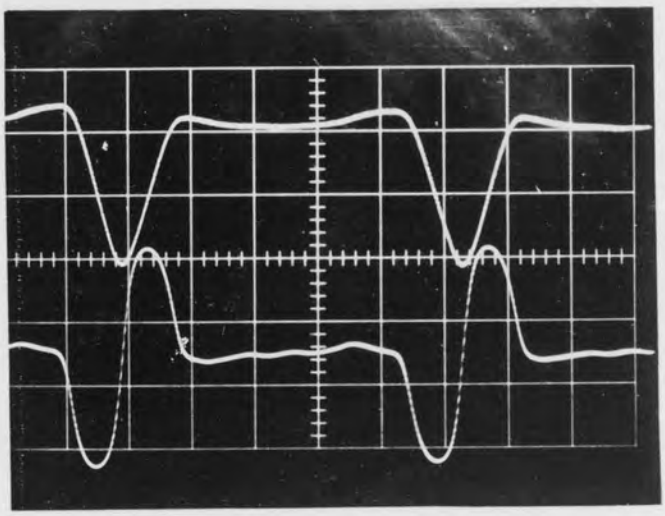

Total harmonic variation at the peak position of the fundamental

Scales:		
Top curve(flux wave)	0.05	mWb/cm
Bottom curve(e.m.f.)	0.5	V/cm
Time base	2	ms/cm
Sweeping magnification	10	
e.m.f. amplification	50	

Fig 7.17 Oscillograms of search coil 34 taken at synchronous speed, 415 V applied line voltage and short-circuited cage
(SECONDARY SURFACE SEARCH COIL)

(a)

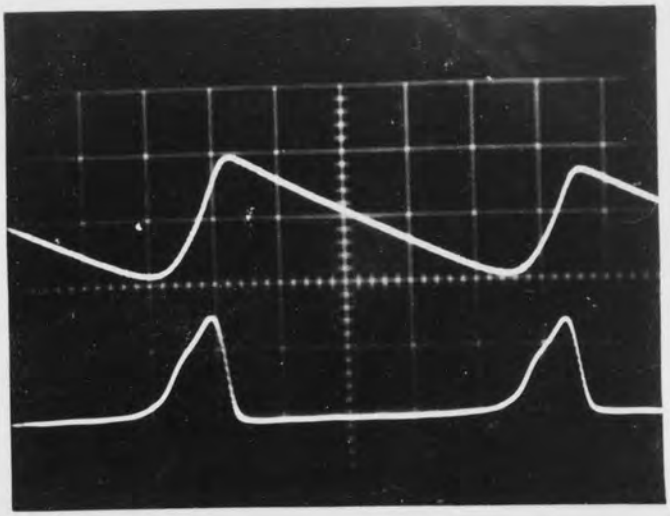

Total harmonic variation at the zero position of the fundamental

Scales:	
Top curve(flux wave)	0.05 mWb/cm
Bottom curve(e.m.f.)	0.5 V/cm
Time base	2 ms/cm
Sweeping magnification	10
e.m.f. amplification	50

(b)

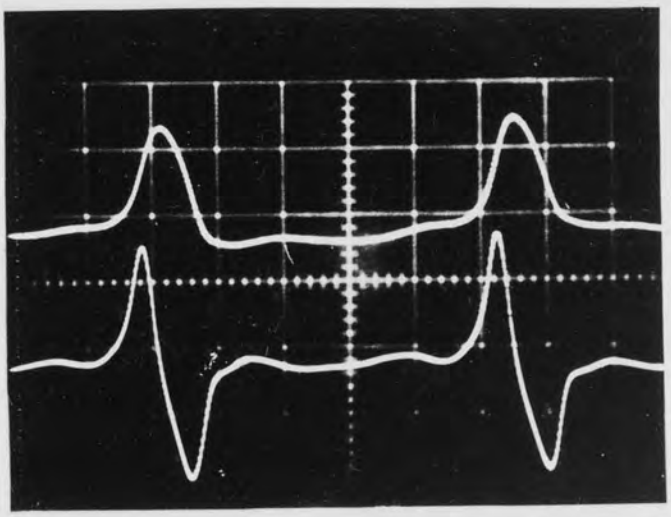

Total harmonic variation at the peak position of the fundamental

Scales:	
Top curve(flux wave)	0.05 mWb/cm
Bottom curve(e.m.f.)	0.5 V/cm
Time base	2 ms/cm
Sweeping magnification	10
e.m.f. amplification	50

Fig 7.18 Oscillograms of search coil 42 taken at synchronous speed, 415 V applied line voltage and disconnected cage (SECONDARY TOOTH LIP SEARCH COIL)

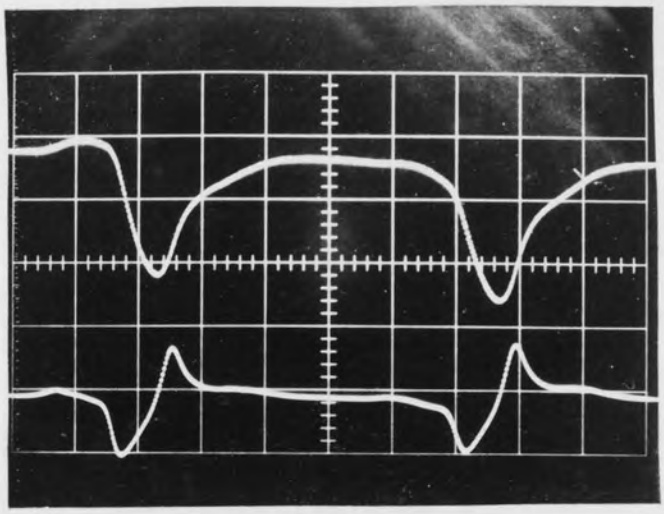

Total harmonic variation at the peak position of the fundamental

Scales:

Top curve(flux wave)	0.05 mWb/cm
Bottom curve(e.m.f.)	1.0 V/cm
Time base	2 ms/cm
Sweeping magnification	10
e.m.f. amplification	50

Fig 7.19

Oscillogram of search coil 42 taken at synchronous speed, 550 V applied line voltage and disconnected cage
(SECONDARY TOOTH LIP SEARCH COIL)

(a)

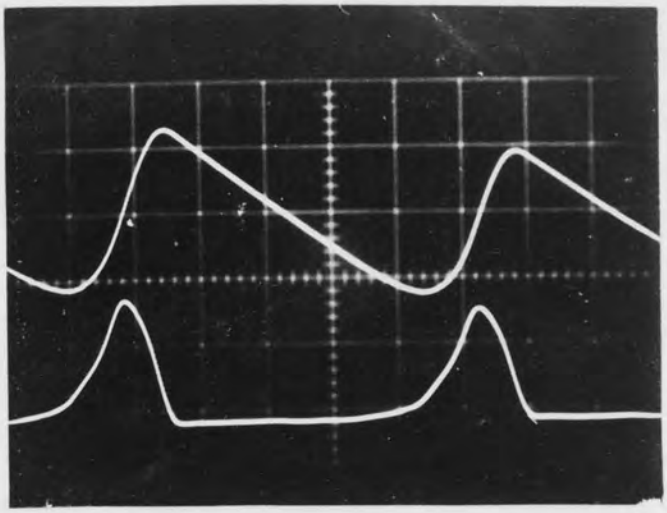

Total harmonic variation at the zero position of the fundamental

Scales:		
Top curve(flux wave)	0.1	mWb/cm
Bottom curve(e.m.f.)	1	V/cm
Time base	2	ms/cm
Sweeping magnification	10	
e.m.f. amplification	50	

(b)

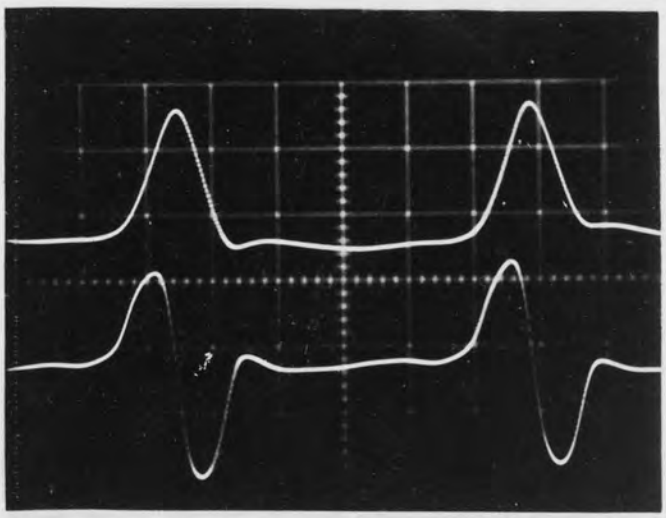

Total harmonic varition at the peak position of the fundamental

Scales:		
Top curve(flux wave)	0.1	mWb/cm
Bottom curve(e.m.f.)	1	V/cm
Time base	2	ms/cm
Sweeping magnification	10	
e.m.f. amplification	50	

Fig 7.20 Oscillograms of search coil 41 taken at synchronous speed, 415 V applied line voltage and disconnected cage

(SECONDARY TOOTH LIP SEARCH COIL)

(a)

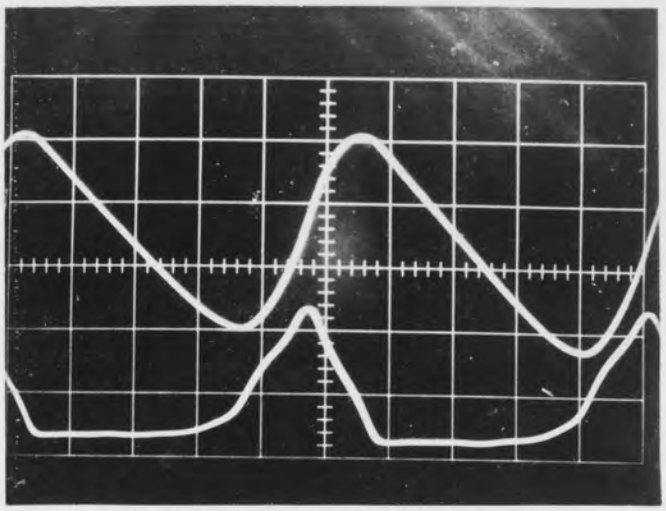

Total harmonic variation at the zero position of the fundamental

Scales:

Top curve(flux wave)	0.1	mWb/cm
Bottom curve(e.m.f.)	1	V/cm
Time base	2	ms/cm
Sweeping magnification	10	
e.m.f. amplification	50	

(b)

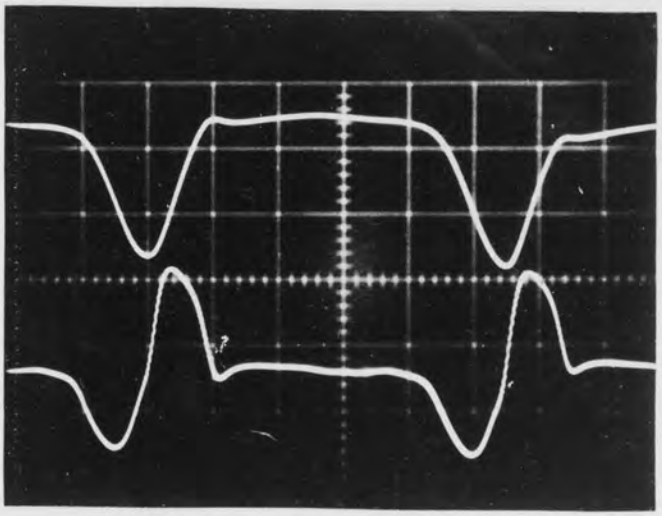

Total harmonic variation at the peak position of the fundamental

Scales:

Top curve(flux wave)	0.1	mWb/cm
Bottom curve(e.m.f.)	1	V/cm
Time base	2	ms/cm
Sweeping magnification	10	
e.m.f. amplification	50	

Fig 7.21 Oscillograms of search coil 40 taken at synchronous speed, 415 V applied line voltage and disconnected cage

(SECONDARY TOOTH LIP SEARCH COIL)

(a)

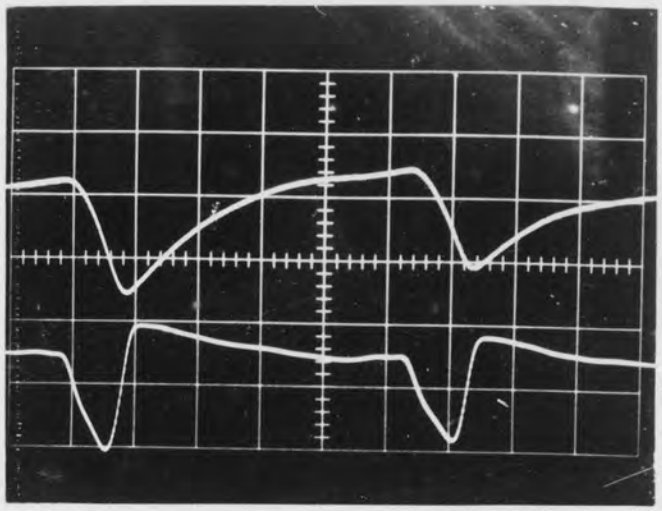

Total harmonic variation at the zero position of the fundamental

Scales:

Top curve (flux wave)	0.05	mWb/cm
Bottom curve (e.m.f.)	0.5	V/cm
Time base	2	ms/cm
Sweeping magnification	10	
e.m.f. amplification	50	

(b)

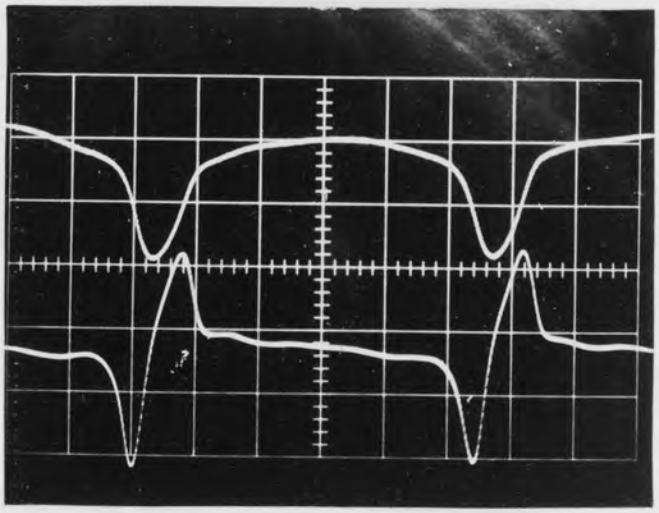

Total harmonic variation at the peak position of the fundamental

Scales:

Top curve (flux wave)	0.05	mWb/cm
Bottom curve (e.m.f.)	0.5	V/cm
Time base	2	ms/cm
Sweeping magnification	10	
e.m.f. amplification	50	

Fig 7.22 Oscillograms of search coil 42 taken at synchronous speed, 415 V applied line voltage and short-circuited cage

(SECONDARY TOOTH LIP SEARCH COIL)

(a)

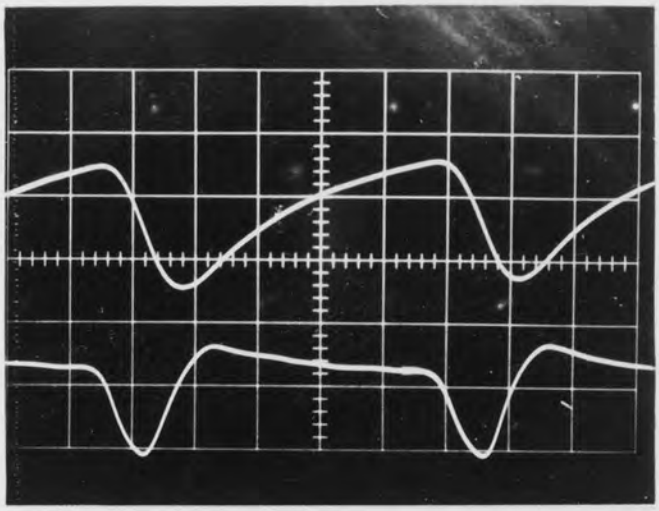

Total harmonic variation at the zero position of the fundamental

Scales:

Top curve (flux wave)	0.1	mWb/cm
Bottom curve (e.m.f.)	1	V/cm
Time base	2	ms/cm
Sweeping magnification	10	
e.m.f. amplification	50	

(b)

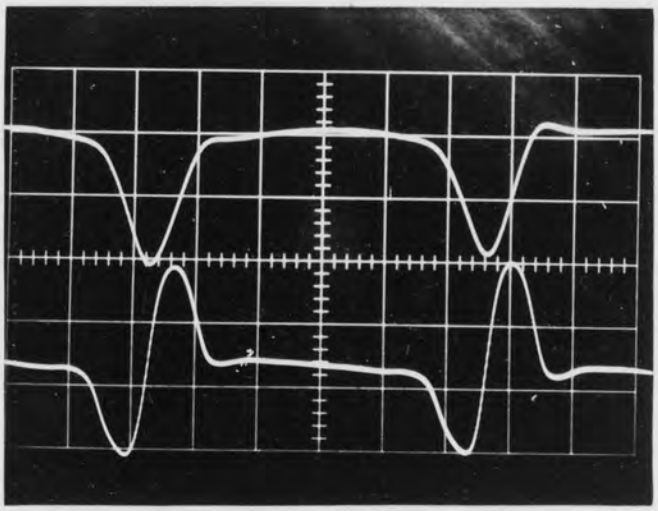

Total harmonic variation at the peak position of the fundamental

Scales:

Top curve (flux wave)	0.1	mWb/cm
Bottom curve (e.m.f.)	1	V/cm
Time base	2	ms/cm
Sweeping magnification	10	
e.m.f. amplification	50	

Fig 7.23 Oscillograms of search coil 41 taken at synchronous speed, 415 v applied line voltage and short-circuited cage

(SECONDARY TOOTH LIP SEARCH COIL)

(a)

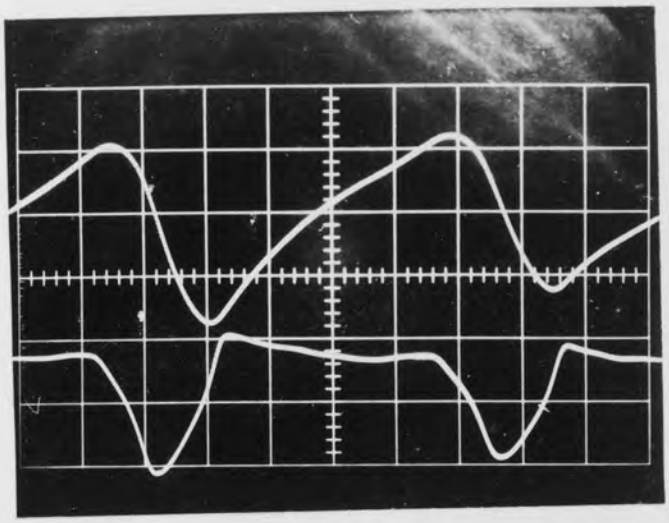

Total harmonic variayion at the zero position of the fundamental

Scales:		
Top curve(flux wave)	0.1	mWb/cm
Bottom curve(e.m.f.)	1	V/cm
Time base	2	ms/cm
Sweeping magnification	10	
e.m.f. amplification	50	

(b)

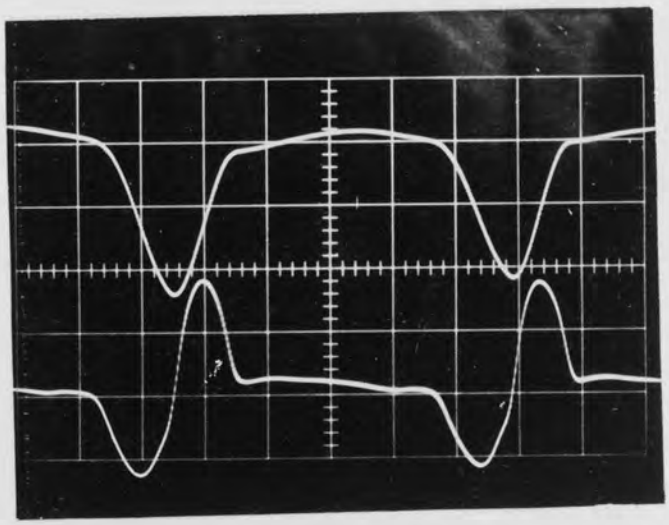

Total harmonic variation at the peak position of the fundamental

Scales:		
Top curve(flux wave)	0.1	mWb/cm
Bottom curve(e.m.f.)	1	V/cm
Time base	2	ms/cm
Sweeping magnification	10	
e.m.f. amplification	50	

Fig 7.24 Oscillograms of search coil 40 taken at synchronous speed, 415 V applied line voltage and short-circuited cage

(SECONDARY TOOTH LIP SEARCH COIL)

(a)

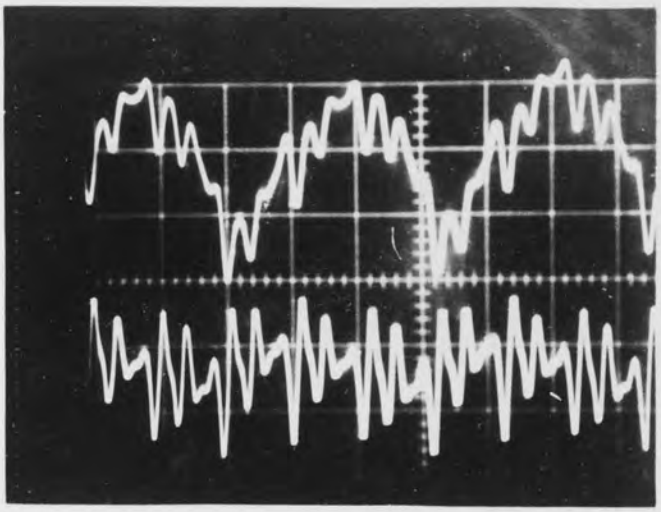

Total harmonic variation at the zero position of the fundamental

Scales:		
Top curve(flux wave)	0.1	mWb/cm
Bottom curve(e.m.f.)	1	V/cm
Time base	2	ms/cm
Sweeping magnification	2	
e.m.f. amplification	50	

(b)

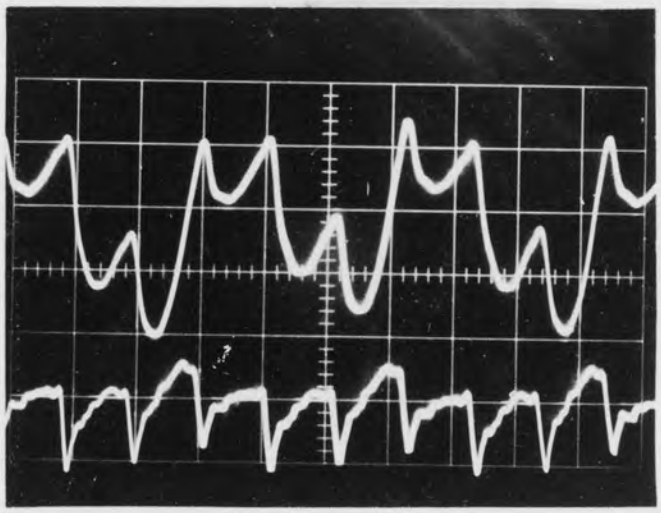

Total harmonic variation at the peak position of the fundamental

Scales:		
Top curve(flux wave)	0.1	mWb/cm
Bottom curve(e.m.f.)	1	V/cm
Time base	2	ms/cm
Sweeping magnification	2	
e.m.f. amplification	50	

Fig 7.25 Oscillograms of search coil 45 taken at synchronous speed, 415 V applied line voltage and disconnected cage

(SECONDARY TOOTH SEARCH COIL)

(a)

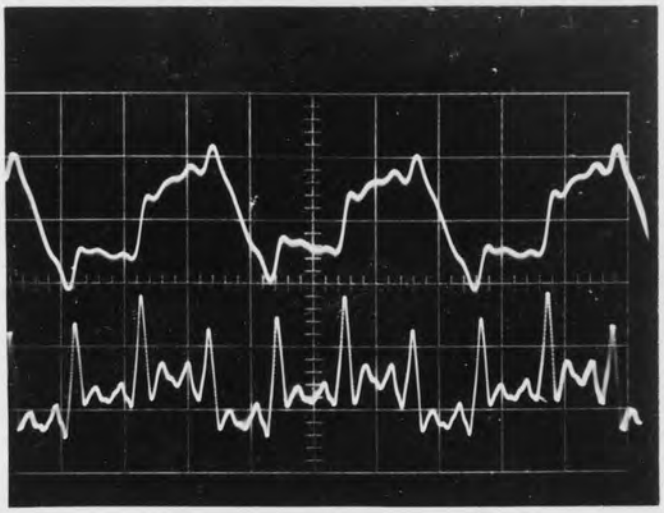

Total harmonic variation at the zero position of the fundamental

Scales:		
Top curve(flux wave)	0.1	mWb/cm
Bottom curve(e.m.f.)	2.0	V/cm
Time base	2	ms/cm
Sweeping magnification	2	
e.m.f. amplification	100	

(b)

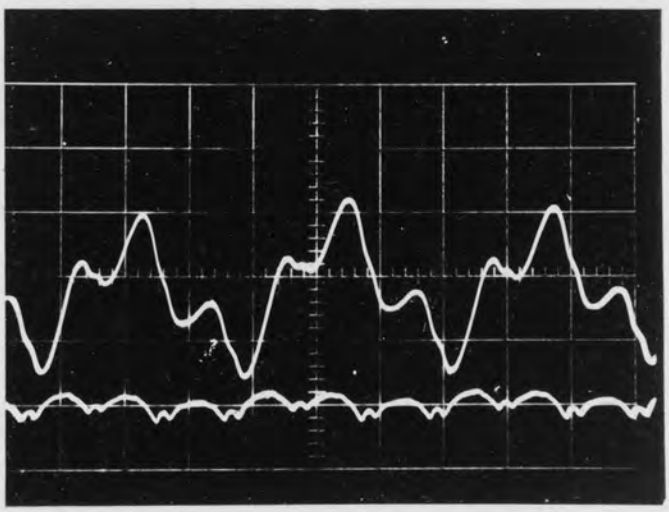

Total harmonic variation at the peak position of the fundamental

Scales:		
Top curve(flux wave)	0.1	mWb/cm
Bottom curve(e.m.f.)	2	V/cm
Time base	2	ms/cm
Sweeping magnification	2	
e.m.f. amplification	20	

Fig 7.26 Oscillograms of search coil 44 taken at synchronous speed, 300 V applied line voltage and disconnected cage
(SECONDARY TOOTH SEARCH COIL)

(a)

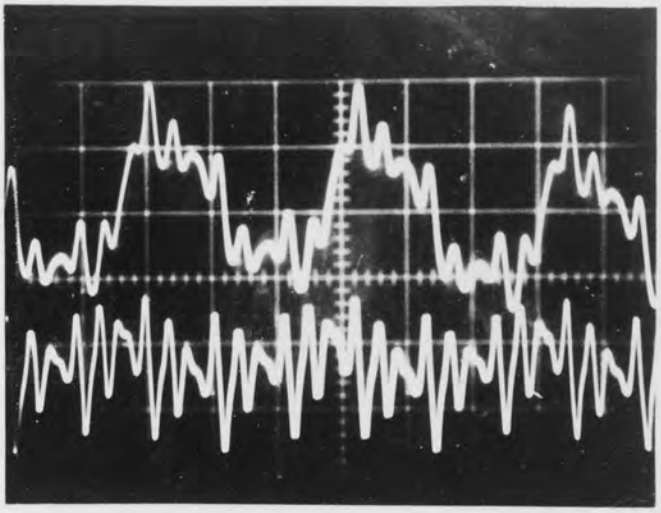

Total harmonic variation at the zero position of the fundamental

Scales:		
Top curve(flux wave)	0.1	mWb/cm
Bottom curve(e.m.f.)	1	V/cm
Time base	2	ms/cm
Sweeping magnification	2	
e.m.f. amplification	50	

(b)

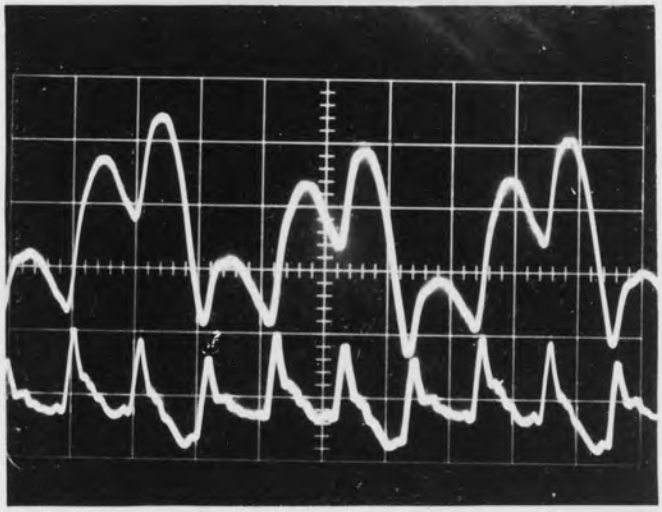

Total harmonic variation at the peak position of the fundamental

Scales:		
Top curve(flux wave)	0.1	mWb/cm
Bottom curve(e.m.f.)	1	V/cm
Time base	2	ms/cm
Sweeping magnification	2	
e.m.f. amplification	50	

Fig 7.27 Oscillograms of search coil 44 taken at synchronous speed, 415 V applied line voltage and disconnected cage

(SECONDARY TOOTH SEARCH COIL)

(a)

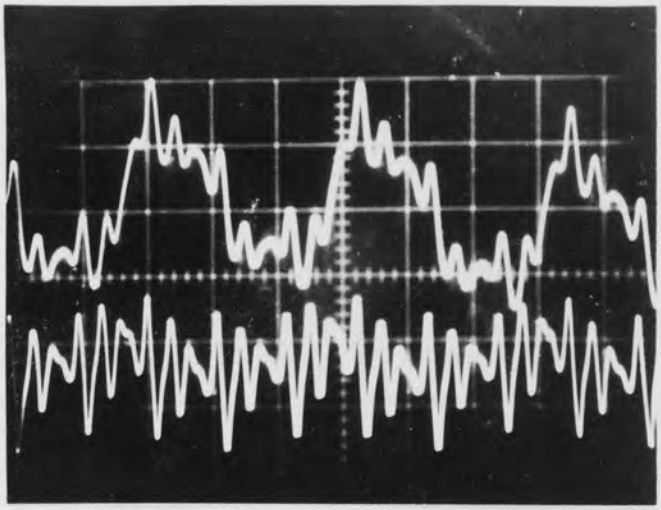

Total harmonic variation at the zero position of the fundamental

Scales:

Top curve(flux wave)	0.1	mWb/cm
Bottom curve(e.m.f.)	1	V/cm
Time base	2	ms/cm
Sweeping magnification	2	
e.m.f. amplification	50	

(b)

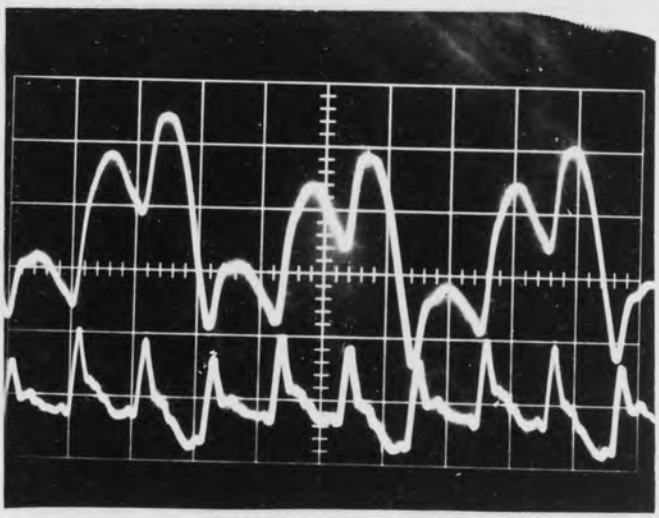

Total harmonic variation at the peak position of the fundamental

Scales:

Top curve(flux wave)	0.1	mWb/cm
Bottom curve(e.m.f.)	1	V/cm
Time base	2	ms/cm
Sweeping magnification	2	
e.m.f. amplification	50	

Fig 7.28 Oscillograms of search coil 43 taken at synchronous speed, 415 V applied line voltage and disconnected cage

(SECONDARY TOOTH SEARCH COIL)

(a)

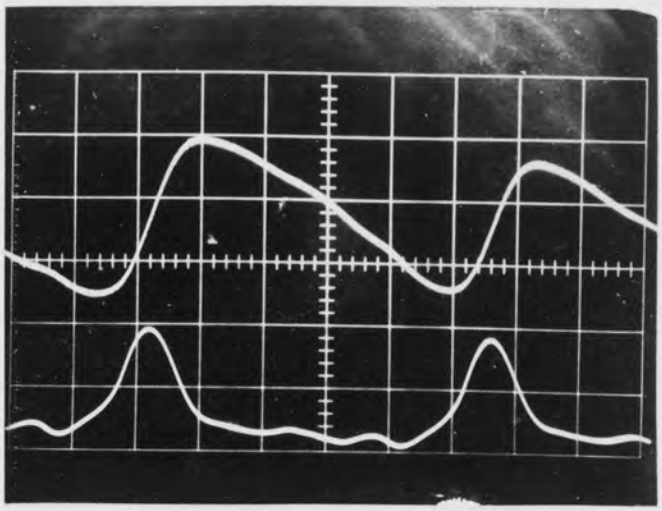

Total harmonic variation at the zero position of the fundamental

Scales:

Top curve(flux wave)	0.05	mWb/cm
Bottom curve(e.m.f.)	0.5	V/cm
Time base	2	ms/cm
Sweeping magnification	10	
e.m.f. amplification	50	

(b)

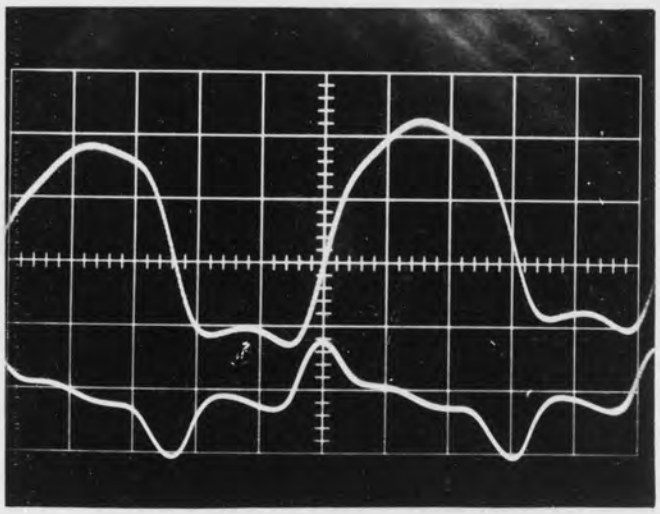

Total harmonic variation at the peak position of the fundamental

Scales:

Top curve(flux wave)	0.05	mWb/cm
Bottom curve(e.m.f.)	1	V/cm
Time base	2	ms/cm
Sweeping magnification	10	
e.m.f. amplification	50	

Fig 7.29(a) Oscillograms of search coil 45 taken at synchronous speed, 550 V applied line voltage and short-circuited cage

(SECONDARY TOOTH SEARCH COIL)

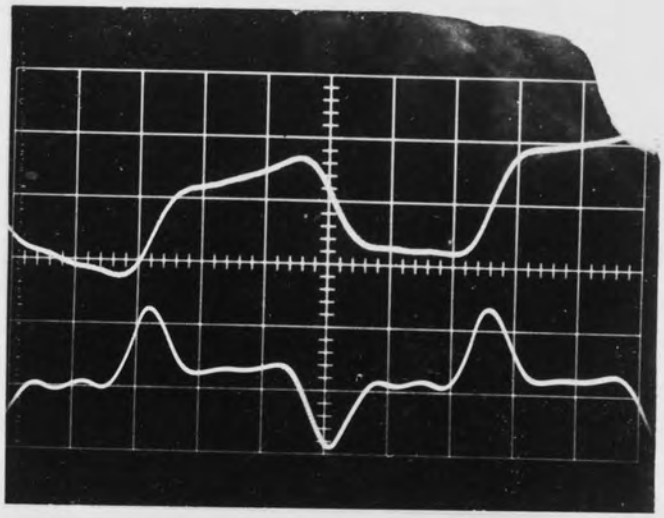

Total harmonic variation at the peak position of the fundamental

Scales:

Top curve(flux wave)	0.05	mWb/cm
Bottom curve(e.m.f.)	0.5	V/cm
Time base	2	ms/cm
Sweeping magnification	10	
e.m.f. amplification	50	

Fig 7.29(b)

Oscillogram of search coil 45 taken at synchronous speed, 415 V applied line voltage and short-circuited cage

(SECONDARY TOOTH SEARCH COIL)

(a)

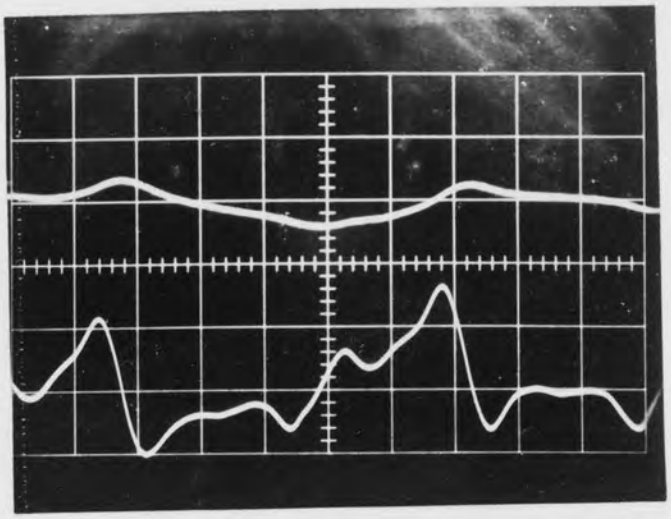

Total harmonic variation at the zero position of the fundamental

Scales:

Top curve(flux wave)	0.05	mWb/cm
Bottom curve(e.m.f.)	0.1	V/cm
Time base	2	ms/cm
Sweeping magnification	10	
e.m.f. amplification	50	

(b)

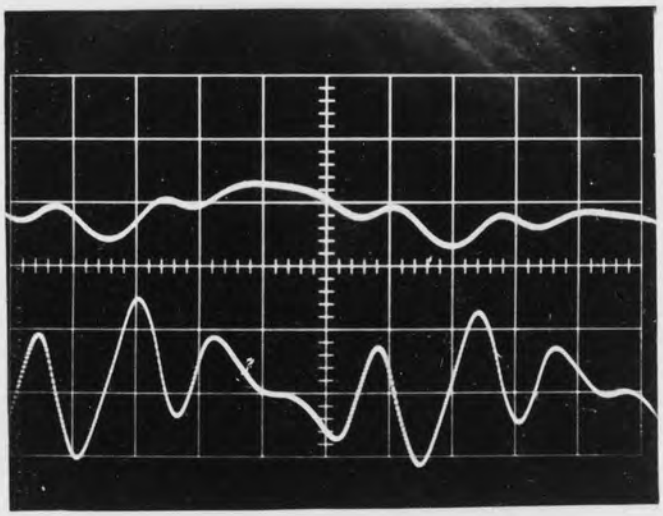

Total harmonic variation at the peak position of the fundamental

Scales:

Top curve(flux wave)	0.05	mWb/cm
Bottom curve(e.m.f.)	0.1	v/cm
Time base	2	ms/cm
Sweeping magnification	10	
e.m.f. amplification	50	

Fig 7.30 Oscillograms of search coil 44 taken at synchronous speed, 550 V applied line voltage and short-circuited cage

(SECONDARY TOOTH SEARCH COIL)

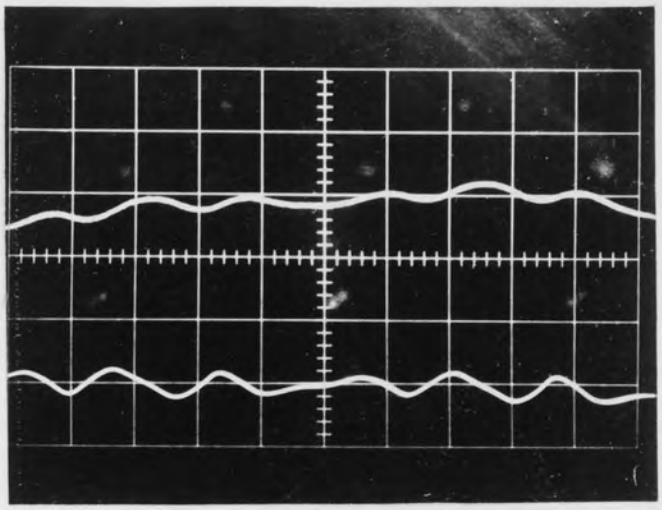

Total harmonic variation at the peak position of the fundamental

Scales:

Top curve(flux wave)	0.05	mWb/cm
Bottom curve(e.m.f.)	0.5	V/cm
Time base	2	ms/cm
Sweeping magnification	10	
e.m.f. amplification	50	

Fig 7.31 Oscillogram of search coil 43 taken at synchronous speed, 415 V applied line voltage and short-circuited cage

(SECONDARY TOOTH SEARCH COIL)

(a)

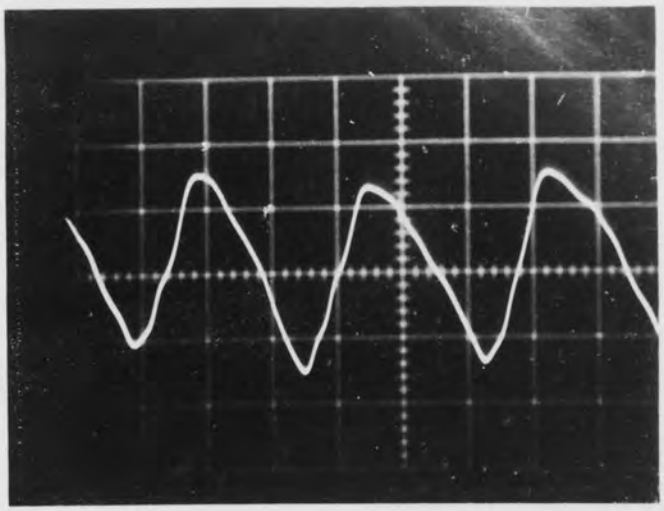

Current density waveform at the zero position of the fundamental

Scales:

Current density wave	6.74	$(A/mm^2)/cm$
Time base	2	ms/cm
Sweeping magnification	5	
Signal amplification	50	

(b)

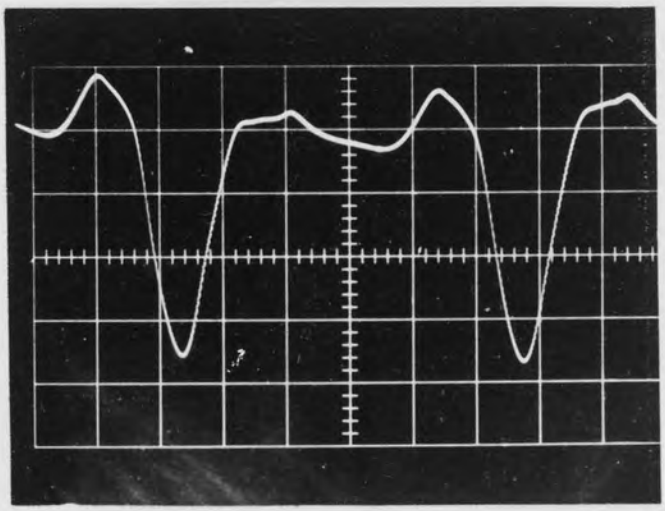

Current density waveform at the peak position of the fundamental

Scales:

Current density wave	13.5	$(A/mm^2)/cm$
Time base	2	ms/cm
Sweeping magnification	10	
Signal amplification	50	

Fig 7.32 Oscillograms of J-probe 6 taken at synchronous speed, 415 V applied line voltage

(BAR SURFACE CURRENT DENSITY)

(a)

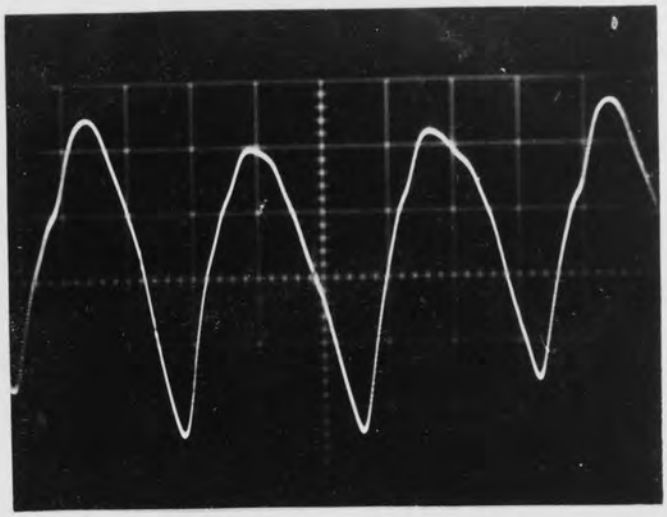

Current density waveform at the zero position of the fundamental

Scales:

Current density wave	2.7	$(A/mm^2)/cm$
Time base	2	ms/cm
Sweeping magnification	5	
Signal amplification	50	

(b)

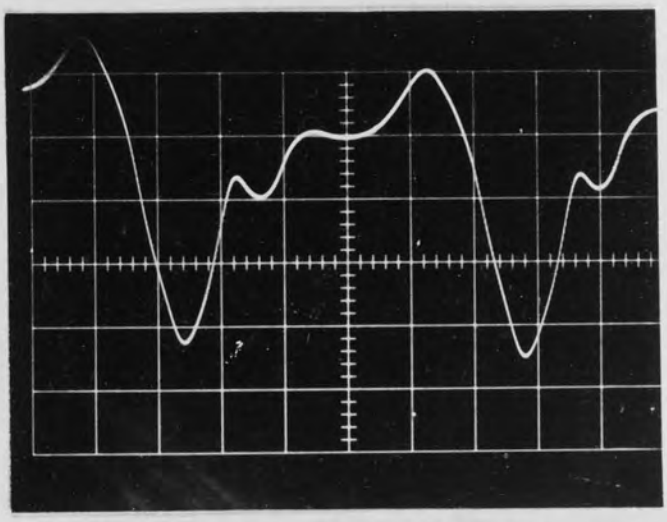

Current density waveform at the peak position of the fundamental

Scales:

Current density wave	6.74	$(A/mm^2)/cm$
Time base	2	ms/cm
Sweeping magnification	10	
Signal amplification	50	

Fig 7.33 Oscillograms of J-probe 5 taken at synchronous speed, 415 V applied line voltage

(BAR SURFACE CURRENT DENSITY)

(a)

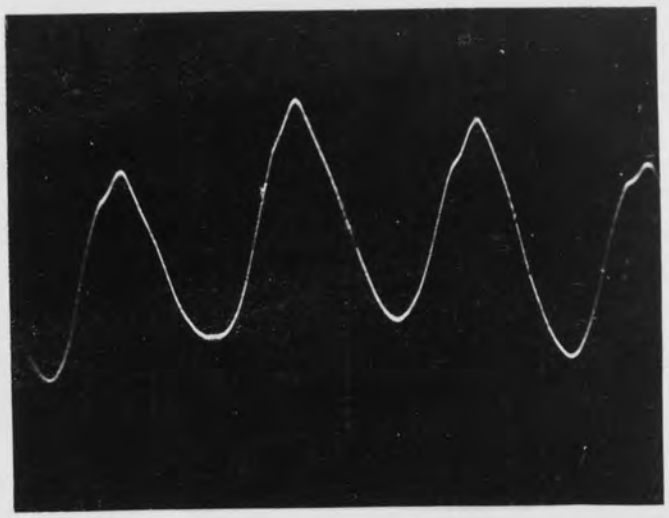

Current density waveform at the zero position of the fundamental

Scales:

Current density wave	1.35 $(A/mm^2)/cm$
Time base	2 ms/cm
Sweeping magnification	5
Signal amplification	50

(b)

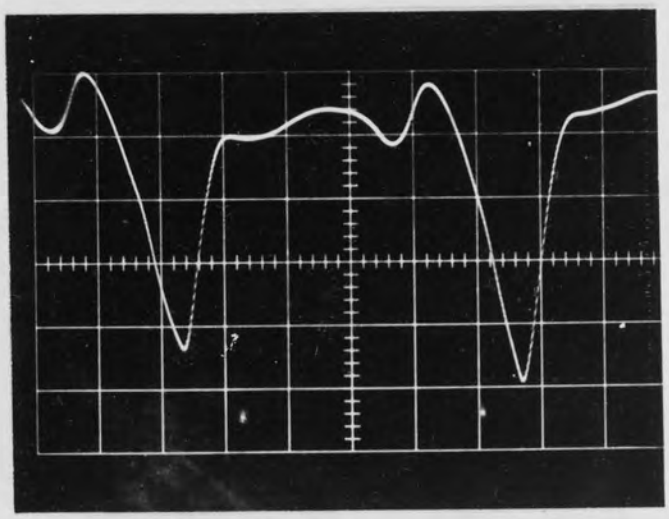

Current density waveform at the peak position of the fundamental

Scales:

Current density wave	13.5 $(A/mm^2)/cm$
Time base	2 ms/cm
Sweeping magnification	10
Signal amplification	50

Fig 7.34 Oscillograms of J-probe 4 taken at synchronous speed, 415 V applied line voltage

(BAR SURFACE CURRENT DENSITY)

(a)

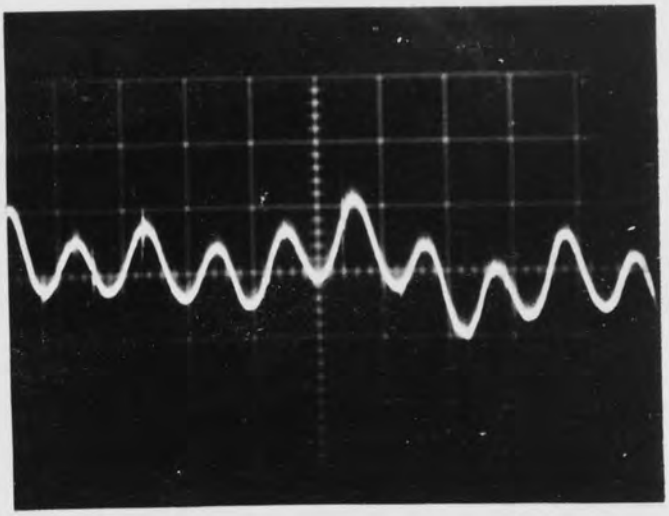

Current density waveform at the zero position of the fundamental

Scales:

Current density wave	0.674	$(A/mm^2)/cm$
Time base	2	ms/cm
Sweeping magnification	2	
Signal amplification	50	

(b)

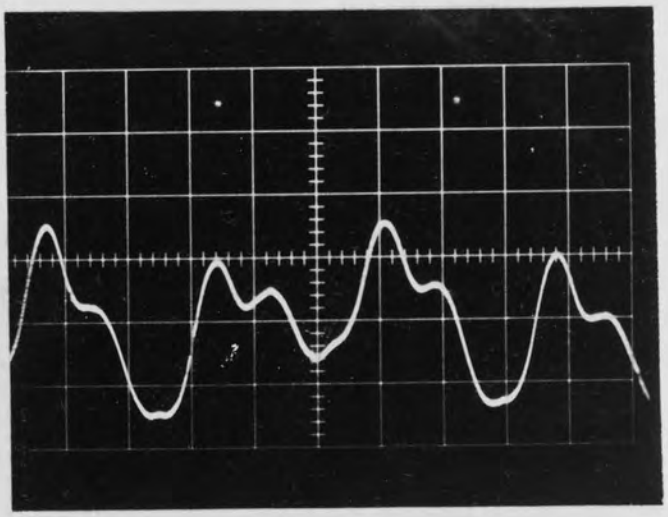

Current density waveform at the peak position of the fundamental

Scales:

Current density wave	0.674	$(A/mm^2)/cm$
Time base	2	ms/cm
Sweeping magnification	5	
Signal amplification	50	

Fig 7.35 Oscillograms of J-probe 1 taken at synchronous speed, 415 V applied line voltage

(BAR SURFACE CURRENT DENSITY)

(a)

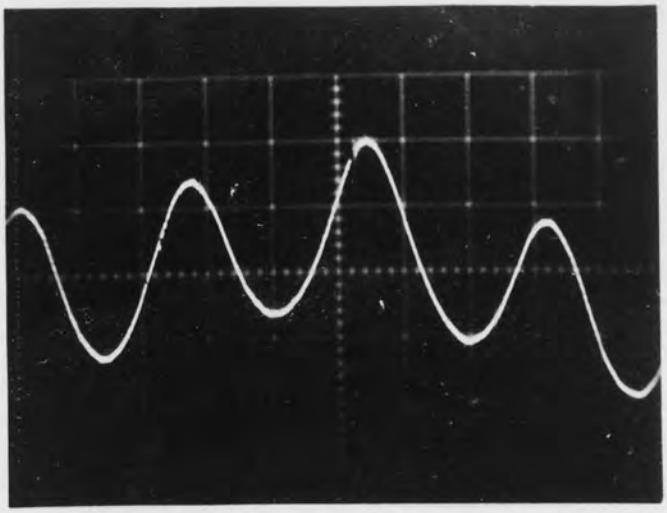

Current density waveform at the zero position of the fundamental

Scales:

Current density wave	0.674	$(A/mm^2)/cm$
Time base	2	ms/cm
Sweeping magnification	5	
Signal amplification	50	

(b)

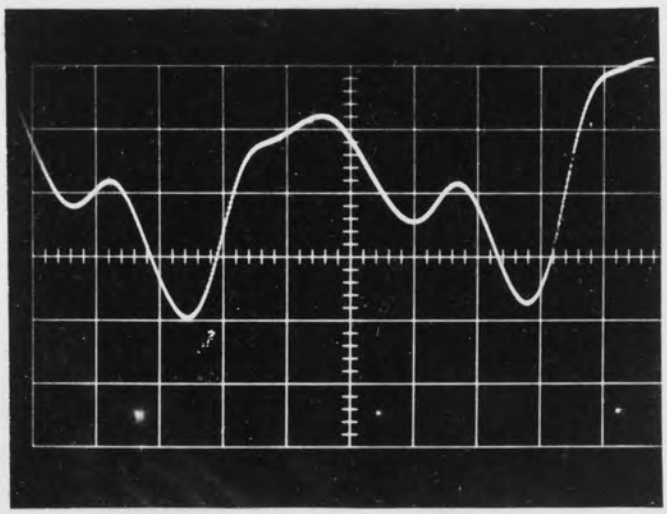

Current density waveform at the peak position of the fundamental

Scales:

Current density wave	1.35	$(A/mm^2)/cm$
Time base	2	ms/cm
Sweeping magnification	10	
Signal amplification	50	

Fig 7.36 Oscillograms of J-probe 2 taken at synchronous speed, 415 V applied line voltage

(BAR SURFACE CURRENT DENSITY)

(a)

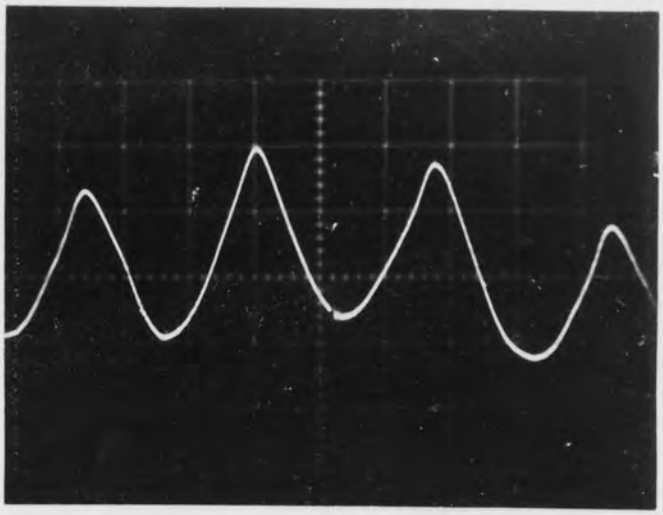

Current density waveform at the zero position of the fundamental

Scales:

Current density wave	1.35 $(A/mm^2)/cm$
Time base	2 ms/cm
Sweeping magnification	5
Signal amplification	50

(b)

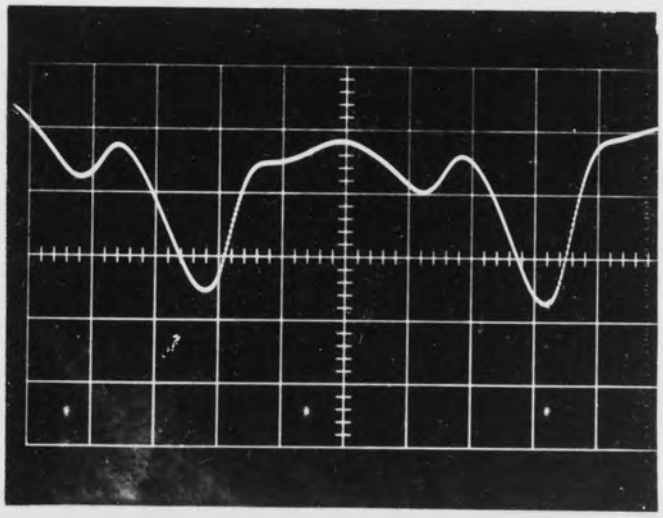

Current density waveform at the peak position of the fundamental

Scales:

Current density wave	6.74 $(A/mm^2)/cm$
Time base	2 ms/cm
Sweeping magnification	10
Signal amplification	50

Fig 7.37 Oscillograms of J-probe 3 taken at synchronous speed, 415 V applied line voltage

(BAR SURFACE CURRENT DENSITY)

(a)

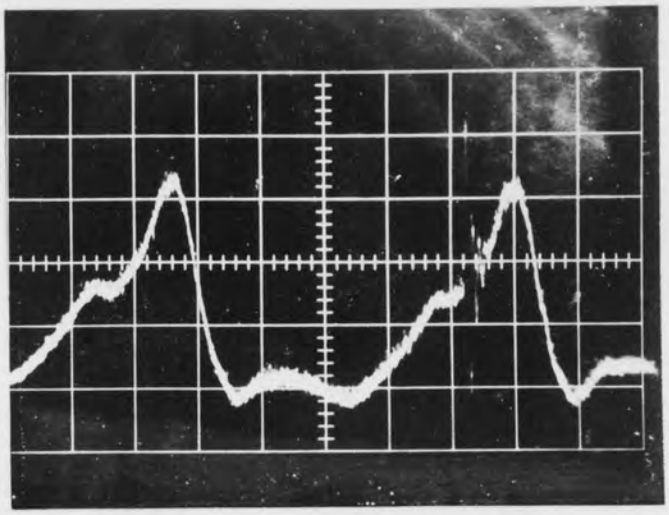

Current density waveform at the zero position of the fundamental

Scales:

Current density wave	0.33	$(A/mm^2)/cm$
Time base	2	ms/cm
Sweeping magnification	10	
Signal amplification	50	

(b)

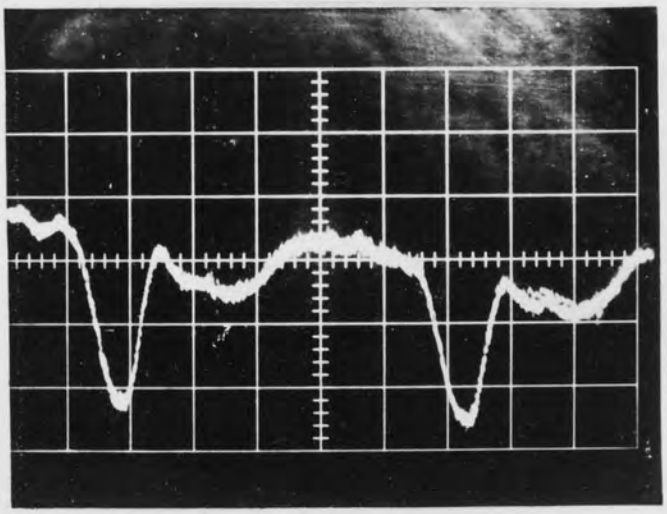

Current density waveform at the peak position of the fundamental

Scales:

Current density wave	0.33	$(A/mm^2)/cm$
Time base	2	ms/cm
Sweeping magnification	10	
Signal amplification	50	

Fig 7.38 Oscillograms of iron surface current density taken at synchronous speed, 415 V applied line voltage

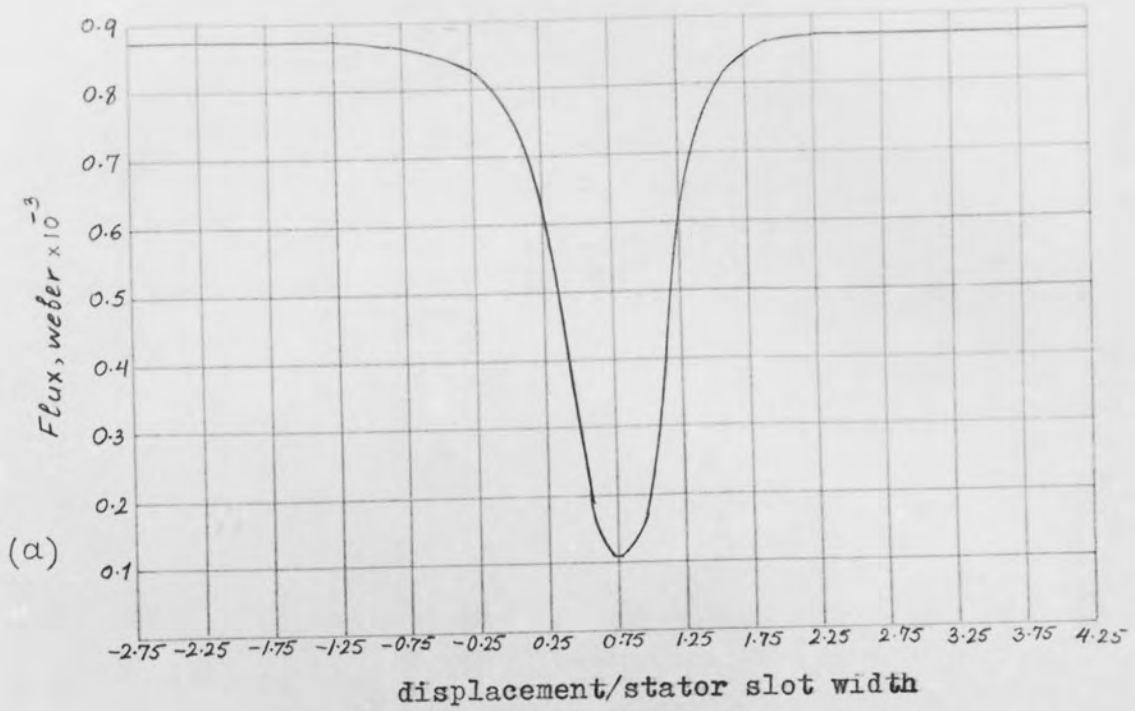

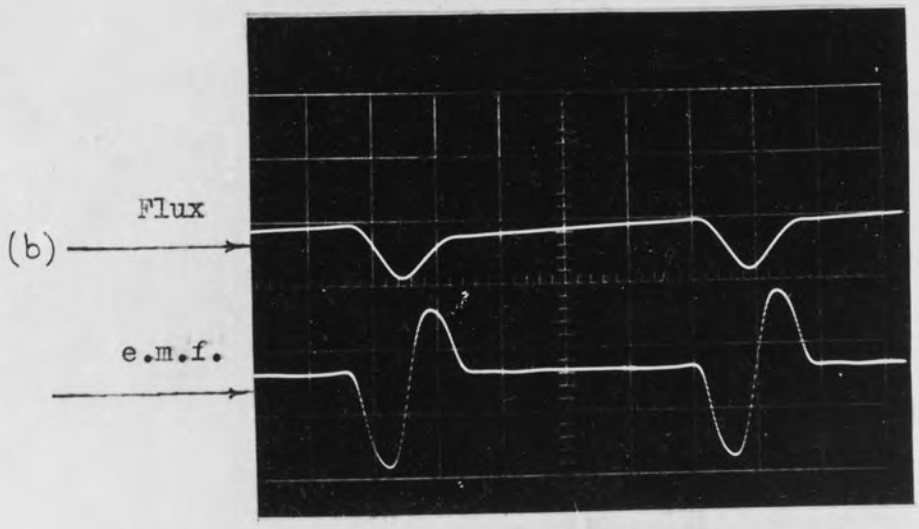

Fig 7.39 A comparison between the flux waveforms of the secondary surface search coil 25 obtained theoretically and experimentally

(a)-theoretical
(b)-experimental

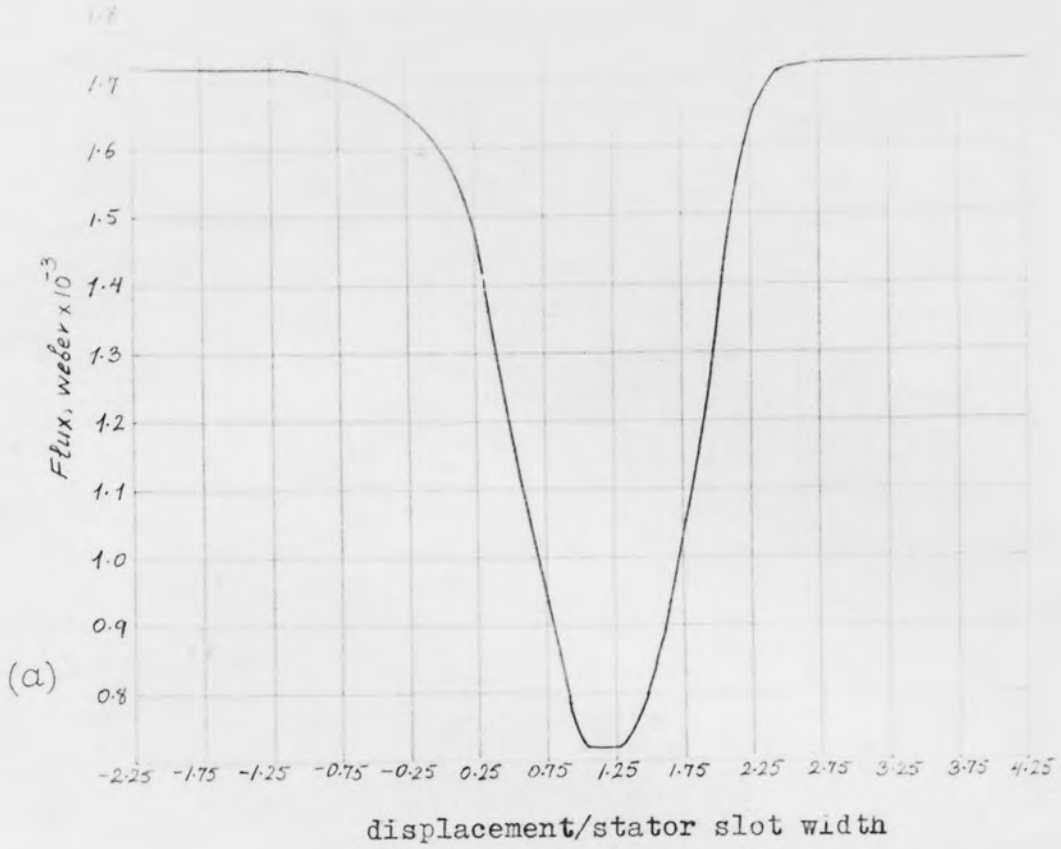

Fig 7.40 A comparison between the flux waveforms of the secondary surface search coil 26 obtained theoretically and experimentally

(a)-theoretical
(b)-experimental

(a)

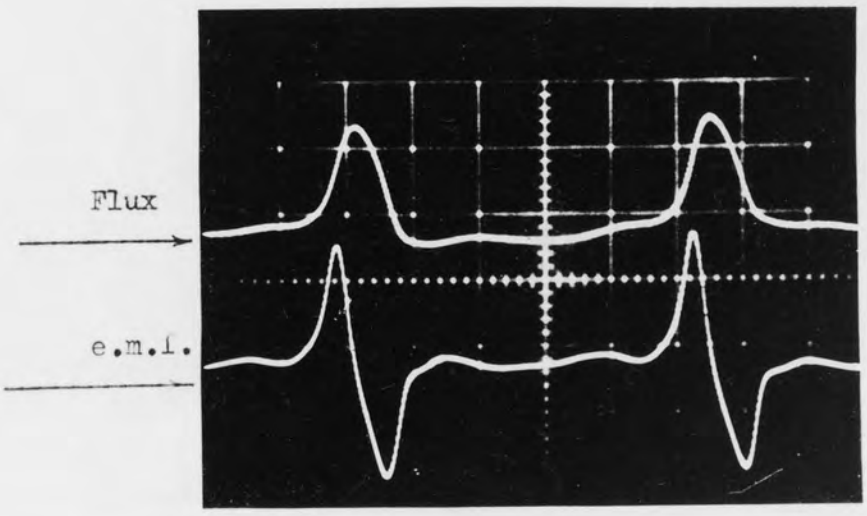

(b)

Fig 7.41 A comparison between the flux waveforms of the secondary tooth tip search coil 42 obtained theoretically and experimentally

(a)-theoretical
(b)-experimental

(a)

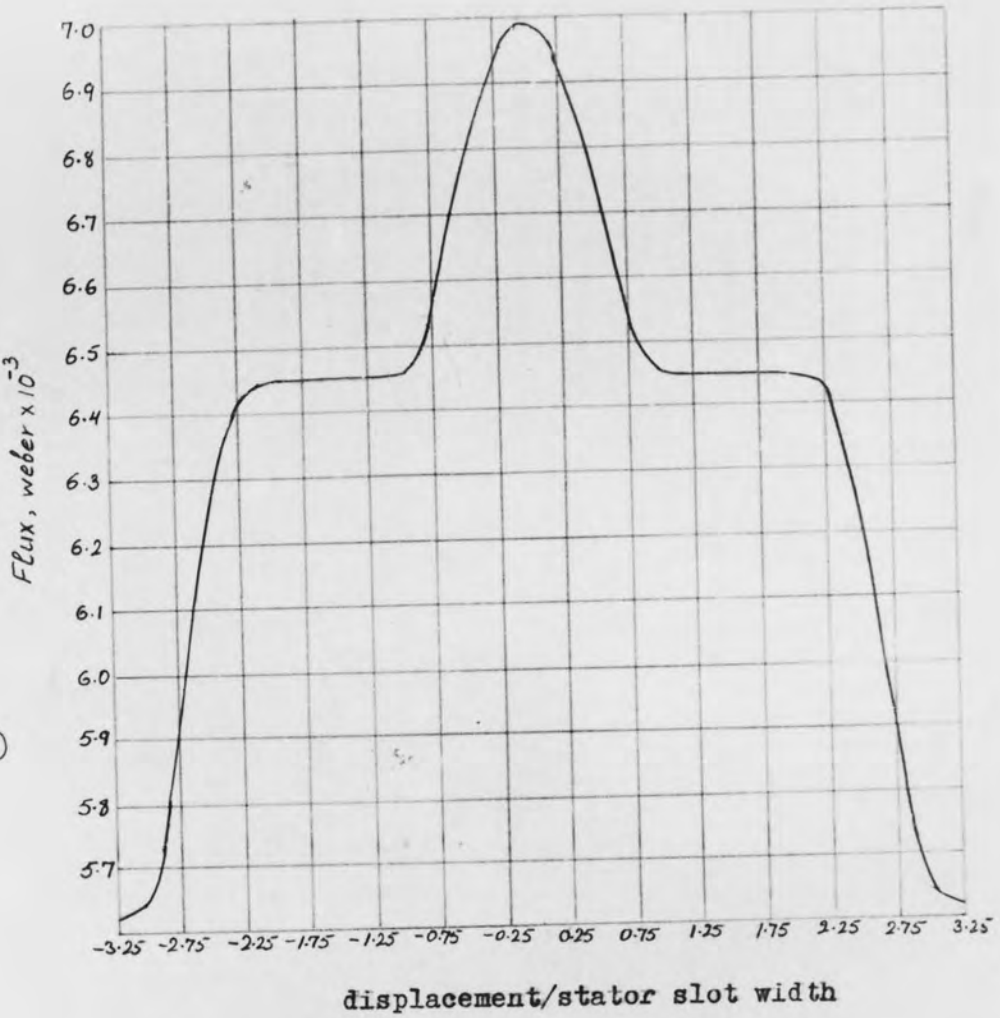

(b)

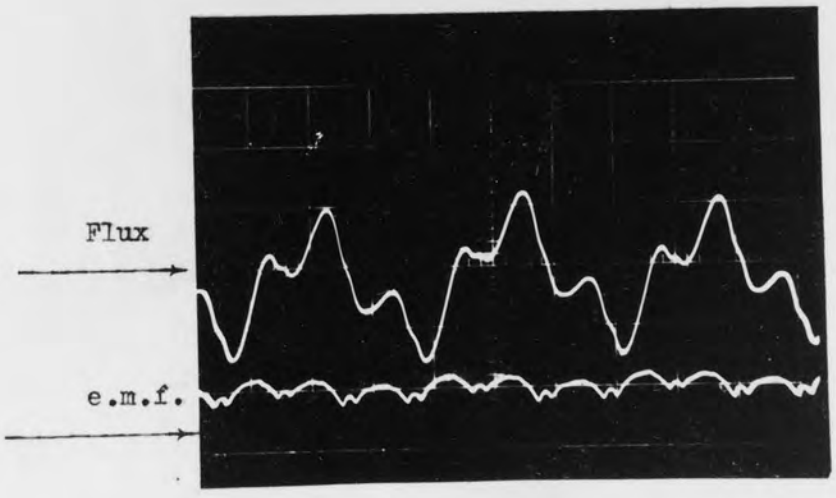

Fig 7.42 A comparison between the flux waveforms of the secondary tooth search coil 44 obtained theoretically and experimentally

(a) theoretical
(b) experimental

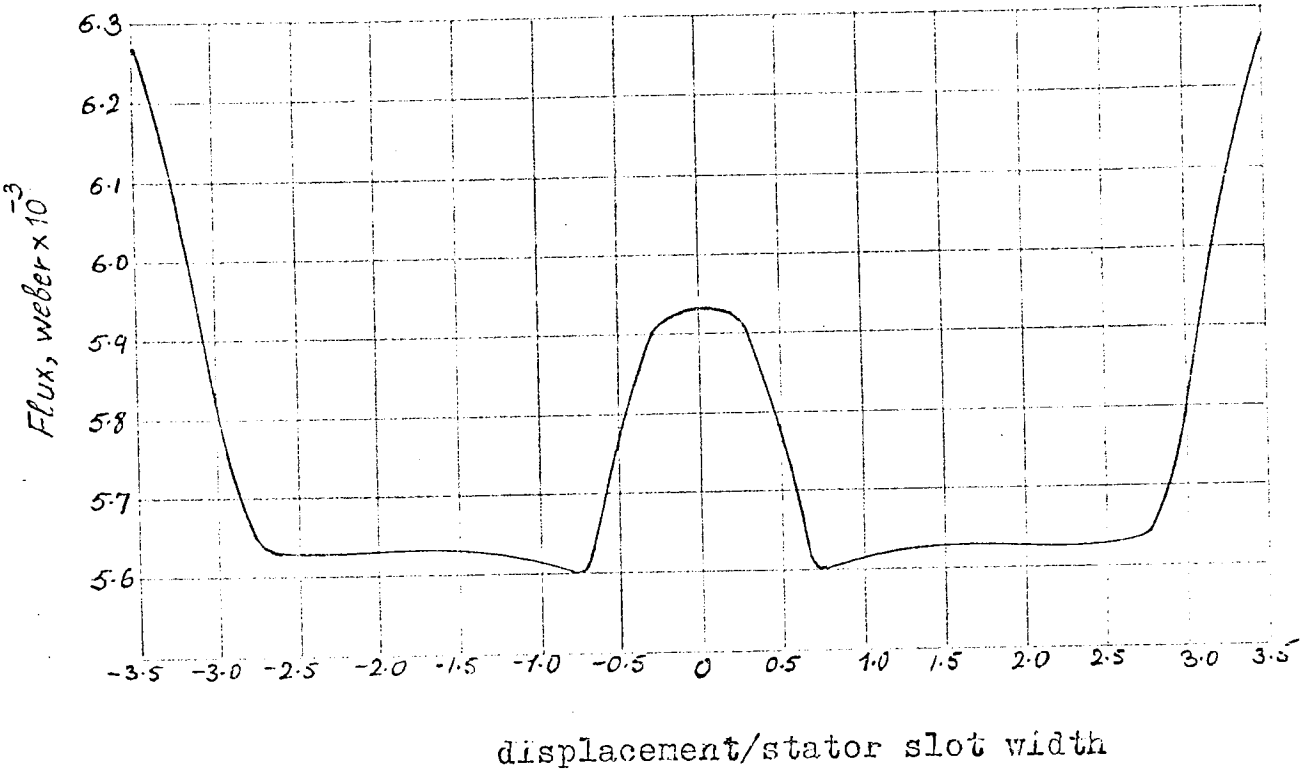

Fig 7.43

Computed waveform of the total stator tooth flux

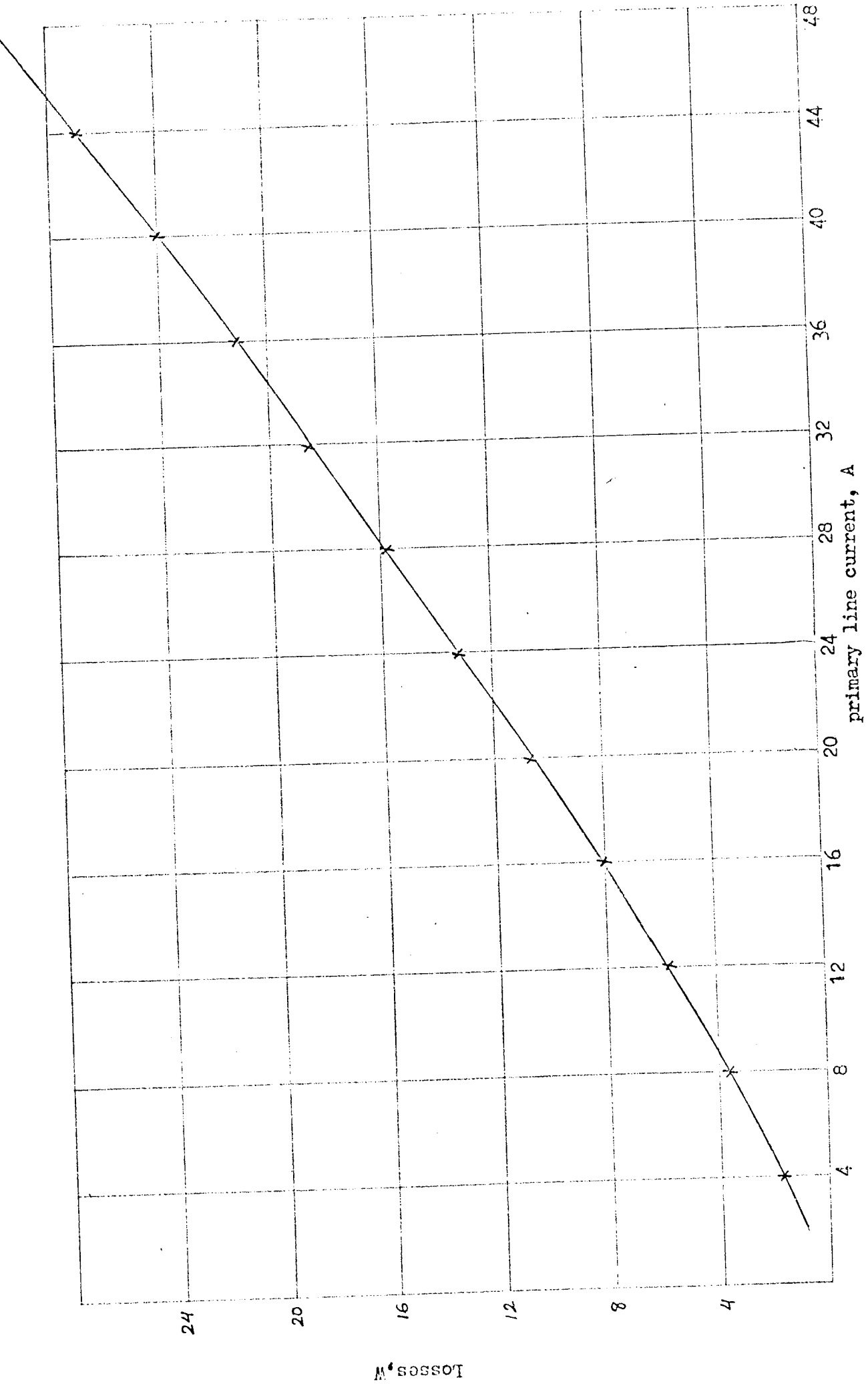

Fig 8.1 Brush losses per phase against current

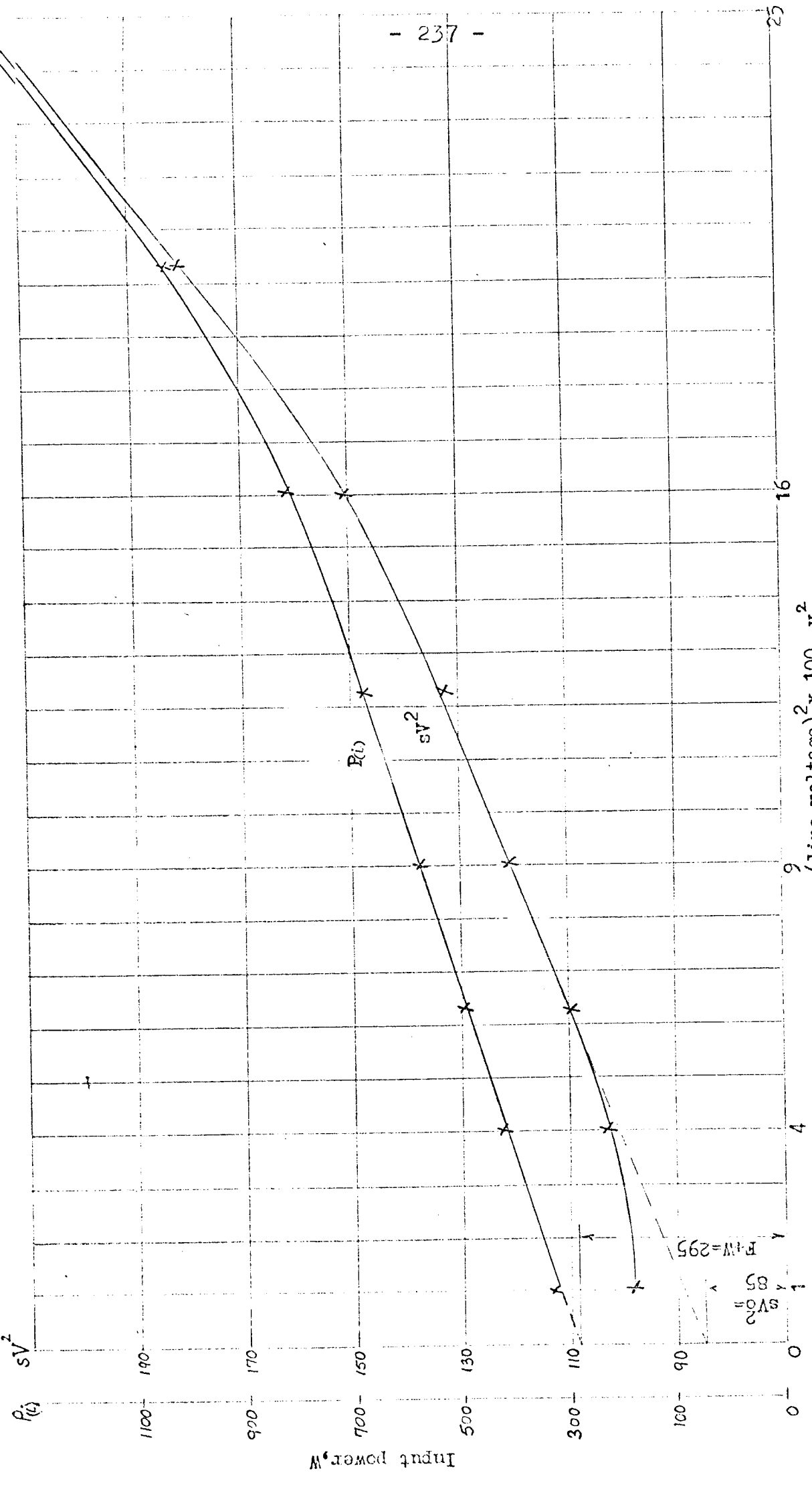

Fig 8.2 Variation of the input power and sV^2 with applied line voltage (Rawcliffe-Menon test)

$P_{(i)}$-Input power less I^2R
F+W-Friction and windage

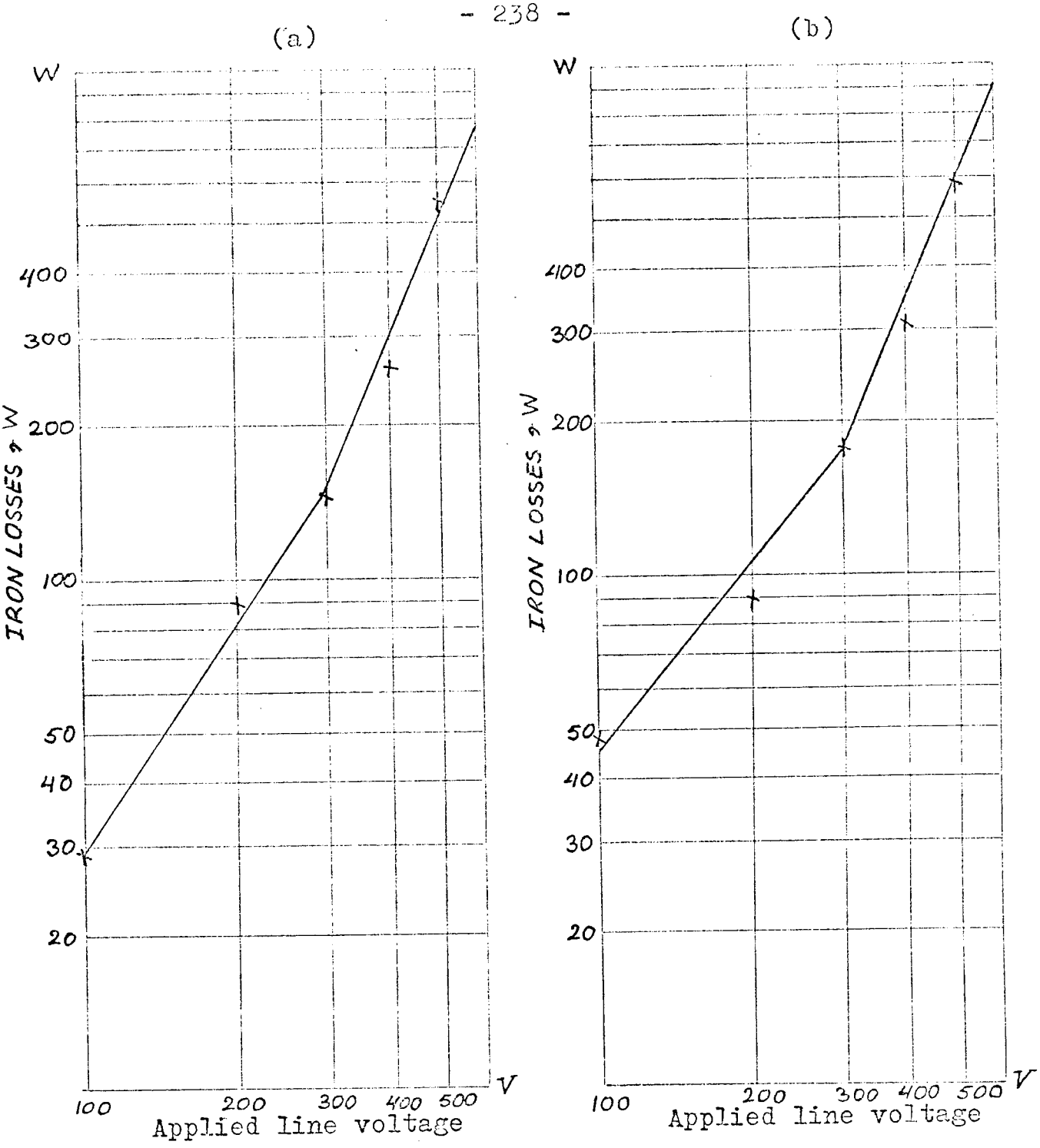

Fig 8.3

Iron losses versus applied voltage
(a)-Fundamental frequency losses
(b)-High frequency losses

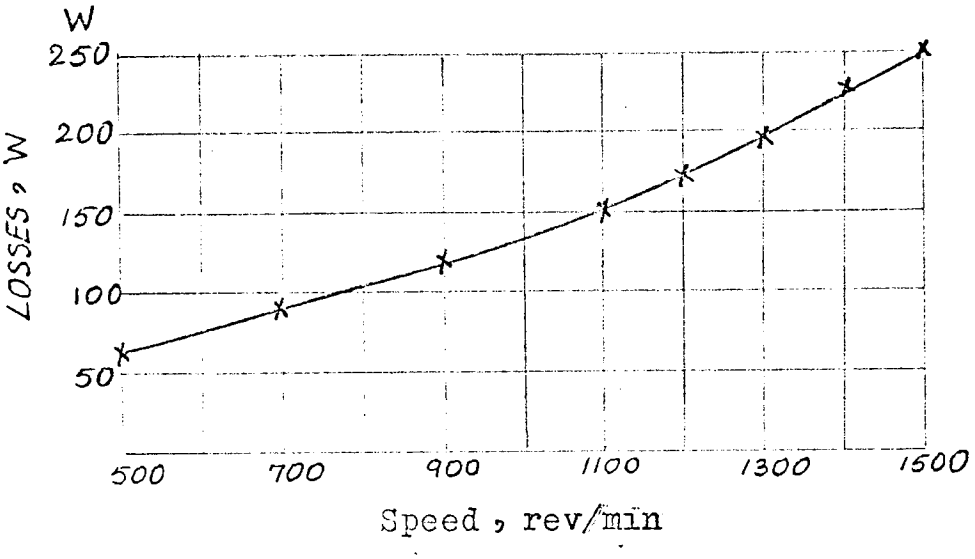

Fig 8.4 Friction and windage losses versus rotor speed

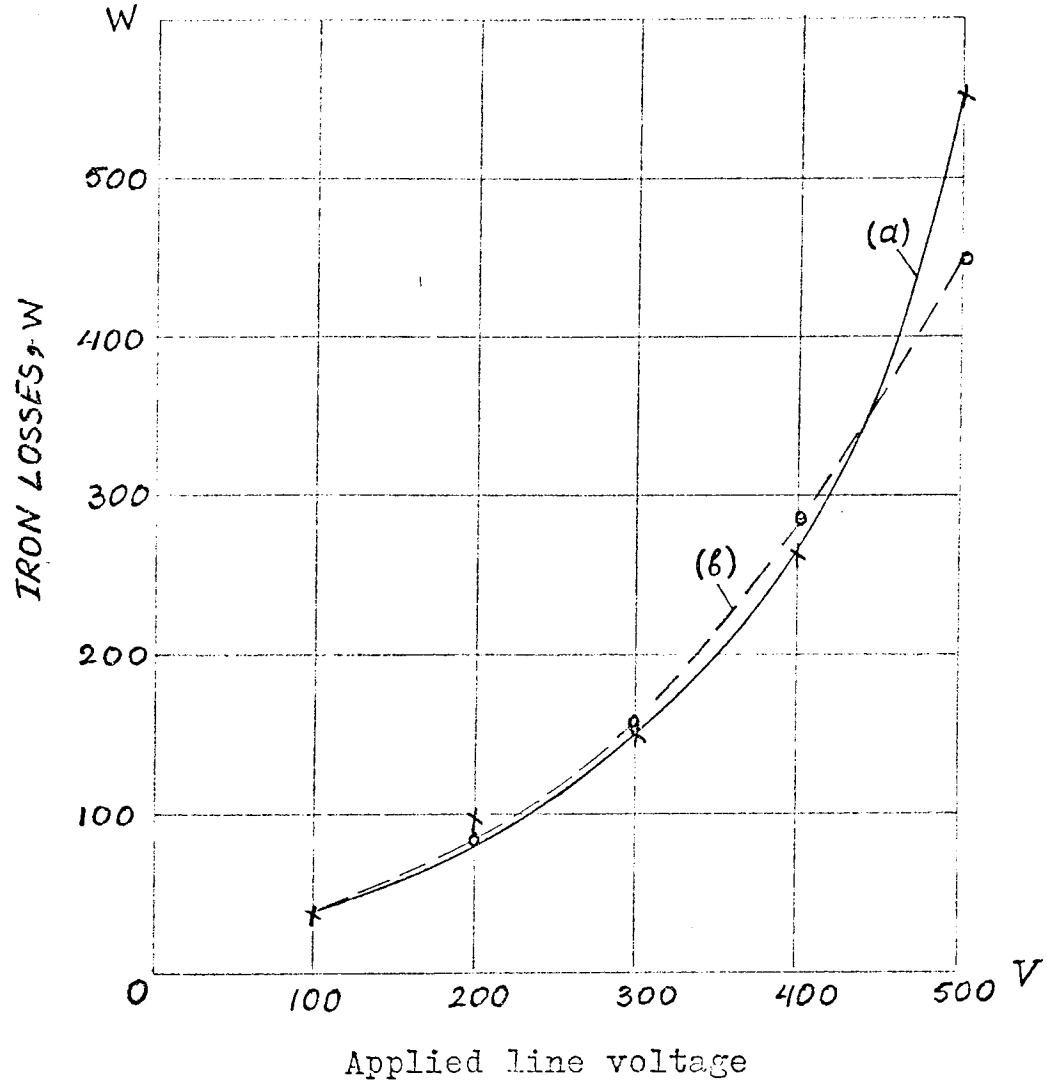

Fig 8.5 Fundamental frequency iron losses versus voltage

(a)-Rawcliffe-Menon test
(b)-Driven rotor test

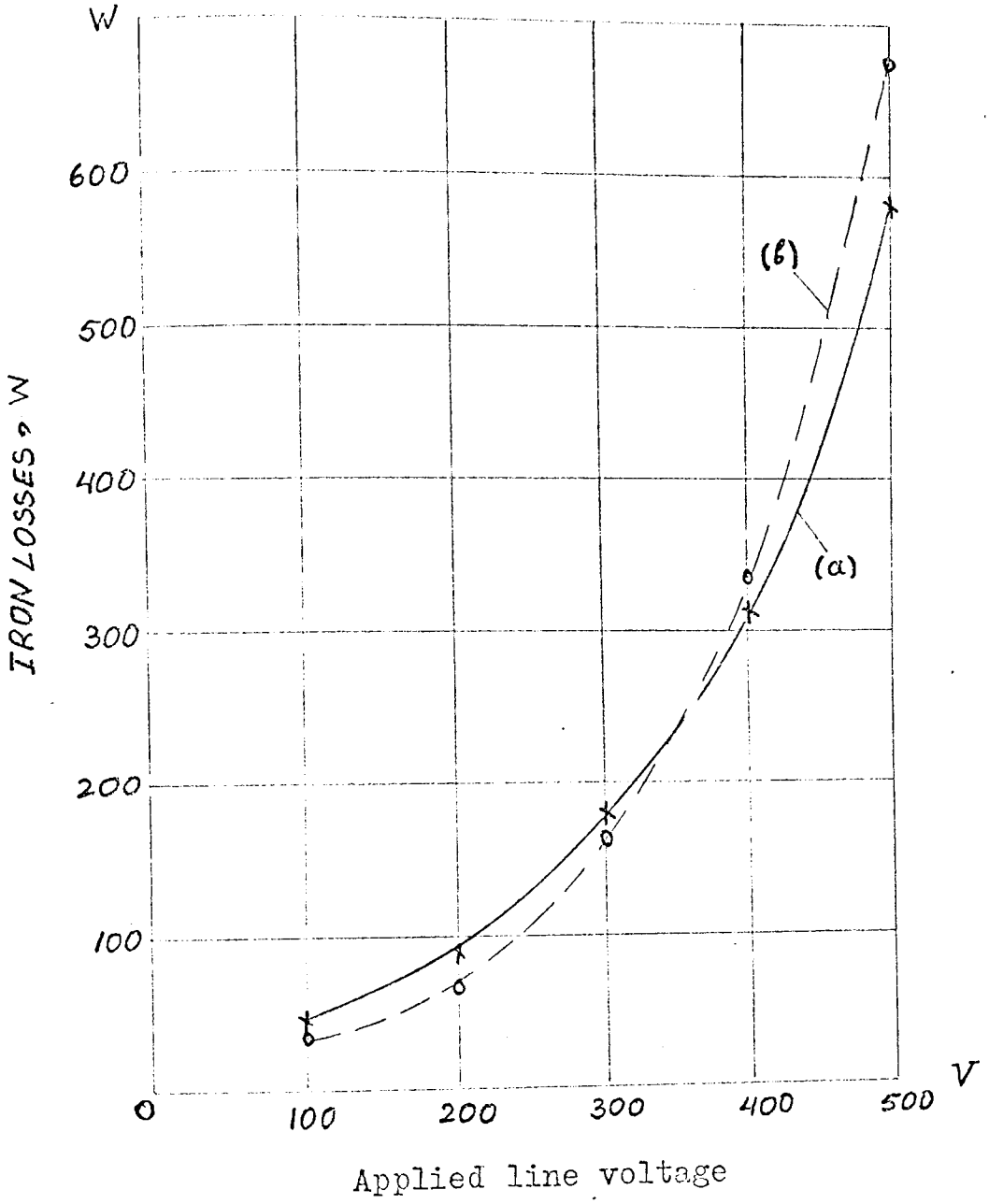

Fig 8.6

High frequency iron losses versus voltage

(a)-Rawcliffe-Henon test
(b)-Driven rotor test

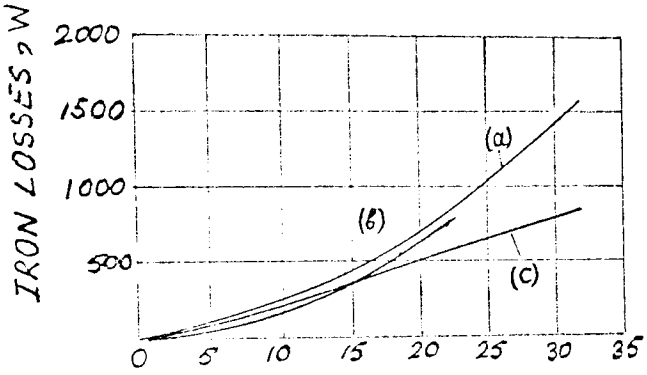

Fig 8.7

Pulsation losses-60 cycles [56]
(Reproduced from Spooners paper)
(a)-Unconnected bars
(b)-Connected bars
(c)-No bars

COMPUTER PROGRAM FOR THE ANALYSIS OF CHAPTER 4 AND APPENDIX 10.4

In the program, the notations used for the stator, rotor, and air gap dimensions are as follows :

PS- half stator slot width (rad)

PR- half rotor slot width (rad)

G- air gap length (rad)

S1- stator slot width (rad)

S2- rotor slot width (rad)

T1- rotor slot pitch (rad)

2π -stator slot pitch (rad)

All dimensions are expressed in terms of one stator slot pitch which is made equal to 2π. (For examle, the stator slot pith of the experimental machine ,see Ch. 6, is 25.1 mm and this dimension is made equal to 2π. The stator slot width is 4 mm , therefore this dimension in terms of one stator slot pitch is 0.318π ;or per π unit is 0.318.) The dimension DIS which denotes the displacement between the centre of a stator slot width and the centre of a rotor slot width (see, Fig. 4.1) is also expressed per π unit.

The notations in the out-put of the program indicate the followings :

Bø -the average air gap flux density, per unit (P)

A1, A2, ...etc. -the amplitude of the flux density harmonics of the order of stator slot pitch, per unit.

B1, B2,, ...etc. -the amplitude of the flux density harmonics of the order of rotor slot pitch, per unit.

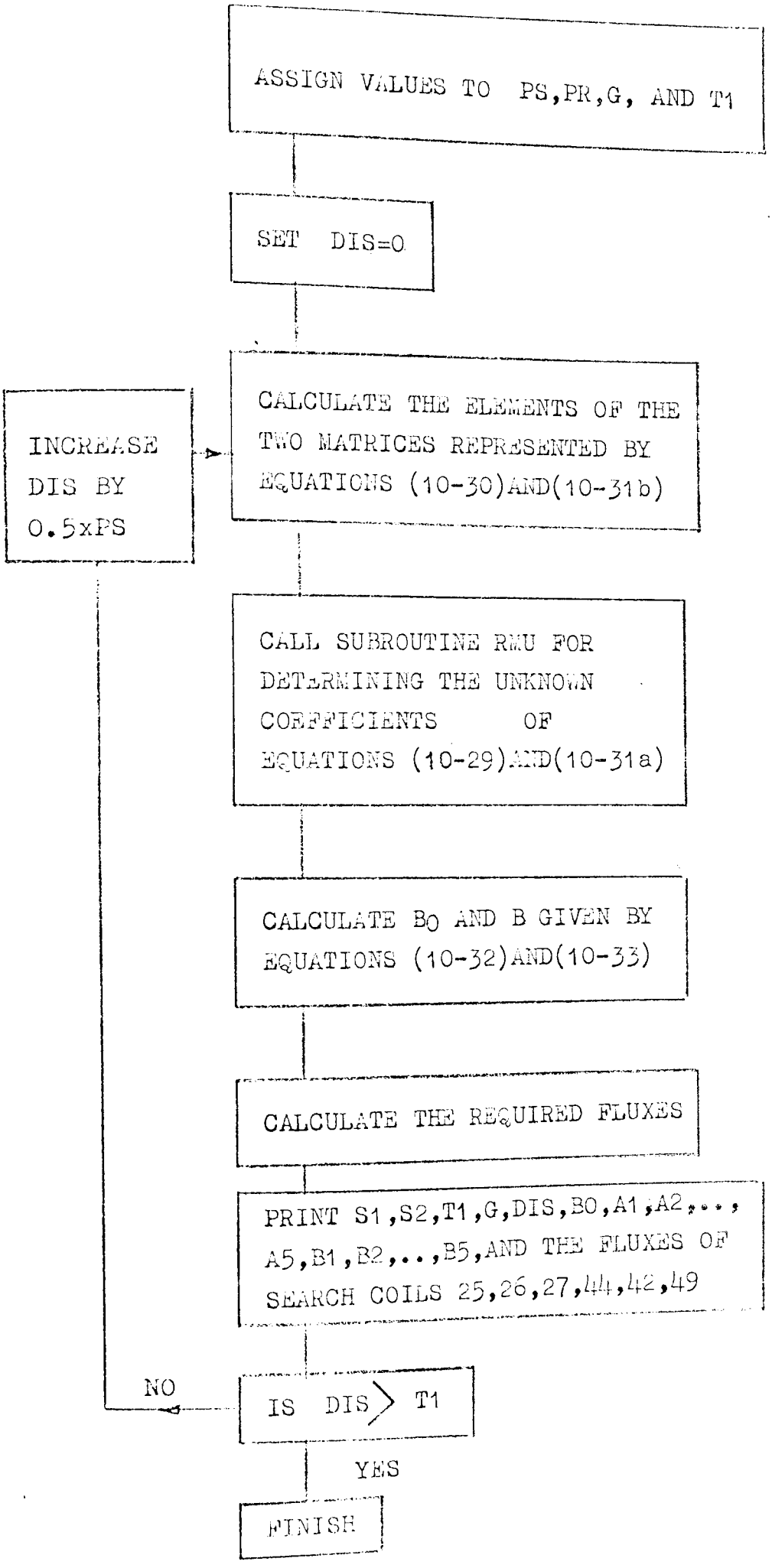

FLOW DIAGRAM FOR THE COMPUTER PROGRAM

THE PROGRAM

```
      DIMENSION A(10,10),C(10,10),A1(50),A2(50),A3(50),A4(50)
     1,A5(50),A6(50),A7(50),A8(50),A9(50),A10(50),A11(50),A12
     1(50),A13(50),A14(50),B(10),BN(10),BF1(20),BF2(20),B1(10)
1,T(6)
SINH(Z)=(EXP(Z)-EXP(-Z))/2.0
       P=3.141592653
        PSQR=P*P
       PS=0.1593
       PR=0.1195
       G=0.0478
       T1=1.129
       S1=2.*PS
       S2=2.*PR
       DO 800 J4=1,30
       DJ4=J4-14
       DIS=0.5*PS*DJ4
IF(ABS(DIS).GT.T1)GO TO 800
       DO 10 K=1,10
KK=K+10
BF1(KK)=0.
BF2(KK)=0.
       B(K)=0.
       BN(K)=0.
       BF1(K)=0.
       BF2(K)=0.
       B1(K)=0.
       DO 10 I=1,10
       A(K,I)=0.
10     C(K,I)=0.
       DO 20 K=I,6
20        T(K)=0.
       E1=PS*PS
       E2=PR*PR
       E3=T1*T1
E4=32.*E1/(PSQR*G)
E5=E4*E2/E1
E6=4.*E1/P
E7=4.*E2/(P*E3)
E8=4.*PS/(P*G)
E9=E8*PR/PS
E10=4.*E1
E11=4.*E2
E12=4.*E1/E3
E13=4.*E2/E3
E14=P*(1.-PS)
E15=P*(1.+PS)
E16=P*(T1-PS-DIS)/T1
E17=P*(T1+PS-DIS)/T1
E18=P*(T1-PR)/T1
E19=P*(T1+PR)/T1
E20=P*(1.+DIS-PR)
E21=P*(1.+DIS+PR)
E22=P*G
E23=P*G/T1
```

continued

continuation

```
      DO 30 K=1,50
      RK=K
      A1(K)=COS(RK*E14)
      A2(K)=COS(RK*E15)
      A3(K)=COS(RK*E16)
      A4(K)=COS(RK*E17)
      A5(K)=COS(RK*E18)
      A6(K)=COS(RK*E19)
      A7(K)=COS(RK*E20)
      A8(K)=COS(RK*E21)
A9(K)=SINH(RK*E22)
A10(K)=TANH(RK*E22)
A11(K)=SINH(RK*E23)
A12(K)=TANH(RK*E23)
A13(K)=(1./A9(K)-1./A10(K))/(A11(K)*(1./A11(K)-1./A12
1(K)))
30A14(K)=(1./A12(K)-1./A11(K))/(A9(K)*(1./A10(K)-1./A9
1(K)))
      ODI=1.
      DO 270 I=1,10
      ODI=-ODI
      RI=I
      RIS=RI*RI
      IF(ODI.GT.0.)GO TO 40
      B(I)=-E8/RI
      B1(I)=-E9/RI
40      A(I,I)=RI*P/2.
      C(I,I)=-A(I,I)
      ODM=1.
      DO 260 M=1,10
      ODM=-ODM
      RM=M
      RMS=RM*RM
      IF((ODM.GT.0.).OR.(ODI.GT.0.))GO TO 50
      A(I,M)=E4/(RI*RM)+A(I,M)
      C(I,M)=-E5/(RI*RM)+C(I,M)
50DO 250 K=1,50
RK=K
RKS=RK*RK
DM1=RMS-RKS*E10
IF(ABS(DM1)-1E-3)60,60,70
60T(1)=E6*RM*RI*(E14*SIN(RK*E14)-E15*ODM*SIN(RK*E15))/
1(8.*E1)
GO TO 80
70T(1)=E6*RK*RM*RI*(A1(K)-ODM*A2(K))/DM1
80DI11=RIS-RKS*E10
IF(ABS(DI11)-1E-3)90,90,100
90T(2)=(E14*SIN(RK*E14)-E15*ODI*SIN(RK*E15))/(8.*A10(K)
1*RK*E1)
GO TO 110
100T(2)=(A1(K)-ODI*A2(K))/(A10(K)*DI11)
110DI12=RIS-RKS*E12
IF(ABS(DI12)-1E-3)120,120,130
120T(3)=A13(K)*(E16*SIN(RK*E16)-E17*ODI*SIN(RK*E17))/
1(2.*RK*E12)
```

continued

continuation

```
GO TO 140
130T(3)=A13(K)*(A3(K)-ODI*A4(K))/DI12
140DM2=RMS-RKS*E13
IF(ABS(DM2)-1E-3)150,150,160
150T(4)=E7*RM*RI*(E18*SIN(RK*E18)-E19*ODM*SIN(RK*E19))/
1(2.*E13)
GO TO 170
160T(4)=E7*RK*RM*RI*(A5(K)-ODM*A6(K))/DM2
170DI21=RIS-RKS*E13
IF(ABS(DI21)-1E-3)180,180,190
180T(5)=(E18*SIN(RK*E18)-E19*ODI*SIN(RK*E19))/(2.*E13*RK
1*A12(K))
GO TO 200
190T(5)=(A5(K)-ODI*A6(K))/(DI21*A12(K))
200DI22=RIS-RKS*E11
IF(ABS(DI22)-1E-3)210,210,220
210T(6)=A14(K)*(E20*SIN(RK*E20)-E21*ODI*SIN(RK*E21))/(8.
1*RK*E2)
GO TO 230
220T(6)=A14(K)*(A7(K)-ODI*A8(K))/DI22
230A(I,M)=T(1)*(T(2)+T(3))+A(I,M)
C(I,M)=-T(4)*(T(5)+T(6))+C(I,M)
DO 240 JJ=1,6
240T(JJ)=0.0
250CONTINUE
260CONTINUE
270CONTINUE
      N=10
CALL RMIU(A,N,ISING,B)
      DO 280 K=1,10
      BN(K)=B(K)
      B(K)=BI(K)
      DO 280 I=1,10
280   A(K,I)=C(K,I)
N=10
CALL RMIU(A,N,ISING,B)
R1=P*(1.+DIS-3.*PR)
R2=P*(1.+DIS-PR)
R3=P*(T1-3.*PR)/T1
R4=P*(T1-PR)/T1
R5=P*(1.+DIS-5.*PR)
R6=P*(T1-5.*PR)/T1
R7=P*(1.+DIS-7.*PR)
R8=P*(T1-7.*PR)/T1
R9=P*(1.+DIS-T1)
R10=P*(1.+DIS+T1)
R11=P*(1.+DIS+PR)
R12=P*(T1+PR)/T1
      ODM=1.
CX5=0.
CX6=0.
      B0=1.
      DO 360 M=1,10
      ODM=-ODM
      RM=M
RMS=RM*RM
```

continued

continuation

```
CX5=CX5+B(M)*E22
CX6=CX6+B(M)*ODM*E22
      IF(ODM.GT.0.)GO TO 290
B0=B0+(2./(P*RM))*(PS*BN(M)-PR*B(M)/T1)
CX1=B0*P*S2
CX2=2.*CX1
CX3=3.*CX1
CX4=B0*P*(2.*T1-S2)
290       DO 360 K=1,20
      RK=K
      RKS=RK*RK
DN1=RMS-RKS*E10
IF(ABS(DN1)-1E-3)310,310,320
310BF1(K)=BF1(K)+P*G*RM*PS*BN(M)*(E14*SIN(RK*E14)-E15*ODM*SIN
1(RK*E15))/(P*A9(K)*E10)
      GO TO 330
320BF1(K)=BF1(K)+2.*P*G*PS*RK*RM*BN(M)*(A1(K)-ODM*A2(K))/(P*
1A9(K)*DN1)
330DN2=RMS-RKS*E13
      IF(ABS(DN2)-1E-3)340,340,350
340BF2(K)=BF2(K)-P*G*RM*PR*B(M)*(E18*SIN(RK*E18)-E19*ODM*
1SIN(RK*E19))/(P*E11*A12(K))
      GO TO 355
350BF2(K)=BF2(K)-2.*P*G*PR*RK*RM*B(M)*(A5(K)-ODM*A6(K))/(P*
1E3*A12(K)*DN2)
355A3(K)=SIN(RK*R2)
A4(K)=SIN(RK*R4)
CX1=CX1+BF1(K)*(A3(K)-SIN(RK*R1))/RK+BF2(K)*T1*(A4(K)
1-SIN(RK*R3))/RK
CX2=CX2+BF1(K)*(A3(K)-SIN(RK*R5))/RK+BF2(K)*T1*(A4(K)
1-SIN(RK*R6))/RK
CX3=CX3+BF1(K)*(A3(K)-SIN(RK*R7))/RK+BF2(K)*T1*(A4(K)
1-SIN(RK*R8))/RK
CX4=CX4+BF1(K)*((A3(K)-SIN(RK*R9))+(SIN(RK*R10)-SIN(
1RK*R11)))/RK+BF2(K)*T1*(A4(K)-SIN(RK*R12))/RK
360CONTINUE
CX5=ABS(CX5)
CX6=ABS(CX6)
CX4=CX4+CX5+CX6
      WRITE(2,700)S1,S2,T1,G,DIS
      WRITE(2,710)B0,(BF1(II),II=1,5),(BF2(KK),KK=1,5)
WRITE(2,720)CX1,CX2,CX3,CX4,CX5,CX6
720FORMAT(5X,25HFLUX OF SEARCH COIL 25 = ,1E14.6/,5X,25
1HFLUX OF SEARCH COIL 26 = ,1E14.6/,5X,25HFLUX OF SEA
1RCH COIL 27 = ,1E14.6/,5X,19HTOTAL TOOTH FLUX = ,1
1E14.6/,5X,25HFLUX OF SEARCH COIL 42 = ,1E14.6/,5X,25
1HFLUX OF SEARCH COIL 49 = ,1E14.6///)
700   FORMAT(5X,2HS1,14X,2HS2,14X,2HT1,14X,1HG,14X,3HDIS/,
     15E14.6///)
710   FORMAT(5X,5HB0 = ,1E14.6/,5X,2HA1,13X,2HA2,13X,2HA3,13X
     1,2HA4,13X,2HA5/,5E14.6/,5X,2HB1,13X,2HB2,13X,2HB3,13X,2H
     1B4,13X,2HB5/,5E14.6//)
800   CONTINUE
      END
```

COMPUTER PRINT OUT RELATING TO TABLE 4.1(SECTION 4.3.1)

S1	S2	T1	G	DIS
0.200000E+00	0.200000E+00	0.100000E+01	0.100000E+00	0.000000E+00

B0 = 0.957175E+00

S1	S2	T1	G	DIS
0.400000E+00	0.400000E+00	0.100000E+01	0.100000E+00	0.000000E+00

B0 = 0.890622E+00

S1	S2	T1	G	DIS
0.600000E+00	0.600000E+00	0.100000E+01	0.100000E+00	0.000000E+00

B0 = 0.826992E+00

S1	S2	T1	G	DIS
0.800000E+00	0.800000E+00	0.100000E+01	0.100000E+00	0.000000E+00

B0 = 0.769798E+00

COMPUTER PRINT OUT RELATING TO Figs. 4.2-4.6 (SECTION 4.3.1)

Computer print out for Fig. 4.2

S1	S2	T1	G	DIS
0.300000E+00	0.300000E+00	0.110000E+01	0.100000E+00	0.000000E+00

TOTAL ROTOR TOOTH FLUX = , 0.678630E+01 (mWb)

S1	S2	T1	G	DIS
0.300000E+00	0.300000E+00	0.110000E+01	0.100000E+00	0.750000E-01

TOTAL ROTOR TOOTH FLUX = , 0.675147E+01 (mWb)

S1	S2	T1	G	DIS
0.300000E+00	0.300000E+00	0.110000E+01	0.100000E+00	0.150000E+00

TOTAL ROTOR TOOTH FLUX = , 0.666456E+01 (mWb)

S1	S2	T1	G	DIS
0.300000E+00	0.300000E+00	0.110000E+01	0.100000E+00	0.225000E+00

TOTAL ROTOR TOOTH FLUX = , 0.654952E+01 (mWb)

S1	S2	T1	G	DIS
0.300000E+00	0.300000E+00	0.110000E+01	0.100000E+00	0.300000E+00

TOTAL ROTOR TOOTH FLUX = , 0.646233E+01 (mWb)

S1	S2	T1	G	DIS
0.300000E+00	0.300000E+00	0.110000E+01	0.100000E+00	0.375000E+00

continued

continuation

TOTAL ROTOR TOOTH FLUX = , 0.643510E+01 (mWb)

S1	S2	T1	G	DIS
0.300000E+00	0.300000E+00	0.110000E+01	0.100000E+00	0.450000E+00

TOTAL ROTOR TOOTH FLUX = , 0.643139E+01 (mWb)

S1	S2	T1	G	DIS
0.300000E+00	0.300000E+00	0.110000E+01	0.100000E+00	0.525000E+00

TOTAL ROTOR TOOTH FLUX = , 0.643096E+01 (mWb)

S1	S2	T1	G	DIS
0.300000E+00	0.300000E+00	0.110000E+01	0.100000E+00	0.600000E+00

TOTAL ROTOR TOOTH FLUX = , 0.643058E+01 (mWb)

S1	S2	T1	G	DIS
0.300000E+00	0.300000E+00	0.110000E+01	0.100000E+00	0.675000E+00

TOTAL ROTOR TOOTH FLUX = , 0.642713E+01 (mWb)

S1	S2	T1	G	DIS
0.300000E+00	0.300000E+00	0.110000E+01	0.100000E+00	0.750000E+00

TOTAL ROTOR TOOTH FLUX = , 0.639882E+01 (mWb)

S1	S2	T1	G	DIS
0.300000E+00	0.300000E+00	0.110000E+01	0.100000E+00	0.825000E+00

TOTAL ROTOR TOOTH FLUX = , 0.629054E+01 (mWb)

S1	S2	T1	G	DIS
0.300000E+00	0.300000E+00	0.110000E+01	0.100000E+00	0.900000E+00

TOTAL ROTOR TOOTH FLUX = , 0.611934E+01 (mWb)

S1	S2	T1	G	DIS
0.300000E+00	0.300000E+00	0.110000E+01	0.100000E+00	0.975000E+00

0.589040E+01

Computer print out for Fig. 4.3

S1	S2	T1	G	DIS
0.300000E+00	0.300000E+00	0.120000E+01	0.100000E+00	0.000000E+00

TOTAL ROTOR TOOTH FLUX = , 0.747992E+01 (mWb)

S1	S2	T1	G	DIS
0.300000E+00	0.300000E+00	0.120000E+01	0.100000E+00	0.750000E-01

TOTAL ROTOR TOOTH FLUX = , 0.744693E+01 (mWb)

S1	S2	T1	G	DIS
0.300000E+00	0.300000E+00	0.120000E+01	0.100000E+00	0.150000E+00

TOTAL ROTOR TOOTH FLUX = , 0.736707E+01 (mWb)

S1	S2	T1	G	DIS
0.300000E+00	0.300000E+00	0.120000E+01	0.100000E+00	0.225000E+00

TOTAL ROTOR TOOTH FLUX = , 0.725294E+01 (mWb)

S1	S2	T1	G	DIS
0.300000E+00	0.300000E+00	0.120000E+01	0.100000E+00	0.300000E+00

TOTAL ROTOR TOOTH FLUX = , 0.715679E+01 (mWb)

S1	S2	T1	G	DIS
0.300000E+00	0.300000E+00	0.120000E+01	0.100000E+00	0.375000E+00

TOTAL ROTOR TOOTH FLUX = , 0.712443E+01 (mWb)

S1	S2	T1	G	DIS
0.300000E+00	0.300000E+00	0.120000E+01	0.100000E+00	0.450000E+00

TOTAL ROTOR TOOTH FLUX = , 0.711963E+01 (mWb)

continued

continuation

S1	S2	T1	G	DIS
0.300000E+00	0.300000E+00	0.120000E+01	0.100000E+00	0.525000E+00

TOTAL ROTOR TOOTH FLUX = , 0.711834E+01 (mWb)

S1	S2	T1	G	DIS
0.300000E+00	0.300000E+00	0.120000E+01	0.100000E+00	0.600000E+00

TOTAL ROTOR TOOTH FLUX = , 0.711090E+01 (mWb)

S1	S2	T1	G	DIS
0.300000E+00	0.300000E+00	0.120000E+01	0.100000E+00	0.675000E+00

TOTAL ROTOR TOOTH FLUX = , 0.706074E+01 (mWb)

S1	S2	T1	G	DIS
0.300000E+00	0.300000E+00	0.120000E+01	0.100000E+00	0.750000E+00

TOTAL ROTOR TOOTH FLUX = , 0.692051E+01 (mWb)

S1	S2	T1	G	DIS
0.300000E+00	0.300000E+00	0.120000E+01	0.100000E+00	0.825000E+00

TOTAL ROTOR TOOTH FLUX = , 0.673182E+01 (mWb)

S1	S2	T1	G	DIS
0.300000E+00	0.300000E+00	0.120000E+01	0.100000E+00	0.900000E+00

TOTAL ROTOR TOOTH FLUX = , 0.656785E+01 (mWb)

S1	S2	T1	G	DIS
0.300000E+00	0.300000E+00	0.120000E+01	0.100000E+00	0.975000E+00

TOTAL ROTOR TOOTH FLUX = , 0.649276E+01 (mWb)

Computer print out for Fig. 4.4

S1	S2	T1	G	DIS
0.300000E+00	0.900000E+00	0.120000E+01	0.100000E+00	0.000000E+00

TOTAL ROTOR TOOTH FLUX = , 0.675038E+01 (mWb)

S1	S2	T1	G	DIS
0.300000E+00	0.900000E+00	0.120000E+01	0.100000E+00	0.750000E-01

TOTAL ROTOR TOOTH FLUX = , 0.676009E+01 (mWb)

S1	S2	T1	G	DIS
0.300000E+00	0.900000E+00	0.120000E+01	0.100000E+00	0.150000E+00

TOTAL ROTOR TOOTH FLUX = , 0.680389E+01 (mWb)

S1	S2	T1	G	DIS
0.300000E+00	0.900000E+00	0.120000E+01	0.100000E+00	0.225000E+00

TOTAL ROTOR TOOTH FLUX = , 0.680629E+01 (mWb)

S1	S2	T1	G	DIS
0.300000E+00	0.900000E+00	0.120000E+01	0.100000E+00	0.300000E+00

TOTAL ROTOR TOOTH FLUX = , 0.669203E+01 (mWb)

S1	S2	T1	G	DIS
0.300000E+00	0.900000E+00	0.120000E+01	0.100000E+00	0.375000E+00

TOTAL ROTOR TOOTH FLUX = , 0.647620E+01 (mWb)

S1	S2	T1	G	DIS
0.300000E+00	0.900000E+00	0.120000E+01	0.100000E+00	0.450000E+00

TOTAL ROTOR TOOTH FLUX = , 0.624630E+01 (mWb)

continued

continuation

S1	S2	T1	G	DIS
0.300000E+00	0.900000E+00	0.120000E+01	0.100000E+00	0.525000E+00

TOTAL ROTOR TOOTH FLUX = , 0.610197E+01 (mWb)

S1	S2	T1	G	DIS
0.300000E+00	0.900000E+00	0.120000E+01	0.100000E+00	0.600000E+00

TOTAL ROTOR TOOTH FLUX = , 0.608679E+01 (mWb)

S1	S2	T1	G	DIS
0.300000E+00	0.900000E+00	0.120000E+01	0.100000E+00	0.675000E+00

TOTAL ROTOR TOOTH FLUX = , 0.612217E+01 (mWb)

S1	S2	T1	G	DIS
0.300000E+00	0.900000E+00	0.120000E+01	0.100000E+00	0.750000E+00

TOTAL ROTOR TOOTH FLUX = , 0.607758E+01 (mWb)

S1	S2	T1	G	DIS
0.300000E+00	0.900000E+00	0.120000E+01	0.100000E+00	0.825000E+00

TOTAL ROTOR TOOTH FLUX = , 0.593659E+01 (mWb)

S1	S2	T1	G	DIS
0.300000E+00	0.900000E+00	0.120000E+01	0.100000E+00	0.900000E+00

TOTAL ROTOR TOOTH FLUX = , 0.578105E+01 (mWb)

S1	S2	T1	G	DIS
0.300000E+00	0.900000E+00	0.120000E+01	0.100000E+00	0.975000E+00

TOTAL ROTOR TOOTH FLUX = , 0.570665E+01 (mWb)

Computer print out for Fig. 4.5

S1	S2	T1	G	DIS
0.300000E+00	0.300000E+00	0.140000E+01	0.100000E+00	0.000000E+00

TOTAL ROTOR TOOTH FLUX = , 0.874949E+01 (mWb)

S1	S2	T1	G	DIS
0.300000E+00	0.300000E+00	0.140000E+01	0.100000E+00	0.750000E-01

TOTAL ROTOR TOOTH FLUX = , 0.871680E+01 (mWb)

S1	S2	T1	G	DIS
0.300000E+00	0.300000E+00	0.140000E+01	0.100000E+00	0.150000E+00

TOTAL ROTOR TOOTH FLUX = , 0.864424E+01 (mWb)

S1	S2	T1	G	DIS
0.300000E+00	0.300000E+00	0.140000E+01	0.100000E+00	0.225000E+00

TOTAL ROTOR TOOTH FLUX = , 0.853558E+01 (mWb)

S1	S2	T1	G	DIS
0.300000E+00	0.300000E+00	0.140000E+01	0.100000E+00	0.300000E+00

TOTAL ROTOR TOOTH FLUX = , 0.843115E+01 (mWb)

S1	S2	T1	G	DIS
0.300000E+00	0.300000E+00	0.140000E+01	0.100000E+00	0.375000E+00

TOTAL ROTOR TOOTH FLUX = , 0.838748E+01 (mWb)

S1	S2	T1	G	DIS
0.300000E+00	0.300000E+00	0.140000E+01	0.100000E+00	0.450000E+00

TOTAL ROTOR TOOTH FLUX = , 0.835064E+01 (mWb)

continued

continuation

S1	S2	T1	G	DIS
0.300000E+00	0.300000E+00	0.140000E+01	0.100000E+00	0.525000E+00

TOTAL ROTOR TOOTH FLUX = , 0.823613E+01 (mWb)

S1	S2	T1	G	DIS
0.300000E+00	0.300000E+00	0.140000E+01	0.100000E+00	0.600000E+00

TOTAL ROTOR TOOTH FLUX = , 0.805030E+01 (mWb)

S1	S2	T1	G	DIS
0.300000E+00	0.300000E+00	0.140000E+01	0.100000E+00	0.675000E+00

TOTAL ROTOR TOOTH FLUX = , 0.786466E+01 (mWb)

S1	S2	T1	G	DIS
0.300000E+00	0.300000E+00	0.140000E+01	0.100000E+00	0.750000E+00

TOTAL ROTOR TOOTH FLUX = , 0.775130E+01 (mWb)

S1	S2	T1	G	DIS
0.300000E+00	0.300000E+00	0.140000E+01	0.100000E+00	0.825000E+00

TOTAL ROTOR TOOTH FLUX = , 0.772180E+01 (mWb)

S1	S2	T1	G	DIS
0.300000E+00	0.300000E+00	0.140000E+01	0.100000E+00	0.900000E+00

TOTAL ROTOR TOOTH FLUX = , 0.771821E+01 (mWb)

S1	S2	T1	G	DIS
0.300000E+00	0.300000E+00	0.140000E+01	0.100000E+00	0.975000E+00

TOTAL ROTOR TOOTH FLUX = , 0.771786E+01 (mWb)

Computer print out for Fig. 4.6

S1	S2	T1	G	DIS
0.300000E+00	0.900000E+00	0.140000E+01	0.100000E+00	0.000000E+00

TOTAL ROTOR TOOTH FLUX = , 0.731466E+01 (mWb)

S1	S2	T1	G	DIS
0.300000E+00	0.900000E+00	0.140000E+01	0.100000E+00	0.750000E-01

TOTAL ROTOR TOOTH FLUX = , 0.731956E+01 (mWb)

S1	S2	T1	G	DIS
0.300000E+00	0.900000E+00	0.140000E+01	0.100000E+00	0.150000E+00

TOTAL ROTOR TOOTH FLUX = , 0.733514E+01 (mWb)

S1	S2	T1	G	DIS
0.300000E+00	0.900000E+00	0.140000E+01	0.100000E+00	0.225000E+00

TOTAL ROTOR TOOTH FLUX = , 0.736453E+01 (mWb)

S1	S2	T1	G	DIS
0.300000E+00	0.900000E+00	0.140000E+01	0.100000E+00	0.300000E+00

TOTAL ROTOR TOOTH FLUX = , 0.738310E+01 (mWb)

S1	S2	T1	G	DIS
0.300000E+00	0.900000E+00	0.140000E+01	0.100000E+00	0.375000E+00

TOTAL ROTOR TOOTH FLUX = , 0.729423E+01 (mWb)

S1	S2	T1	G	DIS
0.300000E+00	0.900000E+00	0.140000E+01	0.100000E+00	0.450000E+00

TOTAL ROTOR TOOTH FLUX = , 0.709230E+01 (mWb)

continued

continuation

S1	S2	T1	G	DIS
0.300000E+00	0.900000E+00	0.140000E+01	0.100000E+00	0.525000E+00

TOTAL ROTOR TOOTH FLUX = , 0.681670E+01 (mWb)

S1	S2	T1	G	DIS
0.300000E+00	0.900000E+00	0.140000E+01	0.100000E+00	0.600000E+00

TOTAL ROTOR TOOTH FLUX = , 0.653629E+01 (mWb)

S1	S2	T1	G	DIS
0.300000E+00	0.900000E+00	0.140000E+01	0.100000E+00	0.675000E+00

TOTAL ROTOR TOOTH FLUX = , 0.634504E+01 (mWb)

S1	S2	T1	G	DIS
0.300000E+00	0.900000E+00	0.140000E+01	0.100000E+00	0.750000E+00

TOTAL ROTOR TOOTH FLUX = , 0.625236E+01 (mWb)

S1	S2	T1	G	DIS
0.300000E+00	0.900000E+00	0.140000E+01	0.100000E+00	0.825000E+00

TOTAL ROTOR TOOTH FLUX = , 0.622904E+01 (mWb)

S1	S2	T1	G	DIS
0.300000E+00	0.900000E+00	0.140000E+01	0.100000E+00	0.900000E+00

TOTAL ROTOR TOOTH FLUX = , 0.622596E+01 (mWb)

S1	S2	T1	G	DIS
0.300000E+00	0.900000E+00	0.140000E+01	0.100000E+00	0.975000E+00

TOTAL ROTOR TOOTH FLUX = , 0.622564E+01 (mWb)

COMPUTER PRINT OUT RELATING TO Figs. 7.39-7.43 (SECTION 7.6)

IMPORTANT NOTE

The flux values given below for search coils 42 and 49 should be divided by (π x G)

```
   S1              S2              T1              G               DIS
0.318600E+00  0.239000E+00  0.112900E+01  0.478000E-01 -0.103545E+01


   B0 =    0.874691E+00
   A1              A2              A3              A4              A5
0.152206E+00 -0.136865E+00  0.113793E+00 -0.862057E-01  0.576863E-01
   B1              B2              B3              B4              B5
0.923345E-01 -0.902104E-01  0.865873E-01 -0.813747E-01  0.745070E-01

   FLUX OF SEARCH COIL 25 =    0.869472E+00   (mWb)
   FLUX OF SEARCH COIL 26 =    0.171584E+01   (mWb)
   FLUX OF SEARCH COIL 27 =    0.249961E+01   (mWb)
   TOTAL TOOTH FLUX =   0.562337E+01 (SEARCH COIL44 )  (mWb)
   FLUX OF SEARCH COIL 42 =    0.124782E+00   (mWb)
   FLUX OF SEARCH COIL 49 =    0.124782E+00   (mWb)


   S1              S2              T1              G               DIS
0.318600E+00  0.239000E+00  0.112900E+01  0.478000E-01 -0.955800E+00


   B0 =    0.874691E+00
   A1              A2              A3              A4              A5
0.152206E+00 -0.136865E+00  0.113793E+00 -0.862056E-01  0.576863E-01
   B1              B2              B3              B4              B5
0.923345E-01 -0.902104E-01  0.865873E-01 -0.813747E-01  0.745070E-01

   FLUX OF SEARCH COIL 25 =    0.869490E+00   (mWb)
   FLUX OF SEARCH COIL 26 =    0.171577E+01   (mWb)
   FLUX OF SEARCH COIL 27 =    0.255998E+01   (mWb)
   TOTAL TOOTH FLUX =   0.564685E+01 (SEARCH COIL44 )  (mWb)
   FLUX OF SEARCH COIL 42 =    0.124782E+00   (mWb)
   FLUX OF SEARCH COIL 49 =    0.124782E+00   (mWb)
```

continued

continuation

S1	S2	T1	G	DIS
0.318600E+00	0.239000E+00	0.112900E+01	0.478000E-01	-0.876150E+00

B0 = 0.874691E+00

A1	A2	A3	A4	A5
0.152206E+00	-0.136865E+00	0.113793E+00	-0.862056E-01	0.576863E-01
B1	B2	B3	B4	B5
0.923344E-01	-0.902104E-01	0.865873E-01	-0.813747E-01	0.745070E-01

FLUX OF SEARCH COIL 25 = 0.869515E+00 (mWb)
FLUX OF SEARCH COIL 26 = 0.171573E+01 (mWb)
FLUX OF SEARCH COIL 27 = 0.256085E+01 (mWb)
TOTAL TOOTH FLUX = 0.593303E+01 (SEARCH COIL 44) (mWb)
FLUX OF SEARCH COIL 42 = 0.124782E+00 (mWb)
FLUX OF SEARCH COIL 49 = 0.124782E+00 (mWb)

S1	S2	T1	G	DIS
0.318600E+00	0.239000E+00	0.112900E+01	0.478000E-01	-0.796500E+00

B0 = 0.874691E+00

A1	A2	A3	A4	A5
0.152206E+00	-0.136865E+00	0.113793E+00	-0.862056E-01	0.576863E-01
B1	B2	B3	B4	B5
0.923344E-01	-0.902104E-01	0.865873E-01	-0.813747E-01	0.745070E-01

FLUX OF SEARCH COIL 25 = 0.869532E+00 (mWb)
FLUX OF SEARCH COIL 26 = 0.171573E+01 (mWb)
FLUX OF SEARCH COIL 27 = 0.256085E+01 (mWb)
TOTAL TOOTH FLUX = 0.623114E+01 (SEARCH COIL 44) (mWb)
FLUX OF SEARCH COIL 42 = 0.124782E+00 (mWb)
FLUX OF SEARCH COIL 49 = 0.124782E+00 (mWb)

S1	S2	T1	G	DIS
0.318600E+00	0.239000E+00	0.112900E+01	0.478000E-01	-0.716850E+00

B0 = 0.874691E+00

A1	A2	A3	A4	A5
0.152206E+00	-0.136865E+00	0.113793E+00	-0.862056E-01	0.576862E-01
B1	B2	B3	B4	B5
0.923345E-01	-0.902104E-01	0.865873E-01	-0.813747E-01	0.745070E-01

FLUX OF SEARCH COIL 25 = 0.869537E+00 (mWb)
FLUX OF SEARCH COIL 26 = 0.171575E+01 (mWb)
FLUX OF SEARCH COIL 27 = 0.256079E+01 (mWb)
TOTAL TOOTH FLUX = 0.642770E+01 (SEARCH COIL 44) (mWb)
FLUX OF SEARCH COIL 42 = 0.124782E+00 (mWb)
FLUX OF SEARCH COIL 49 = 0.124782E+00 (mWb)

continued

continuation

S1	S2	T1	G	DIS
0.318600E+00	0.239000E+00	0.112900E+01	0.478000E-01	-0.637200E+00

B0 = 0.874691E+00

A1	A2	A3	A4	A5
0.152206E+00	-0.136865E+00	0.113793E+00	-0.862055E-01	0.576862E-01
B1	B2	B3	B4	B5
0.923345E-01	-0.902104E-01	0.865873E-01	-0.813747E-01	0.745071E-01

FLUX OF SEARCH COIL 25 = 0.869530E+00 (mWb)
FLUX OF SEARCH COIL 26 = 0.171577E+01 (mWb)
FLUX OF SEARCH COIL 27 = 0.256074E+01 (mWb)
TOTAL TOOTH FLUX = 0.644780E+01 (SEARCH COIL 44) (mWb)
FLUX OF SEARCH COIL 42 = 0.124782E+00 (mWb)
FLUX OF SEARCH COIL 49 = 0.124782E+00 (mWb)

S1	S2	T1	G	DIS
0.318600E+00	0.239000E+00	0.112900E+01	0.478000E-01	-0.557550E+00

B0 = 0.874691E+00

A1	A2	A3	A4	A5
0.152206E+00	-0.136865E+00	0.113793E+00	-0.862055E-01	0.576862E-01
B1	B2	B3	B4	B5
0.923345E-01	-0.902104E-01	0.865874E-01	-0.813748E-01	0.745071E-01

FLUX OF SEARCH COIL 25 = 0.869506E+00 (mWb)
FLUX OF SEARCH COIL 26 = 0.171577E+01 (mWb)
FLUX OF SEARCH COIL 27 = 0.256071E+01 (mWb)
TOTAL TOOTH FLUX = 0.644800E+01 (SEARCH COIL 44) (mWb)
FLUX OF SEARCH COIL 42 = 0.124782E+00 (mWb)
FLUX OF SEARCH COIL 49 = 0.124782E+00 (mWb)

S1	S2	T1	G	DIS
0.318600E+00	0.239000E+00	0.112900E+01	0.478000E-01	-0.477900E+00

B0 = 0.874691E+00

A1	A2	A3	A4	A5
0.152205E+00	-0.136865E+00	0.113793E+00	-0.862055E-01	0.576862E-01
B1	B2	B3	B4	B5
0.923345E-01	-0.902104E-01	0.865873E-01	-0.813747E-01	0.745071E-01

FLUX OF SEARCH COIL 25 = 0.869473E+00 (mWb)
FLUX OF SEARCH COIL 26 = 0.171574E+01 (mWb)
FLUX OF SEARCH COIL 27 = 0.256071E+01 (mWb)
TOTAL TOOTH FLUX = 0.644800E+01 (SEARCH COIL 44) (mWb)
FLUX OF SEARCH COIL 42 = 0.124782E+00 (mWb)
FLUX OF SEARCH COIL 49 = 0.124782E+00 (mWb)

continued

continuation

S1	S2	T1	G	DIS
0.318600E+00	0.239000E+00	0.112900E+01	0.478000E-01	-0.398250E+00

B0 = 0.874704E+00

A1	A2	A3	A4	A5
0.152182E+00	-0.136847E+00	0.113782E+00	-0.862031E-01	0.576915E-01
B1	B2	B3	B4	B5
0.923345E-01	-0.902104E-01	0.865873E-01	-0.813747E-01	0.745071E-01

FLUX OF SEARCH COIL 25 = 0.869454E+00 (mWb)
FLUX OF SEARCH COIL 26 = 0.171570E+01 (mWb)
FLUX OF SEARCH COIL 27 = 0.256069E+01 (mWb)
TOTAL TOOTH FLUX = 0.644804E+01 (SEARCH COIL 44) (mWb)
FLUX OF SEARCH COIL 42 = 0.124782E+00 (mWb)
FLUX OF SEARCH COIL 49 = 0.124782E+00 (mWb)

S1	S2	T1	G	DIS
0.318600E+00	0.239000E+00	0.112900E+01	0.478000E-01	-0.318600E+00

B0 = 0.875668E+00

A1	A2	A3	A4	A5
0.150390E+00	-0.135436E+00	0.112926E+00	-0.859718E-01	0.580451E-01
B1	B2	B3	B4	B5
0.923340E-01	-0.902100E-01	0.865869E-01	-0.813744E-01	0.745068E-01

FLUX OF SEARCH COIL 25 = 0.868793E+00 (mWb)
FLUX OF SEARCH COIL 26 = 0.171428E+01 (mWb)
FLUX OF SEARCH COIL 27 = 0.255857E+01 (mWb)
TOTAL TOOTH FLUX = 0.645535E+01 (SEARCH COIL 44) (mWb)
FLUX OF SEARCH COIL 41 = 0.124784E+00 (mWb)
FLUX OF SEARCH COIL 49 = 0.124778E+00 (mWb)

S1	S2	T1	G	DIS
0.318600E+00	0.239000E+00	0.112900E+01	0.478000E-01	-0.238950E+00

B0 = 0.883301E+00

A1	A2	A3	A4	A5
0.136056E+00	-0.123295E+00	0.104034E+00	-0.808680E-01	0.567027E-01
B1	B2	B3	B4	B5
0.921805E-01	-0.900672E-01	0.864619E-01	-0.812740E-01	0.744375E-01

FLUX OF SEARCH COIL 25 = 0.863103E+00 (mWb)
FLUX OF SEARCH COIL 26 = 0.170285E+01 (mWb)
FLUX OF SEARCH COIL 27 = 0.254139E+01 (mWb)
TOTAL TOOTH FLUX = 0.656367E+01 (SEARCH COIL 44) (mWb)
FLUX OF SEARCH COIL 42 = 0.125163E+00 (mWb)
FLUX OF SEARCH COIL 49 = 0.123530E+00 (mWb)

continued

continuation

S1	S2	T1	G	DIS
0.318600E+00	0.239000E+00	0.112900E+01	0.478000E-01	-0.159300E+00

B0 = 0.897696E+00

A1	A2	A3	A4	A5
0.113087E+00	-0.101927E+00	0.851256E-01	-0.650052E-01	0.441546E-01
B1	**B2**	**B3**	**B4**	**B5**
0.869961E-01	-0.851293E-01	0.819381E-01	-0.773334E-01	0.712456E-01

FLUX OF SEARCH COIL 25 = 0.850328E+00 (mWb)
FLUX OF SEARCH COIL 26 = 0.167915E+01 (mWb)
FLUX OF SEARCH COIL 27 = 0.250685E+01 (mWb)
TOTAL TOOTH FLUX = 0.678344E+01 (SEARCH COIL 44) (mWb)
FLUX OF SEARCH COIL 42 = 0.132712E+00 (mWb)
FLUX OF SEARCH COIL 49 = 0.956265E-01 (mWb)

S1	S2	T1	G	DIS
0.318600E+00	0.239000E+00	0.112900E+01	0.478000E-01	-0.796500E-01

B0 = 0.911786E+00

A1	A2	A3	A4	A5
0.968282E-01	-0.863236E-01	0.705756E-01	-0.518472E-01	0.326487E-01
B1	**B2**	**B3**	**B4**	**B5**
0.753332E-01	-0.735762E-01	0.705802E-01	-0.662718E-01	0.605986E-01

FLUX OF SEARCH COIL 25 = 0.836573E+00 (mWb)
FLUX OF SEARCH COIL 26 = 0.165475E+01 (mWb)
FLUX OF SEARCH COIL 27 = 0.247187E+01 (mWb)
TOTAL TOOTH FLUX = 0.692255E+01 (SEARCH COIL 44) (mWb)
FLUX OF SEARCH COIL 42 = 0.129933E+00 (mWb)
FLUX OF SEARCH COIL 49 = 0.747704E-01 (mWb)

S1	S2	T1	G	DIS
0.318600E+00	0.239000E+00	0.112900E+01	0.478000E-01	0.000000E+00

B0 = 0.918420E+00

A1	A2	A3	A4	A5
0.899735E-01	-0.804726E-01	0.662203E-01	-0.492519E-01	0.318258E-01
B1	**B2**	**B3**	**B4**	**B5**
0.692723E-01	-0.675151E-01	0.645266E-01	-0.602446E-01	0.546304E-01

FLUX OF SEARCH COIL 25 = 0.779521E+00 (mWb)
FLUX OF SEARCH COIL 26 = 0.159265E+01 (mWb)
FLUX OF SEARCH COIL 27 = 0.240483E+01 (mWb)
TOTAL TOOTH FLUX = 0.699295E+01 (SEARCH COIL 44) (mWb)
FLUX OF SEARCH COIL 42 = 0.980423E-01 (mWb)
FLUX OF SEARCH COIL 49 = 0.980424E-01 (mWb)

continued

continuation

S1	S2	T1	G	DIS
0.318600E+00	0.239000E+00	0.112900E+01	0.478000E-01	0.796500E-01

B0 = 0.911786E+00

A1	A2	A3	A4	A5
0.968282E-01	-0.863236E-01	0.705756E-01	-0.518472E-01	0.326488E-01
B1	B2	B3	B4	B5
0.753333E-01	-0.735762E-01	0.705802E-01	-0.662719E-01	0.605986E-01

FLUX OF SEARCH COIL 25 = 0.611373E+00 (mWb)
FLUX OF SEARCH COIL 26 = 0.142971E+01 (mWb)
FLUX OF SEARCH COIL 27 = 0.224680E+01 (mWb)
TOTAL TOOTH FLUX = 0.692255E+01 (SEARCH COIL 44) (mWb)
FLUX OF SEARCH COIL 42 = 0.747703E-01 (mWb)
FLUX OF SEARCH COIL 49 = 0.129933E+00 (mWb)

S1	S2	T1	G	DIS
0.318600E+00	0.239000E+00	0.112900E+01	0.478000E-01	0.159300E+00

B0 = 0.897696E+00

A1	A2	A3	A4	A5
0.113087E+00	-0.101927E+00	0.851257E-01	-0.650053E-01	0.441547E-01
B1	B2	B3	B4	B5
0.869961E-01	-0.851293E-01	0.819381E-01	-0.773334E-01	0.712456E-01

FLUX OF SEARCH COIL 25 = 0.367572E+00 (mWb)
FLUX OF SEARCH COIL 26 = 0.119563E+01 (mWb)
FLUX OF SEARCH COIL 27 = 0.202332E+01 (mWb)
TOTAL TOOTH FLUX = 0.678344E+01 (SEARCH COIL 44) (mWb)
FLUX OF SEARCH COIL 42 = 0.956265E-01 (mWb)
FLUX OF SEARCH COIL 49 = 0.132712E+00 (mWb)

S1	S2	T1	G	DIS
0.318600E+00	0.239000E+00	0.112900E+01	0.473000E-01	0.238950E+00

B0 = 0.883301E+00

A1	A2	A3	A4	A5
0.136056E+00	-0.123295E+00	0.104034E+00	-0.808680E-01	0.567027E-01
B1	B2	B3	B4	B5
0.921805E-01	-0.900671E-01	0.864619E-01	-0.812740E-01	0.744375E-01

FLUX OF SEARCH COIL 25 = 0.107497E+00 (mWb)
FLUX OF SEARCH COIL 26 = 0.883610E+00 (mWb)
FLUX OF SEARCH COIL 27 = 0.172222E+01 (mWb)
TOTAL TOOTH FLUX = 0.656367E+01 (SEARCH COIL 44) (mWb)
FLUX OF SEARCH COIL 42 = 0.123530E+00 (mWb)
FLUX OF SEARCH COIL 49 = 0.125163E+00 (mWb)

continued

continuation

S1	S2	T1	G	DIS
0.318600E+00	0.239000E+00	0.112900E+01	0.478000E-01	0.318600E+00

B0 = 0.875668E+00

A1	A2	A3	A4	A5
0.150390E+00	-0.135436E+00	0.112926E+00	-0.859718E-01	0.580451E-01
B1	**B2**	**B3**	**B4**	**B5**
0.923340E-01	-0.902100E-01	0.865869E-01	-0.813744E-01	0.745068E-01

FLUX OF SEARCH COIL 25 = 0.228255E+00 (mWb)
FLUX OF SEARCH COIL 26 = 0.737375E+00 (mWb)
FLUX OF SEARCH COIL 27 = 0.158182E+01 (mWb)
TOTAL TOOTH FLUX = 0.645535E+01 (SEARCH COIL 44) (mWb)
FLUX OF SEARCH COIL 42 = 0.124778E+00 (mWb)
FLUX OF SEARCH COIL 49 = 0.124784E+00 (mWb)

S1	S2	T1	G	DIS
0.318600E+00	0.239000E+00	0.112900E+01	0.478000E-01	0.398250E+00

B0 = 0.874704E+00

A1	A2	A3	A4	A5
0.152182E+00	-0.136847E+00	0.113782E+00	-0.862031E-01	0.576915E-01
B1	**B2**	**B3**	**B4**	**B5**
0.923345E-01	-0.902104E-01	0.865873E-01	-0.813747E-01	0.745071E-01

FLUX OF SEARCH COIL 25 = 0.526856E+00 (mWb)
FLUX OF SEARCH COIL 26 = 0.726705E+00 (mWb)
FLUX OF SEARCH COIL 27 = 0.157058E+01 (mWb)
TOTAL TOOTH FLUX = 0.644804E+01 (SEARCH COIL 44) (mWb)
FLUX OF SEARCH COIL 42 = 0.124782E+00 (mWb)
FLUX OF SEARCH COIL 49 = 0.124782E+00 (mWb)

S1	S2	T1	G	DIS
0.318600E+00	0.239000E+00	0.112900E+01	0.478000E-01	0.477900E+00

B0 = 0.874691E+00

A1	A2	A3	A4	A5
0.152205E+00	-0.136865E+00	0.113793E+00	-0.862055E-01	0.576862E-01
B1	**B2**	**B3**	**B4**	**B5**
0.923345E-01	-0.902104E-01	0.865873E-01	-0.813748E-01	0.745071E-01

FLUX OF SEARCH COIL 25 = 0.788821E+00 (mWb)
FLUX OF SEARCH COIL 26 = 0.805675E+00 (mWb)
FLUX OF SEARCH COIL 27 = 0.157046E+01 (mWb)
TOTAL TOOTH FLUX = 0.644800E+01 (SEARCH COIL 44) (mWb)
FLUX OF SEARCH COIL 42 = 0.124782E+00 (mWb)
FLUX OF SEARCH COIL 49 = 0.124782E+00 (mWb)

continued

S1	S2	T1	G	DIS
0.318600E+00	0.239000E+00	0.112900E+01	0.478000E-01	0.557550E+00

B0 = 0.874691E+00

A1	A2	A3	A4	A5
0.152206E+00	-0.136865E+00	0.113793E+00	-0.862055E-01	0.576862E-01
B1	B2	B3	B4	B5
0.923345E-01	-0.902105E-01	0.865874E-01	-0.813748E-01	0.745071E-01

FLUX OF SEARCH COIL 25 = 0.868392E+00 (mWb)
FLUX OF SEARCH COIL 26 = 0.106743E+01 (mWb)
FLUX OF SEARCH COIL 27 = 0.157045E+01 (mWb)
TOTAL TOOTH FLUX = 0.644800E+01 (SEARCH COIL 44) (mWb)
FLUX OF SEARCH COIL 42 = 0.124782E+00 (mWb)
FLUX OF SEARCH COIL 49 = 0.124782E+00 (mWb)

S1	S2	T1	G	DIS
0.318600E+00	0.239000E+00	0.112900E+01	0.478000E-01	0.637200E+00

B0 = 0.874691E+00

A1	A2	A3	A4	A5
0.152206E+00	-0.136865E+00	0.113793E+00	-0.862055E-01	0.576862E-01
B1	B2	B3	B4	B5
0.923345E-01	-0.902104E-01	0.865873E-01	-0.813747E-01	0.745071E-01

FLUX OF SEARCH COIL 25 = 0.869718E+00 (mWb)
FLUX OF SEARCH COIL 26 = 0.137305E+01 (mWb)
FLUX OF SEARCH COIL 27 = 0.157176E+01 (mWb)
TOTAL TOOTH FLUX = 0.644780E+01 (SEARCH COIL 44) (mWb)
FLUX OF SEARCH COIL 42 = 0.124782E+00 (mWb)
FLUX OF SEARCH COIL 49 = 0.124782E+00 (mWb)

S1	S2	T1	G	DIS
0.318600E+00	0.239000E+00	0.112900E+01	0.478000E-01	0.716850E+00

B0 = 0.874691E+00

A1	A2	A3	A4	A5
0.152206E+00	-0.136865E+00	0.113793E+00	-0.862056E-01	0.576862E-01
B1	B2	B3	B4	B5
0.923345E-01	-0.902104E-01	0.865873E-01	-0.813747E-01	0.745070E-01

FLUX OF SEARCH COIL 25 = 0.869619E+00 (mWb)
FLUX OF SEARCH COIL 26 = 0.163505E+01 (mWb)
FLUX OF SEARCH COIL 27 = 0.165065E+01 (mWb)
TOTAL TOOTH FLUX = 0.642770E+01 (SEARCH COIL 44) (mWb)
FLUX OF SEARCH COIL 42 = 0.124782E+00 (mWb)
FLUX OF SEARCH COIL 49 = 0.124782E+00 (mWb)

continued

continuation

S1	S2	T1	G	DIS
0.318600E+00	0.239000E+00	0.112900E+01	0.478000E-01	0.796500E+00

B0 = 0.874691E+00

A1	A2	A3	A4	A5
0.152206E+00	-0.136865E+00	0.113793E+00	-0.862056E-01	0.576863E-01
B1	B2	B3	B4	B5
0.923344E-01	-0.902104E-01	0.865873E-01	-0.813747E-01	0.745070E-01

FLUX OF SEARCH COIL 25 = 0.869511E+00 (mWb)
FLUX OF SEARCH COIL 26 = 0.171463E+01 (mWb)
FLUX OF SEARCH COIL 27 = 0.191224E+01 (mWb)
TOTAL TOOTH FLUX = 0.623114E+01 (SEARCH COIL 44) (mWb)
FLUX OF SEARCH COIL 42 = 0.124782E+00 (mWb)
FLUX OF SEARCH COIL 49 = 0.124782E+00 (mWb)

S1	S2	T1	G	DIS
0.318600E+00	0.239000E+00	0.112900E+01	0.478000E-01	0.876150E+00

B0 = 0.874691E+00

A1	A2	A3	A4	A5
0.152206E+00	-0.136865E+00	0.113793E+00	-0.862056E-01	0.576863E-01
B1	B2	B3	B4	B5
0.923344E-01	-0.902104E-01	0.865873E-01	-0.813747E-01	0.745070E-01

FLUX OF SEARCH COIL 25 = 0.869463E+00 (mWb)
FLUX OF SEARCH COIL 26 = 0.171591E+01 (mWb)
FLUX OF SEARCH COIL 27 = 0.221780E+01 (mWb)
TOTAL TOOTH FLUX = 0.593303E+01 (SEARCH COIL 44) (mWb)
FLUX OF SEARCH COIL 42 = 0.124782E+00 (mWb)
FLUX OF SEARCH COIL 49 = 0.124782E+00 (mWb)

S1	S2	T1	G	DIS
0.318600E+00	0.239000E+00	0.112900E+01	0.478000E-01	0.955800E+00

B0 = 0.874691E+00

A1	A2	A3	A4	A5
0.152206E+00	-0.136865E+00	0.113793E+00	-0.862056E-01	0.576863E-01
B1	B2	B3	B4	B5
0.923345E-01	-0.902104E-01	0.865873E-01	-0.813747E-01	0.745070E-01

FLUX OF SEARCH COIL 25 = 0.869473E+00 (mWb)
FLUX OF SEARCH COIL 26 = 0.171582E+01 (mWb)
FLUX OF SEARCH COIL 27 = 0.247988E+01 (mWb)
TOTAL TOOTH FLUX = 0.564685E+01 (SEARCH COIL 44) (mWb)
FLUX OF SEARCH COIL 42 = 0.124782E+00 (mWb)
FLUX OF SEARCH COIL 49 = 0.124782E+00 (mWb)

continued

continuation

S1	S2	T1	G	DIS
0.318600E+00	0.239000E+00	0.112900E+01	0.478000E-01	0.103545E+01

B0 = 0.874691E+00

A1	A2	A3	A4	A5
0.152206E+00	-0.136865E+00	0.113793E+00	-0.862056E-01	0.576863E-01
B1	B2	B3	B4	B5
0.923345E-01	-0.902104E-01	0.865873E-01	-0.813747E-01	0.745070E-01

FLUX OF SEARCH COIL 25 = 0.869506E+00 (mWb)
FLUX OF SEARCH COIL 26 = 0.171575E+01 (mWb)
FLUX OF SEARCH COIL 27 = 0.255961E+01 (mWb)
TOTAL TOOTH FLUX = 0.562337E+01 (SEARCH COIL 44) (mWb)
FLUX OF SEARCH COIL 42 = 0.124782E+00 (mWb)
FLUX OF SEARCH COIL 49 = 0.124782E+00 (mWb)

S1	S2	T1	G	DIS
0.318600E+00	0.239000E+00	0.112900E+01	0.478000E-01	0.111510E+01

B0 = 0.874691E+00

A1	A2	A3	A4	A5
0.152206E+00	-0.136865E+00	0.113793E+00	-0.862057E-01	0.576863E-01
B1	B2	B3	B4	B5
0.923344E-01	-0.902104E-01	0.865873E-01	-0.813747E-01	0.745070E-01

FLUX OF SEARCH COIL 25 = 0.869530E+00 (mWb)
FLUX OF SEARCH COIL 26 = 0.171572E+01 (mWb)
FLUX OF SEARCH COIL 27 = 0.256092E+01 (mWb)
TOTAL TOOTH FLUX = 0.589924E+01 (SEARCH COIL 44) (mWb)
FLUX OF SEARCH COIL 42 = 0.124782E+00 (mWb)
FLUX OF SEARCH COIL 49 = 0.124782E+00 (mWb)

Computer print out for Fig. 7.43

S1	S2	T1	G	DIS
0.318600E+00	0.239000E+00	0.112900E+01	0.478000E-01	0.000000E+00

TOTAL STATOR TOOTH FLUX = , 0.592300E+01 (mWb)

S1	S2	T1	G	DIS
0.318600E+00	0.239000E+00	0.112900E+01	0.478000E-01	0.796500E-01

TOTAL STATOR TOOTH FLUX = , 0.591483E+01 (mWb)

S1	S2	T1	G	DIS
0.318600E+00	0.239000E+00	0.112900E+01	0.478000E-01	0.159300E+00

TOTAL STATOR TOOTH FLUX = , 0.575932E+01 (mWb)

S1	S2	T1	G	DIS
0.318600E+00	0.239000E+00	0.112900E+01	0.478000E-01	0.238950E+00

TOTAL STATOR TOOTH FLUX = , 0.560223E+01 (mWb)

S1	S2	T1	G	DIS
0.318600E+00	0.239000E+00	0.112900E+01	0.478000E-01	0.318600E+00

TOTAL STATOR TOOTH FLUX = , 0.561046E+01 (mWb)

S1	S2	T1	G	DIS
0.318600E+00	0.239000E+00	0.112900E+01	0.478000E-01	0.398250E+00

TOTAL STATOR TOOTH FLUX = , 0.562376E+01 (mWb)

continued

continuation

S1	S2	T1	G	DIS
0.318600E+00	0.239000E+00	0.112900E+01	0.478000E-01	0.477900E+00

TOTAL STATOR TOOTH FLUX = , 0.562419E+01 (mWb)

S1	S2	T1	G	DIS
0.318600E+00	0.239000E+00	0.112900E+01	0.478000E-01	0.557550E+00

TOTAL STATOR TOOTH FLUX = , 0.562400E+01 (mWb)

S1	S2	T1	G	DIS
0.318600E+00	0.239000E+00	0.112900E+01	0.478000E-01	0.637200E+00

TOTAL STATOR TOOTH FLUX = , 0.562388E+01 (mWb)

S1	S2	T1	G	DIS
0.318600E+00	0.239000E+00	0.112900E+01	0.478000E-01	0.716850E+00

TOTAL STATOR TOOTH FLUX = , 0.562418E+01 (mWb)

S1	S2	T1	G	DIS
0.318600E+00	0.239000E+00	0.112900E+01	0.478000E-01	0.796500E+00

TOTAL STATOR TOOTH FLUX = , 0.562454E+01 (mWb)

S1	S2	T1	G	DIS
0.318600E+00	0.239000E+00	0.112900E+01	0.478000E-01	0.876150E+00

TOTAL STATOR TOOTH FLUX = , 0.563683E+01 (mWb)

S1	S2	T1	G	DIS
0.318600E+00	0.239000E+00	0.112900E+01	0.478000E-01	0.955800E+00

TOTAL STATOR TOOTH FLUX = , 0.580548E+01 (mWb)

continued

continuation

S1	S2	T1	G	DIS
0.318600E+00	0.239000E+00	0.112900E+01	0.478000E-01	0.103545E+01

TOTAL STATOR TOOTH FLUX = , 0.607381E+01 (mWb)

S1	S2	T1	G	DIS
0.318600E+00	0.239000E+00	0.112900E+01	0.478000E-01	0.111510E+01

TOTAL STATOR TOOTH FLUX = , 0.625991E+01 (mWb)

STOP 000000